Aix*Marseille université
Socialement engagée

NNT : 2024AIXM0001

THÈSE DE DOCTORAT

Soutenue à Aix-Marseille Université
le 7 novembre 2024 par

Mathieu CAROLE

Développement d'un diagnostic de diffusion Thomson Haute Résolution pour le contrôle temps réel de l'extraction de particules et de puissance à partir des profils cinétiques de bords

Discipline
Physique et Sciences de la Matière

Spécialité
Energie, Rayonnement et Plasmas

École doctorale
ED352, PHYSIQUE ET SCIENCES DE LA MATIERE

Laboratoire/Partenaires de recherche
Institut de Recherche sur la Fusion par confinement Magnétique - CEA Saint-Paul-lez-Durance

Composition du jury

Sedina Tsikata Carbon Neutral Energy Solutions Laboratory	Rapporteure
Roberto Pasqualotto Consortium RFX	Rapporteur
Petra Bilkova Institute of Plasma Physics	Examinatrice
Olivier Peyrusse Aix-Marseille University	Président du jury
Roland Sabot CEA/IRFM	Directeur de thèse
Nicolas Fedorczak CEA/IRFM	Co-encadrant
Patrick Blanchard Swiss Plasma Center	Membre invité
Rory Scannel UKAEA/CCFE	Membre invité

EUROfusion

cea irfm

Affidavit

Je soussigné, Mathieu Carole, déclare par la présente que le travail présenté dans ce manuscrit est mon propre travail, réalisé sous la direction scientifique de Roland Sabot, dans le respect des principes d'honnêteté, d'intégrité et de responsabilité inhérents à la mission de recherche. Les travaux de recherche et la rédaction de ce manuscrit ont été réalisés dans le respect à la fois de la charte nationale de déontologie des métiers de la recherche et de la charte d'Aix-Marseille Université relative à la lutte contre le plagiat.

Ce travail n'a pas été précédemment soumis en France ou à l'étranger dans une version identique ou similaire à un organisme examinateur.

Fait à Marseille 12 septembre 2024



Cette œuvre est mise à disposition selon les termes de la Licence Creative Commons Attribution - Pas d'Utilisation Commerciale - Pas de Modification 4.0 International.

Liste de publications et participation aux conférences

Liste des publications et/ou brevets réalisées dans le cadre du projet de thèse:

1. M Carole, Ch Bouchand, G Colledani, N Fedorczak, A Magnino, Y Moudden, G Moureau, L Schiesko, S Vives, R Sabot, A Diallo. " Synthetic diagnostic for the design of WEST High Resolution Thomson Scattering diagnostic", accepté pour publication dans Journal of Instrumentation le 31 Juillet 2024.

Participation aux conférences et écoles d'été au cours de la période de thèse:

1. Posters : LAPD conference - September 10th to 14 th 2023 - Kyoto, Japan
2. Summer School : SUMTRAIC - August 27th to September 8th 2023 - Prague, Czech Republic
3. Virtual event : 8 Bit PHD event - November 22nd to 23 rd 2021 (Online)

Résumé et mots clés

La fusion par confinement magnétique est explorée pour répondre aux besoins énergétiques mondiaux, mais sa maîtrise reste un défi, nécessitant l'étude approfondie de la physique des plasmas dans des réacteurs tels que les tokamaks. Le tokamak WEST, un dispositif français, est conçu pour maintenir des plasmas de longue durée en utilisant des divertors activement refroidis. Pour caractériser ces plasmas, divers diagnostics sont utilisés, mais des limitations subsistent, notamment pour mesurer certaines régions spécifiques du plasma.

Pour surmonter ces limitations, un nouveau diagnostic de diffusion Thomson est en cours d'installation sur WEST. Ce système, basé sur la diffusion de photons, permettra d'estimer avec précision la température et la densité électroniques à différents points du plasma. Le diagnostic utilise des détecteurs spécifiques appelés polychromateurs qui analysent le spectre diffusé en plusieurs canaux, permettant ainsi des mesures plus précises.

La thèse a pour objectif de développer ce diagnostic et de l'utiliser pour étudier les modes de confinement et le transport des particules dans divers scénarios plasma. La mise en service du diagnostic a permi d'acquérir et de traiter les premiers signaux du diagnostic en troisième année.

L'auteur a contribué au développement du diagnostic à travers trois aspects : la conception d'une ligne laser, le développement d'un banc de calibration spectral, et la création d'une interface de contrôle pour l'acquisition des données. Des modèles numériques ont également été développés pour simuler les performances du diagnostic et estimer les erreurs potentielles dues à divers facteurs.

Des tests ont montré que les erreurs de mesure du diagnostic étaient comparables à celles d'autres dispositifs similaires utilisés dans le monde. Des efforts sont en cours pour améliorer la précision des mesures et minimiser les erreurs. La première phase de tests a permis d'acquérir des données qui seront utilisées pour affiner les méthodes de traitement du signal et valider le diagnostic.

En conclusion, ce travail préliminaire est essentiel pour le développement et l'amélioration du diagnostic de diffusion Thomson sur le tokamak WEST. Ce diagnostic est crucial pour l'étude des plasmas, car il fournit des mesures indépendantes et absolues, contribuant ainsi de manière significative à la compréhension et à l'optimisation de l'équilibre magnétique dans les réacteurs de fusion.

Mots clés : Instrumentation Optique, Physique du laser, Interaction laser-plasma, tokamak, diagnostic de diffusion Thomson, diagnostic synthétique, flux de chaleur, Rayonnement Bremsstrahlung, charge effective.

Abstract and keywords

Magnetic confinement fusion is being explored to meet the world's energy needs. Still, its mastery remains challenging, requiring the in-depth study of plasma physics in reactors such as tokamaks. The WEST tokamak, a French device, is designed to maintain long discharge plasmas using actively cooled divertors. Various diagnostics are used to characterize these plasmas, but limitations remain, particularly for measuring the Scrape off-layer regions of the plasma.
To overcome these limitations, a new High-Resolution Thomson Scattering diagnostic is being installed on WEST. Based on photon scattering, this system will make it possible to estimate the electronic temperature and density at different points in the plasma accurately. The diagnosis uses specific detectors called polychromators, which analyze the scattered spectrum in several channels, thus allowing for more precise measurements. The thesis's objective is to develop this diagnosis and use it to study the confinement modes and particle transport in various plasma scenarios. The commissioning of the diagnostic, initially planned for the first two years, took time. The first usable results were only obtained in the third year, revealing certain measurement errors that needed to be corrected. The thesis deals with the work done on the Thomson Scattering design and on the performances evaluated with a synthetic diagnostic during the first commissioning. The author's contributions to the development of diagnostics have been significant. These include the design of a laser line, the development of a spectral calibration bench, and the creation of a control interface for data acquisition. In addition, the author has developed numerical models to simulate diagnostic performance and estimate potential errors due to various factors. While tests have shown that diagnostic measurement errors are comparable to similar devices used worldwide, we are not resting on our laurels. Efforts are ongoing to improve measurement accuracy and minimize errors. The first testing phase has already provided valuable data, which will be used to refine our signal processing methods and further validate the diagnosis.
In conclusion, this preliminary work is essential for developing and improving Thomson diffusion diagnostics on the WEST tokamak. This diagnostic is crucial for studying plasmas, as it provides independent and absolute measurements, thus contributing significantly to understanding and optimizing the magnetic balance in fusion reactors.

Keywords: Optical instrument, laser physics, laser-plasma interaction, tokamak, Thomson scattering diagnostics, synthetic diagnostics, heat flux, Bremsstrahlung radiation, effective charge.

Résumé étendu

En 2024, il est clair que nous avons pris conscience que chaque pays est dépendant de l'énergie quelle que soit sa forme. De nos jours, cette ressource est indispensable pour le bon fonctionnement de notre société, que ce soit pour l'acheminement d'eau dans les champs agricoles, l'utilisation de tracteurs pour la récolte du blé ou encore l'utilisation de l'énergie électrique pour l'alimentation des hôpitaux, cette ressource physique est indispensable dans notre vie du quotidien. La crise énergétique de 2021 à 2023 a fait prendre conscience aux français et à son gouvernement de l'importance de cette ressource et particulièrement de l'importance du nucléaire dans la production de l'énergie. Le nucléaire fait référence à l'énergie produite par fission nucléaire. Autrement dit, l'énergie générée par les réactions de fission nucléaire résulte de la division du noyau d'un atome, souvent de l'uranium-235, en deux fragments plus légers lorsqu'il est frappé par un neutron. Ce processus libère de l'énergie sous forme de chaleur. En France, le nucléaire est la principale source d'énergie électrique représentant environ 70 % de l'électricité produite répartis sur 18 sites. Un point fort du nucléaire est sa faible production de CO2 contrairement aux centrales thermique à charbon ou à gaz, ce qui le rend attrayant dans le contexte climatique actuel afin de lutter contre le réchauffement climatique en réduisant l'empreinte carbone de la production d'électricité. De plus, les centrales nucléaires ont l'avantage, contrairement au solaire et l'éolien, d'être pilotables et de produire de lénergie en continue, en fonction de la demande, assurant une stabilité de l'approvisionnement en électricité à l'échelle nationale. Cependant, Il est clair que les réacteurs à fission nucléaire peuvent représenter un risque d'accident nucléaire. Rappelons l'accident nucléaire de Tchernobyl en 1986 ou encore celui de Fukushima en 2011.

Une solution à ces problèmes serait de développer de nouveaux réacteurs nucléaires basés sur le principe de la fusion nucléaire, un processus dans lequel deux atomes légers, comme les iostopes de l'hydrogène (Deutérium D et Tritium T), fusionnent pour former un atome plus lourd, libérant ainsi une grande quantité d'énergie cinétique.

$$\begin{cases} D + D \longrightarrow T\ (1.01MeV) + p\ (3.03MeV) & (0.1) \\ D + D \longrightarrow {}^3He\ (0.82MeV) + n\ (2.45MeV) & (0.2) \\ D + {}^3He \longrightarrow \alpha\ (3.67MeV) + p\ (14.67MeV) & (0.3) \\ D + T \longrightarrow \alpha\ (3.52MeV) + n\ (14.06MeV) & (0.4) \end{cases}$$

Contrairement à la fission, la fusion ne produit pas de déchets radioactifs à vie longue et élimine pratiquement les risques d'emballement incontrôlé des réactions,

rendant cette technologie potentiellement plus sûre et plus propre.
Pour produire de l'énergie par fusion, il est nécessaire d'atteindre des températures de l'ordre de 15 millions de degré au cœur du réacteur pour permettre la fusion des réactifs. Or cela représente un défi technique car aucun matériau ne peut résister à ces températures. Pour pallier à ce problème une solution serait d'utiliser un tokamak, un réacteur par confinement magnétique, qui va exploiter les propriétés d'un gaz ionisé appelé plasma afin de le confiner sans que celui-ci soit en contact avec les parois du réacteur. Cependant, le processus de fusion n'est pas encore maîtrisé, nécessitant l'étude de différentes architectures de tokamak, de divertor, différent matériaux (mur en Carbone, en Béryllium, en Tungstène ...) ou encore différentes configurations magnétiques afin d'apporter les solutions pour des réacteurs industriels.

Du fait de la haute température du plasma en son cœur les produits de fusion sont ionisés et ne peuvent être extrait aisément dans une configuration torique, diluant ainsi le plasma et impactant son confinement. Pour pallier à cette problématique, une configuration dite "configuration divertor" a été développée pour permettre l'extraction des particules et l'amélioration du confinement. Cette configuration se traduit par un équilibre magnétique pouvant se décomposer en deux.
Dans la zone centrale appelée le plasma de cœur, les lignes de champ magnétique sont fermées et confinent efficacement le plasma pour atteindre des températures de l'ordre de 1 à 8 keV et des densités de l'ordre de 10^{19} m-3.
Une seconde région désignée comme le bord du plasma est décrit par l'ouverture des lignes champ magnétique qui sont alors en contact avec le divertor permettant l'extraction des produits de fusion. Ce transport est décrit par un effet diffusif qui transporte les produits de fusion du cœur vers le bord en traversant la dernière ligne de surface magnétique fermé (DSMF). Une fois les produits de fusion soumis au champ magnétique des lignes de champ ouverte, ces derniers se dirigent vers ledit divertor. Le divertor doit ainsi supporter des flux de particules et par conséquent des flux de chaleur, important de l'ordre de 10 MW.m^{-2} pouvant mener à l'érosion de la pièce et donc la dégradation de la machine.

Le tokamak WEST est un tokamak supraconducteur, basé en France, dont les parois internes sont métalliques et entièrement refroidis par eau : Du tungstène sur les zones en contact du plasma (divertor et limiteur) et de l'acier sur les zones exposées au rayonnement du plasma. La particularité de ce tokamak est de pouvoir réalisé des plasmas de longue durée, environ 1000 s pour étudier l'interaction du plasma avec les parois. Afin de maintenir un plasma sur des temps relativement longs deux divertors activement refroidi reçoivent le flux de chaleur provenant du plasma de cœur. Différents scénarios et différentes configuration sont possibles : Parmi les scénarios, il existe une configuration simple correspondant à la formation d'un point X (divertor bas ou haut). D'autre part, il existe des configuration magnétique complexe tel que la configuration double nulle correspondant à la formation de deux points X.

Dans des scénarios plasmas, en configuration simple correspondant à la formation

d'un point X ou double nulle, formation de deux points X. La caractérisation des plasmas produits lors des différents scénarios est réalisé à l'aide de diagnostics, permettant de mesurer dans diverses régions du plasma la densité et la température électroniques. Les diagnostics de réflectométrie et les sondes de Langmuir, sont complémentaires et fournissent des informations sur les profils de densité du cœur jusqu'au bord du plasma. D'autre part le diagnostic ECE et les sondes de Langmuir mesurent la température électronique. L'association des mesures de l'ECE et des sondes Langmuir permettent d'obtenir un profil. Cependant suite à des limites physiques, le diagnostic ECE ne peut pas mesurer correctement la température dans la partie externe de la zone confinée. D'autre part, comme les sondes ne peuvent pas supporter un flux de chaleur trop important, leur utilisation est restreinte à la zone de bord du plasma, à l'extérieur de la dernière surface de flux (séparatrice). Il y a donc une lacune dans le mesure du profil de température entre les mesures du diagnostic ECE et celles fournies par les sondes de Langmuir.

Pour remédier à ce problème, un nouveau diagnostic optique de diffusion Thomson est en cours d'installation sur le tokamak afin d'estimer localement la température et la densité électronique du plan médian jusqu'en haut de la machine. Ce système sera composé de deux télescopes qui observeront le faisceau laser latéralement afin de collecter les photons diffusés. Cela représentera 50 points de mesure locale dans le plan poloidal : 20 points de mesure dans le plasma de coeur avec une résolution verticale de 25 mm et 30 points de mesure dans le plasma de bord avec une résolution de 6 mm. Les longueurs de gradient au bord étant de l'ordre du centimètre (~ 3 cm), ce diagnostic permettra de fournir de profils de densité et température permettant de caractériser le piédestal, la zone au bord du plasma où se développe des modes de confinement amélioré comme le mode H.

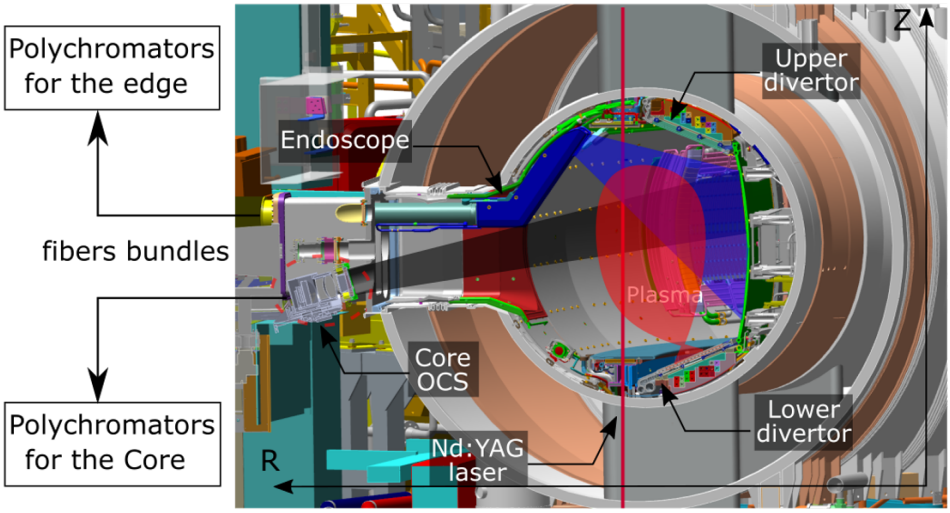

FIGURE 1 : Implémentation du diagnostic de diffusion Thomson sur le tokamak WEST

Le principe de la diffusion Thomson repose sur l'interaction des particules chargés

du milieu avec un champ électrique incident. Dans notre cas, nous étudions une diffusion Thomson incohérente qui résulte de la diffusion des photons incidents avec les électrons du milieu. Lorsque le faisceau laser est envoyé dans le plasma, il entre en collision avec lesdites particules provoquant une diffusion du rayonnement lumineux par élargissement Doppler à partir duquel on va pouvoir remonter à la température locale des électrons. Induisant ainsi une puissance de diffusion dépendant du spectre des électrons, dépendant lui-même de la température électronique locale et de la densité électronique.

La puissance diffusée en diffusion Thomson incohérente dépend de l'énergie photonique incidente, de la densité d'électrons, du volume de diffusion et de l'angle solide du détection. L'amplitude du signal permet ainsi de remonter à la densité électronique. La section efficace de diffusion étant très petite, il faut utiliser des laser impulsionnels de l'ordre du Joule par impulsion. De plus, si on souhaite une bonne résolution sub-centimétrique, il faut augmenter l'angle solide de détection.

En physique des tokamaks, il est d'usage d'utiliser comme détecteur un polychromateur. Cet instrument optique qui joue un rôle clé dans l'analyse de ce rayonnement diffusé décompose la lumière diffusée sur plusieurs canaux à l'aide de filtres interférentiels. Permettant de mesurer l'intensité de la lumière dans différentes gammes spectrales $\Delta\lambda$ ainsi que la température électronique. Chaque canal est conçu d'un filtre interférentiel transmettant les photons sur un domaine spectral $\Delta\lambda$, d'une photodiode à avalanche, convertissant les flux incident en un signal électrique et d'une carte électronique pour amplifier le signal et réduire le bruit associé à la mesure. Les signaux électriques issus des différents canaux sont ensuite analysés pour estimer la température et la densité électroniques. En d'autres mots, l'ensemble des signaux mesurés nous informe sur l'élargissement du spectre diffusé, et donc sur la température locale. Tandis que l'amplitude du signal sur les différents canaux nous permet d'estimer la densité électronique locale. Notons que ce diagnostic est crucial pour obtenir des mesures précises dans un environnement complexe tel que le tokamak. Dans le cas de WEST, trois types de polychromateur sont utilisés : des polychromateur pour les mesure de cœur et des polychromateurs pour les mesures de bord tout deux composés de 5 canaux adaptés adaptés à la gamme de température (1eV à 2 keV au bord, 10 eV à 10 keV pour les voies centrales). Un troisième type de polychromateur composé d'un seul canal est utilisé pour l'alignement du diagnostic sur la machine.

Le transport de particules et l'extraction de puissance sont fortement liés aux conditions au bord du plasma. La formation de gradient de densité et de température induit des gradients de pression importants impactant le transport de matière et d'énergie en le rendant turbulent. Afin d'étudier et caractériser ce transport, il a été proposé dans le cadre de cette thèse de travailler sur le développement du diagnostic et de l'exploiter afin de caractériser les modes de confinement en fonction des scénarios plasma. Le plan initial était de mettre en service le diagnostic au cours des deux premières années

de thèse afin de pouvoir déterminer des profils de densité et de température avec une résolution spatiale élevée. La dernière année de thèse serait consacrée à l'étude et à la caractérisation du transport de particule et à l'estimation du flux de chaleur, reliant les mesures dite "upstream" au mesure des cibles du divertor pour différent scénarios de plasma.

Le diagnostic de diffusion étant en phase de conception à mon arrivé j'ai pris part à son développement sous trois aspects. Premièrement par un aspect technique, j'ai travaillé sur le développement de la ligne laser permettant le transport du faisceau du sous-sol du halle Tore vers le haut du tokamak. Ce travail consista à concevoir un système d'alignement pilotable à distance, depuis la salle de contrôle, tout en préservant la sécurité des opérateurs lors de l'exploitation de deux lasers Nd :YAG, lasers de classe IV. Tout d'abord le travail consista à définir un cahier des charges contenant l'ensemble des contraintes techniques et électrotechniques afin de dimensionner un système d'alignement laser pouvant être piloté à distance, depuis la salle contrôle commande, et étant compatible avec l'architecture du réseau pour des mesures en temps réel. Cette première phase mena au dimensionnement du système optique ainsi qu'à la sélection des montures piézoélectriques, des caméras et à leurs vérifications en laboratoire de test. Notamment, un système d'alignement reproduisant le chemin optique du laser sur environ 20 m a été réalisé en laboratoire pour avoir une procédure d'alignement lors de l'opération sur le tokamak. De plus, cette tâche mena au développement d'une interface Homme-Machine permettant le pilotage de montures et l'acquisition de flux vidéo depuis la salle contrôle commande (en Labview).

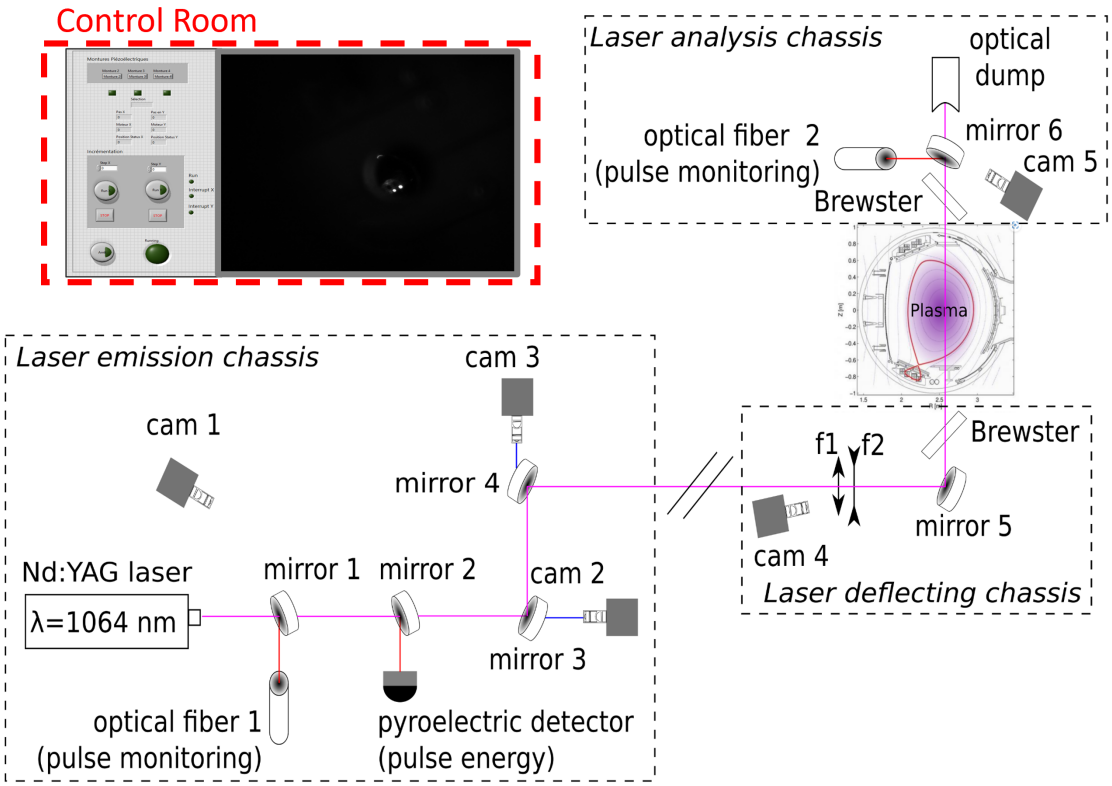

FIGURE 2 : Ligne laser sur WEST

A ceci s'ajoute la conception d'un banc de calibration spectral, utile à la caractérisation des détecteurs. Ce travail fut réalisé à la suite d'une collaboration avec l'Institut de Physique des Plasmas de Prague (IPP) qui me forma à cette procédure nécessaire à l'estimation de la température et de la densité électronique. En particulier, ce travail mena au développement d'un programme permettant de déterminer les fonctions de transfert des cinq voies des polychromateurs, à l'achat de composants opto-mécaniques, d'un monochromateur et d'une avalanche à photodiode.

Un deuxième aspect du projet de thèse fut le développement d'un diagnostic synthétique : jumeau numérique du diagnostic de diffusion Thomson permettant de valider le design, d'évaluer les performances du diagnostic et d'interpréter les signaux expérimentaux dans le cadre de WEST. Des modèles physiques tels que la propagation du faisceau laser, la création de spectre théorique de diffusion Thomson, de diffusion Raman, du rayonnement Bremsstrahlung, de la transmission des photons et la conversion du spectre en signaux ont été implémentés pour permettre la validation du diagnostic en évaluant ses performances à travers des tests de sensibilité. Une validation de l'architecture du diagnostic fut validée par un budget photonique qui fut comparé aux résultats obtenu le tokamak anglais MASTU et le tokamak Tchèque COMPASS.

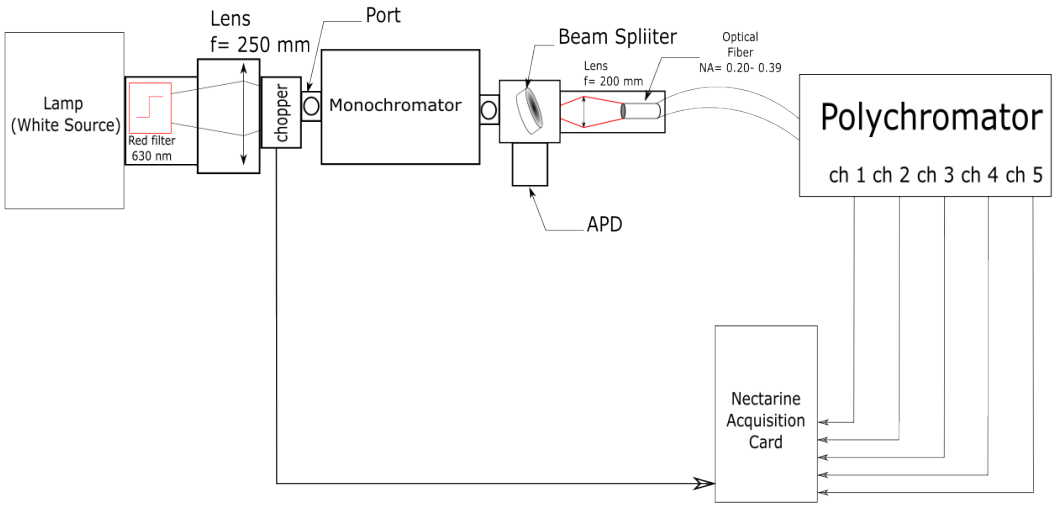

FIGURE 3 : Banc de Calibration sur WEST

Le diagnostic synthétique été utilisé pour estimer l'erreur sytématique qu'induirait un léger désalignement du diagnostic lors du montage. De plus, des simulations de signaux intégrant un bruit de mesure mena à l'estimation des erreurs relatives de la température, de la densité et de la pression électronique pour les polychromateurs de cœur et de bord. En tenant compte du design du diagnostic et en supposant un niveau de bruit de 5 % sur les signaux acquis. En considérant les fonctions d'instrument des polychromateurs, le diagnostic a permis de mettre en évidence une erreur relative compris entre 5 et 20 % pour la température, 5 à 10 % pour la densité électronique et 4 à 12 % pour la pression. De même, une recherche de linéarité entre l'erreur relative associée à la pression électronique a été initiée mais n'a pour l'instant pas montrer de résultat probant. Une incertitude de 5 à 10% est comparable aux estimations d'erreurs publiées par les différentes équipes travaillant sur les diagnostics de diffusion Thomson sur les tokamaks. Il n'est pour l'instant pas exclu qu'une estimation sera faite à l'avenir en intégrant dans le code des paramètres expérimentaux, le code le permettant. A titre d'exemple l'ensemble des signaux des simulations a été réalisé à partir des fonctions de transfert calibrées par le fabricant anglais.

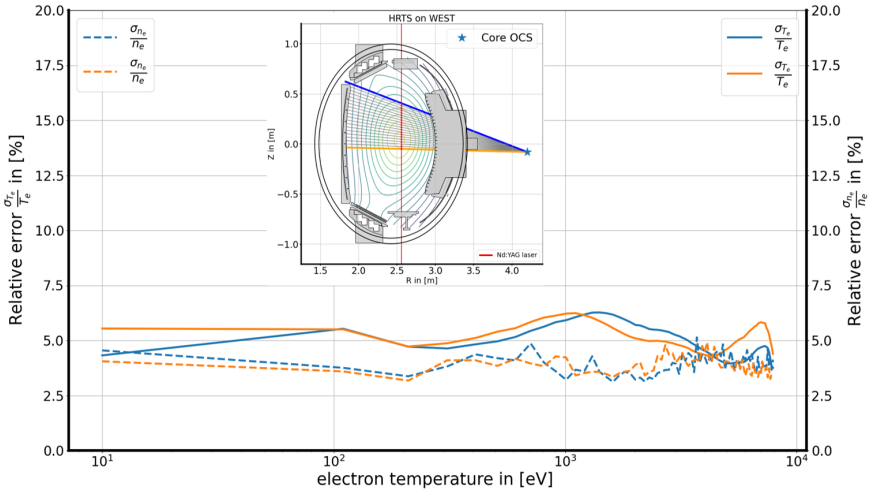

FIGURE 4 : Estimation de l'erreurs relatives pour le télescope de coeur en exploitant les fonctions instrumentales des polychromateurs.

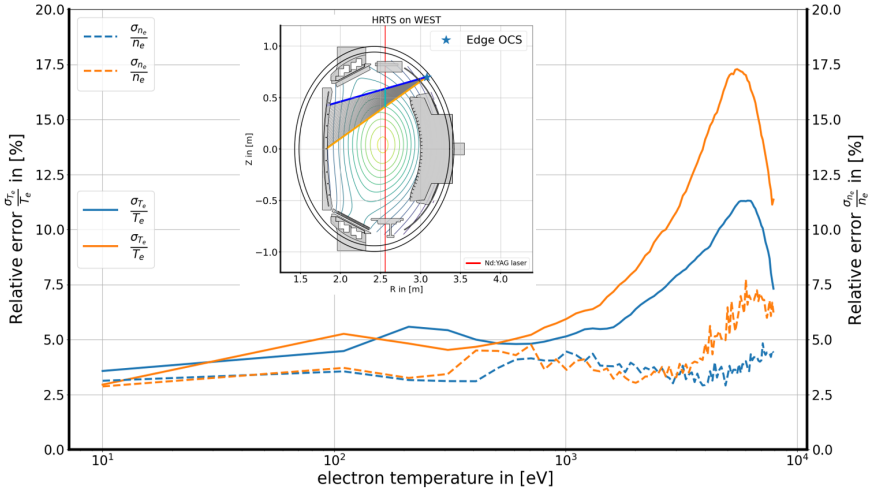

FIGURE 5 : Estimation de l'erreurs relatives pour le télescope de bord en exploitant les fonctions instrumentales des polychromateurs.

Pour finir, une première mise en service partielle du diagnostic a été réalisées lors de la campagne expérimentale C9. Les premières mesures du diagnostic de diffusion Thomson ont été acquis le 24 janvier 2024 et l'exploitation s'est poursuivi jusqu'en mai 2024 sur différents scénarios plasma. Cette mise en service du diagnostic a été réalisée à partir d'un système laser simplifié avec seulement deux points de mesures au cœur du plasma. L'objectif principal était de mesurer la température au centre du plasma afin de pouvoir comparer nos résultats avec les autres diagnostics tels que l'ECE et le spectroscope XICS. Dans un premier temps, les mesures acquises ont fait l'objet d'une analyse du signal par la caractérisation du bruit et du rapport bruit sur signal (RBS), par l'identification de deux sources de bruits : le bruit électronique et

le bruit associé au rayonnement Bremsstraglung. En particulier, une estimation du rapport signal sur bruit a été réalisée et il a été observé que le bruit est différent des bruits simulés avec le diagnostic synthétique. En effet, il a été observé que les canaux des polychromateurs ne répondent de manière identique aux différentes sources de bruit, de par la propriété des filtres interférentiels n'ayant pas les mêmes facteurs de transmission. Dans un second temps, les données ont été exploitées afin de valider la méthode de traitement du signal. L'estimation s'est faite à partir d'une méthode de régression par la méthode des moindres carrés.

Ce travail permit de mettre en évidence les points forts de ce code pour estimer une température dans un environnement bruité. Des comparaisons ont été réalisées entre un algorithme simplifié dédié au temps réel et un programme plus complexe permettant de supprimer les impacts du bruit sur les signaux. Cette comparaison mit en évidence une linéarité entre les deux algorithmes, cependant, l'algorithme temps réel induit un biais de 15% sur l'estimation de la température et de 10 % sur l'estimation de la densité.

Dans un troisième temps, une estimation de l'erreur relative sur la température électronique sur différents chocs plasma ont été effectué puis représenté en fonction du courant plasma moyen afin de déterminer si l'amplitude du courant pouvait être corrélé aux fluctuation des mesures. Tout d'abord, bien que le nombre de donnée soit limité, ce résultat ne semble pas montrer de corrélation entre le courant le plasma et l'erreur relative de mesure. Cependant, il faut noter que les erreurs relatives estimées sont supérieures aux erreurs relatives simulés par le diagnostic synthétique mais pour autant du même ordre. On explique ce résultat par la caractéristiques des fonctions d'instrument qui expérimentalement ont des sources et des niveaux de bruit différent.

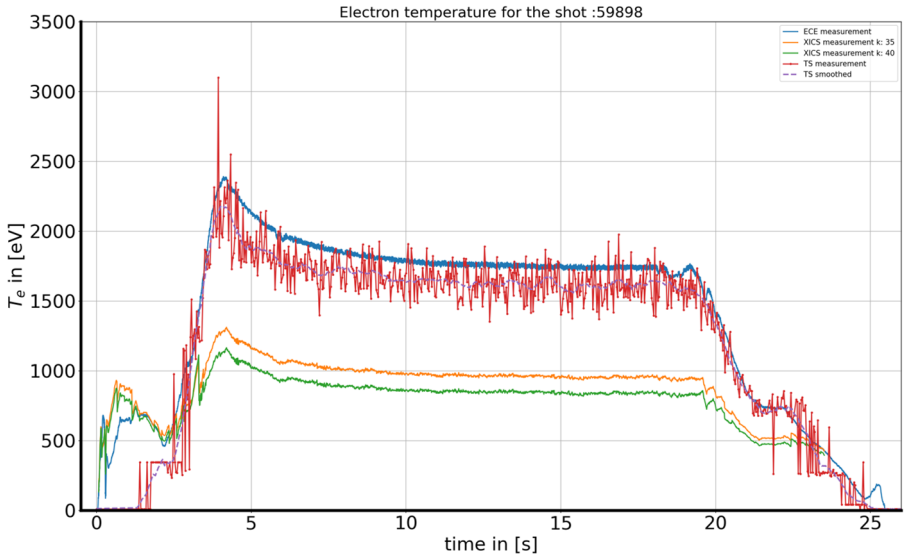

FIGURE 6 : Comparaison au cours du temps de la température électronique estimé avec le diagnostic de diffusion Thomon, l'ECE et la spectroscopie XICS

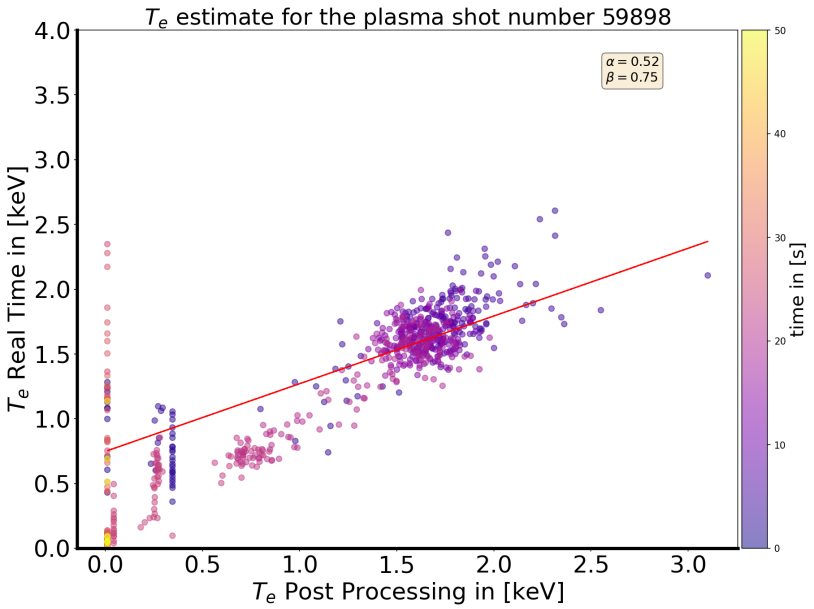

FIGURE 7 : Comparaison de l'estimation de la température électronique entre l'algorithme temps réel et le post-traitement

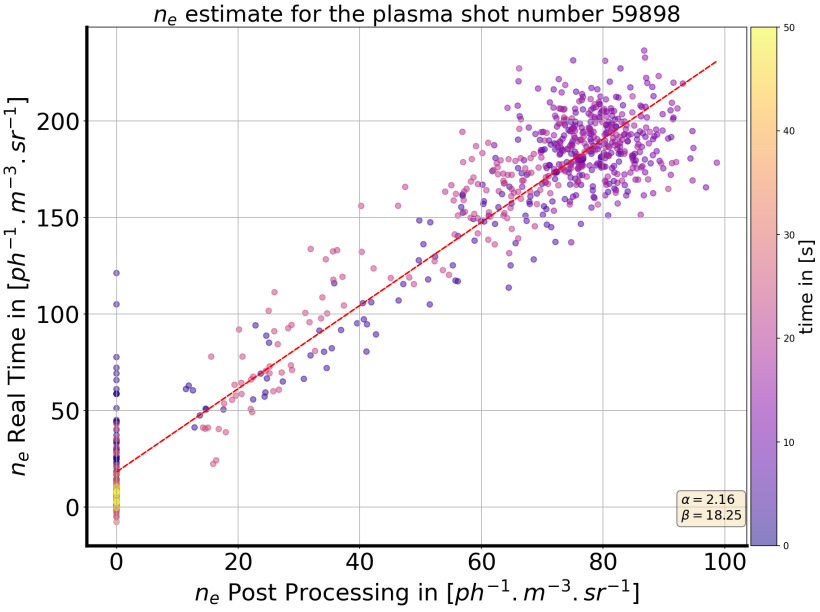

FIGURE 8 : Comparaison de l'estimation de la densité électronique entre l'algorithme temps réel et le post-traitement

En conclusion, le diagnostic de diffusion Thomson est un diagnostic fondamentale présent dans de nombreux Tokamaks, du fait de sa mesure absolue dans la référence machine. Ce diagnostic est indépendant de l'équilibre magnétique et de ce fait il

apportera une plus value pour l'amélioration de la reconstruction de l'équilibre magnétique ou encore de la validation des données des autres diagnostics. Le travail mené dans le cadre de cette thèse fut un travail s'inscrivant dans le développement du diagnostic jusqu'à la première mesure sur plasma. Ce travail a été essentiel pour mettre en place l'ensemble des outils nécessaires, qui prendront tout leur sens une fois le diagnostic pleinement opérationnel.
Le développment de la ligne laser ...
Le diagnostic synthétique ...
Le développement des algorithmes permettant l'organisation et l'exploitation des données brutes a permis d'évaluer la température électronique dans le plasma de coeur. Ces outils permettront d'obtenir automatiquement des profils de densité et de température, essentiels pour diverses applications telles que le contrôle de la position du plasma, la caractérisation du plasma de bord par l'étude du transport des particules, des flux de chaleur et de la turbulence.

Remerciements

Je remercie mon responsable le Dr Roland Sabot, ingénieur-chercheur à l'IRFM, pour m'avoir offert l'opportunité de travailler sur le futur diagnostic de diffusion de Thomson du tokamak WEST. Cette expérience m'a permis de développer mes connaissance et mes compétences en physique des plasmas et en ingénierie optique. Des Domaines qui me passionnent et dont j'espère pouvoir travailler à l'avenir.
Je remercie Monsieur Gilles Colledani, chef de projet pour le temps qu'il m'a accordé lors de mon alternance ainsi que durant ma thèse. Son expérience et ses connaissances m'ont été d'une aide précieuse pour réaliser les tâches qui m'ont été confiées.
Je remercie le Dr Nicolas Fedorczak, chercheur à l'IRFM, pour m'avoir supervisé durant ma thèse. Ces conseils m'ont été utiles pour cerner les problématiques liés au pilotage laser et à la difficulté d'obtenir un signal exploitable, ainsi que pour le développement du diagnostic synthétique. Commencer un programme n'est jamais chose aisée, ces conseils m'ont permis de développer progressivement un code qui je l'espère pourra permettre de déterminer le signal de diffusion Thomson.
Je remercie le Dr Loïc Schiesko, chercheur responsable du diagnostic de diffusion Thomson pour le temps qu'il m'a consacré. Nos échanges m'ont permis de m'ouvrir à de nouvelles notions de physique et de mathématique que je ne connaissais pas encore.
Je remerice le Dr Ahmed Diallo, pour son retour d'expérience sur NSTX. L'intérêt porté sur mon travail m'a permis d'acquérir en rigueur.
Je remercie Gilles Moreau, technicien qui m'a aidé pour la mise en place du diagnostic et pour l'ensemble des tests réalisés au cours de ma thèse.
Je remercie le Dr Jean-luc Farjon pour son expertise dans le câblage électrique et ses connaissances sur les bruits parasites liés à l'alimentation sur WEST.
Je remercie le Dr Yassir Moudden ingénieur électronique pour ses conseils et son travail sur les cartes d'acquisition rapide ayant permis l'enregistrement des données du tokamak WEST.
Je ramercie la Dr Betra bilkova, chercheur au sein de l'Insitute of plasma physics of the Czech academic of sciences.
Je ramercie le Dr Petr Bohm, chercheur au sein de l'Insitute of plasma physics of the Czech academic of sciences.
Je ramercie Miroslav Sos, doctorant au sein de l'Insitute of plasma physics of the Czech academic of sciences.
Je remercie le Dr Ekkehard Pasch, chercheur au sein du Max Planck Institute for Plasma Physic de m'avoir aidé à comprendre les problématiques du diagnostic de diffusion Thomson. Ainsi que pour la clarté des articles qu'il a rédigé et publié en 2017, ils m'ont

été d'une grande aide pour cerner les problématique lié à la calibration spectrale et à l'exploitation des données brutes.
Je remercie les chercheurs et ingénieurs de l'IRFM, qui ont participé de près comme de loin à la mise en place du diagnostic de diffusion Thomson sur la machine.
Je remercie mes camarades Amélia Deleau, Maxime Lemetais, Luigi Salazar, David Moiraf, Louis Fevre et bien d'autres encore pour nos échanges, débat et interrogations sur la fusion par confinement magnétique. Ces échanges ont été riches et d'une aide précieuse pour s'assurer de la compréhension de mon sujet et des problématiques liés à la fusion.

Contents

Affidavit 2

Liste de publications et participation aux conférences 3

Résumé et mots clés 4

Abstract and keywords 5

Résumé étendu 6

Remerciements 17

Contents 19

List of Figures 22

List of Tables 27

Liste des acronymes 28

1 Intoduction 32
- 1.1 Fusion energy principle . . . 32
- 1.2 Fusion reactors : Tokamak . . . 34
  - 1.2.1 Magnetic confinement principle . . . 34
  - 1.2.2 The tokamak configuration . . . 35
- 1.3 Fusion Process condition . . . 36
- 1.4 Heating Systems . . . 37
  - 1.4.1 Ohmic heating . . . 38
  - 1.4.2 Radio-frequency heating systems . . . 38
  - 1.4.3 Neutral beam injection systems . . . 38
- 1.5 Power losses in a magnetic fusion device . . . 39
  - 1.5.1 Confinement Energy time . . . 39
  - 1.5.2 Particles transport: Heat flux physics . . . 40
- 1.6 The international ITER project . . . 43
- 1.7 WEST tokamak . . . 44
- 1.8 WEST heating system . . . 45
- 1.9 Electronic density and temperature measurement . . . 46
  - 1.9.1 Atomic Spectroscopy . . . 46
  - 1.9.2 Electromagnetic wave propagation in plasma. . . . 48

1.9.3 Interfero-polarimetry Diagnostic . . . 48
1.9.4 Reflectometry . . . 50
1.9.5 Electron Cyclotron Emission Diagnostic . . . 51
1.9.6 Plasma equilibrium . . . 52
1.10 Discussion: Problematic related to tokamak and link with my study . . . 55
1.11 Summary . . . 60

2 Wave Matter interaction **61**
2.1 Electromagnetic Scattering . . . 61
2.1.1 Compton Scattering . . . 61
2.1.2 Thomson Scattering in the electrodynamics framework . . . 63
2.2 Discussion about the scattered power provided by charged particles . . . 65
2.2.1 Coherent Thomson Scattering . . . 66
2.2.2 Incoherent Thomson Spectra . . . 67
2.3 Principle of Thomson Scattering Diagnostic . . . 70
2.3.1 Measurement principle . . . 70
2.3.2 Pulsed laser for Thomson scattering diagnostic . . . 70
2.4 Summary . . . 73

3 High Resolution Thomson Scattering design on WEST **74**
3.1 Laser beam transport system . . . 75
3.1.1 Optical engineering basis . . . 76
3.1.2 Steering laser line system on WEST . . . 82
3.1.3 Laser alignment Architecture . . . 84
3.2 Optical collecting system . . . 86
3.2.1 Core Optical Collecting System (COCS) . . . 87
3.2.2 Edge Optical Collecting System (EOCS) . . . 88
3.3 Optical properties requirements . . . 90
3.4 Optical fiber bundles . . . 90
3.5 Polychromator . . . 91
3.5.1 Principle . . . 91
3.6 WEST acquisition system . . . 96
3.7 Photonic Budget . . . 97
3.8 Summary . . . 99

4 Synthetic diagnostic in the WEST framework **100**
4.1 Thomson Scattering signal processing basis . . . 101
4.2 Thomson Scattering flux model . . . 103
4.2.1 Laser Beam propagation module . . . 104
4.2.2 Scattering photon flux . . . 107
4.2.3 Scattering photon flux collected . . . 108
4.3 Bremsstrahlung photon flux model . . . 109
4.3.1 Bremsstrahlung power . . . 109
4.3.2 Method . . . 111

4.3.3 Geometrical extent . . . 112
4.4 Optical collecting systems model . . . 113
4.5 Synthetic Signal and processing method . . . 115
4.5.1 Signal modeled . . . 115
4.6 Fitting tools module . . . 119
4.6.1 Ratio evaluation method . . . 119
4.6.2 Least Square regression method . . . 119
4.7 Performances and sensitivity test . . . 121
4.7.1 Impact of the misalignment . . . 121
4.7.2 Impact of the electronic noise on the least square regression method 122
4.8 Summary . . . 129

5 Diagnostic Operation 130
5.1 Spectral calibration . . . 131
5.1.1 Monochromator: key instrument for the spectral calibration . . . 131
5.1.2 Spectral calibration of the COMPASS polychromator . . . 132
5.1.3 Spectral calibration bench for WEST polychromator . . . 135
5.2 Absolute Calibration: Raman Scattering . . . 138
5.3 Summary . . . 141

6 Experimental measurements 142
6.1 Steering laser line system . . . 143
6.2 HRTS commissioning during the 2024 experimental campaign . . . 145
6.2.1 First operation phase: HRTS setup . . . 145
6.2.2 Nectarine Acquisition card and raw data retrieving. . . . 147
6.3 Thomson signal Analysis . . . 150
6.3.1 Scattering pulse characterization . . . 151
6.3.2 Noise characterization . . . 153
6.3.3 Processing Signal method . . . 158
6.4 Discussion . . . 161
6.5 Experimental Result from the C9 campaign. . . . 163
6.6 Discussion about the Noise-to-Signal Ratio observed experimentally . . . 167
6.7 Perspective . . . 168
6.7.1 Steering laser line system . . . 168
6.7.2 Plasma parameters retrieving . . . 170
6.7.3 Real-time measurement . . . 171

7 Conclusion 173

Bibliography 176

List of Figures

1 Implémentation du diagnostic de diffusion Thomson sur le tokamak WEST 8
2 Ligne laser sur WEST 11
3 Banc de Calibration sur WEST 12
4 Estimation de l'erreurs relatives pour le télescope de coeur en exploitant les fonctions instrumentales des polychromateurs. 13
5 Estimation de l'erreurs relatives pour le télescope de bord en exploitant les fonctions instrumentales des polychromateurs. 13
6 Comparaison au cours du temps de la température électronique estimé avec le diagnostic de diffusion Thomon, l'ECE et la spectroscopie XICS 14
7 Comparaison de l'estimation de la température électronique entre l'algorithme temps réel et le post-traitement 15
8 Comparaison de l'estimation de la densité électronique entre l'algorithme temps réel et le post-traitement 15

1.1 Aston curve representing the average binding energy per nucleon versus the number of nucleons in one element edited from [59] 33
1.2 Cross section for the light elements edited from [40] 34
1.3 Confinement basis where the charged particle q turns around the magnetic field lines edited from [59]. 35
1.4 Optimal magnetic confinement in a tokamak edited from [59] 36
1.5 Poloidal cross-section showing the divertor configuration edited from [59] 40
1.6 L and H confinement modes, edited from [32] 43
1.7 Illustration of the ITER tokamak plant 44
1.8 WEST tokamak vessel 45
1.9 Langmuir measurement principle on WEST 47
1.10 Interferometry diagnostic on WEST 50
1.11 Reflectometry principle measurement measuring the electron density at the edge 51
1.12 ECE diagnostic implemented on WEST. The diagnostic measures the electron temperature at the mid-plane with high temporal resolution. 52
1.13 Magnetic probe used to measure the poloidal magnetic flux, edited from [25] 53
1.14 T_e profiles and the pedestal characteristics, from [81] 57
1.15 Decay length measurement, edited from [81] 57
1.16 Plasma parameters profile on ASDEXU, edited from [39] 57

2.1 Photon scattering by an electron assumed to be at rest, edited from [73]. 62
2.2 Schematic Thomson Scattering spectra for one electron edited from [65] 64
2.3 Cross section regarding the charged particle velocity edited from [65]. . 65
2.4 Scattering spectra in coherent Thomson scattering case [54] 67
2.5 Depolarisation Term versus the normalized wavelength. 69
2.6 Thomson Scattering spectra S_{zh} given from the Zuralev function 69
2.7 Ideal Gaussian beam, edited from [24] 72

3.1 Schematic of the High-Resolution Thomson Scattering on WEST tokamak, with OCS fields of view. 75
3.2 Steering laser line system implemented on WEST. The first part of the SLLS was installed in the basement, close to the polychromator. 76
3.3 Lasers combination system 77
3.4 Innolas laser system 78
3.5 Camera quantum efficiency, taken from [20] 80
3.6 Pyroelectric measurement principle [62] 81
3.7 Schematic view of the Beam dump principle. The incident pulse, represented by the red disc, will reflect inside the dump before being absorbed by this last. The red line is a schematic view of the reflection line while the laser pulse is divided the cone. 82
3.8 Schematic of the steering laser line system. The blue line illustrates the optical path of the P-polarization beam. The Purple line represents the laser beam combination of the S-polarization Nd:YAG laser and the laser alignment. The panel is the first version of the LabView program used to steer the mirror and visualize the video stream. 84
3.9 System analysis of the steering laser line system 86
3.10 Zemax simulations for the EOCS (left) and the COCS (right). The EOCS comprises the aperture, a mirror, a pupil, and 5 optics down to an in-situ array of fiber bundles. Below are schematized the shape of the fiber arrays projected on the laser path. 87
3.11 CAD of Core Optical Collecting system installed on the Tokamak. . . . 88
3.12 Longitudinal section of the endoscope allocated to the edge measurement. 89
3.13 Multiplexed fiber used for the alignment polychromator, the sizes is given in [mm] 91
3.14 Polychromator architecture edited from [21] 92
3.15 Conceptual filter curve with definition of λ_{min},λ_{min}, $d\lambda$ and definition of pass-band and out of bands, edited from [21]. 93
3.16 Instrumental functions for the edge and core polychromators 95
3.17 Instrumental function for the alignment polychromators 95
3.18 Acquisition setup for the real-time High-Resolution Thomson Scattering diagnostic. 96

4.1 Convolutions principle 101
4.2 Synthetic diagnostic flowchart where 4 inputs parameters are needed . 103

4.3 Schematic of the synthetic diagnostic workflow, illustrating the five modules implemented in the synthetic diagnostic. 103
4.4 Optical matrix theory 105
4.5 Schematic of the laser alignment system. The laser is first defocused by a focal lens ($f_1 = -250$ mm), then focused through a second translatable lens ($f_2 = 200$ mm). This allows tuning of the position of the laser waist inside the tokamak vessel concerning collecting lines of sight. 106
4.6 Simulation of the beam diameter along the optical path after the second lens. This simulation has been done for a beam diameter of 0.7 mm and a quality factor M^2 equals 1 107
4.7 Scattering angle calculation from the HRTS design on WEST 108
4.8 Free-free Gaunt factor model versus the wavelength for an effective charge Z_{eff} equal to 2 and several electronic temperatures T_e 110
4.9 Bremsstrahlung photon flux model 111
4.10 Transmission simulation of the COCS and the EOCS given by the Optical collecting system module for a scattering spectrum at 1 keV and $n_e = 1.10^{19}$ m^{-3}. The equation 4.31 is applied by using a Monte-Carlo method to simulate the photon transmitted at each normalized wavelength for a laser at 1064 nm and a laser energy equals 2 J. 114
4.11 Edge polychromators: Instrumental functions of each channel function of the wavelength, shown as plain curves (left y-axis). The function integral of the first channel normalizes these functions. Several theoretical diffusion spectra S (from Eq.2.22) built for electron temperatures from 10 eV to 900 eV are shown in dashed curves (right y-axis). The thin red vertical line at $\lambda = 1064$ nm represents the laser wavelength. 116
4.12 Core polychromators: Instrumental functions of each channel function of the wavelength, shown as plain curves (left y-axis). The function integral of the first channel normalizes these functions. Several theoretical diffusion spectra S (from Eq.2.22) built for electron temperatures from 1 keV to 10 keV are shown in dashed curves (right y-axis). The thin red vertical line at $\lambda = 1064$ nm represents the laser wavelength. 117
4.13 $\psi_{k,mod}$ over the T_e. The curves illustrate the pre-processed data which will be used to retrieve n_e and T_e. This data set corresponds to the polychromator 19, designed for the edge measurement. 118
4.14 Least squares regression method test for 3 different electronic temperatures 121
4.15 Relative error on T_e by considering a ±7% LOS misalignment around three reference angles 95°, 102°, 109°, for three different electron temperatures T_e 129 eV, 1 keV, 4 keV 122
4.16 PDF of the signal model for channel 3 with an NSR of 5 % with 100 samples. This corresponds to the signal injected into the program to estimate the error on T_e 123

4.17 Output PDF of T_e model with an NSR of 5 % with 100 samples. T_e is estimated from the least square method by using the pre-processed data set $\psi_{k,mod}$ . . . 124
4.18 Relative error versus the NSR for TS signal simulated at 1 keV and a scattering angle θ at 102° and a constant noise for the 5 polychromator channels . . . 125
4.19 Relative error for the COCS by using the instrumental functions of the core polychromator. . . . 126
4.20 Relative error for EOCS by using the instrumental functions of the edge polychromator. . . . 126
4.21 Relativistic error on the p_e regarding $\frac{\sigma_{n_e}}{n_e}$ and $\frac{\sigma_{T_e}}{T_e}$ for the polychromator 23, for Noise to Signal Ratio (NSR) of 5 % and 100 iterations. . . . 128
4.22 Correlation term computed from T_e retrieved for the polychromator 23, for NSR of 5 % and 100 iterations. . . . 128

5.1 Diffraction grating principle, edited from [22] . . . 132
5.2 spectral calibration bench from COMPASS. . . . 133
5.3 COMPASS APD detector responsivity and white source spectrum used for the spectral calibration as a reference . . . 134
5.4 Normalized instrumental functions of the COMPASS polychromator 504 during the spectral calibration . . . 135
5.5 Schematic of the spectral calibration for WEST . . . 136
5.6 Beam splitter transmission and reflectivity, edited from [17] . . . 137
5.7 APD responsivity versus the wavelength, edited from [23] . . . 138

6.1 Alignment procedure during C9 campaign and stray light evidence from the laser alignment. The picture shows the Brewster windows and the multiple reflections observed. The picture b shows the alignment cases, whereas the picture f corresponds to the correct alignment. . . . 144
6.2 Misalignment observed from the LAC. Misalignment is due to reflection in the two Brewster windows. . . . 144
6.3 COCS installation for C9 experimental campaign. The picture was taken with the AIA-embedded camera. . . . 145
6.4 Laser alignment during the Raman Scattering . . . 146
6.5 Timestamp difference for the plasma shot 59898 . . . 148
6.6 Raw Thomson scattering acquired during a plasma shot. The Raw Signal can be used until the 17th samples and the noise pattern are not removed. 149
6.7 Thomson Scattering signals acquired during the experimental campaign after removing the periodic noise from the Switched capacitor array (SCA). 149
6.8 Signal characterization for the 50th laser shot of the 59901 plasma shot for the 4th channel of the polychromator 19 after chip noise correction. 151
6.9 Pulse duration measured from the signal acquisition . . . 152
6.10 Index pulse maximum measured from the signal acquisition . . . 153
6.11 Electric noise at High and Low-frequency channel during laboratory test 154

6.12 Noise visualization for the 5 channels for the plasma shot 60030 155
6.13 PDF of noise from all channels of a nectarine card. 155
6.14 Noise estimated on 640 first samples for each acquisition during the plasma shots 156
6.15 Correlation time estimation 157
6.16 NSR estimate for three channels for the fast measurement during shot 59898 for the polychromator 19 158
6.17 Post-processing method: Gaussian fitting with the Thomson Scattering pulse 159
6.18 Comparison of synthetic signals with experimental signals 159
6.19 Pulse characterization for the real-time processing 160
6.20 Fit comparisons of real-time and post-processing TS evaluation for the electron temperature 161
6.21 Fit comparisons of real-time and post-processing TS evaluation for the electron density 162
6.22 Electron temperature evolution in the plasma core over the time for different diagnostics 164
6.23 Plasma current for the shot number 59898 164
6.24 PDF of T_e for the first measurement point during a plateau for the shot 59898. 165
6.25 Plasma current for several plasma shots 166
6.26 Temporal trace for the line of sight 10 166
6.27 Temporal trace for the line of sight 18 167
6.28 Experimental Relative error estimation during a plateau for the shot 59910,59898,60158,60167 167
6.29 Pyroelectric test 169
6.30 Signals acquired during the pyroelectric test 169
6.31 Electron density trace 170
6.32 T_e profile for the plasma shot 59898. This is compared with the ECE measurement at the same position. 171
6.33 Real time diagram 172

List of Tables

1.1 Tokamaks in the world 45
1.2 WEST tokamak setting 46
1.3 WEST diagnostic summary table 55

3.1 Optical collecting systems parameters for the HRTS on WEST. 90
3.2 Interference filters used for the WEST polychromators. 95
3.3 Photonic Budget assess for WEST compared to others devices 98

5.1 Molecular constant for the Raman scattering process, taken from [57] . 140

6.1 Optical collecting systems parameters for the HRTS on WEST. 157
6.2 NSR of polychromator channel for several plasma shots 168

List of acronyms

ADC

analog-to-digital converter. 96, 147

AIA

Articulated Inspection Arm. 146

APD

Avalanche photo-diode detector. 93, 94, 115, 131, 134, 137, 138

COCS

Core Optical Collecting System. 87, 125, 145, 146

CTS

Coherent Thomson Scattering. 66

ECE

Electron cyclotron emission. 51, 52, 56, 163, 165, 170

ELM

Edge Localized Mode. 42, 46

EMF

Electromotive Force. 38

EOCS

Edge Optical Collecting System. 88, 113, 114, 146

FA

Faraday Angle. 49

FIR

Far Infrared. 49

FWHM

Full width at half maximum. 92, 151

HRTS

High Resolution Thomson Scattering. 58, 74, 94, 96, 98, 99, 145, 163, 171

ICRH

Ion Cyclotron Resonance Heating. 45, 46

IRFM

Institute for Magnetic Confinement Fusion Research. 44

ITS

Incoherent Thomson Scattering. 67, 70

LAC

Laser analysis chassis. 143, 144

laser

Light amplification by stimulated emission of radiation. 70, 147

LCFS

last closed flux surface. 41, 53

LDC

Laser deflecting chassis. 82

LEC

Laser emission chassis. 82

LHCD

Lower Hybrid Current drive. 45, 46

LID

Line Integrated Density. 49

LIDT

Laser induce damage threshold. 79

LOS

Line of sight. 49, 63, 111, 125

LP

Langmuir Probe. 47, 48

MHD

magnetohydrodynamics. 52

NIR

Near Infrared. 80, 143, 144

NSR

Noise to Signal Ratio. 25, 122, 124, 126, 128, 157, 165, 167

OCS

Optical collecting System. 83, 91, 97, 98, 106, 108, 111, 113, 116, 119, 125, 131, 139

OCSs

Optical collecting Systems. 74, 83, 86, 90, 102, 109, 114

O-mode

Ordinary mode. 48, 50

pe

photo-electron. 94

RT

Real time. 162, 168, 171

SCA

Switched capacitor array. 25, 148, 149

SD

Synthetic Diagnostic. 101, 107, 117, 122, 146

SLLS

Steering Laser Line System. 77, 82, 85, 105, 143, 168

SNR

Signal to Noise Ratio. 77, 88, 92, 94, 102, 153

SOL

Scrappe off layer. 41, 56, 60, 127

TS

Thomson Scattering. 56, 63, 88, 94, 97, 101, 102, 111, 122, 129, 151, 157, 158, 162, 170

UDP

User datagram protocol. 96, 147, 148

WEST

W Environment in Steady-state Tokamak. 44–47, 49, 50, 56, 58, 59, 74, 82, 86–88, 93, 95, 97, 99, 101, 102, 111

XICS

X-ray imaging crystal spectrometer. 47, 53, 163, 165, 170

X-mode

Extraordinary mode. 48, 53

XPR

X point radiator. 163, 166

XUV

extreme ultraviolet. 47

1 Intoduction

Sommaire

1.1 Fusion energy principle . . . 32
1.2 Fusion reactors : Tokamak . . . 34
1.2.1 Magnetic confinement principle . . . 34
1.2.2 The tokamak configuration . . . 35
1.3 Fusion Process condition . . . 36
1.4 Heating Systems . . . 37
1.4.1 Ohmic heating . . . 38
1.4.2 Radio-frequency heating systems . . . 38
1.4.3 Neutral beam injection systems . . . 38
1.5 Power losses in a magnetic fusion device . . . 39
1.5.1 Confinement Energy time . . . 39
1.5.2 Particles transport: Heat flux physics . . . 40
1.5.2.1 Particle Transport and the Scrape of Layer . . . 40
1.5.2.2 Divertor configuration . . . 41
1.5.2.3 Heat flux . . . 41
1.5.2.4 Confinement mode L and H . . . 42
1.6 The international ITER project . . . 43
1.7 WEST tokamak . . . 44
1.8 WEST heating system . . . 45
1.9 Electronic density and temperature measurement . . . 46
1.9.1 Atomic Spectroscopy . . . 46
1.9.1.1 Langmuir Probe . . . 47
1.9.2 Electromagnetic wave propagation in plasma. . . . 48
1.9.3 Interfero-polarimetry Diagnostic . . . 48
1.9.4 Reflectometry . . . 50
1.9.5 Electron Cyclotron Emission Diagnostic . . . 51
1.9.6 Plasma equilibrium . . . 52
1.10 Discussion: Problematic related to tokamak and link with my study . . . 55
1.11 Summary . . . 60

1.1 Fusion energy principle

Atomic nuclei comprise subatomic particles named nucleons; naively, we can think that the atomic mass is the sum of the subatomic particles, the positive charge named

proton of mass m_p, and the neutron mass m_n. However, twentieth-century research has revealed that the sum of the masses of the elements is greater than that of the atomic nuclei, leading to the idea that a part of the mass is used to hold the nuclei together. This physical process is called binding energy B(A,Z) and corresponds to the energy needed to bring nucleons together and prevent the repulsion of positive charges (protons). The atomic mass is then expressed as :

$$M(A,Z)c^2 = Zm_pc^2 + Nm_nc^2 - B(A,Z) \tag{1.1}$$

, where Z and N are the number of protons and neutrons that compose the nuclei, respectively.

In 1920, Arthur Eddington suggested that the sun's radiation was due to the fusion of two atoms, and Hans Bethe explained this in 1939. He concluded that particles can fuse by collision when they have sufficient speed. This phenomenon is possible in extreme conditions, such as the sun, where the temperature is 15 million degrees, allowing the nuclei to cross the Coulomb barrier. The fusion process is, therefore, a nuclear reaction leading, in the case of light elements, to an exo-energetic reaction resulting from the difference in mass between the fused nuclei and the fusion products. Figure 1.1 represents the Aston curve, i.e., the binding energy per nucleon for each element from the periodic table. This quantity passes through a maximum of around 9 MeV, corresponding to the intermediate atomic masses. The first branch corresponds to exo-energetic reactions, i.e., reactions that release energy from light elements. Once the light elements have fused, they form a new, heavier element and release energy in kinetic form.

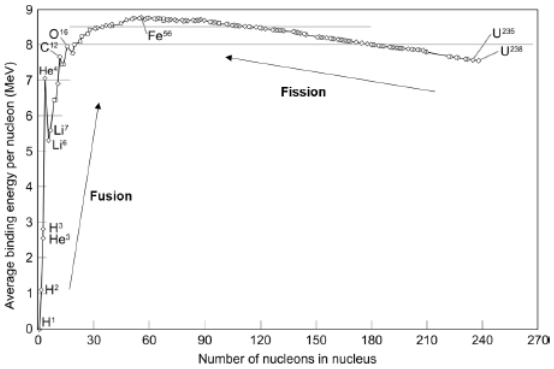

Figure 1.1: Aston curve representing the average binding energy per nucleon versus the number of nucleons in one element edited from [59]

This nuclear energy is six orders of magnitude larger than the energy released in chemical reactions of burning fossil fuels (eV) and proportional to the mass defect defined as the difference between the total individual masses of each nucleon at rest and the mass of the bound nucleus they compose, according to Einstein's energy-mass relation. Consequently, harnessing fusion processes to produce energy seems

to be a solution for the future. This would enable the provision of low-carbon energy while overcoming the impairment of the fission reactors. Nevertheless, fusion is a complex nuclear process that requires extreme conditions. Figure 1.2 shows the cross-section for light elements. The cross-section is not constant and depends on the incident particle energy. In addition, the cross-section is small and in the barn order (1 barn = 10^{-28} m^2). For the D-T reaction, the cross-section reaches a peak at 100 keV, involving the following reactions:

$$\begin{cases} D + D \longrightarrow T\ (1.01MeV) + p\ (3.03MeV) & (1.2) \\ D + D \longrightarrow {}^3He\ (0.82MeV) + n\ (2.45MeV) & (1.3) \\ D + {}^3He \longrightarrow \alpha\ (3.67MeV) + p\ (14.67MeV) & (1.4) \\ D + T \longrightarrow \alpha\ (3.52MeV) + n\ (14.06MeV) & (1.5) \end{cases}$$

, where D is the Deuterium hydrogen isotope. T is the tritium, hydrogen isotope, ${}^3He$ is the Helium. α corresponds to the alpha particle. n is the neutron and p is the proton. For the industrial reactor, the fusion community has decided to investigate the D-T fusion process where the neutron carries the fusion energy (14.06 MeV).

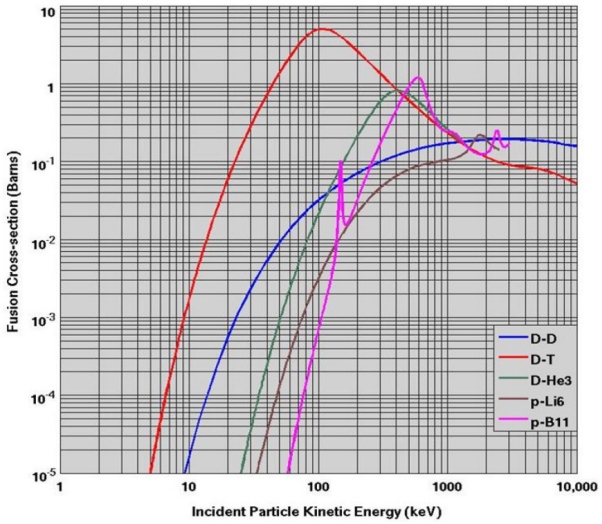

Figure 1.2: Cross section for the light elements edited from [40]

1.2 Fusion reactors : Tokamak

1.2.1 Magnetic confinement principle

Unlike the sun, which confines the particles thanks to gravity, a reactor can not proceed as follows. At high temperatures, the gas is not neutral anymore; it transforms into an ionized gas made of ions and electrons, named plasma. This plasma can be confined in an appropriate device such as the Tokamak. The Tokamak is a thermonuclear fusion

reactor invented in the USSR in 1949 by Oleg Lavrentiev and designed in the 1950s by the Russian physicist Andrei Sakharov. This reactor confines a plasma in a vacuum chamber using an intense magnetic field. It is based on one of the fundamental forces, Laplace's force :

$$\vec{F} = q\vec{v} \times \vec{B} \tag{1.6}$$

Where q is a charged particle (ion or electron), $\vec{v}$ is the velocity vector of the particle considered, and $\vec{B}$ is the magnetic field. As illustrated in the figure 1.3, the charged particles will have a helical motion along the magnetic field line, enabling them to confine a plasma. On the other hand, neutral particles, such as neutrons, can be released and captured out of the reactor to produce energy by converting the kinetic energy with a heat transfer fluid.

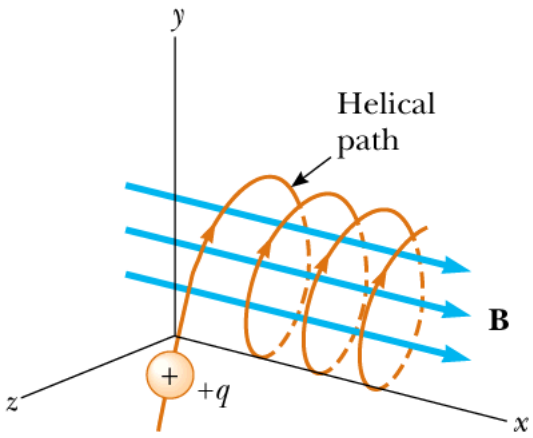

Figure 1.3: Confinement basis where the charged particle q turns around the magnetic field lines edited from [59].

1.2.2 The tokamak configuration

However, using a unique magnetic component does not confine the plasma. This is due to the particles drifting from the curvature of the field lines, leading to a charge separation. The consequence is then to form an electric field, which leads to a rapid loss of the plasma on the wall. To solve this problem, one adds a second component to the magnetic field line - the poloidal magnetic field B_θ. Unlike the Stellarator, the Tokamak used the plasma current (of the MA order)) to provide the poloidal magnetic field line. Hence, the magnetic field consists of the sum of a toroidal magnetic field B_ϕ (of the order of a few Tesla) and the poloidal one B_θ, which is along the torus axis. The application of this magnetic field configuration enables optimum confinement of the plasma, shown in figure 1.4 :

$$\vec{B} = \vec{B_\phi} + \vec{B_\theta} \tag{1.7}$$

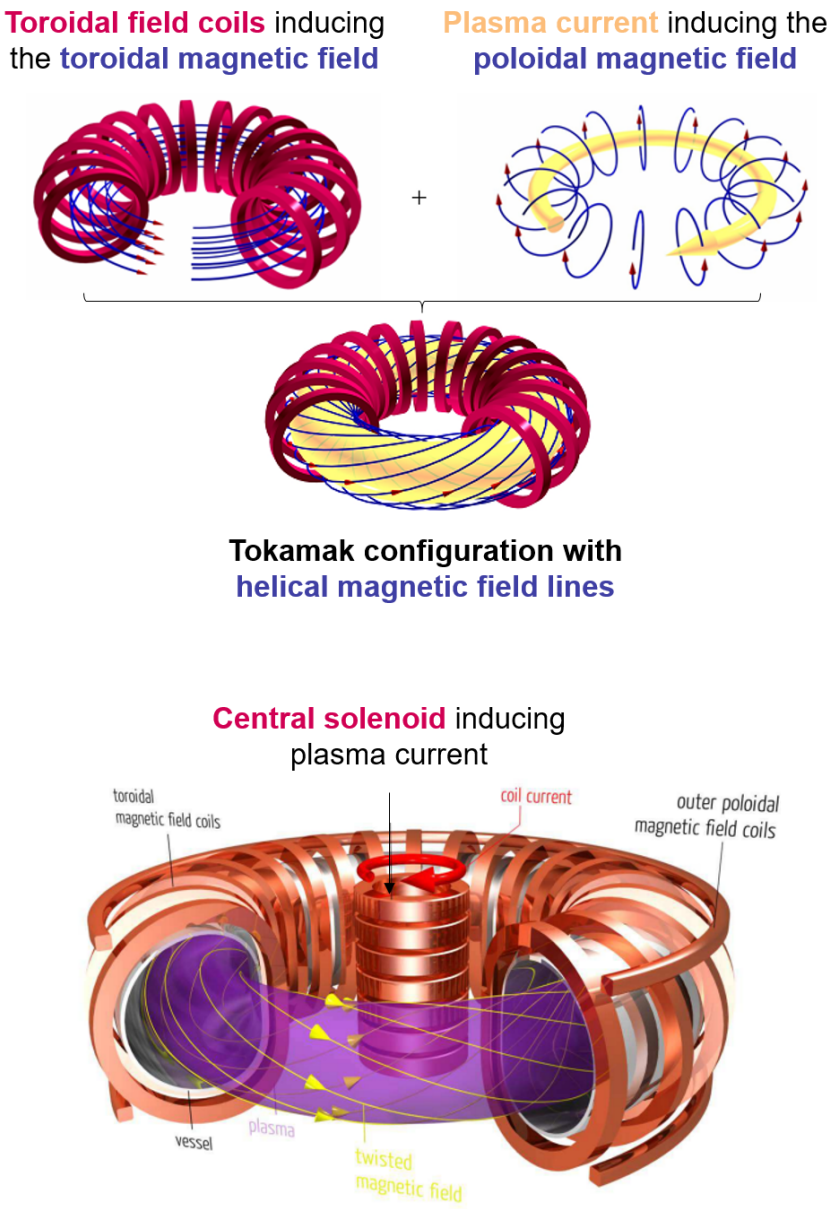

Figure 1.4: Optimal magnetic confinement in a tokamak edited from [59]

1.3 Fusion Process condition

Figure 1.2 shows the fusion reaction rates as a function of temperature for Deuterium and Tritium. Fusion reactions occur at high temperatures of the order of keV ($1\ eV = 11604$ K). The minimum criterion for a fusion reactor is an amplification gain factor $Q > 1$. The amplification factor Q is the dimensionless ratio of the fusion reaction's power over the additional power provided by external heating systems to reach the steady state during the reaction.

$$Q = \frac{P_{out}}{P_{in}} \tag{1.8}$$

The input power is the sum of the auxiliary systems employed to achieve the fusion process. In practice, auxiliary systems create plasma and reach high temperatures (as presented in the following section).
In the first order, the output power corresponds to the number of reactions N_{fus} at the given fusion energy E_{fus}, where V is the volume considered, $\langle \sigma v \rangle$ is the reaction rate for the D-T fusion process:

$$\begin{cases} P_{fusion} = N_{fusion} E_{fusion} & (1.9) \\ N_{fusion} = \int_V n_D n_T \langle \sigma v \rangle dV & (1.10) \end{cases}$$

The fusion power (P_{fusion}) coming from the thermonuclear reaction between atoms can be expressed as follows:

$$P_{fusion} = N_{fusion} E_{fusion} = \frac{n^2}{4} \langle \sigma v \rangle V E_{fusion} \tag{1.11}$$

Wherein N_{fusion} is the total amount of nuclear reaction occurring per unit of time in the plasma [s^{-1}], E_{fusion} being the released energy per fusion reaction ($\approx$ 17.6 MeV for D-T fusion reaction).
From the relation 1.8, three steps must be considered for the Q factor. The break-even case corresponds to a fusion gain factor $Q = 1$, where the input power equals the output power. For energy production, $Q \gg 1$ represents the condition where the output power is superior to the input power. In the future, reactors will use auxiliary systems and α particles to heat the plasma. In this situation, α particles produced by the fusion reaction can contribute to plasma heating for one-fifth of the contribution. Note that a particular scenario exists. It corresponds to the case where the plasma ignites itself, and no auxiliary systems are needed ($P_{in} \to 0$ leading to $Q \to \infty$).

1.4 Heating Systems

As mentioned in the previous section, for fusion reactions to take place, it is necessary to dissociate the electrons from the nucleus. This leads to the ionization of the gas, which can then be confined using the Lorentz force. In order to initiate this process and reach melting temperatures in the keV range, auxiliary heating systems are required. In this section, we present the three most common methods for heating plasmas in tokamaks: Ohmic heating, Radio-frequency heating, and neutral beam injection.

1.4.1 Ohmic heating

Ohmic heating (or resistive heating) is a primary way to heat plasmas in magnetic confinement devices such as Tokamaks. This heating method often initializes the plasma and reaches the first operating temperatures. It is based on the principle of the Joule effect, where an electric current is passed through the plasma, causing energy to be dissipated due to the plasma's electrical resistance. Ohmic heating is relatively simple and does not require complex or expensive technologies. An alternating current is passed through the central solenoid, creating an Electromotive Force (EMF) in the Tokamak vessel (the plasma acts as the transformer's secondary), leading to the expression [78]:

$$P_{Ohmic} = 2.8.10^{-15} \frac{Z_{eff} I_{plasma}^2}{a^4 T_e^{\frac{3}{2}}} \tag{1.12}$$

Where the Ohmic power P_{Ohmic} is expressed in [MW.m^{-3}], I_{plasma} is the plasma current in [A], T_e is the electron temperature in [keV], a is the minor radius in [m], and Z_{eff} is the effective charge presented later.

1.4.2 Radio-frequency heating systems

Ohmic heating alone cannot achieve the extremely high temperatures required for fusion reactions. Other heating methods, such as radiofrequency (RF), are needed to complement ohmic heating and achieve these conditions. Power is transmitted to the plasma through RF antennas located inside the vacuum vessel, at the edge of the plasma. The wave frequency is set to the cyclotronic frequency of the particles to accelerate them and heat the plasma. Three different frequencies are used : Ion cyclotron radio-frequency and electron cyclotron radio-frequency heat ions and electrons, respectively, transferring their kinetic energy through collisions, leading to overall plasma heating. The lower hybrid radio-frequency current drive involves intermediate electromagnetic waves coupling with fast electrons in the 10 to 100 keV range.

1.4.3 Neutral beam injection systems

Another heating method, called neutral injection heating (NBI), is used to heat the plasma and inject a beam of neutral atoms (such as deuterium, hydrogen, or tritium). Initially, these particles are ionized and then accelerated by an electric field to energies up to 1 MeV. The ions then pass through a gas cell to regain their electrons, becoming fast neutrals that can be injected into the plasma. Energy is transferred to the plasma core through collisions. The depth of penetration into the core depends on the speed of the neutrals, as ionization processes can cause the newly charged particles to deviate from their original paths.

1.5 Power losses in a magnetic fusion device

A condition for fusion to be energetically viable is that the heating power counterbalances energy losses. This corresponds to the self-sustainment of the plasma, where a fraction of the energy released by the plasma must maintain the plasma temperature. This condition is given by the Lawson criterion, which relates the energy confinement time τ_e to the plasma temperature, ion density, and alpha particle energy E_α (see the system of equations in 1.5). P_{losses} is mainly due to plasma radiation (depending on impurity content in the core) and particle diffusion toward the vessel walls, such as:

- Bremsstrahlung power
- Cyclotronic power
- Ray lines emission
- Heat flux
- Particles not confine

1.5.1 Confinement Energy time

The plasma produces enough energy in the steady state regime to compensate the losses. This leads to a power balance between the energy sources ($P_{sources} = P_{fusion} + P_{heating}$) that heat the plasma and the energy losses that cool it (for instance, the radiative losses mentioned before):

$$\begin{cases} \frac{dW_{th}}{dt} = P_{sources} - P_{losses} & (1.13) \\ W_{th} = 3nk_bT_eV & (1.14) \end{cases}$$

V is the plasma volume (m^3), n (m^{-3}) is its density, and T is its temperature (K) with W_{th} in [J] is the thermal energy content in the plasma volume V in [m^{-3}] at the density n in [m^{-3}].

Contrary to the α particles, the neutrons are not charged in the plasma; they can escape without transmitting energy to the central plasma. They carry 80 % from the fusion process neutron. On the other hand, since α particles are charged, they follow the magnetic field, leading to confining the α particles. However, due to collisions in the plasma volume, these last transfer a part of their energy to the central plasma ($\frac{1}{5}P_\alpha$. A fraction of α particle energy is coupled with plasma particles).

In a steady state, the plasma confinement time is established by the plasma energy and power losses P_{losses} by:

$$P_{loss} = P_{sources} = P_\alpha + P_{ext} = \frac{W_{th}}{\tau_e} \quad (1.15)$$

The ignition or Lawson criterion expresses the limitations on plasma parameters regarding density, temperature, and confinement time needed for a plasma. The Lawson criterion is given by :

$$n_i \tau_e > \frac{12T}{<\sigma v>_{DT} E_\alpha} \, m^{-3} s \tag{1.16}$$

This last relation traduces the need to efficiently confine a hot and dense plasma for a duration long enough to produce energy.

1.5.2 Particles transport: Heat flux physics

In theory, charged fusion products can remain in the plasma during fusion reactions. This leads to dilution of the plasma, which can affect its performance and even lead to disruption (extinction of the plasma). To remedy this problem, Spitzer developed a divertor configuration in the 1950s; see figure 1.5.

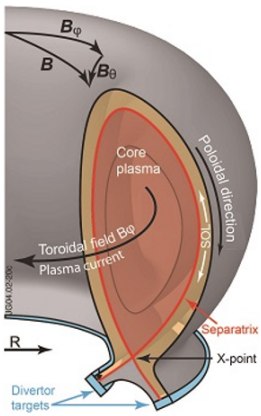

Figure 1.5: Poloidal cross-section showing the divertor configuration edited from [59]

1.5.2.1 Particle Transport and the Scrape of Layer

In a tokamak, the particle flux transport is described by a parallel and perpendicular flux along the poloidal magnetic field line due to a convective and diffusive transport:

$$\Gamma = \Gamma_\perp + \Gamma_\parallel \tag{1.17}$$

The extraction of heat and particles is explained by the particle diffusion from the plasma core toward the separatrix. This diffusion is perpendicular to magnetic field lines, leading to a particle flux $\Gamma_\perp$.

$$\Gamma = -D_\perp \frac{\partial n}{\partial r} \tag{1.18}$$

1.5.2.2 Divertor configuration

Initially, a metallic component was in contact with the last closed flux surface (LCFS), named a limiter, to control the plasma position. However, although the limiter restricts the plasma position, this last induced the injection of impurities due to its erosion. Hence, The uncontrolled injection of impurities into the plasma can lead to its cooling and decrease confinement time. To solve this problem, a new configuration named divertor configuration is employed. The divertor is a metallic element within the reactor that evacuates particles or "ashes" and must reduce the erosion of the plasma-facing component [48].
This can be achieved thanks to external toroidal magnetic field coils that induce the formation of a point X, usually at a few centimeters from the divertor. This allows the open field lines to contact the divertor to extract the fusion products. Confining the core region at higher temperatures without contact with material components is beneficial. Figure 1.5 represents a tokamak poloidal cross-section, wherein the divertor is illustrated in blue. As shown in the figure, this configuration allows the closing of magnetic field lines that confine the plasma at its core until the LCFS, represented in red.
Furthermore, a particularity of the divertor configuration is the formation of open magnetic field lines, described in light orange color in the figure. This corresponds to the plasma edge and is called the Scrappe off layer (SOL). In this region, the particle flux follows the open magnetic field lines toward the divertor target. Therefore, the heat flux, provided from the core, is transferred through the separatrix into the SOL region. From this description, it is clear that the heat flux is related to the physics in the SOL region, particularly to the electron density $n_e(r)$ and temperature $T_e(r)$ profiles. Experiments [1, 41, 49, 50, 52, 79] have shown that the profiles follow a decreasing exponential law characterized by a characteristic decay length λ_q, defining the radial extent of the SOL. An empirical scaling law is given by taking into account the toroidal magnetic field B_T in [T], the cylindrical safety factor q_{cyl}, the heating power P_h in [MW], the geometric radius of the plasma in [m] like [7]:

$$\lambda_{q_\parallel} = (0.73 \pm 0.8) B_T^{-0.78\pm0.25} q_{cyl}^{1.2\pm0.27} P_h^{0.1\pm0.11} R_{geo}^{0.02\pm0.2} \tag{1.19}$$

1.5.2.3 Heat flux

Assuming that plasma transport is classical and electrons and ions are thermally coupled, the parallel electron heat flux, along magnetic field line $q_{\parallel,e}$ [28], can be expressed as:

$$q_{//} = -\kappa_0 T_e^{\frac{5}{2}} \overrightarrow{\nabla} T_e \tag{1.20}$$

, where κ_0 is the parallel heat conductivity coefficient, $\overrightarrow{\nabla}$ refers to the gradient.

Nevertheless, experiments in the tokamaks have shown the existence of three operating regimes, which are slightly presented in the following [40].

- Sheath-limited regime, wherein the collisionality is low (the number of collisions $\nu* < 10$). In this case, the temperature is constant along a magnetic field line, leading to a power flux on the divertor target expressed as:

$$q_{//} = \gamma_{sh} \Gamma_t T_t \tag{1.21}$$

- Conduction-limited regime. In principle, the particle flux follows the magnetic field lines over a distance $\lambda_\perp$ to reach the divertor plates. Assuming that plasma transport is classical along the magnetic field line, electrons and ions are thermally coupled, the heat parallel transport $q_\parallel$ is given by electron heat flux can be expressed by the relation 1.20:

- Detached plasma regime, which is not detailed in the scope of this thesis.

1.5.2.4 Confinement mode L and H

In Tokamak physics, there are two distinct plasma confinement modes: Low and high. Significant differences in plasma behavior and confinement efficiency characterize them. Studying the transition between these two modes, known as the L-H transition, is essential for optimizing confinement and improving the performance of fusion reactors.

Low confinement mode:

The L mode is characterized by a high level of turbulence in the plasma, which results in significant heat and particle losses. The quality of energy and particle confinement is relatively low, limiting the efficiency of plasma heating at its core. This mode is generally easily achieved and typical of initial heating and confinement conditions.

High confinement mode:

H mode confinement [86] appears when an external transport barrier is formed, significantly reducing heat and particle losses. This is due to the plasma pressure gradient. The H mode significantly reduces turbulence, leading to much-improved energy confinement. The temperatures and densities achieved are higher than in L mode, promoting more efficient fusion reactions. Figure 1.6 represents the electron density and temperature profiles measured the Thomson Scattering in the Compass tokamak [80],. They might be used in operational regimes designed to achieve conditions close to self-sustaining fusion. However, a new class of instabilities named Edge Localized Mode (ELM) was found to be distinctive and unique to H-mode. These ELM could be a problem for long pulse scenarios. These transient phenomena are an essential area of research for the community. They seek to understand their influence on particle transport, heat flux, and their effects on the reactor's inner walls to better control and mitigate their amplitude.

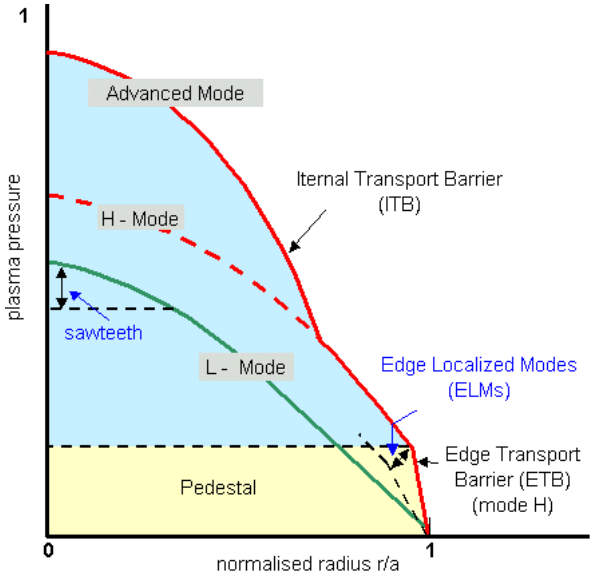

Figure 1.6: L and H confinement modes, edited from [32]

1.6 The international ITER project

In 1985, the ITER (International Thermonuclear Experimental Reactor) project was proposed. The aim was to develop future nuclear reactors (see figure 1.7) based on the fusion of deuterium and tritium to provide a safer and more environmentally friendly form of energy that does not emit CO_2 or long-lived radioactive waste. The objectives of the ITER project are :

1. *Generation of* 500 *MW for* 50 *MW injected.* The aim is to demonstrate that nuclear fusion can lead to the production of energy with an amplification factor $Q = 10$. To obtain this Q factor, the preferred fusion reaction will be the $D-T$ reaction, given by the system of equations 1.5. Note, however, that in the case of ITER, fusion energy production will not lead to electricity production. Indeed, the future function of a fusion reactor is to produce energy, and improving confinement for a constant injected power is desirable. One ambition is to achieve an amplification factor Q, the ratio between injected and produced power, between 30 and 40.

2. *Integrate the technologies needed for fusion.* This includes all the technologies required for the smooth operation of a future fusion power plant, such as diagnostics, heating, cryogenics, remote maintenance, and control.

3. *Tritium production in the vacuum vessel.* By testing the Breeding blanket design. Since Tritium is radioactive and not very abundant on Earth, producing it within the facility from a neutron and a Lithium atom is desirable. Therefore, ITER will

aim to set up a system enabling Tritium to be produced and injected into the Tokamak.

$$\begin{aligned} n + {}^{6}Li &\longrightarrow \alpha + T\,(1.01MeV) + (4.8MeV) \\ n + {}^{7}Li &\longrightarrow \alpha + T\,(1.01MeV) + n - (2.47MeV) \end{aligned} \tag{1.22}$$

, where n is the neutron, Li is the lithium, T is the tritium, α correspond to the alpha particle, helium 4.

4. *Finally the demonstration of a safe nuclear fusion device.* The plasma produces no long-lived radioactive waste. The demonstration of such a reactor will revolutionise nuclear energy production.

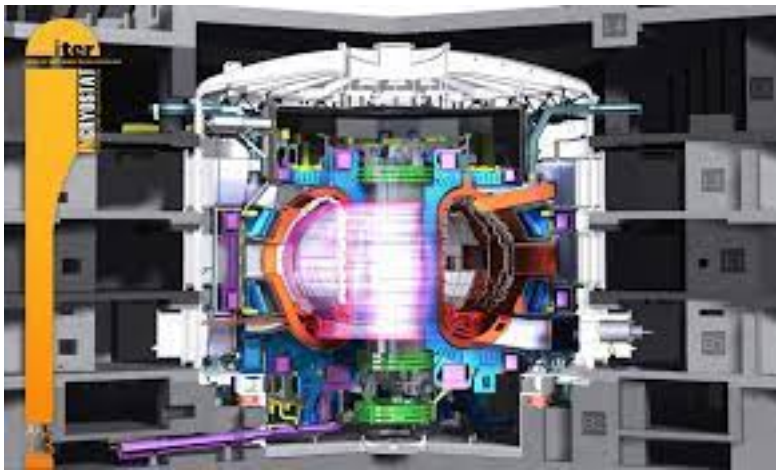

Figure 1.7: Illustration of the ITER tokamak plant

1.7 WEST tokamak

The Institute for Magnetic Confinement Fusion Research (IRFM) [7], located at the CEA site in Cadarache, operates within this framework. The institute investigates the physical phenomena within the plasma and its interaction with the internal walls of the reactor. W Environment in Steady-state Tokamak (WEST) is a medium-sized Tokamak featuring superconducting magnets and an ITER-like divertor. It aids in understanding physical phenomena such as L mode confinement and LH transition. One of the institute's objectives is to study actively cooled tungsten monoblocks, leveraging long plasma discharges from WEST, lasting up to 1000 s, to examine magnetic confinement and the effects of tungsten impurities in the reactor (see table 1.1). Figure 1.8 shows the WEST tokamak vessel with the main components of the reactor.

Countries	Tokamak	B [T]	R [m]	a [m]	I_p [MA]	t [s]
USA	DIII-D	2.17	1.7	0.6	2	1
United Kingdom	MASTU	0.55	0.9	0.6	1.3	1
Switzerland	TCV	1.43	0.875	0.25	1.2	2
Czech Republic	Compass	5	0.84	0.28	2	5
Germany	ASDEX-U	3.1	1.65	0.8	2	10
Japan	JT60SA	2.25	2.96	1.18	5.5	100
South Korea	KSTAR	3.5	1.8	0.5	2	300
International Project	ITER	5.3	6.2	2	15	400
France	WEST	3.7	2.5	0.5	1	1000
China	EAST	3.5	1.85	0.45	1	1000

Table 1.1: Tokamaks in the world

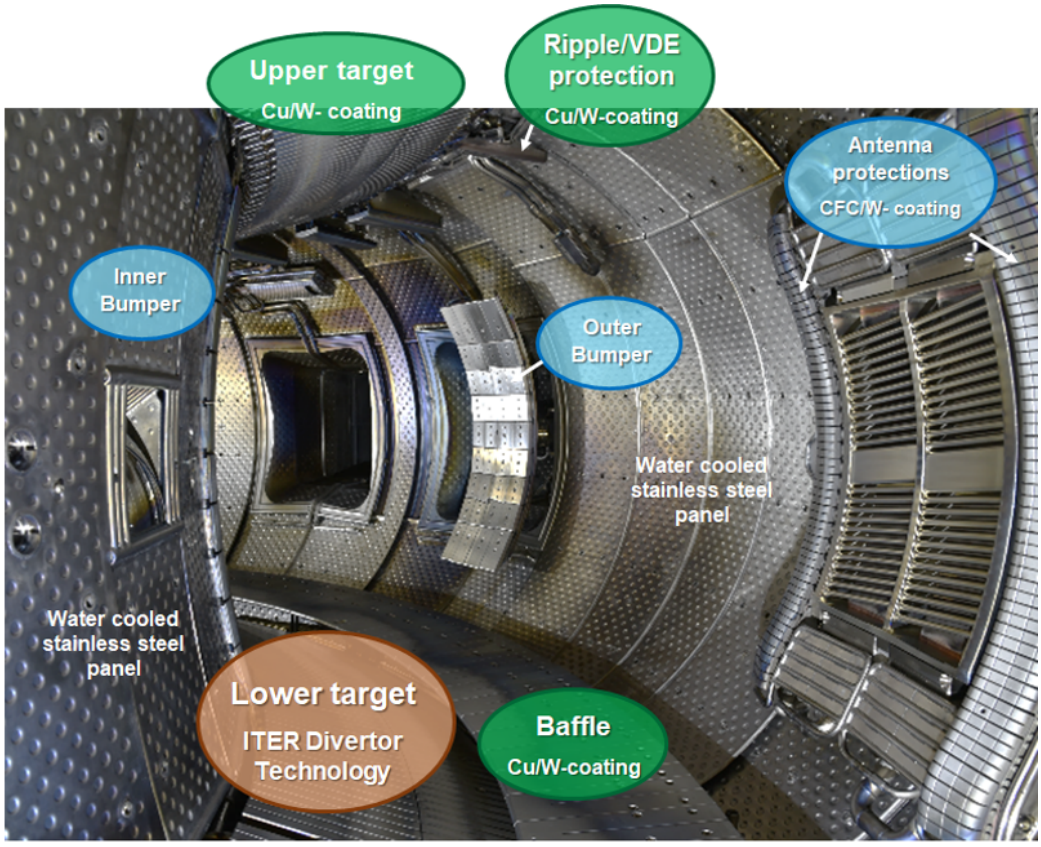

Figure 1.8: WEST tokamak vessel

1.8 WEST heating system

Currently, WEST tokamak has two auxiliary heating systems: the Lower Hybrid Current drive (LHCD) and the Ion Cyclotron Resonance Heating (ICRH), summarized in the

table 1.2.
The LHCD system comprises two antennas with carbon protection limiters and a W coating, each powering 3 to 4 MW. They can be moved radially to optimize their position regarding the plasma equilibrium, and this system enables the delivery of 7 MW coupled to the plasma for up to 1000 s. In addition, to improve coupling, which can be an issue in H-mode plasmas, the two antennas are equipped with local gas injection and four embedded Langmuir probes to measure the local density in the top and bottom parts of the launchers.

The WEST ICRH system has been designed to withstand the ELM during H-modes. It can deliver 9 MW for 30 seconds, 6 MW for 60 seconds, and 3 MW for up to 1000 seconds from three identical antennas.

	WEST
P_{ICRH} $[MW]$	9
P_{LHCD} $[MW]$	7
P_{ECRH} $[MW]$ (in 2025)	3
P_{NBI} $[MW]$	Not installed

Table 1.2: WEST tokamak setting

1.9 Electronic density and temperature measurement

1.9.1 Atomic Spectroscopy

As mentioned before, the electrons and the ions can interact between them. This can lead to Bremsstrahlung radiation, ionization, or neutralization. In these two last scenarios, the ions can radiate photons in large spectral ranges depending on the physical processes involved, such as :

- De-excitation process
- Recombination process

On WEST, several spectroscopy diagnostics are used to measure the ions' emission spectra. Regarding the different spectrometers used on WEST, the plasma parameters, for instance:

- Visible spectroscopy is used to study the impurity concentration. In addition, it estimates the effective charge Z_{eff}, along a line of sight, in a spectral range where there is no stray light coming from impurities sources.

- extreme ultraviolet (XUV) spectroscopy diagnostic gives information about the impurities concentration c_i contained in the tokamak vessel, such as Tungsten or Copper impurities.
- X-ray imaging crystal spectrometer (XICS) measures the different Argon ionization states (Ar XVII, Ar XVII) and 25th of the Iron ionization state. The electronic and ionic temperature from Ar XVII is measured through a tomographic inversion.

1.9.1.1 Langmuir Probe

At the beginning of the 20th century, the physicist Irving Langmuir developed the Langmuir Probe (LP) Langmuir probe, a technique for measuring local plasma properties such as density, temperature, and plasma potential. Langmuir probes are electrodes immersed in plasma, allowing the measurement of a time-varying I-V characteristic when it is in contact with the plasma (see figure 1.9a). Inside WEST, 158 probes subjected to a voltage of 200 V are distributed throughout the machine to estimate plasma parameters (see table 1.3) so that the heat flux received can be assessed. Some probes are placed on quantities of the upper and lower divertors (see figure 1.9b) to measure the plasma parameters in real-time.

$$I_{i,sat} = \frac{I_{probe}}{1 - e^{\frac{-\Delta V}{T_e}}} \tag{1.23}$$

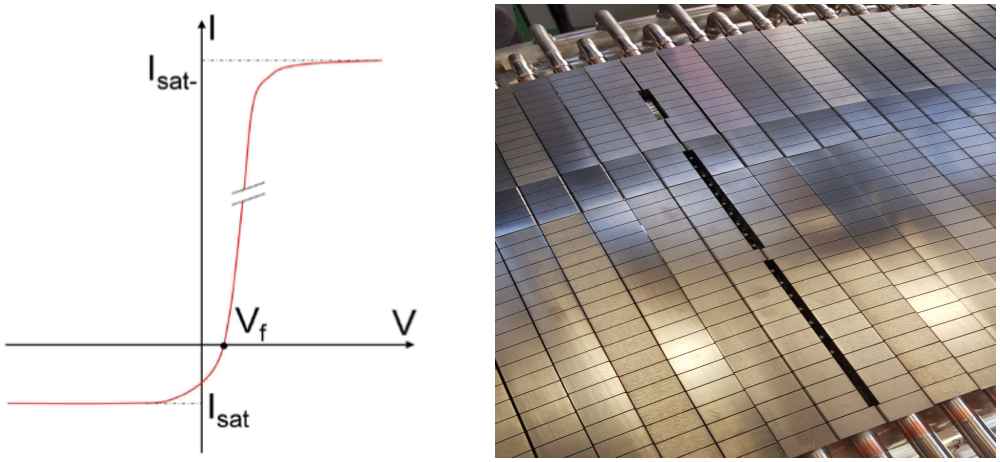

(a) I-V characteristic

(b) Languir probe on the WEST divertor

Figure 1.9: Langmuir measurement principle on WEST

According to the setup on WEST, these probes give vertical and radial profiles of the plasma edge, which can be used to estimate the heat flux on the inner wall or the divertors from the electron density n_e, electron temperature T_e, and the ionic saturation current j_{sat} measurement :

$$q_{//} = \gamma j_{sat} T_e \tag{1.24}$$

It is also worth noting that the interpretation of LP measurements is often subject to significant uncertainties due to plasma fluctuation.

1.9.2 Electromagnetic wave propagation in plasma.

The propagation of electromagnetic waves in plasma is a complex phenomenon crucial to many applications in plasma physics and magnetic confinement machines. Plasma's unique properties strongly influence how electromagnetic waves propagate through it. When an electromagnetic wave enters a plasma, it interacts with charged particles, changing its speed (remember that the wave propagates at the speed of light divided by the index of the medium, which depends on the dielectric permeability factor), amplitude and direction. A key characteristic of wave propagation in plasma is the plasma frequency, which depends on the electron density [38]:

$$\omega_p = \sqrt{\frac{n_e e^2}{m\epsilon_0}} \tag{1.25}$$

Suppose the frequency of the electromagnetic wave is lower than the plasma frequency ($\omega_{EM} < \omega_p$) in a linear homogeneous and Isotropic medium; the wave is strongly attenuated and cannot propagate efficiently. This is because the electrons in the plasma oscillate in response to the electromagnetic wave, creating currents that oppose the propagation of the wave.
On the other hand, if the frequency of the wave is higher than the plasma frequency ($\omega_{EM} > \omega_p$), the wave can propagate, although its speed is reduced compared with its speed in a vacuum. In a plasma subjected to an external magnetic field, the Lorentz force bends the trajectories of charged particles, leading to different propagation behaviors depending on the direction of the magnetic field relative to that of the wave. Thus, the plasma cannot be described as a medium homogeneous isotropic linear, leading to different expressions of wave propagation. Electromagnetic waves can be divided into two distinct modes: the Ordinary mode (O-mode), where the wave oscillates parallel to the magnetic field, and the Extraordinary mode (X-mode), where the wave oscillates perpendicular to the magnetic field. These modes have different propagation properties, particularly in absorption and refraction.

1.9.3 Interfero-polarimetry Diagnostic

For an Ordinary wave, the refractive index is expressed as :

$$n_o = \sqrt{1 - \frac{\omega_p^2}{\omega}} \tag{1.26}$$

, where ω is the wave pulsation.

Interferometry uses this property to measure the electron density using interferometry [38, 40]. WEST Tokamak uses an upgraded Tore Supra Far Infrared (FIR) interferometry-polarimetry for cross-sectional electron density profiles [29–31]. The diagnostic system is a Mach-Zender interferometer combining two H_2O and DCN lasers at 119 and 195 μm wavelengths, delivering 30 and 150 mW, respectively. The diagnostic comprises ten Line of sight (LOS) to cover the entire machine in the poloidal cross-section (see figure 1.10) to estimate the electron density in the core and close the low point X. In principle, the two beams are superimposed along the plasma feedthrough, then separated and directed towards the detectors by either a planar grating or a Mylar foil. This double-phase information lets us calculate the Line Integrated Density (LID), by eliminating the δ path length component from the equation the following equation:

$$\Delta\phi = 2.82.10^{-15}\lambda \int n_{e,l}(l)\,dl + 2\pi\frac{\delta}{\lambda} \tag{1.27}$$

, where $\Delta\phi$ is the phase shift, λ is the wavelength, and δ is the optical path length.

On the other hand, this diagnostic estimates the poloidal magnetic field fields through a Faraday Angle (FA) measurement. It is obtained by measuring the laser's polarization rotation through the plasma.

$$\alpha = 2.62.10^{-13}\lambda^2 \int n_{e,l}(l)B_{//}(l)\,dl \tag{1.28}$$

, where α is the angle, and $B_{//}$ is the parallel magnetic field line.

For FA measurement, a grid separates the two perpendicularly polarized output beams into two separate detectors to account for any elliptization of the beams. The relative amplitudes and phases are measured to estimate the magnetic component, which is outside the scope of this thesis.

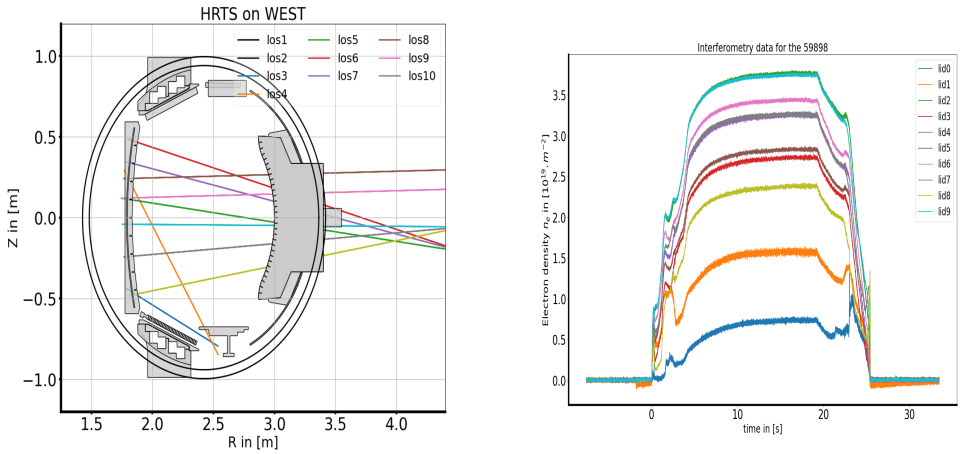

(a) Schematic interferometry line of sights (b) Temporal trace of the electron density

Figure 1.10: Interferometry diagnostic on WEST

1.9.4 Reflectometry

The interferometry measures the electron density along a line of sight, which is not a local measurement that we could expect in a tokamak to characterize the transport. Another solution is to use the plasma refractive index, thanks to reflectometry diagnostics, to measure the electron density and its fluctuation locally. This technique is based on the reflection of electromagnetic waves on the plasma layers, where the electron density corresponds to the frequency cut-off, defined as the plasma optical index layer equals zero.

The measurement principle follows: A reflectometer sends an electromagnetic wave into the plasma. This wave propagates until it reaches a layer of plasma where its frequency corresponds to the local plasma frequency cut-off. At a given distance, the wave is reflected for a given electron density. By analyzing the reflection of this wave (in amplitude and phase), we can obtain information about electron density.

On WEST, the reflectometers are used to scan the electron density with aims at getting a high spatial and temporal resolution radially that allows for tracking rapid and fine variations in electron density [36, 68, 85]. Three frequency bands are used for this purpose; the frequency bands correspond to 50 and 75 GHz for the O-mode,75 to 110, and 110 to 150 GHz for the X-mode, as shown in figure 1.11. The cutoff frequency along the radial axis is represented on the left-hand side, whereas the radial electron density measurement measured with the reflectometry on Tore Supra is presented.

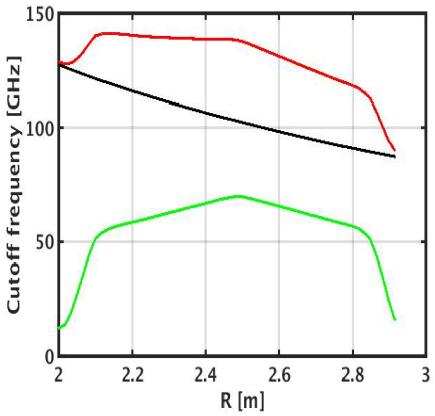

(a) ECE in black, O-mode in green, and X-mode in red

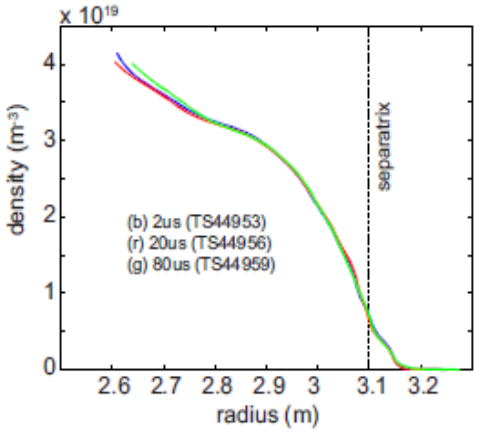

(b) Electron density profile retrieving

Figure 1.11: Reflectometry principle measurement measuring the electron density at the edge

1.9.5 Electron Cyclotron Emission Diagnostic

Electron cyclotron emission (ECE) diagnostic is a non-intrusive technique used in plasma physics to measure the local electron temperature and temperature profiles in plasma confinement devices such as tokamaks [38, 66, 76]. The method is based on detecting and analyzing the electromagnetic emission of plasma electrons in cyclotronic motion around magnetic field lines. Electrons moving helically around magnetic field lines in a plasma emit electromagnetic waves at specific frequencies called cyclotron frequencies given by :

$$\omega_c = \frac{qB}{\gamma m_e} \tag{1.29}$$

This relationship shows that the emission frequency is proportional to the strength of the local magnetic field. By measuring the spectrum of cyclotron emission, we can obtain information about the temperature distribution of the electrons. Each frequency in the spectrum corresponds to a different position in the plasma due to the variation of the magnetic field with radius in toroidal devices such as Tokamaks. This enables localized electron temperature measurements with high spatial and temporal resolution (temperature estimated along a field line). The radiative intensity is given by:

$$I_{\omega_{c,e}}(r,t) = \frac{\omega_{c,e}^2 T_e(r,t)}{8\pi^3 c^2} f \tag{1.30}$$

However, the ECE measurement depends on the amplitude of the magnetic field and, therefore, on its profile. So, we need to know precisely the local magnetic field and its position. In addition, interpreting the data can be complex. ECE signals can be

affected by re-absorption and relativistic effects, requiring sophisticated analysis.

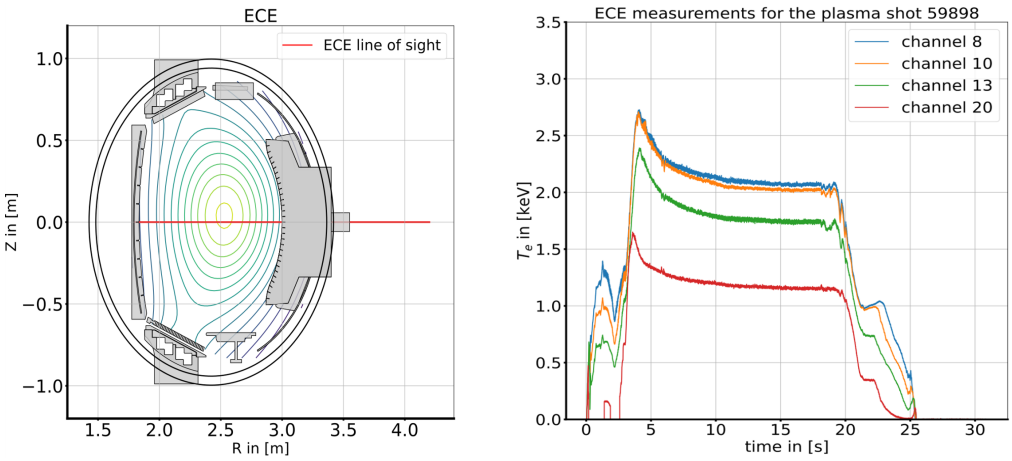

(a) Schematic architecture of ECE radiometer (b) Electron temporal trace

Figure 1.12: ECE diagnostic implemented on WEST. The diagnostic measures the electron temperature at the mid-plane with high temporal resolution.

Figure 1.12 illustrates the ECE diagnostics on WEST. The ECE line of sight is at the midplane. This last measures the electron in the plasma core, allowing us to observe the electron temperature evolution over time or the magnetic field lines.

1.9.6 Plasma equilibrium

In principle, the magnetic equilibrium is settled to compensate for the plasma thermal pressure gradient and reduce the diffusive losses of particles and energy from the core towards the inner walls [46]. The magnetohydrodynamics (MHD) approach is sufficient to describe the macroscopic equilibrium. According to this theory, the plasma equilibrium is reached when the total thermal pressure from the plasma p compensates for the external force, the Lorentz force.

$$\vec{\nabla} p = \vec{j} \times \vec{B} \tag{1.31}$$

This equilibrium can be described from the Grad-Shafranov equation :

$$\frac{\partial^2 \psi}{\partial R^2} - \frac{1}{R}\frac{\partial \psi}{\partial R} + \frac{\partial^2 \psi}{\partial z^2} = -\mu_0 R^2 \tag{1.32}$$

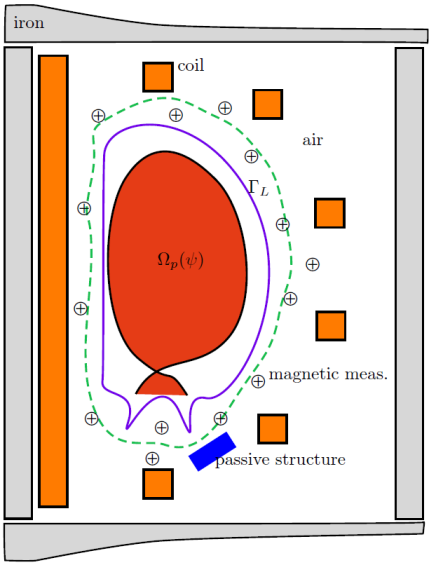

Figure 1.13: Magnetic probe used to measure the poloidal magnetic flux, edited from [25]

The magnetic reconstruction is needed to allow the plasma parameter retrieving for some diagnostic such as the reflectometers, which work in X-mode, or XICS to estimate the electron temperature through a tomographic inversion [18]. Furthermore, magnetic equilibrium is essential to map electron density and temperature, aiming to compare the diagnostics. Since some diagnostics do not measure the plasma parameters in the same region and are sensitive to magnetic reconstruction, comparing them in absolute coordinates like R and Z in the reference machine might be difficult. Usually, the data is compared in the normalized poloidal flux coordinate or remapped by projecting at the mid-plane.

$$\psi_{norm} = \frac{\psi - \psi_0}{\psi_{LCFS} - \psi_0} \tag{1.33}$$

, where ψ_0 is poloidal magnetic flux at the plasma center and ψ_{LCFS} at the LCFS.

From the relation 1.32, a code called NICE [25] retrieves the plasma equilibrium in reference machine (R, Z). This code reconstructs the magnetic equilibrium from a model, taking the Grad-Shafranov equation and the plasma current density into account. The code will estimate the magnetic equilibrium by fitting the 2D magnetic equilibrium that best approximates the magnetic probe measurements. Or by formulating the local magnetic equilibrium as an inverse problem, enabling it to impose constraints on physical quantities by considering experimental measurements from other diagnostics such as interfero-polarimetry or magnetic probe represented in the figure 1.13.
Up to now, equilibrium has been reconstructed using magnetic probes, with interfero-polarimetry providing a magnetic equilibrium accurate to plus or minus 2.8 cm. In

the future, to improve reconstruction and better control the plasma's position concerning the tokamak's inner walls or the position of the antennae, we wish to estimate the electron pressure gradient using the new Thomson scattering to impose a new constraint.

Two solutions are possible for retrieving the plasma equilibrium. The code can retrieve the equilibrium from the magnetic probe installed in the Tokamak or use the experimental data from the diagnostics as the interfero-polarimetry to improve the equilibrium reconstruction.

Diagnostic	Parameter Estimated
Langmuir Probe	local electron temperature T_e local electron density n_e ion saturation current j_{sat}
Reflectometry	local electron density n_e electron perpendicular velocity v_{perp} electron density fluctuation δn_e
Electron Cyclotron Emission	electron temperature T_e
Interfero-polarimeter	line-integrated density $n_{e,l}$ magnetic field B
Atomic Spectroscopy	impurities concentration c_i ionic Temperature along a line of sight T_i electron temperature along a line of sight T_i

Table 1.3: WEST diagnostic summary table

1.10 Discussion: Problematic related to tokamak and link with my study

As mentioned before, a high temperature at the center and a low temperature at the edge seem optimal for achieving good performance. The H-mode, characterized by

forming a pedestal at the edge of the density and electron temperature profiles, appears suitable for fusion reactors. At the top of these pedestals, steep gradient lengths are found, reflecting a solid reduction in transport in this region. Consequently, it is essential to understand the characteristics of the pedestal by determining its position, height, and width, as well as the gradient lengths (in density n_e, in temperature T_e, and in pressure p_e see figures 1.14, 1.15 and 1.6), to predict the performance of future devices.
Therefore, the SOL must be investigated to study particle transport and the heat flux extracted from it by measuring kinetic profiles. WEST offers a wide range of diagnostics for measuring plasma parameters, which can help us better understand the observed phenomena. However, each diagnostic has limitations and can be sensitive to magnetic equilibrium. Indeed, some diagnostics are limited by the plasma scenario. For instance, the supra-thermal electron can impact the ECE measurement. Currently, no diagnostic allows measuring the electron temperature at the edge. In addition, due to the high temperature in the SOL, close to the separatrix, the Langmuir probes cannot resolve the entire pedestal. This makes it impossible to investigate the physics of the plasma edges, limiting the SOL investigation.

One solution would be an optical diagnostic that allows local temperature T_e and electron density n_e measurements independently of the plasma scenarios or magnetic equilibrium. Thomson Scattering (TS) diagnostic was developed in the '60s and demonstrated its usefulness in 1969 on the Russian T-3A tokamak [27]. The physical principle is based on analyzing an extended Doppler scattering spectrum to estimate T_e and to use signal amplitude to estimate n_e.
Nowadays, the Thomson scattering diagnostic is used to measure the electron density and temperature profiles as illustrated in figure 1.14 to characterize L and H confinement modes and particle transport through scaling laws by using n_e and T_e at the pedestal. A second benefit is to evaluate the electronic pressure profile from n_e and T_e profiles, as shown in the figure 1.16. In addition, the plasma confinement mode, notably the LH transition, can be studied by evaluating density and temperature gradient lengths to qualify edge turbulence.

$$\begin{cases} L_{T_e} = \left[\frac{\partial ln T_e}{\partial R}\right]^{-1} & (1.34) \\ L_{n_e} = \left[\frac{\partial ln n_e}{\partial R}\right]^{-1} & (1.35) \\ \eta_{turb} = \frac{\partial ln(n_e)}{\partial ln(T_e)} = \frac{L_n}{L_{T_e}} & (1.36) \end{cases}$$

Thanks to this gradient length, the η_{turb} parameter can be computed to assess the stability and particle transport.

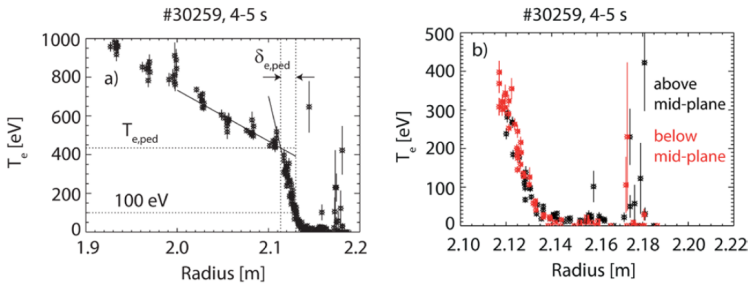

Figure 1.14: T_e profiles and the pedestal characteristics, from [81]

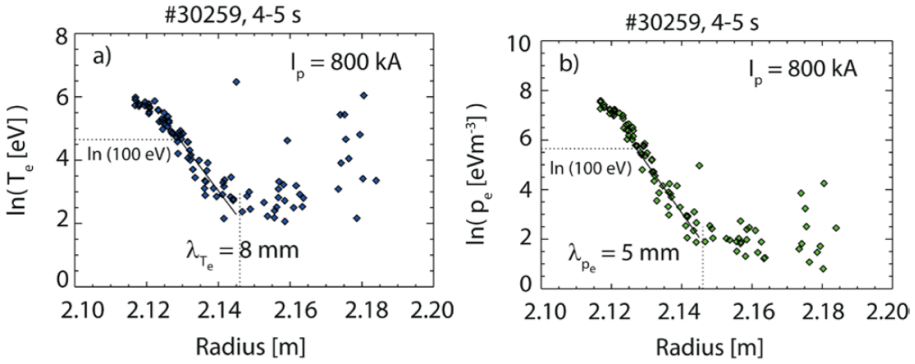

Figure 1.15: Decay length measurement, edited from [81]

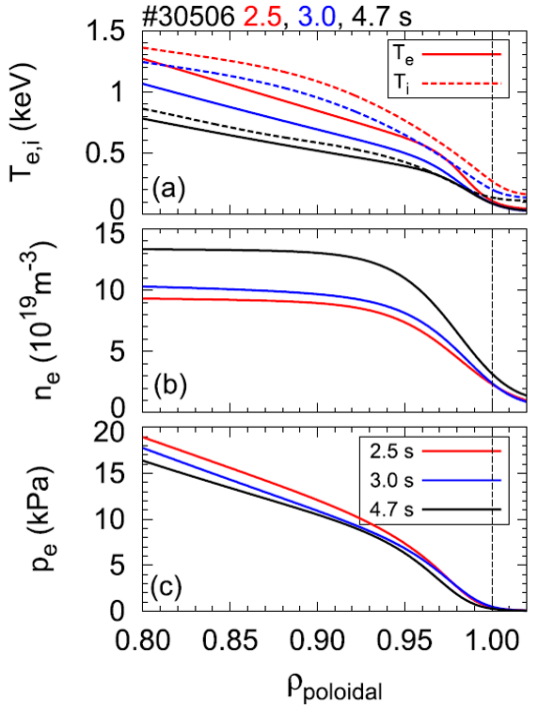

Figure 1.16: Plasma parameters profile on ASDEXU, edited from [39]

To improve our understanding of the physical mechanisms in WEST scenarios, we need to measure local electron density and temperature in the SOL at a high resolution. For this reason, a new High Resolution Thomson Scattering (HRTS) diagnostic has been installed to measure plasma parameters in the core and edge regions.
Adding a new diagnostic will provide more information on plasma behavior in the core and the edge to complete the other diagnostics and also enable us to validate the measurements of other diagnostics regarding plasma scenarios. My thesis topic falls within this field of research since the diagnostic was not operational when I arrived. I participated in the High-Resolution Thomson Scattering design. During my thesis, my work focused on three aspects.

A technical aspect consists of developing and installing HRTS on WEST. A steering laser line system has been designed considering the technical requirements and the physical constraints specific to the Tokamak. The first part of the project was to work on the design of the laser line to ensure that the diagnostics would function properly during operation, presented in chapter 3. In particular, the design will enable the system to be upgraded for real-time measurements of the three parameters mentioned above. High-quality measurements will be ensured using several detectors to estimate laser energy. A second part of the work-study subject consisted of defining the laser control system that would enable the beams' misalignment to be corrected. During the first year, a selection of optical components was made to set up a test bench to control the piezoelectric mounts in the laboratory. The system has been tested in the laboratory to verify the capacity to control the laser alignment and confirm the specifications given by the manufacturer. In addition, a LabView interface has been developed to control from control the steering laser line system, which will be installed in the future in the control room. The third part was to design a spectral calibration bench and select the optical component needed for the spectral calibration mentioned in chapter 5. This calibration is essential to reduce the error on T_e and n_e temperature measurements.

A numerical aspect consists of developing a synthetic diagnostic to validate the design of the diagnostic by evaluating its performance through a sensitivity test presented in chapter 4. The code development demonstrated that it was possible to determine the electron temperature using the least squares regression method. Based on this synthetic diagnostic, the measurement error on temperature, density, and electron pressure was estimated to validate the system design and enable future prediction or interpretation of experimental results. From the sensitivity tests, an error of around 5% was estimated for density and temperature, while an error of 15% was evaluated for electronic pressure. Finally, the current code has only been used to create a pre-processed data set. This pre-processed data set will estimate the electron density and temperature in real-time for the next campaign.

An experimental aspect: during the C9 experimental campaign, it was possible to estimate the electronic temperature in the core plasma to validate and study the actual performance of the diagnostic through the characterization of signals and noise associated with the measurement presented in chapter 6. The goal is to demonstrate that the temperature can be estimated from the signal. The diagnostic's performance during the operation was evaluated to identify the various noise sources, validate the signal processing for post-processing and real-time, and compare the temperature and relative density measurements with the diagnostics already present on WEST. This work concluded that the primary noise source comes from Bremsstrahlung radiation, which impacts temperature estimation. However, the experimental relative error estimated is 5% and corresponds to the error evaluated by the synthetic diagnostic. Therefore, this work validates the model implemented in the synthetic diagnostic and the temperature estimate for the various plasma scenarios. In the future, the diagnostic will be able to operate with two Nd:YAG lasers to improve temporal resolution and estimate temperature and electron density. This will allow the study of heat flux transport in L and H confinement modes and investigate the LH transition.

1.11 Summary

This chapter is devoted to the operating principle of the tokamak, highlighting its importance for energy production. Nuclear fusion, which takes place under extreme conditions, requires temperatures in the keV range to be reached. To achieve this, auxiliary heating systems raise the plasma temperature in the core.
To overcome the technical and physical limitations of the "limiter" configuration, a so-called "divertor" configuration was proposed in the 1950s. This approach improves plasma confinement by increasing core temperature while minimizing peripheral temperature. It also makes it possible to achieve enhanced confinement modes, such as the H-mode, which increases the density and temperature of the core plasma thanks to the appearance of a transport barrier at the edge.
However, a major problem remains: particle transport and heat flux extraction, which can damage reactor walls and generate impurities, thus degrading plasma confinement through divertor erosion. The heat flux from particle transport through the separator is closely linked to the electron density and temperature profile at the edge, making it a crucial issue for the ITER tokamak and future power reactors.
The WEST tokamak plays a central role in studying particle transport and power extraction, particularly by characterizing electron density and temperature profiles as a function of scenarios in a long-shock tungsten environment. Plasma characterization uses diagnostics such as Langmuir probes, reflectometers, spectrometers, etc., enabling plasma parameters such as temperature and electron density to be measured and related to heat flux at the upper and lower divertors.
However, current diagnostics have technical and physical limitations that prevent high-resolution measurements in the peripheral layer region (SOL). To overcome these limitations, a new high-resolution Thomson scattering diagnostic has been developed to measure electron density and temperature in the plasma in the machine reference (R, Z). This diagnostic will enable us to characterize the confinement mode, estimate the temperature in the SOL, evaluate gradient lengths, and better understand turbulent transport.

2 Wave Matter interaction

Sommaire

2.1 Electromagnetic Scattering 61
2.1.1 Compton Scattering 61
2.1.2 Thomson Scattering in the electrodynamics framework 63
2.2 Discussion about the scattered power provided by charged particles . . 65
2.2.1 Coherent Thomson Scattering 66
2.2.2 Incoherent Thomson Spectra 67
2.3 Principle of Thomson Scattering Diagnostic 70
2.3.1 Measurement principle 70
2.3.2 Pulsed laser for Thomson scattering diagnostic 70
2.4 Summary 73

2.1 Electromagnetic Scattering

The wave-corpuscle duality of light allows it to behave as much like a wave or like a particle. In the corpuscular approach, the photon behaves like a particle that can collide with other particles, such as electrons, atoms, or molecules. This photon-matter interaction can be described by scattering, leading to the deviation of photons and, consequently, light properties. This phenomenon is fundamental in plasma diagnostics physics. It manifests itself in different forms depending on the conditions and properties of the particles with which the photons interact, such as Compton scattering, Thomson scattering, Raman scattering, and so on ...

2.1.1 Compton Scattering

In the case wherein the photon is considered like a particle. This last can be characterized by energy ($E = h\nu$) and wavelength (λ). While the photon interacts with matter, its direction can be altered, leading to the particle motions that compose the matter with a velocity $\vec{\beta}$ defined as the particle velocity v divided by the light speed c. This lead to a Doppler shift ω_s for initial pulsation $\omega_i \equiv 2\pi\nu_i$,

$$\omega_s = \frac{1 - \vec{\beta}.\vec{i}}{1 - \vec{\beta}.\vec{s}}\omega_i \tag{2.1}$$

, which consequently changes the photon's wavelength. Figure 2.1 shows a schematic photon scattering in the case of charged particles. This process is named Compton scattering and can be described in the relativistic case as follows:

An incident photon propagates in one direction and interacts with a charged particle, in this case, an electron. Due to this interaction, the photon will collide with the electron and transfer part of its energy to it in kinetic form before being deflected. Since the photon momentum ($p = \hbar k$) is related to photon wavelength $\left(k = \frac{2\pi}{\lambda}\right)$ an energy transfer, as small as it may be, this leads to wavelength shift of the incident photon (λ'). In figure 2.1, it can be assumed that the Doppler shift is as significant as the deflection angle and leads to a small energy transfer. A relativistic mechanical description of an electron is given in the following section.

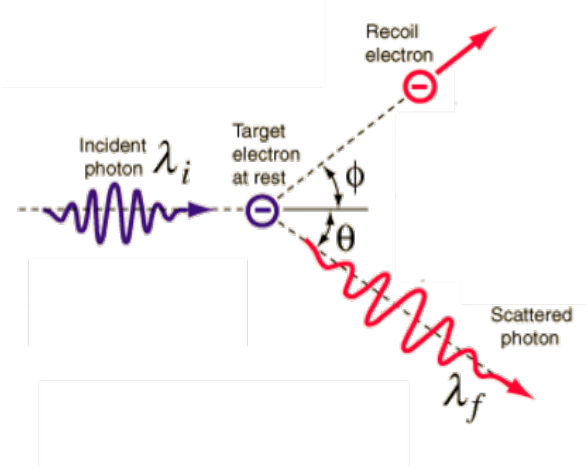

Figure 2.1: Photon scattering by an electron assumed to be at rest, edited from [73].

The relativistic expression relating the momentum and the electron energy E_e is given by:

$$E_e = \sqrt{(p_e c)^2 + (m_0 c^2)^2} \tag{2.2}$$

, where p_e is the electron momentum, m_0 is electron rest of mass. From the description detailed above, the variation in photon energy can be given from the initial photon energy E_p, the final photon energy E'_p, and the electron momentum. If the collision is considered inelastic between the photon and an electron at rest, the system equation follows:

$$\begin{cases} \frac{E_p}{c} = \frac{E'_p}{c} cos\phi + p_e cos\psi & (2.3) \\ 0 = \frac{E'_p}{c} sin\phi - p_e sin\psi & (2.4) \end{cases}$$

, where ϕ is the angle defined in the figure 2.1. From the energy conservation, the initial energy of the system (the right-hand side) and final energy of the system (the

left-hand side) :

$$E_p + m_0c^2 = E'_p + \sqrt{(p_e c^2)^2 + (m_0 c^2)^2} \tag{2.5}$$

Leading to :

$$E_p - E'_p = \left(\frac{E_p^2}{m_0 c^2} \frac{(1 - cos\phi)}{1 + \frac{E_p}{m_0 c^2}(1 - cos\phi)} \right) \tag{2.6}$$

The relation 2.6 links the energy variation $E_p - E'_p$ corresponding to the energy gained or lost by the electron to the energy lost by the photon (More details are given in the Prunty paper [65]). According to this relation, if the photon energy is minimal compared to the electron rest of mass ($E_p \ll m_0 c^2$), the scattering process is named Thomson Scattering and will be explained in the next section.

2.1.2 Thomson Scattering in the electrodynamics framework

Thomson Scattering describes the photon scattering at low energy compared to the charged particle rest of mass ($E_p \ll m_0 c^2$). In this section, an electrodynamics approach is employed by considering only one charged particle to explain this phenomenon. An incident electromagnetic wave with electric amplitude E_{inc} interacts with the charged particle in the medium. This particle, subjected to the incident electric field, emits electromagnetic waves in all directions due to energy conservation. The TS phenomenon can be described within the framework of classical electrodynamics by calculating the electric field scattered by the particle (see Figure 2.2). In the Thomson scattering framework, the system is given by the particle rest of mass m_0 and its charged e, which is subjected to an incident electric field $\vec{E}_{inc}$. From the fundamental principle of dynamics (FPD):

$$\frac{d\gamma\vec{\beta}}{dt} = -\frac{q}{m_0 c}\overrightarrow{E_{inc}} \tag{2.7}$$

wherein, $\frac{d\gamma\vec{\beta}}{dt}$ is the acceleration, $\gamma \equiv \frac{1}{\sqrt{1-\beta^2}}$ is the Lorentz factor.

The scattering electric field E_s, received by an observer located at a distance R along a LOS $\vec{s}$ is expressed as:

$$\overrightarrow{E_s(r,t)} = -\frac{q}{4\pi\epsilon_0}\left[\frac{1}{\tilde{\kappa}^3 Rc} \times \left(\vec{s} \times (\vec{s} - \vec{\beta}) \times \frac{d\vec{\beta}}{dt}\right)\right]_{ret} \tag{2.8}$$

wherein, ϵ_0 is the permittivity of free space, $\tilde{\kappa}$ is ..

From the Poynting vector expression, the scattering power is expressed as a function of the scattering electric field E_s as:

$$P_s = \frac{1}{\mu_0 c} |\vec{E_s}|^2 \tag{2.9}$$

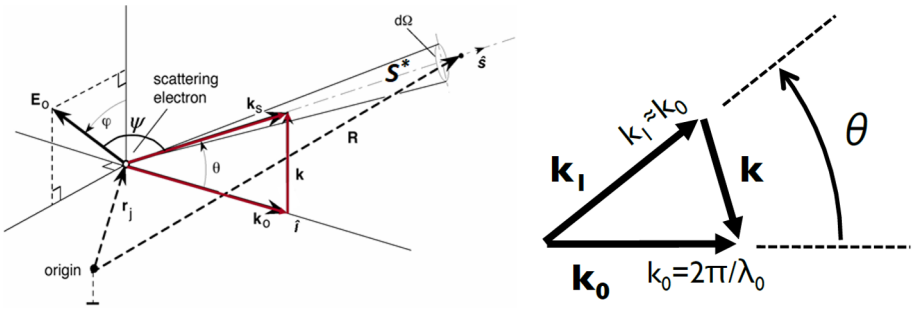

Figure 2.2: Schematic Thomson Scattering spectra for one electron edited from [65]

Figure 2.2 shows the scattered electric field in one direction. Note that the scattered electric field is not isotropic and depends on the direction of observation; see figure 2.3. The scattering power is most significant at the equator, and the reader is referred to [38] for more information. The relation 2.10 one notices that the scattering power per solid angle is proportional to a cross-section $r_e^2 sin^2(\phi)$ which depends on the observer orientation. The relation 2.10 shows that the scattering power of one electron is related to incident electromagnetic wave E_{inc}.

$$\frac{dP_{s,e,i}}{d\Omega_s} = r_{e,i}^2 sin^2(\phi) c\epsilon_0 |E_i|^2 \tag{2.10}$$

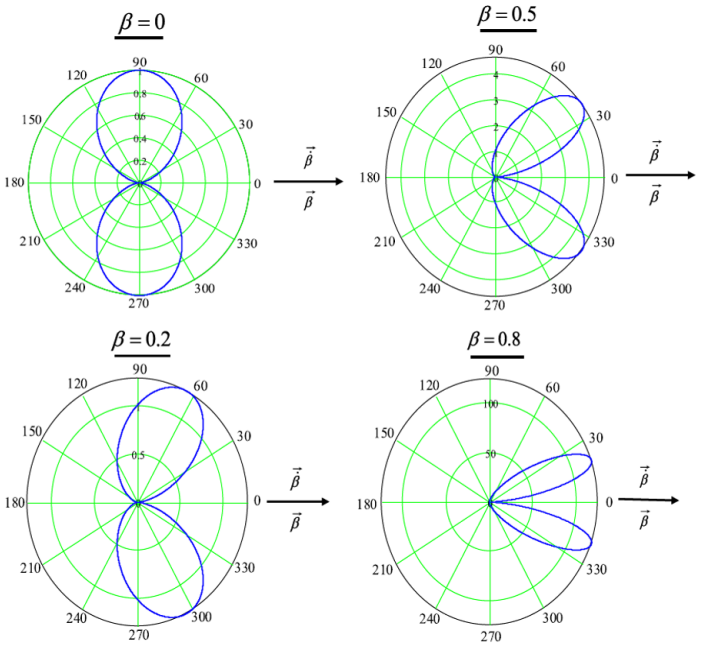

Figure 2.3: Cross section regarding the charged particle velocity edited from [65].

2.2 Discussion about the scattered power provided by charged particles

In the previous section, the scattering power for one electron was presented. In general, several particles must be considered in the Thomson Scattering process to estimate the scattering power an observer collects at the position $\vec{R}$ for a scattering volume V_{scatt}. This section presents the scattering power and the hypothesis made to understand the subtleties of Thomson Scattering power. To express the total scattering power $E_{s,tot}$ collected by an observer from the scattering electric E_s given by the relation 2.8, it is needed to sum the scattering electric field produced by each particle:

$$E_{s,tot} = \sum_{i=1}^{N} E_{s,i} = \sum_{i=1}^{N} -\frac{q}{4\pi\epsilon_0 c}\left[\frac{1}{R_i}\vec{s}\times\left(\vec{s}\times\frac{d\vec{v}_i}{dt}\right)\right] \tag{2.11}$$

The total scattering power detected by the observer is then given by :

$$P_s = \frac{1}{\mu_0 c}\left|\sum_{i=1}^{N} E_{s,i}\right|^2 = \frac{1}{\mu_0 c}\left(\sum_{i}^{N} E_{s,N}^2 + 2\sum_{i=0}^{N-1}\vec{E}_{s,i}\vec{E}_{s,i+1}\right) \tag{2.12}$$

The relation 2.12 shows that in some cases, the total scattering power leads to interference patterns. This is explained by a coherence between the scattering electric field amplitude emitted by each charged particle (ions and electrons). For short wavelengths, the electrons are subjected to the amplitude of the laser's electric field

and the average electric field of neighboring charges. The movement of the electrons is no longer random but collective, resulting in correlated phases of the scattered electromagnetic waves. To simplify the total scattering power expression, it is usual to distinguish the two Thomson Scattering phenomena, the Incoherent and Collective Thomson Scattering. The Salpeter parameter is introduced to determine whether the system is collective or non-collective and is given for the equation below:

$$\alpha_{Salpeter} = \frac{1}{k\lambda_D} \tag{2.13}$$

This parameter takes into account the wavenumber shift $k(= k_s - k_i)$ and the screening effect described by a characteristic length called the Debye length λ_D:

$$\lambda_D = \sqrt{\frac{\epsilon_0 k_b T_e}{n_e e^2}} \tag{2.14}$$

2.2.1 Coherent Thomson Scattering

For $\alpha_{Salpeter} > 1$, we are in the Coherent Thomson Scattering (CTS) case, also known as Collective Thomson Scattering. In this case, the charged respond collectively to the electric field, making them coherent. We then have the situation where the electric scattering fields add up, not the powers. This results in an expression for the total scattering power that depends on the sum of the scattered electric fields emitted locally by the charged particles in the medium (ions and electrons). Therefore this phenomenon gives a spectral density $S(k,\omega)$ which is given by :

$$S(k,\omega) = S_e + S_i = S(k,\omega)d\omega \tag{2.15}$$

, where S_e is the scattering spectra for the electrons, S_i is the scattering spectra devoted to the ions leading to different spectra shapes as shown in figure 2.4. $x_{e,i} = \frac{\Delta\omega}{k v_{t,e,i}}$ is the normalized wavelength normalized by the shift k and the thermal velocity $v_{t,e,i}$.

$$S(k,\omega)d\omega \approx \frac{1}{\sqrt{\pi}}\Gamma_{\alpha_{Salpeter}}(x_e)dx_e + Z_{eff}\left(\frac{\alpha^2_{Salpeter}}{1+\alpha^2_{Salpeter}}\right)^2 \frac{1}{\sqrt{\pi}}\Gamma_v(x_i)dx_i \tag{2.16}$$

wherein

$$\Gamma_{\alpha_{Salpeter}}(x_e) = \frac{e^{-x_e^2}}{|1+\alpha^2_{Salpeter}w(x_e)|^2} \tag{2.17}$$

$$\Gamma_v(x_i) = \frac{e^{-x_i^2}}{|1+v^2 w(x_i)|^2} \tag{2.18}$$

where $v = \sqrt{Z_{eff}\left(\frac{\alpha^2_{Salpeter}}{1+\alpha^2_{Salpeter}}\right)^2 \frac{T_e}{T_i}}$, w is respectively the electron and ion plasma dispersion function.
The Incoherent Thomson Scattering (ITS) has the advantage of measuring ionic temperature and electron density fluctuations [38].

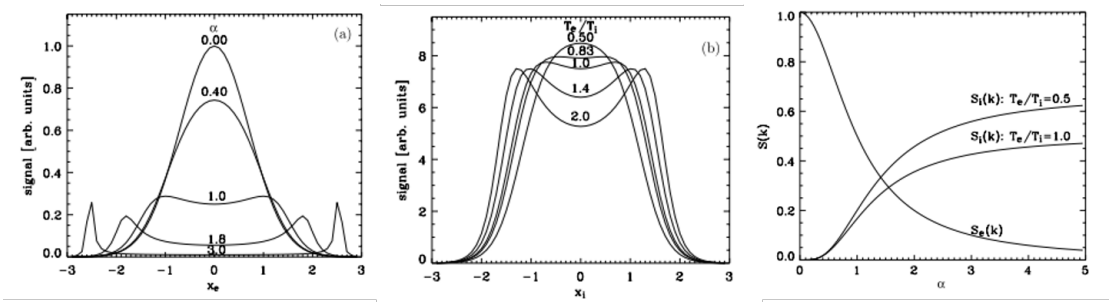

Figure 2.4: Scattering spectra in coherent Thomson scattering case [54]

2.2.2 Incoherent Thomson Spectra

Thomson scattering is incoherent for $\alpha_{Salpeter} < 1$. The consequence of ITS is the absence of correlation between the phases of the scattered electric fields. This is due to the plasma condition and diagnostic properties (presented later), which give a Salpeter parameter lower than 1. Then, the contribution of the ions can be ignored in the first order by assuming that the ions are in rest since the mass ratio is lower than $\left(\frac{m_e}{m_i} \ll 1\right)$. Hence, this makes it possible to sum the local scattering power associated with each electron.

$$\frac{d^2P_s}{d\Omega_s d\omega_s} = r_e^2 \int \Pi_i n_e d^3\vec{r} \int \left(\frac{\omega_s}{\omega_i}\right)^2 \left(1 - \frac{\beta_e^2(1-cos\theta)}{(1-\beta_i)(1-\beta_s)}\right)^2 (1-\beta^2) f(\beta)\delta(\vec{k}.\vec{v}-\omega) d^3\vec{\beta} \tag{2.19}$$

The first integral $\int \Pi_i n_e d^3\vec{r}$ gives instantaneous Scattering power amplitude of differential scattering power $\frac{d^2P_s}{d\Omega_s d\omega_s}$ for an instantaneous incident power Π_i.

The second integral $\int \left(\frac{\omega_s}{\omega_i}\right)^2 \left(1 - \frac{\beta_e^2(1-cos\theta)}{(1-\beta_i)(1-\beta_s)}\right)^2 (1-\beta^2) f(\beta)\delta(\vec{k}.\vec{v}-\omega) d^3\vec{\beta}$ corresponds to the Incoherent Thomson Scattering spectra. We can see that this spectra is based on two terms:

Electron distribution function:

In tokamak plasma, electron velocities can reach relativistic speeds. A relativistic distribution function was considered to correct the spectra.

$$f(\beta, T_e) = \frac{\alpha}{2\pi K_2(2\alpha)} \frac{e^{-2\alpha(1-\beta^2)^{-\frac{1}{2}}}}{(1-\beta^2)^{\frac{5}{2}}} \tag{2.20}$$

The depolarisation term:

$$\left(1 - \frac{\beta_e^2(1-cos\theta)}{(1-\beta_i)(1-\beta_s)}\right)^2 \tag{2.21}$$

The depolarization effect is due to the velocity component parallel to the diffusion electric field. The larger the scattering angle or velocity component, the greater the effect. Note that this effect has little impact at low electron temperatures. However, in the case of a tokamak plasma, it is no longer negligible and must be considered.

In the case of hot plasma magnetized, the spectra are given by [58] as :

$$S(\epsilon, \theta, \alpha) = q_{11} S_{zh} \tag{2.22}$$

The spectral density $S(\epsilon, \theta, \alpha)$ describes the dependence of the scattered photon distribution function of wavelength ϵ, diagnostic geometry θ and electron temperature α [2, 64, 67]. $\alpha \equiv \frac{m_e c^2}{2T_e}$ is the normalized inverse temperature (with m_e the electron rest of mass and c the light velocity). The wavelength of the scattered photons λ_s is here normalized to the Laser wavelength λ_l by introducing a normalized scattered wavelength $\epsilon \equiv \frac{\lambda_s}{\lambda_l} - 1$. q_{11} refer to the depolarization approximation, illustrated in the figure 2.5 and given by :

$$\begin{cases} u = \frac{sin\theta}{1-cos\theta} & (2.23) \\ x = \sqrt{1 + \frac{\epsilon^2}{2(1-cos\theta)(1+\epsilon)}} & (2.24) \\ y = \frac{1}{\sqrt{x^2+u^2}} & (2.25) \\ \eta = \frac{y}{2\alpha} & (2.26) \end{cases}$$

and S_{zh} indicate the Zuralev spectra , illustrated in the figure 2.6 and as :

$$\begin{cases} S_{zh} = \frac{C}{A} e^{-2\alpha B} & (2.27) \\ A = (1+\epsilon)^3)\sqrt{2(1-cos\theta)(1+\epsilon)+\epsilon^2} & (2.28) \\ B = \sqrt{1 + \frac{\epsilon^2}{2(1-cos\theta)(1+\epsilon)}} - 1 & (2.29) \\ C = \sqrt{\frac{\alpha}{\pi}}\left(1 - \frac{15}{16}\frac{1}{\alpha} + \frac{345}{512}\frac{1}{\alpha^2}\right) & (2.30) \end{cases}$$

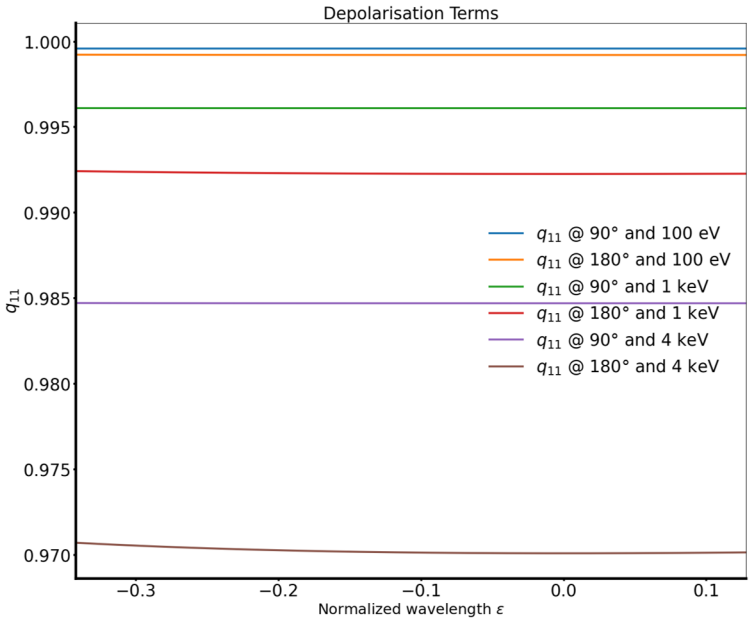

Figure 2.5: Depolarisation Term versus the normalized wavelength.

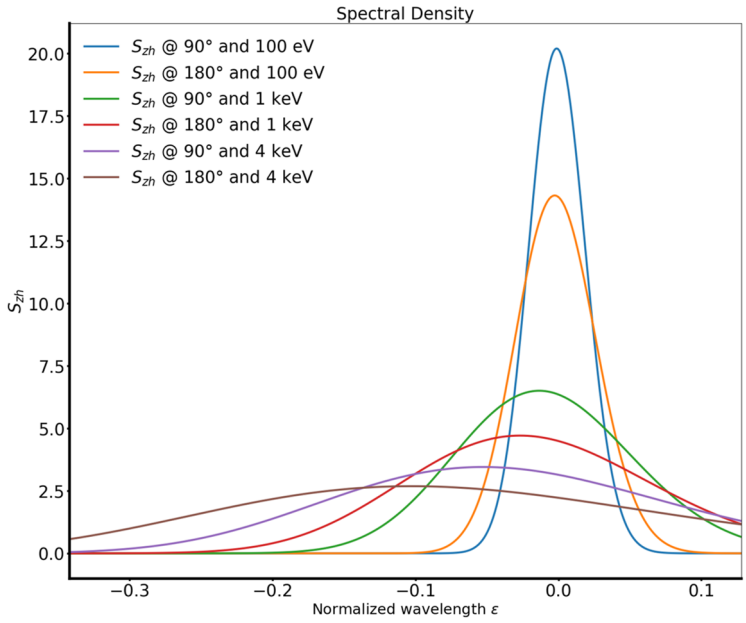

Figure 2.6: Thomson Scattering spectra S_{zh} given from the Zuralev function

2.3 Principle of Thomson Scattering Diagnostic

2.3.1 Measurement principle

From this section to the end of the thesis, we consider the ITS phenomenon. We introduce a new expression of the differential scattering power d^3P_s [8], given in [W.m^{-3}.sr^{-1}.s^{-1}] (power per unit volume per unit solid angle per unit of normalized wavelength ϵ):

$$\frac{d^3P_s}{d\epsilon d\Omega dV} = r_e^2 n_e \Pi_l S(\epsilon,\theta,\alpha) \tag{2.31}$$

From relation 2.31, one observes that the scattering power is linearly proportional to the electron density and the incident Poynting vector Π_l in [W.m^{-2}] whereas the spectra depend on the electron temperature and the scattering angle θ settled by the diagnostic. Therefore, measuring the signal amplitude will allow us to determine the electron density, whereas the electron temperature can be retrieved if a detector is sensitive to the scattering spectrum. However, this measurement might be possible if the norm of the Poynting vector is known and sufficient to estimate the plasma parameters.

2.3.2 Pulsed laser for Thomson scattering diagnostic

Because of the small effective cross-section of interaction between the photons and the electron ($\sigma_e \approx 7.93 \times 10^{-29}\ m^2$), the efficiency of a Thomson scattering diagnostic is very low. To overcome this problem, a high energy source is needed to emit a large number of photons .
Light amplification by stimulated emission of radiation (laser) is a coherent light source [43, 45]. This light source generally emits photons of close wavelength, often leading to the assumption that the laser is a monochromatic source where all the photons are emitted at a central wavelength λ_{CWL}.
Pulse Nd:YAG lasers with a central wavelength at 1064 nm meet this criterion, and their unique feature is the large number of photons emitted (10^{19} photons per pulse) in a short pulse duration (~ ns) at low repetition rate (Hz). Theoretically, the laser can be described from the Maxwell equation, namely the electromagnetic wave propagation:

$$\Delta\vec{E} - \frac{1}{c^2}\frac{\partial^2\vec{E}}{\partial t^2} = 0 \tag{2.32}$$

One solution possible of the equation 2.32 is a Gaussian function given by :

$$\begin{cases} \vec{E}(r,z) = \vec{E}_0 \left(\frac{\omega_0}{\omega(z)}\right) e^{-\frac{r^2}{\omega^2(z)}} e^{-ikz - ik\frac{r^2}{2R(z)} + i\zeta(z)} & (2.33) \\ \omega(z) = \omega_0 \sqrt{1 + \left(\frac{z}{z_r}\right)^2} & (2.34) \\ z_r = \frac{\pi\omega_0^2}{\lambda_l} & (2.35) \end{cases}$$

Figure 2.7 describes a Gaussian beam's theoretical beam width $\omega(z)$. One observes that the laser beam size evolves along the optical axis z regarding the laser properties. The beam diameter is observed to reach a minimum radius named waist ω_0, constant over a characteristic length z_r called the Rayleigh range.
In addition, the relation 2.35 and the relation 2.35 show that the beam width depends on the laser wavelength λ_l and the Rayleigh range z_r. So, the approximation of the Gaussian pulse (spatially) agrees with the theory. Hence, the intensity $I(r,z)$ of the beam can be expressed as :

$$I(r,z) = I_{peak} \left(\frac{\omega_p}{\omega(z)}\right)^2 e^{-\frac{2r^2}{\omega(z)}} \tag{2.36}$$

where I_{peak} is the laser peak intensity in [W.m^{-2}] expressed from the laser energy E in [J], the pulse duration dt and the beam surface A_{beam} in [m^{-2}] :

$$I_{peak} = \frac{E_l}{A_{beam} dt} \tag{2.37}$$

The reader will notice that laser enables a local n_e, T_e measurement in the Tokamak reference. Indeed, as shown in relation 2.19, the scattering volume V_{scatt} is given by the interaction of the Poynting vector with the electron density. The laser can be integrated along the laser path dz by taking into the beam width $\omega(z)$.
Moreover, the use of Nd:YAG laser makes it possible to dissociate the scattered signal from the noise during measurement and get local information on the plasma parameters after collecting the scattering photon by an imaging system (see chapter 6 for more details). Nevertheless, the laser properties must be characterized to know the energy injected inside the tokamak or usually to know the beam size inside the machine. In practice, these parameters depend on the laser properties such as the central wavelength λ_l, the divergence θ, the Rayleigh range z_r or even the M^2 mentioned before.
They must be measured to estimate the experimental scattering volume $V_{scattering}$ inside the machine. For this purpose, a laser line system has been developed and will be presented in the next chapter.

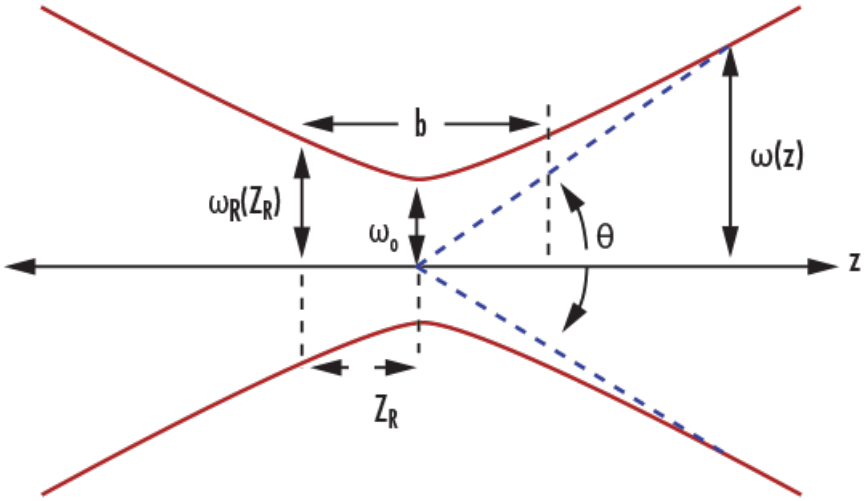

Figure 2.7: Ideal Gaussian beam, edited from [24]

Figure 2.7 shows the theoretical laser beam profile for different z positions along the optical axis. As shown, the beam diameter is not constant and many experiments show that the laser is not a perfect Gaussian source. Therefore, the beam width and the waist are not exactly circular but elliptic; to take the real beam diameter into account, the quality factor M^2 is introduced :

$$M^2 = \frac{\pi \omega_0 \theta_{laser}}{\lambda} \tag{2.38}$$

, where θ_{laser} is the laser divergence. The quality factor evaluates the beam quality, i.e., the beam ellipticity. The diameter of a beam is considered excellent when the M^2 is equal to or close to 1.

2.4 Summary

The scattering of photons by matter is a complex phenomenon that can be analyzed from many different angles, whether by wave or particle mechanics (as in the case of Compton scattering). This complexity stems from the wave-particle duality of photons, which exhibit both wave and particle properties. This chapter presents a non-exhaustive overview of the scattering of photons by electrons. Thomson scattering, a special case of Compton scattering, describes the scattering of photons by charged particles (such as ions or electrons) and is introduced here to clarify the phenomenon and its relationship with particle velocity. In particular, we examine the expression of the scattered power for the incident electric field and the expression of the scattering spectrum concerning the plasma condition through the Salpeter parameter. The particles' collective motion is considered in the incoherent Thomson scattering framework. The power is then expressed as the sum of the electric fields scattered by each charge in the medium, and the expression of the scattering spectrum is the sum of the ionic and electronic scattering spectra. Note that these spectra depend on electron temperature (T_e) and distribution function (f), effective charge (Z_{eff}) and ion temperature (T_i). Incoherent scattering, on the other hand, takes no account of the ion scattering spectrum, and the scattering power is expressed as follows:

$$\frac{d^3P_s}{d\epsilon d\Omega dV} = r_e^2 n_e \Pi_l S(\epsilon,\theta,\alpha) \tag{2.39}$$

In the context of this thesis, the analysis focuses solely on electrons due to the low mass ratio between electrons and ions ($\frac{m_e}{m_i} \ll 1$). Moreover, since the Salpeter parameter is less than 1, this approximation justifies using incoherent Thomson scattering.

Finally, we present the principle of Thomson scattering measurement. Since the effective cross-section between photons and electrons is small ($\sim 10^{-29}$), it is necessary to use pulsed lasers to generate enough photons to obtain a detectable signal. In particular, we show that scattering power depends on two key parameters in plasma physics: proportional electron density and electron temperature, which determines spectrum broadening.

3 High Resolution Thomson Scattering design on WEST

Sommaire

3.1 Laser beam transport system . . . 75
3.1.1 Optical engineering basis . . . 76
3.1.1.1 Laser system . . . 76
3.1.1.2 Piezoelectric mounts and set of dielectric mirrors. . . . 78
3.1.1.3 Detectors for the beam positioning and characterization 79
3.1.1.4 Beam dump principle . . . 81
3.1.2 Steering laser line system on WEST . . . 82
3.1.3 Laser alignment Architecture . . . 84
3.2 Optical collecting system . . . 86
3.2.1 Core Optical Collecting System (COCS) . . . 87
3.2.2 Edge Optical Collecting System (EOCS) . . . 88
3.3 Optical properties requirements . . . 90
3.4 Optical fiber bundles . . . 90
3.5 Polychromator . . . 91
3.5.1 Principle . . . 91
3.5.1.1 Polychromator imaging system . . . 92
3.5.1.2 Interference filter . . . 92
3.5.1.3 APD and electronic system . . . 93
3.5.1.4 Polychromator for WEST . . . 94
3.6 WEST acquisition system . . . 96
3.7 Photonic Budget . . . 97
3.8 Summary . . . 99

A new Thomson scattering diagnostic has been designed for the WEST tokamak. It is a complete renewal of the older system operated on Tore Supra [44]. The only similarity is the implantation of the laser optical path. The HRTS plant is shown in figure 3.1; the laser source is below the Tokamak in the Laser emission chassis, see the figure 3.2. Each laser pulse propagates along the optical axis to cross the plasma vertically, aiming to probe the plasma core up to the magnetic axis and probing the plasma edge. The Optical collecting Systems (OCSs) are at an outer midplane port. Note that laser polarization is perpendicular to the lines of sight of OCSs, as it maximizes the photon flux from the scattering process.

This chapter presents the diagnostic design, including the laser alignment system, the optical collecting systems, and the polychromators.

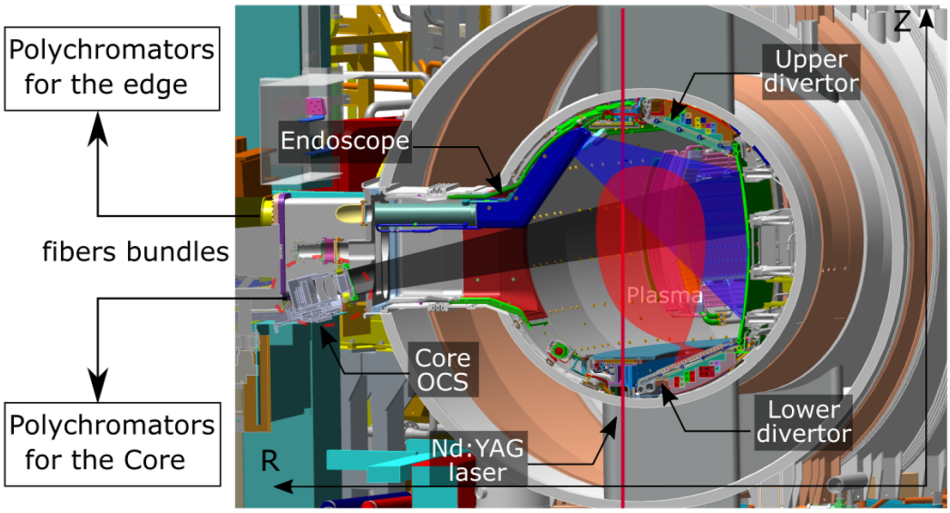

Figure 3.1: Schematic of the High-Resolution Thomson Scattering on WEST tokamak, with OCS fields of view.

3.1 Laser beam transport system

At the beginning of the project, a question arose about the stability of the laser position during the experimental campaign. In particular, the vibrations coming from the Tokamak could lead to a laser misalignment. To avoid this problem, it was therefore planned to develop an alignment system [5, 11, 26, 72, 89] that would be dissociated from the machine and could be used to steer the mirrors from the Control Room. Then, we have designed a steerable optical system taking into account the following constraints:

- Technically, two Nd:YAG lasers from the Innolas laser company [1] are installed in the hall Tore basement and must carry up to the Tokamak with a millimeter accuracy.
- Physics, to get a good data quality, the laser energy has to be monitored with aims at estimating the electron density n_e accurately and enabling the absolute calibration.
- Finally, we had to consider the project budget to develop the system.

[1] https://innolas-laser.com/Applications/Scientific-Applications.html

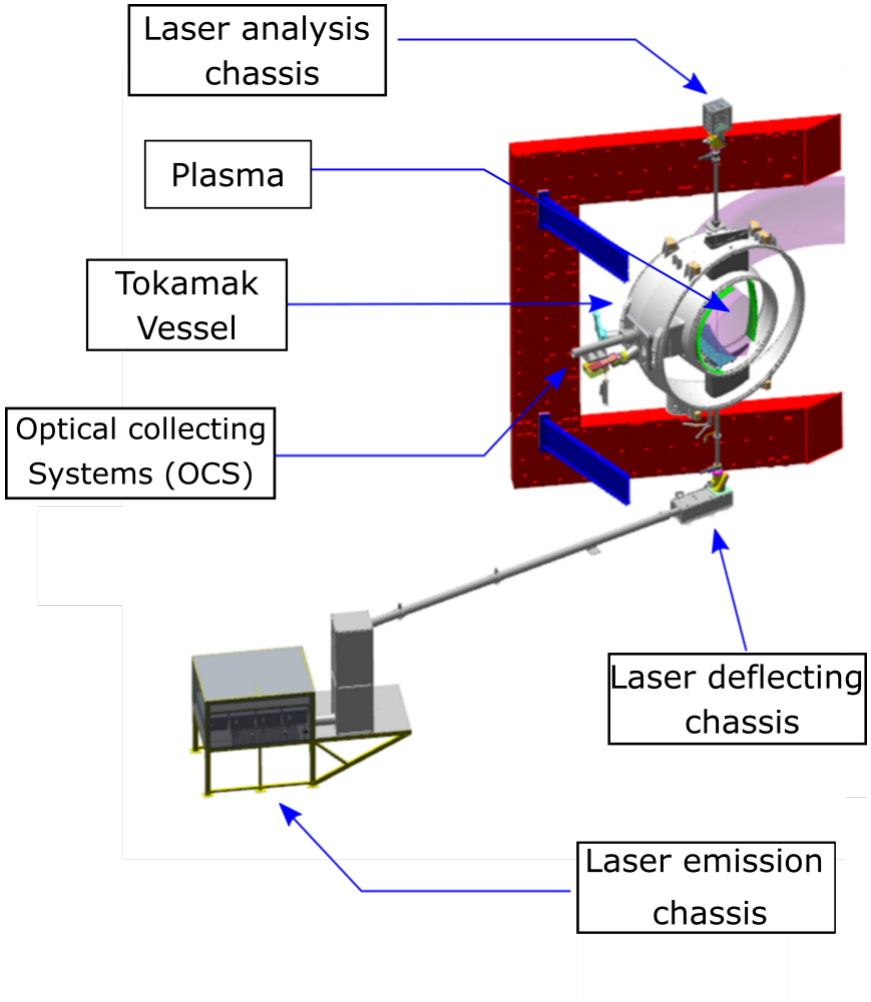

Figure 3.2: Steering laser line system implemented on WEST. The first part of the SLLS was installed in the basement, close to the polychromator.

3.1.1 Optical engineering basis

3.1.1.1 Laser system

The diagnostic has a laser system installed in the Tokamak basement. The unique feature of the Innolas laser system is the installation of the two Nd:YAG lasers in a metal structure that allows the two beams to be parallelized and combined on a single output if required. Each sub-system comprises a class IV laser emitting laser pulses at the central wavelength 1064 nm with an energy of 2 J, a pulse duration of about $\approx 10\ ns$, and a repetition rate of 30 Hz. In addition, each sub-system is equipped with a class II laser (Continuous Wave) at 632 nm to facilitate the laser pulse alignment. Usually, this laser is named an alignment laser and is combined with the pulse laser to follow the same optical path. Figure 3.4 shows the two laser sub-systems, with the amplification and combination stages.
The combination stage used three mirrors to change the S-polarization to P-polarization.

Figure 3.3 shows the combination principle where the P-polarization beam path is represented in the blue arrow, and the S-polarization beam and the alignment laser path are depicted in purple. Note that mirrors 1 and 3 allow the transmission of the S-polarization beam and reflect the P-polarization. In contrast, mirror 2 transforms the S-polarization beam into a P-polarization. Thanks to this stage, the lasers can be synchronized to deliver ~ 4 J at 30 Hz to increase the Signal to Noise Ratio (SNR) or 2 J at 60 Hz to increase the time resolution during operation. These two scenarios will impose thermal constraints on mirrors and the optical dump, which has been taken into account for the Steering Laser Line System (SLLS).

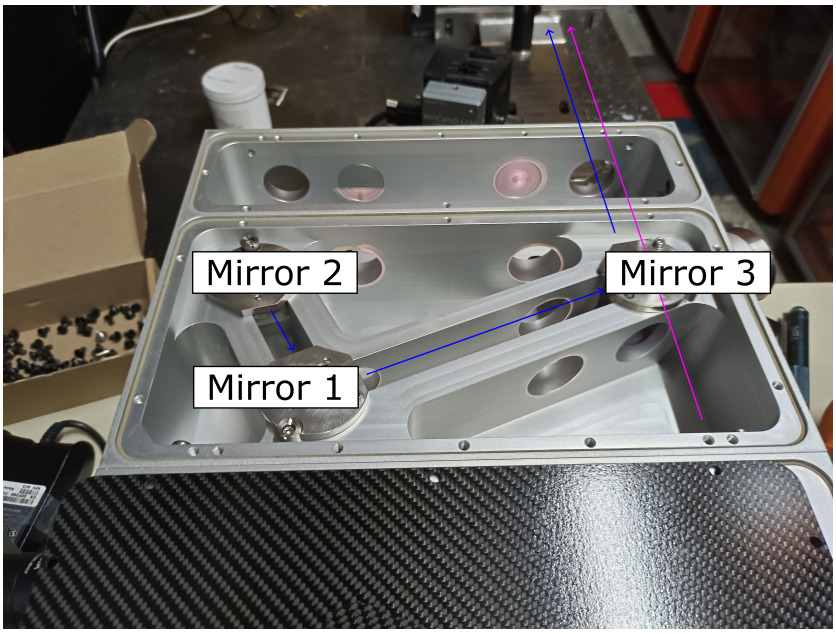

Figure 3.3: Lasers combination system



Figure 3.4: Innolas laser system

3.1.1.2 Piezoelectric mounts and set of dielectric mirrors.

Theoretically, a beam of light passing through an optical component can be split into three parts at the optical component interface: A transmission part designated by a transmission factor T. A reflective part designated by a reflection factor R and a diffusive part designated by a factor D that leads to the following equation :

$$(R+T+D)E_{laser} = E_{laser} \tag{3.1}$$

The mirrors have been optimized to reduce the diffuse part ($D \sim 0$) for the laser polarization considered in this framework. The mirrors are used to separate the laser beam and the alignment laser. To steer one laser beam and characterize it, two types of dielectric mirrors are used : Dielectric mirrors with reflectivity $R \approx 99.7\%$ at 1064 nm and transmission factor $T_{optics} \approx 45\%$ at 632 nm for S-polarization light are used to steer the laser pulses from the laser to the Tokamak, (mirror 3,4 and 5 on the figure 3.8). For S-polarization light, a second set of dielectric mirrors with a transmission factor $T_{optics} \approx 99.7\%$ at 1064 nm and reflectivity $R \approx 45\%$ at 632 nm. They will be used to take a fraction of the pulse (0.03%) to measure each laser pulse energy (mirrors 1 and 2 on figure 3.8). Mirrors are fixed in optical mounts to ensure precise alignment, orientation, and stability. These mounts have two piezoelectric actuators in x and y (coordinate perpendicular to the optical path) to steer the beam position with an accuracy of ±10 nm over a length of 1 m. Note that all the dielectric mirrors are adapted for the high energy laser and have a Laser induce damage threshold (LIDT) of 8 J.cm^{-2} for the Nd:YAG laser properties. This enables it to withstand 4 J of power at 30 Hz in the case wherein the two laser beams are combined or 2 J of power at 60 Hz in the case wherein the two laser beams are temporally shifted [90].

3.1.1.3 Detectors for the beam positioning and characterization

Optical detectors in the laser field play a crucial role in monitoring, measuring, and controlling laser light. They are widely used for:

- Detecting laser power and intensity. Optical detectors, such as photo diodes or thermal sensors, measure the power or intensity of laser light. These measurements are essential for monitoring the stability and coherence of laser power and ensuring safety by detecting potentially dangerous power levels.
- Beam alignment and diagnostics. Detectors are used to visualize or analyze the spatial profile of the laser beam. They evaluate parameters such as beam position, divergence, collimation, and intensity uniformity.
- Time and frequency measurement. Fast detectors (such as ultra-fast photodiodes or photo-multipliers) characterize pulse duration for lasers with ultrashort pulses.
- Feedback systems and active control. In applications requiring fine stability, detectors provide real-time feedback for adjusting laser parameters such as power or frequency stabilization or active control of beam direction or focus (the case scenario of interest in this thesis).
- Safety applications. Detectors can monitor lasers in sensitive environments to prevent accidents or unintentional light leakage. Laser safety is important in developing the laser line system and has been taken into account in the scope of this thesis. However, it will not be explained in detail.

This section presents the various detectors selected for monitoring and characterizing laser pulses during Thomson scattering diagnostics operation.

Camera: Cameras are useful for getting information about misalignments. Cameras are made of a semiconductor array of 1280 × 1024 pixels. Each pixel sizes 5300 nm × 5300 nm and has an 8-bit resolution, providing 2D information in the plane normal to the optical axis.
To visualize the beams, Near Infrared (NIR) cameras [2] will be installed behind the mirrors 3, 4, and 5 with an imaging system to observe the laser alignment position on the mirrors as presented in figures 3.8. Indeed, by using the mirror properties, the alignment laser is partially transmitted, whereas 0.03% of the laser pulse is transmitted by the mirrors. In addition, the detector properties used in figure 3.5 represent the quantum efficiency of the camera used for the system. Even if the camera has a low quantum efficiency at 1064 nm (the quantum efficiency is around 3 – 4%), the camera could be damaged [33]. A solution is to use neutral density filters, which will be fixed from the imaging system to reduce the 600 μJ transmitted by the mirror toward the camera.

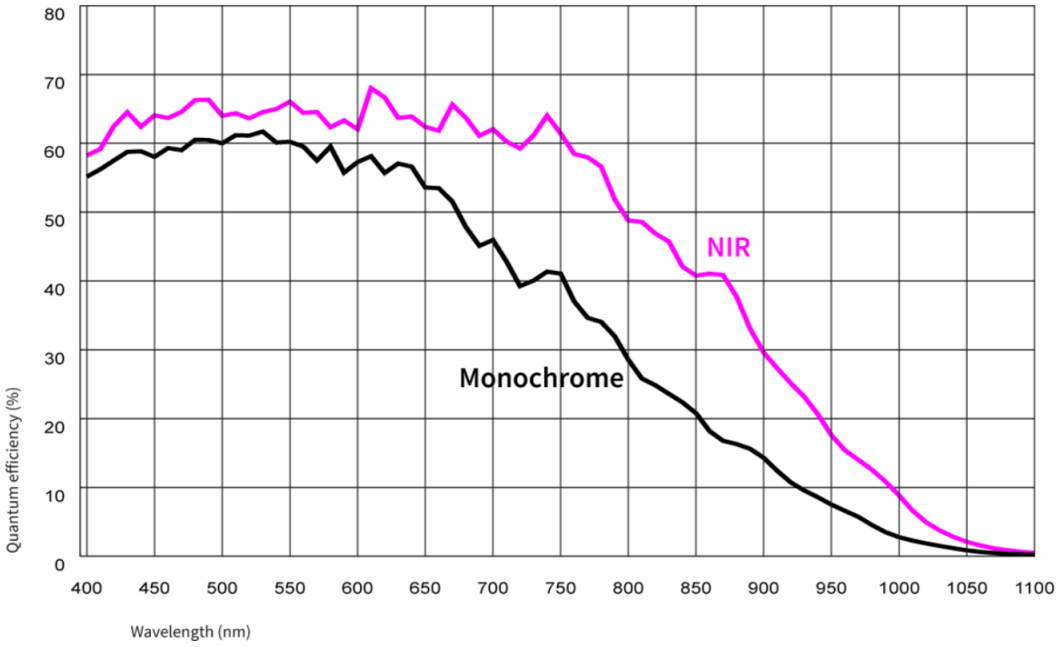

Figure 3.5: Camera quantum efficiency, taken from [20]

Pyroelectric detector: Using cameras to estimate the laser energy is a possible solution. However, pyroelectric detectors measure the energy along the laser line more accurately. Pyroelectric detectors will be used to estimate the laser energy at

[2] GV-5240CP-NIR-GL Rev.2.2 (AB12557)

the tokamak entrance, which acquisition cards will acquire for the post-processing signal. A pyroelectric detector is made of a ceramic that generates an electrical charge when temperature changes [34, 37, 87, 93]. This property is due to the alignment of electrical dipoles in the material, which changes with temperature. Pyroelectric materials exploit the relationship between temperature change and electrical charge generation, making them valuable in various sensing and energy recovery technologies. In other words, when a pyroelectric material is submitted to the laser pulse energy, the temperature changes, and consequently, an output voltage proportional to the pulse energy is provided, as illustrated in the figure 3.6. Hence, we will measure each laser during the HRTS operation using this detector.

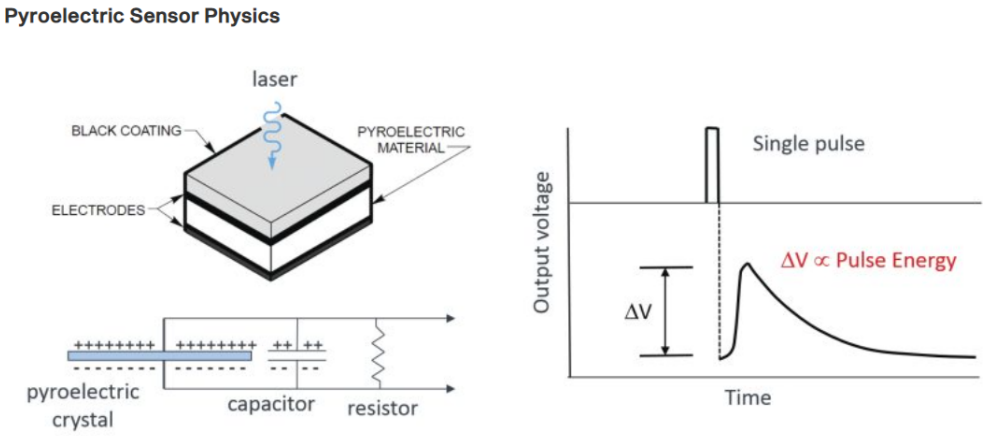

Figure 3.6: Pyroelectric measurement principle [62]

Pulse monitoring system: An optical fiber with a photodiode and a fast-acquisition card will also be used to monitor the pulse. This monitoring system will measure pulse energy and duration to improve data processing by computing the correlation between the laser pulse and the scattering signals.

3.1.1.4 Beam dump principle

The dumps are cylindrical mechanical pieces with a cone inside (see figure 3.7) bought from the LaserComponent company. The cone's particularity is that it reflects each laser pulse inside the Dump's inner wall to absorb the pulse energy. The thermal transfer is then done by convection. According to the manufacturer's specifications, the dump can withstand 70 W without a cooling system and 500 W with a water cooling system. Since each laser pulse contains 2 J of and a repetition rate of 30 Hz, the power to be absorbed equals 60 W. However, combining the laser in one optical path will lead to a power equal to 120 W, requiring a water cooling system for the dump.

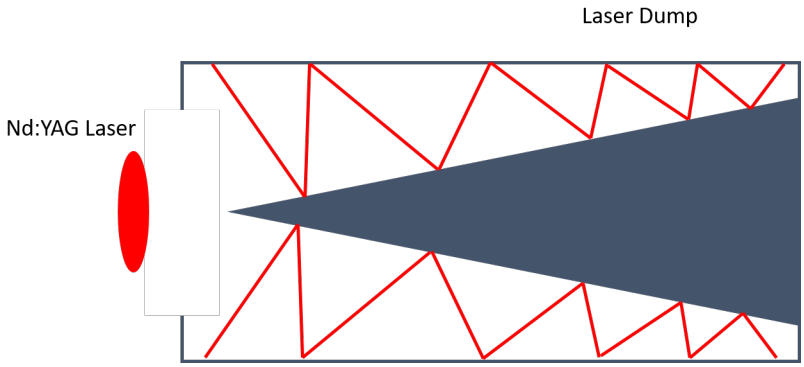

Figure 3.7: Schematic view of the Beam dump principle. The incident pulse, represented by the red disc, will reflect inside the dump before being absorbed by this last. The red line is a schematic view of the reflection line while the laser pulse is divided the cone.

3.1.2 Steering laser line system on WEST

Since the Nd:YAG laser has a high energy and therefore a high power (≈ 352 MW.cm^2), the beam could not be observed easily on camera without damaging it. However, thanks to the unique Innolas feature and the combination system, the position control of the lasers is facilitated, and a nano-positioning system is imaginable.
Figure 3.2 shows the laser alignment system implementation on the Tokamak. The optical alignment system is implemented on the Tokamak reactor at Q1A port. Each laser pulse propagates under the Tokamak over a distance of 16 m from the laser source to the bottom port. The first part is made of two optical chassis (the Laser emission chassis (LEC) and the Laser deflecting chassis (LDC)), enabling the transport of the laser beam inside the Tokamak by minimizing the loss due to the propagation. A second part of the SLLS has been installed at the top of the Tokamak; it is used to stop the beam propagation and characterize the laser pulses that exit the Tokamak.
Figure 3.8 illustrates the schematic view of the steering laser line system. The combination represents the laser combination (purple), the alignment laser (blue), and the Nd:YAG laser (red). The dielectric mirror is represented with the correct orientation 45° and the detector (Camera, Pyroelectric, optical fiber).

Laser emission Chassis: The emission laser chassis sits at approximately 11 m from the Tokamak access port on a concrete floor free of vibrations. Details of the optical system are displayed in figure 3.8. The laser is S-polarized, its width is about 14 mm at the laser output with a quality factor M^2 below 3, and the natural divergence of the beam is $\theta_l = 0.5$ mrad. The laser is actively cooled and can operate continuously for thousands of seconds, fulfilling the WEST long pulse operation requirement. The lasers propagate from the source up to the laser-deflecting chassis via two additional dielectric mirrors (mirrors 3 and 4 in figure 3.8). They transmit 0.03% of the 1064 nm

beam toward control cameras (2 and 3) to monitor the beam position. Note that these mirrors are mounted on piezoelectric supports controlled remotely to correct the beam path.

Laser deflecting chassis: As mentioned in chapter 2, the laser beam cross-section has a Gaussian shape characterized by a radius $\omega(z)$ that evolves along the optical path (z axis). In practice, control of this width is necessary to guarantee the absence of focusing on optical components, leading to damage. More importantly, to ensure that the laser beam is wholly contained in the volumes of sight of the Optical collecting System (OCS). To do so, a focus system ($f_1 = -200$ mm, $f_2 = +250$ mm) is installed as close as possible to the Brewster window (vacuum interface) to tune the position of the beam waist in the plasma chamber. The beam width at the output of the focus system is about 20 mm (minimizing possible damages of the Brewster window) and is focused to approximately 1.4 mm around the equatorial midplane ($Z = 0$ m) of the tokamak chamber, the volumes of sight of both OCSs are about 8 mm wide in the toroidal direction, which shall ensure complete coverage of the laser beam, with margins. A NIR camera (camera 4) visualizes each beam propagating through the focus system. A third dielectric mirror installed in a piezoelectric support (mirror 5 in the figure 3.8) deflects each beam vertically toward the tokamak chamber through a first vacuum interface composed of a Brewster window. Note that the Brewster window is needed to minimize laser losses. In principle, for a S-polarization, the transmission equals 1 for a tilt angle of 54.2°. The laser crosses the plasma vertically at the position $R = 2.556$ in the machine reference.

Laser analysis chassis: A second Brewster window is also installed at the outlet port to reduce the laser reflection in the tokamak vessel. The laser beam ends in the laser analysis chassis, where the optical dump will absorb it. A second pulse monitoring system (composed of a photo-diode) collects a small fraction (0.03 %) of the laser beam for chronology purposes, in particular, to provide a post-trigger signal to the fast acquisition [6].

A set of piezoelectric mounts is used to steer each laser pulse and correct the misalignment. An optical system with a divergent lens at -200 mm and a convergent lens at 250 mm is installed before the first Brewster window to focus the laser beam inside the Tokamak. Once the laser is focused, the waist is below 2 mm at the position $z = 0$ in the reference machine.

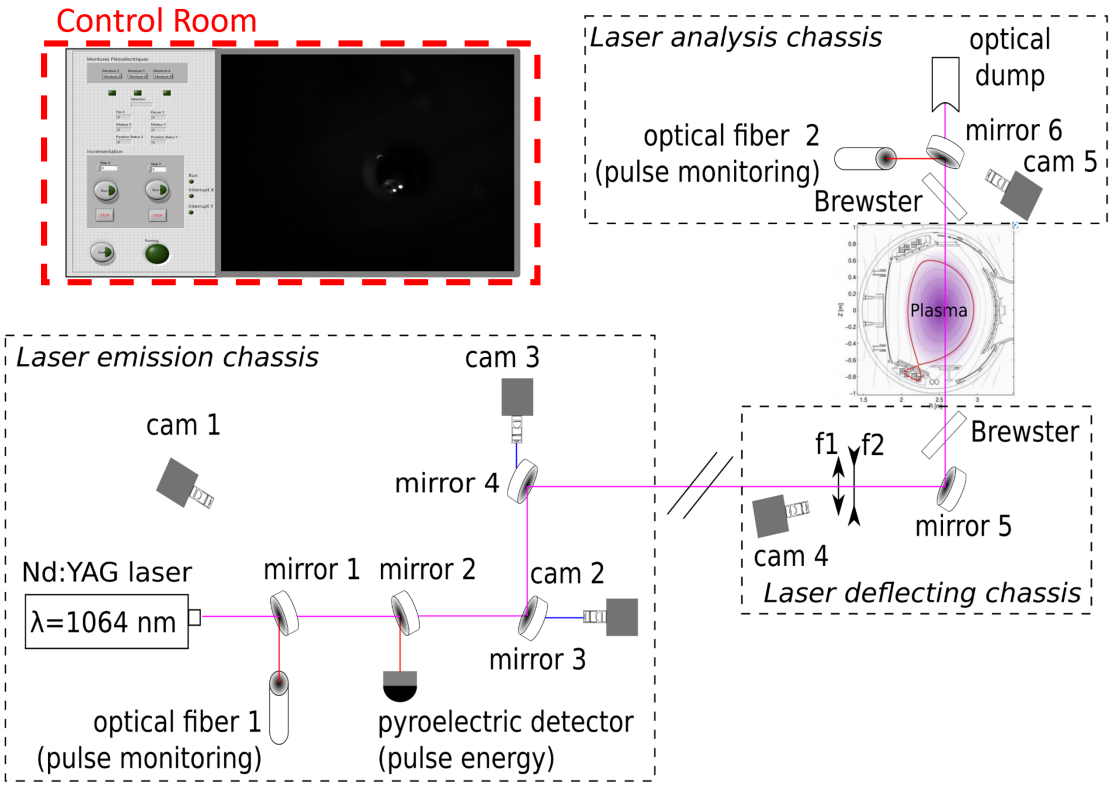

Figure 3.8: Schematic of the steering laser line system. The blue line illustrates the optical path of the P-polarization beam. The Purple line represents the laser beam combination of the S-polarization Nd:YAG laser and the laser alignment. The panel is the first version of the LabView program used to steer the mirror and visualize the video stream.

3.1.3 Laser alignment Architecture

Since the laser line is equipped with class IV lasers, which pose a lethal danger to humans, installing a safety system is imperative. The project team opted for a safety enclosure to manage the laser startup according to the different operating modes defined by the scientific managers and safety engineers. To allow the operation of the line during or after experimental campaigns, four operating modes must be considered:

Alignment mode for maintenance: This mode allows for the optimal alignment of the laser during maintenance periods to facilitate the absolute calibration of the diagnostic.

Alignment mode between plasma shocks: This mode allows for remote intervention on the laser alignment between two plasma experiments if necessary.

Real-time alignment mode: This mode corresponds to the automatic positioning of laser pulses relative to a reference point. This feature involves real-time acquisition of video flow and energy measurements to align the laser within the machine optimally.

Real-time operation mode: This mode corresponds to the real-time acquisition and processing of energy measurements from each laser pulse and Thomson signals. These data will be transmitted via the Dolphin real-time network. This mode will thus enable real-time measurements of electron density. Ideally, accurate measurements of the laser pulse are needed to measure the electron density. For this reason, we decided to use the pyroelectric detectors to measure the laser energy. Since the pyroelectric response is in the millisecond dynamic range, this last will be connected to the slow acquisition channels of the Nectarine card, which will be presented later.

Each mode must operate considering laser security. However, none of the modes requires the use of the RT network, the acquisition network, or even the data acquired by the detectors. Therefore, the diagnostic architecture must suit the requirement, particularly the SLLS. Figure 3.9 illustrates the actual diagnostic architecture that has been used for the post-processing (see chapter 6). Each block represents a sub-system of the diagnostic needed to operate the diagnostic. The arrows indicate the connection between the sub-systems. Namely, the laser security box (red arrows) allows laser operation in the above mode. Two networks were used:

- A local network to acquire the camera's video flow and to steer the piezoelectric mounts. Allowing pulse visualization during alignment from the tokamak basement.
- A acquisition Network used by all the WEST diagnostics. This network was used to acquire the data from the acquisition cards and to control the SLLS from a dedicated computer in the control room.

Note that the lasers can only operate if the safety relays are active (that is, if the doors of the optical enclosures are closed).

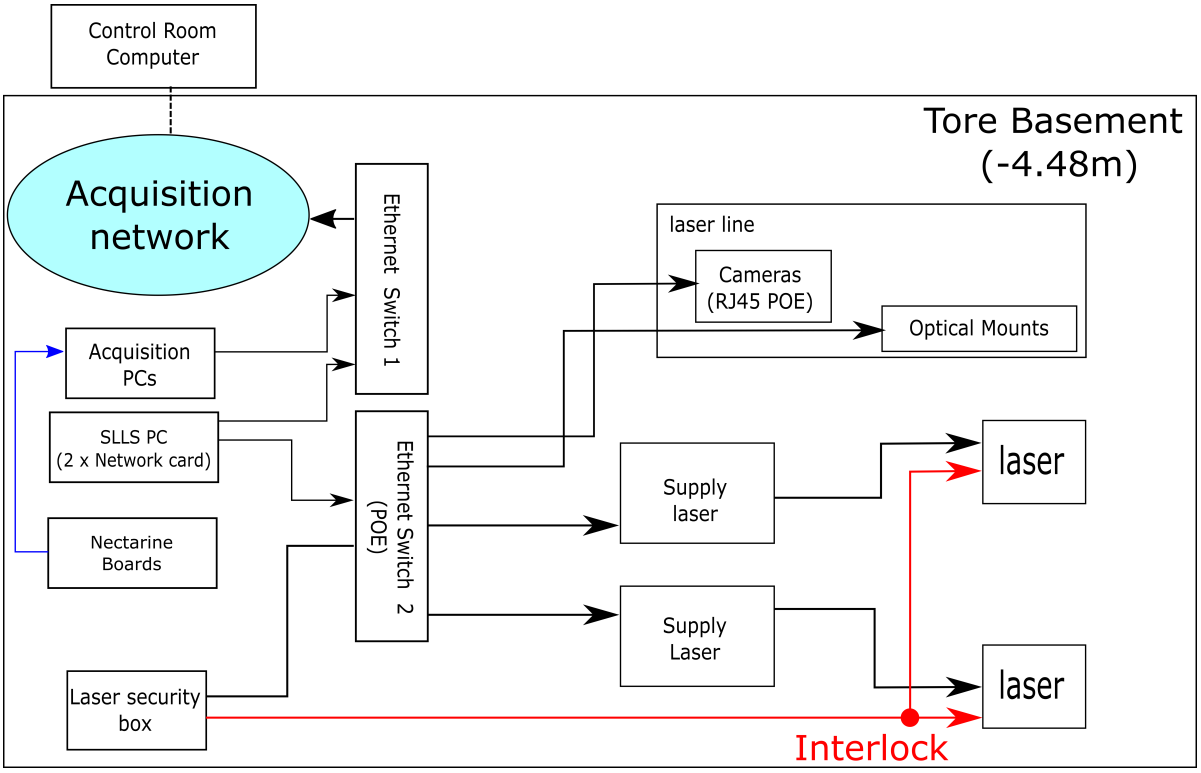

Figure 3.9: System analysis of the steering laser line system

3.2 Optical collecting system

The scattering measurements will be made vertically in WEST, with a sub-centimetric resolution at the edges and a centimetric resolution at the core. The high vertical resolution makes it easier to distinguish variations in electron density and temperature at the edge of the plasma. We remember that the gradient length is in the order of 3 cm for the edge in WEST.
The telescopes' vertical resolution (Δl) plays a crucial role in determining the precise location of the photons scattered by the electrons. Two OCSs have been designed to collect the scattering photons to cover the core and edge plasma regions. Each Optical collecting system is designed to image the scattered volume at the laser position onto arrays of optical fibers as shown in figure 3.10. The position and alignment of the two optical collecting systems are chosen not to intercept the lower divertor surface and to get a spatial continuity between the views along the laser path.

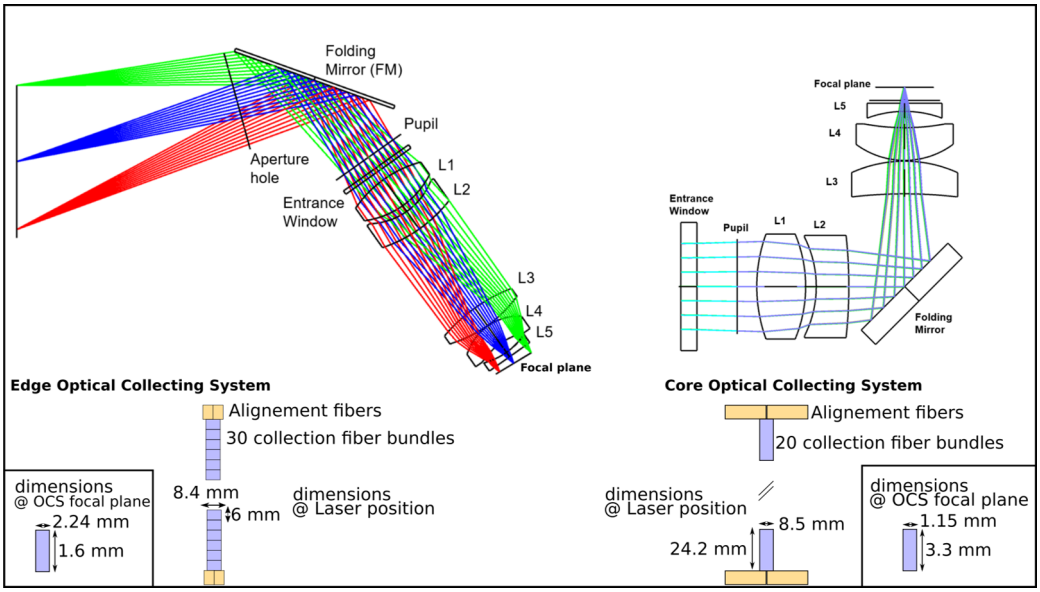

Figure 3.10: Zemax simulations for the EOCS (left) and the COCS (right). The EOCS comprises the aperture, a mirror, a pupil, and 5 optics down to an in-situ array of fiber bundles. Below are schematized the shape of the fiber arrays projected on the laser path.

3.2.1 Core Optical Collecting System (COCS)

The Core Optical Collecting System (COCS) is designed to observe the plasma core, characterized by large gradient scale lengths (order of minor radius $a \approx 50$ cm in WEST) and electron densities above 10^{19} m^{-3}. Placing the collecting system outside the vacuum chamber offered technical simplification while fulfilling adequate photon budgets (discussed later), considering a centimeter spatial resolution (see figure 3.11). The inlet aperture size is 110 mm in diameter; this last was constrained by thermal limitations on the first window (during long pulses). It is placed 1.62 m from the laser path. The geometry of the equatorial port constrained the field of view toward the plasma top. The design offers a vertical field of view of 50 cm spanning from the plasma center ($Z \approx 0$ m) toward the upper edge by tilting the COCS of 14.6°. The outlet system comprises a fiber array of twenty measurement points and four alignment points. Imaged on the laser path, each point has a vertical size of 24.2 mm and a toroidal size of 8.5 mm (larger than multiple laser waists).

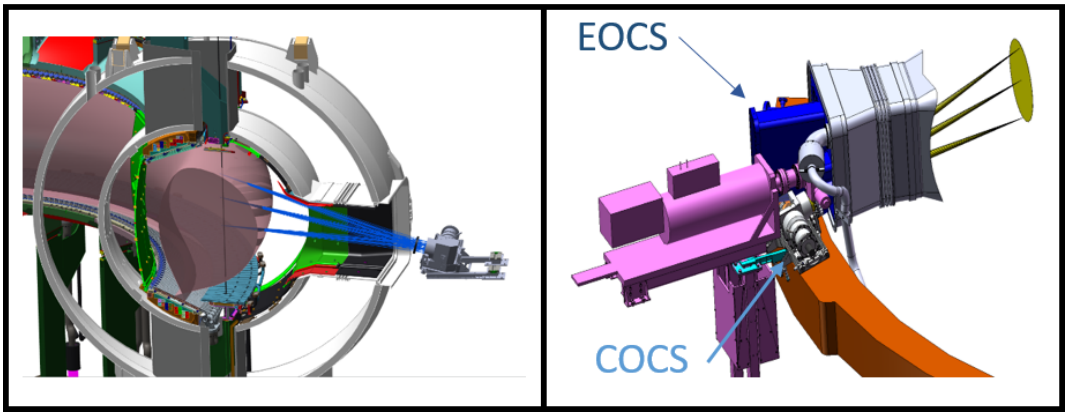

Figure 3.11: CAD of Core Optical Collecting system installed on the Tokamak.

3.2.2 Edge Optical Collecting System (EOCS)

An Edge Optical Collecting System (EOCS) was designed to provide about 10 measurement points across a H-mode pedestal width. To guarantee a sub-centimeter resolution and a good SNR at the edge region, an actively-cooled endoscope has been designed [13], see figure 3.12.
The design of an endoscope for infrared diagnostics in a tokamak environment requires careful attention to several essential criteria: optical, thermal, hydraulic, and vibrational. The optical system, including an actively cooled mirror with a thickness of 30 mm, is the main component of the diagnostic. This system must be optimized to reduce noise related to infrared radiation and to minimize deformations that lead to image distortion, which is crucial for Thomson scattering measurements.

Thermal and Hydraulic Criteria:

Given that the diagnostic measurements are conducted in the infrared, the temperature of the components mustn't exceed 200°C. A higher temperature could lead to photon emission from the mirror, resulting in an additional noise source for the TS measurements. The power radiated by the plasma, particularly from the core plasma and the radiation from the lower divertor, has been evaluated using radiative calculations specific to the WEST tokamak. These power levels were established from simulations, and thermal data was retrieved and analyzed using Ansys software.

Plasma Radiation:

The analyses of plasma radiation for power levels of 10 MW consider several scenarios, including the core plasma and the lower divertor: absorbing (ϵ=1) and specular reflectance (ϵ=0.5). These analyses help understand the maximum thermal fluxes the endoscope must withstand, ensuring a design capable of resisting the extreme conditions inside the Tokamak.

Vibrational Criteria:

The diagnostic is in an environment with several sources of vibrations, such as vacuum pumps and the plasma itself, which oscillate at frequencies between 80 and 833 Hz. To avoid resonance problems, the natural frequencies of the endoscope structure must be above 20 Hz and sufficiently distanced from the operating frequencies of external components.

Tokamak maintenance :

It is also important to note that the endoscope design considers maintenance procedures such as Boronization, which can degrade the mirror's optical properties. A shutter is included to protect the mirror during these maintenance activities and address this possibility.

Therefore, the thermo-mechanical constraints and the water-cooled shielding limit the aperture of the first inlet to 75 mm. As shown in figure 3.12, a golden mirror actively cooled is tilted at 45° and allows a downward field of view of 18 cm from $z = 0.47$ m to $z = 0.65$ m ensuring continuity with the core measurement points with a vertical spatial resolution of 6 mm and 8.3 mm toroidally. The endoscope aperture will be placed 0.38 m from the laser beam. The scattering volume will be imaged at the outlet on 30 in-vessel high-temperature fibers. These fibers will be connected to a flange with a 2 mm vacuum feed-through to carry the photon with additional fiber bundles (needed to maintain the machine vacuum). This vertical resolution corresponds to 3.5 mm resolution once remapped to mid-plane and allows to get approximately 10 radial positions across the pedestal.

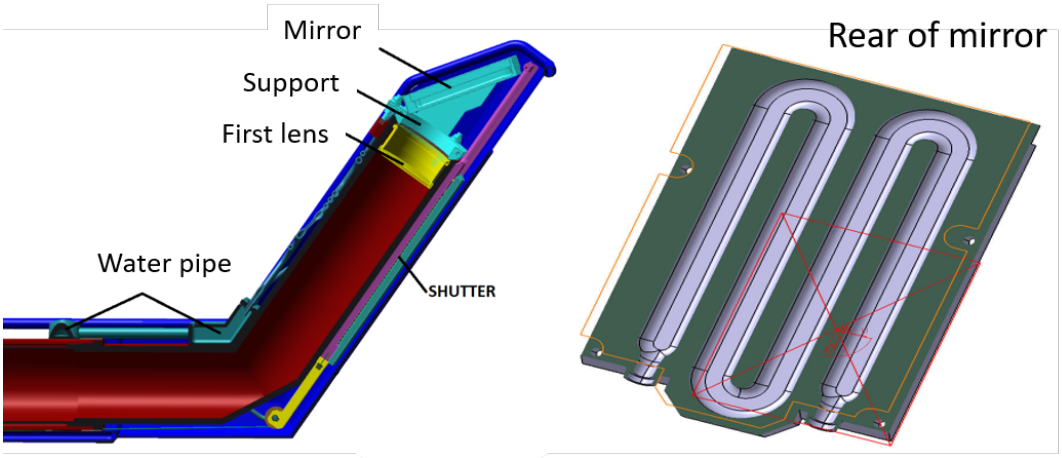

Figure 3.12: Longitudinal section of the endoscope allocated to the edge measurement.

3.3 Optical properties requirements

The technical constraints presented above impose specific limitations on the imaging system, notably on the number of lenses and the size of the optics that can be integrated into the structures. Five lenses have been optimized to cope with the numerical aperture of the fibers (NA=0.26), reduce vignetting and achromatism, accommodate acceptable mounting tolerances, and fit inside allowed volumes. An optical gain of 3.75 for the edge leads to a dimension fiber of 2.24 mm toroidally and 1.6 mm vertically. In contrast, an optical gain of 7.5 for the core leads to a dimension fiber of 1.15 mm toroidally and 3.3 mm vertically.

Simulations using the Zemax software led to the optical properties in the table 3.1, where the f_{number} equals 1.89 for the OCSs but with a different optical gain. As a result, two dimensions are required for optical fibers. Figure 3.10 represents the Zemax simulation realized and the dimensions of the optical fibers for the edge and the core.

In addition, simulations were conducted to assess image quality for each lens at wavelengths between 650 nm and 1100 nm. For each wavelength analyzed in Zemax, ray tracing was carried out to estimate the losses associated with optical transmission. These simulations showed that the lenses transmit 98% of the light energy regardless of wavelength.

Optical collecting systems parameters						
	$\Delta l[mm]$	$\Delta\Omega$ $[msr]$	T [%]	f_{number}	fiber N.A	Optical gain
COCS	24.2	4	47	1.89	0.26	7.5
EOCS	6	33	35	1.89	0.26	3.75

Table 3.1: Optical collecting systems parameters for the HRTS on WEST.

3.4 Optical fiber bundles

Fiber bundles are composed of fibers of 200 µm diameter size that transmit photons in the spectral range from [700;2000] nm. The fiber bundles are duplexed to reduce the number of polychromators, enabling the use of one polychromator for two measurement points. This method has been used in various machines, such as COMPASS, MAST, or W7X; in our case, 20 m of Fibers were added to the initial 25 m to shift the second diffusion pulse temporally by 100 ns. Two fiber bundles are compacted into a ferrule of 3.51 mm^2 area, as shown in figure 3.13 with a different length. However, an important feature concerns the endoscope. Since it is inside the machine, high-temperature optical Fibers are needed to transport the photons collected. 32 rectangular high-temperature mono-fibers will be installed inside the endoscope (after the imaging systems).
These Fibers will be set up in a sealed passageway with the above fiber bundles. In other words, given that the collection area of the fiber bundles is large enough, two

mono-fibers will be associated with one Fiber bundle. It should be noted, however, that this technique will degrade the transmission factor of the endoscope.

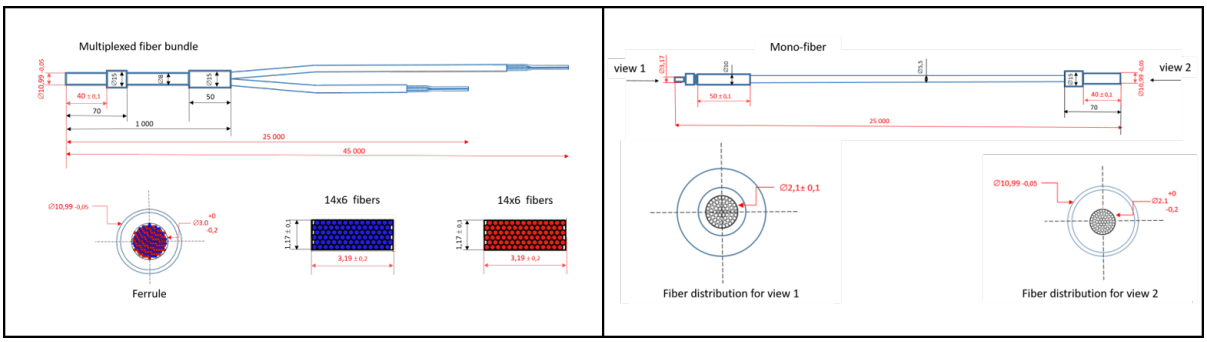

Figure 3.13: Multiplexed fiber used for the alignment polychromator, the sizes is given in [mm]

3.5 Polychromator

3.5.1 Principle

Once the OCS collects the scattered photon flux, fiber bundles carry it to the spectrometers, which are called polychromators. The Thomson scattering signals are related to the photons collected from the OCS and carried by the fiber bundles to the polychromator. The collecting photons are then injected into a polychromator detector. The polychromator comprises optical imaging systems that image the collected photon on the first polychromator channel. According to the filter spectral bandwidth of the filter, the photon is divided into two photons flux: The photon flux transmitted ϕ_{filter} by the interference filter and the photon flux reflected $\phi_{reflected}$ by this one (see figure 3.14).

The photon flux transmitted ϕ_{filter} is defined as the photon flux that crosses the interference filter in the spectral bandwidth, $\lambda \in \left[\lambda_{CWL} - \frac{\Delta\lambda}{2}; \lambda_{CWL} + \frac{\Delta\lambda}{2}\right]$. The avalanche photo-diode will detect the light particles, and the current generated by this last will be converted into a voltage signal and amplified by an operational amplifier module. The reflected photon flux refers to the photon not collected by the interference filter. They are reflected in the next interference filter, which will be again divided into two-photon fluxes: the photon flux reflected and the transmitted one, following the process mentioned before until the last interference filter.

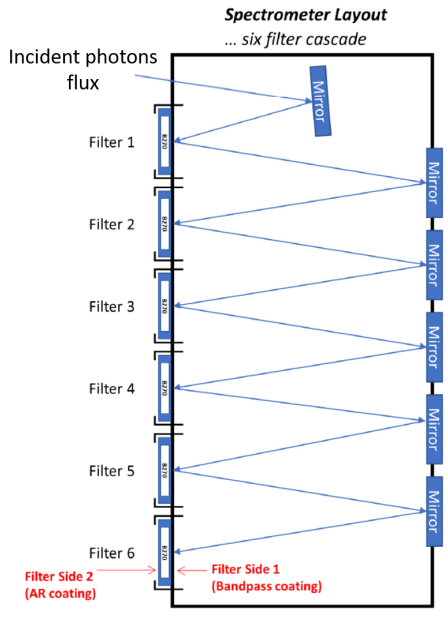

Figure 3.14: Polychromator architecture edited from [21]

3.5.1.1 Polychromator imaging system

The imaging system installed in the polychromator is designed to image the scattering flux, which is the same size as the photo-diode detector of each channel. Ensuring then that the photon flux transmitted by the interference filter are entirely detected by the photo-diode, increasing the SNR.

3.5.1.2 Interference filter

Each channel is composed of an interference filter transmitting the photons included between a minimum wavelength λ_{min} and a maximum wavelength λ_{max} or reflected in the opposite (see figure 3.14). Note that the transmission of filters is generally high, between 90 and 98%, implying negligible loss of photons through the optics. The transmission is not constant, varies with the wavelength, and is not described by a gate function. Usually, the transmission T_{filter} is measured at Full width at half maximum (FWHM) as shown in the figure 3.15.

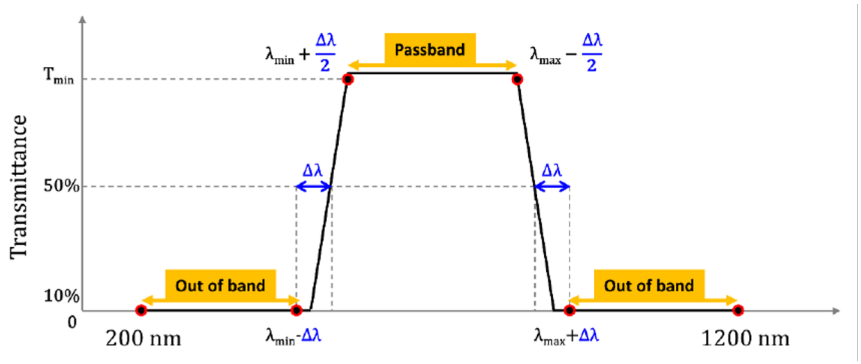

Figure 3.15: Conceptual filter curve with definition of λ_{min},λ_{min}, $d\lambda$ and definition of pass-band and out of bands, edited from [21].

3.5.1.3 APD and electronic system

The photons transmitted by each interference filter are then converted to a signal thanks to a detector placed behind the Avalanche photo-diode detector (APD) filter. An avalanche photodiode is a type of semiconductor photo-detector [35, 47, 51, 53, 69, 70, 82] that converts light into an electrical signal while providing internal gain through an avalanche amplification effect. This internal gain enables them to detect very low light levels, making them ideal for applications requiring high sensitivity. However, the conversion factor from photons to electrons is not constant and depends on the detector response related to the quantum efficiency $\eta(\lambda)$.
The quantum efficiency curve depends on the APD properties (in particular, its doping); this gives information about the electron number produced at a given wavelength λ. In other words, this current is named photo-electron ($p.e$), corresponding to the electron provided by the APD, while this one is subjected to electromagnetic waves. Typically, this current is pretty low and depends on the bias applied to the APD by the pre-amplifier and the intrinsic sources of noise that can come:

- From the photon fluctuation leading to a Poisson noise.
- From electronics noise that can come from the supply sources that bias the APD.
- From thermal noise σ_{th}, for instance the ambient temperature T_{amb}, expressed as :

$$\sigma_{th} = 4 k_b T_{room} R \Delta f \tag{3.2}$$

where R is the equivalent resistor of the electronic system and Δf frequency bandwidth.

Since the APD's current is low and sensitive to temperature, the APD used for WEST has a pre-amplifier stage and a temperature-sensing diode to amplify the signal and compensate for the temperature impact. Indeed, the electronic gain applied to the

APD fluctuates as a function of the ambient temperature, which impacts the signal noise level. A second electronic stage amplifies the signal according to the Thomson Scattering signal amplitude. Typically, the bias voltage applied is about ±5V but can be adapted as needed. in addition, to minimize the temperature effect, the polychromator are installed in temperature controlled cubicles.
To sum up, an electronic stage is allocated to each polychromator channel to filter a part of the intrinsic noise, keep the gain constant, and amplify the signal of interest. To evaluate these impacts, a parameter named factor of noise F is introduced as :

$$F = \frac{SNR_{input}}{SNR_{output}} \tag{3.3}$$

, where SNR_{input} is the SNR associated with the incident signal (in our case, the photon flux fluctuation), and SNR_{output} is the SNR evaluated in the output signal.

The factor of noise is often expressed in decibels (dB), a logarithmic unit that makes it easier to compare and add noise levels. The noise assessment is crucial for evaluating the performance of APDs, as it evaluates the impact of a noise source added by a component (or a light source in our case) compared with the intrinsic noise of the signal source. The lower the noise factor, the more the noise degrades the signal.

3.5.1.4 Polychromator for WEST

To estimate the electron density n_e and temperature T_e profiles, the TS diagnostic on the WEST will exploit 36 polychromators. This detector will convert the scattering photons flux into photo-electron (pe).
4 alignment polychromators with larger band filters will also be used for the diagnostic alignment procedure. This will collect the scattering power on one channel with a filter center at 870 nm with a $\delta\lambda$ equal to 360 nm (see table 3.2 and figure 3.17).
32 polychromators developed on MAST [72] will be installed on WEST basement. The MAST polychromators have the particularity of having 5 high-frequency and 5 low-frequency channels. The high-frequency channels measure pulses of the order of ten nanoseconds whose amplitude at the APD output is between 0 and 1000 mV. The low-frequency channels are used to measure background radiation, the origin of which might be Bremsstrahlung radiation.

The polychromator design allows collecting the spread of the transmitting photon flux on five channels below 1062.1 nm, avoiding stray light from the Nd:YAG laser and easily calibrating the diagnostic by absolute calibration in Raman scattering. The table 3.2 gives the interference filters band-pass chosen for the edge and core polychromators. The filter 1 is allocated to the first channel of the edge polychromators and has a transmission factor of 90%. The Filters 2,3,4,5,6 are used for the core polychromators and have a transmission factor of 95%. Filter 7 is used for the alignment polychromator during the absolute calibration in Raman scattering. The HRTS system

on WEST will measure the low electron temperature in the range of 1 eV to 5 keV for the edge polychromator and the high electron temperature in the core from 10 eV to 10 keV that is in agreement with the scattering spectra. Figures 3.16 and 3.17 represent the polychromator's instrumental functions for the measurement and the alignment, respectively, while the table 3.2 shows the filter spectral bandwidth.

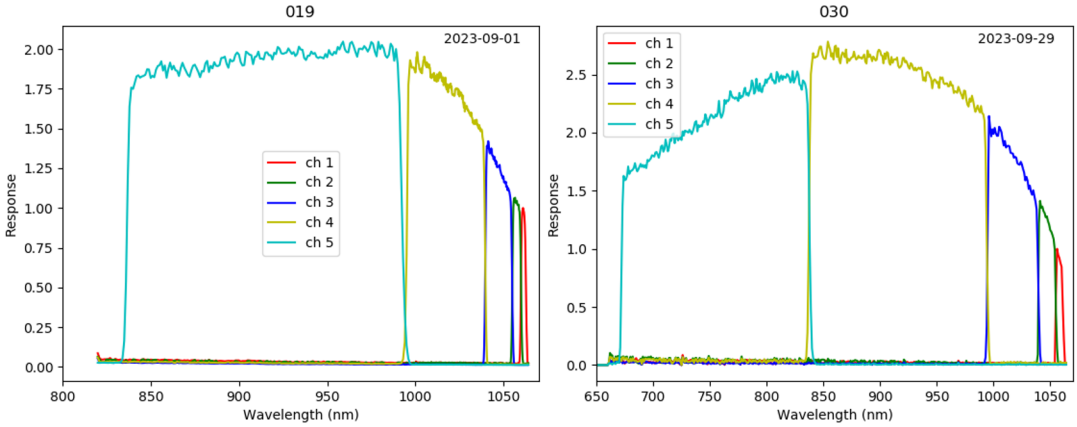

Figure 3.16: Instrumental functions for the edge and core polychromators

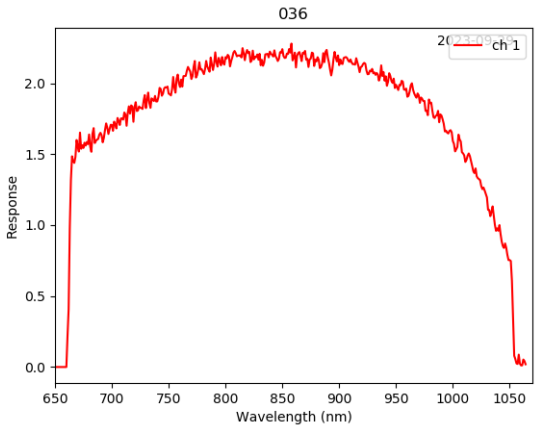

Figure 3.17: Instrumental function for the alignment polychromators

Interference filter	filter 1	filter 2	filter 3	filter 4	filter 5	filter 6	filter 7
Central wavelength λ [nm]	1061.1	1057.7	1047.5	1017.5	917	755	870
Spectral bandwidth $\Delta\lambda$ [nm]	2	5.5	15	45	155	170	360
Edge Polychromators	x	x	x	x	x		
Core Polychromators		x	x	x	x	x	

Table 3.2: Interference filters used for the WEST polychromators.

3.6 WEST acquisition system

The output voltage signals of polychromators are generally acquired at a fast acquisition rate to resolve the pulsed dynamic of the Thomson scattering contribution above the background. A fast acquisition card is needed to obtain the shape of the nanosecond-pulse laser. A commercial hardware [61, 77] solution based on possibly interleaved flash analog-to-digital converter (ADC) with commercial software leaves little room for customization. To reduce expenses and mitigate the acquisition card's obsolescence risk, a custom board based on the Nectar chip developed at CEA/IRFU [3] was preferred. This option is the best for adding and upgrading features in software, such as embedded distributed pre-processing of the recorded pulses for real-time applications. Based on the Nectar chip, a suitable acquisition card has been developed inside the institute for the HRTS system called Nectarine [6]. One Nectarine card is used for one polychromator; it acquires the fast (0.8 to 3.2 GS.s^{-1})and slow channels (up to 1 MS.s^{-1}), which are transferred with Ethernet protocol. This GHz acquisition card allows the digitization of each fast polychromator channel on 1024 samples with a binary resolution of 12 bits and the slow polychromator channel on 24 bits.

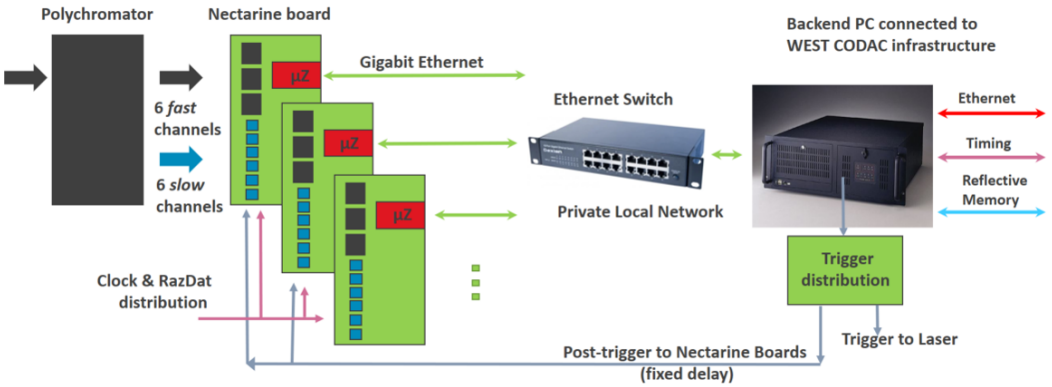

Figure 3.18: Acquisition setup for the real-time High-Resolution Thomson Scattering diagnostic.

Figure 3.18 shows the acquisition setup that will be installed for the real-time HRTS diagnostic. Each polychromator will be connected to one Nectarine board, transmitting the acquired signals using User datagram protocol (UDP) protocol to the acquisition computer. The particularity of the Nectarine card is the post-trigger needed to acquire the signal. In the future, this post-trigger will be produced by the laser pulse. It will be created by the laser pulse illustrated in figure 3.8 by the fiber and will be distributed to the 36 polychromators with a delay of 8 ns.
Note that the acquisition card comprises six channels, but only 5 are needed for the polychromator.

3.7 Photonic Budget

To sum up, the flux of photons transmitted by the imaging system is finally injected into the detector, which will convert the photon flux in a voltage signal V_{TS} in [V]

$$V_{TS,k} = \int T g_k(\epsilon) \phi_{coll} + \sigma_{noise} \tag{3.4}$$

This is a general presentation of the TS measurement principle. Usually, the design depends on the physical requirement, namely the detector choice. To validate the design of the TS diagnostic on WEST, a photonic budget was carried out using the setup presented before. The photonic budget gives a virtual number of photo-electrons that a polychromator would produce per laser pulse. It is essential to consider several key parameters related to the diagnostic. In principle, for a given line of sight, this elementary flux shall be integrated in space over the whole scattering volume, defined by the intersection of the volume of sight and the laser beam. This elementary flux is further integrated toward the OCS over the full solid angle. Let's introduce the collective photon flux $\phi_{TS,coll}$ as:

$$\phi_{TS,coll} = r_e^2 \frac{\lambda_l}{hc} \iint_{V,\Omega} \langle \Pi_l \rangle n_e(R,Z) S(\epsilon,\theta,\alpha)(\epsilon+1) dV d\Omega \tag{3.5}$$

The number of photons emitted N_{scatt} is given by integrating during the laser pulse duration, the solid angle $d\Omega$ and the volume dV:

$$N_{TS,coll} = r_e^2 \frac{\lambda_l}{hc} \iiint_{V,\Omega,t} \langle \Pi_l \rangle n_e(R,Z) S(\epsilon,\theta,\alpha)(\epsilon+1) dV d\Omega dt \tag{3.6}$$

In practice, the scattering volume will be assumed to be minor, meaning that the plasma can be described as uniform across it ($n_e(R,Z) \equiv n_e = constant$). Furthermore, the solid angle of the OCS will be considered negligible, meaning that the scattering angle θ from any point of the scattering volume toward any point of the first optic is considered constant. The total solid angle from the center of the scattering volume toward the OCS is defined as $\Delta\Omega$. The photons scattered from a full scattering volume and collected by the optical system, $N_{TS,coll}$, is therefore approximated as :

$$N_{TS,coll} = r_e^2 \frac{\lambda_l E_{laser}}{hc} n_e(R,Z) S(\epsilon,\theta,\alpha)(\epsilon+1) A_{laser} \Delta l \Delta\Omega \tag{3.7}$$

In addition, the detector response should be considered to assess the number of photo-electrons produced by the detector. In the case of photonic budget, the laser energy E_l and the electron density n_e as well as the quantum efficiency is taken into account. In particular, a constant effective quantum efficiency is considered, and it is divided by the factor of noise F to assess the impact of noise on the measurement. These parameters directly influence the accuracy and reliability of the measurements obtained.

$$p.e = r_e^2 n_e T \frac{\lambda_l E_l}{hc} \frac{\eta(\lambda)}{F} \Delta l \Delta\Omega \tag{3.8}$$

The solid angle ($\Delta\Omega$) the telescopes cover affects the amount of scattered photons the system collects. A larger solid angle allows more photons to be collected, increasing the signal, but can also reduce the spatial resolution. Regarding the physical requirements, the OCS parameters are summarized in the table 3.1 and are used to compute the photonic budget.
The table 3.3 is an overview of HRTS for several Tokamak. Photonic Budget assessed at $n_e = 10^{19}$ m^{-3} and $T_e = 1$ keV, given an effective quantum efficiency of $f \times EQE = 0.45$. for edge and core OCS. Data from COMPASS see [4] for the detailed expression applied here and MAST [72] are given for comparison. The photonic budget is usually given at a density of 1.10^{19} m^{-3} and validates that the photon number is not critical. To check this, the budget is compared with the photon budget given by MAST and COMPASS. During a pulse, one laser emits $\sim 10^{19}$ photons, for a pulse energy equal to 2 J, released over a pulse duration of the order of a nanosecond ($\simeq$ 10 ns).

	E [J]	Δl [mm]	$\Delta\Omega$ [msr]	EQE [%]	T [%]	p.e
COMPASS (Core)	1.5	8.4	22.6	9	40	4370
COMPASS (Edge)	1.5	3.9	21.5	9	40	1930
MASTU (Core)	1.5	10	21.82	15	40	2900
MASTU (Edge)	1.5	10	21.82	15	40	2900
WEST (Core)	2	24.2	4	8	45	1840
WEST (Edge)	2	6	33	8	35	3000

Table 3.3: Photonic Budget assess for WEST compared to others devices

3.8 Summary

The laser sources are in the basement, isolated from tokamak vibrations. Under the tokamak vacuum vessel, the laser-deflecting chassis focuses and redirects the beams toward the plasma. The lasers cross the plasma vertically and are absorbed in the laser analysis chassis at the top of the chamber; see figure 3.2. All elements are dissociated from the tokamak vessel and magnetic structure, preventing misalignment during magnetization and vacuum operation. All alignments can be done in the laboratory reference frame. To reduce the propagation losses along the optical system, each laser pulse emitted at Optical components must be suited to the laser characteristics.

HRTS diagnostic has been designed for WEST tokamak. It will offer full WEST coverage of the plasma upper half, as shown in figure 3.1. 50 vertical measurement points, i.e., 30 for the edge plasma region and 20 for the core plasma region, are planned to be employed. The vertical spatial resolution is relevant to the steep gradient, about 50 cm for the plasma core and 3 cm for the plasma edge in the WEST tokamak.

A Steering laser line system has been designed to guarantee good data quality and control the laser alignment between plasma shots. This optical system comprises piezoelectric mounts and Near-infrared cameras to control the laser beam position in real-time or between plasma shots.

The HRTS optical properties (e.g., spatial resolution, solid angle, and transmission) of WEST are similar to those found in several tokamaks worldwide. What sets the WEST HRTS apart is its unique feature- the endoscope. This will be the first in-situ optical collecting system installed in a tokamak, designed to withstand the extreme conditions of the machine and the plasma scenario, particularly the extended pulse discharge. This innovation is sure to pique your interest. Furthermore, the photonic budget given in the previous section has allowed us to validate the optical collecting system design regarding the physical requirement. Indeed, the edge optical system is an actively cooled telescope made of a golden mirror actively cooled and high-temperature fiber, enabling the sub-centimetric resolution needed at the edge.

It's worth noting that the HRTS design is about more than measuring plasma parameters in real time. The institute has made significant technological strides, developing new acquisition cards that can digitize the scattering pulse on 1024 samples with a Ghz sampling rate while minimizing noise.

4 Synthetic diagnostic in the WEST framework

Sommaire

4.1 Thomson Scattering signal processing basis . . . 101
4.2 Thomson Scattering flux model . . . 103
4.2.1 Laser Beam propagation module . . . 104
4.2.1.1 Laser model . . . 104
4.2.1.2 Optical matrix approach . . . 104
4.2.1.3 Simulation of the beam propagation from the laser to the tokamak entrance . . . 105
4.2.2 Scattering photon flux . . . 107
4.2.3 Scattering photon flux collected . . . 108
4.3 Bremsstrahlung photon flux model . . . 109
4.3.1 Bremsstrahlung power . . . 109
4.3.2 Method . . . 111
4.3.2.1 Electron temperature and density profiles . . . 111
4.3.2.2 Volumetric Bremsstrahlung power map . . . 112
4.3.3 Geometrical extent . . . 112
4.4 Optical collecting systems model . . . 113
4.5 Synthetic Signal and processing method . . . 115
4.5.1 Signal modeled . . . 115
4.5.1.1 Thomson Scattering signal . . . 115
4.5.1.2 Bremsstrahlung signal . . . 118
4.6 Fitting tools module . . . 119
4.6.1 Ratio evaluation method . . . 119
4.6.2 Least Square regression method . . . 119
4.7 Performances and sensitivity test . . . 121
4.7.1 Impact of the misalignment . . . 121
4.7.2 Impact of the electronic noise on the least square regression method 122
4.8 Summary . . . 129

In the previous chapter, we presented the design of the WEST TS diagnostic. Using a photonic budget, we demonstrated that the diagnostic is feasible and that a significant signal will be obtained. However, this calculation does not allow us to interpret the experimental results and estimate the diagnostic's performance. To this end, we propose to develop a Synthetic Diagnostic (SD), a digital twin of the diagnostic, which will allow us to evaluate the diagnostic's future performance.

4.1 Thomson Scattering signal processing basis

In data processing meaning, the output signal from a channel k is related to the photon flux detected by the polychromator channel. In the case of polychromators, the photon flux is transmitted by the interference filter after propagating over a small distance for one channel. Then, the photon flux is converted into electronic current by the photo-diode after a rise time τ^*, filtered electronically, amplified, and finally converted into a signal voltage.

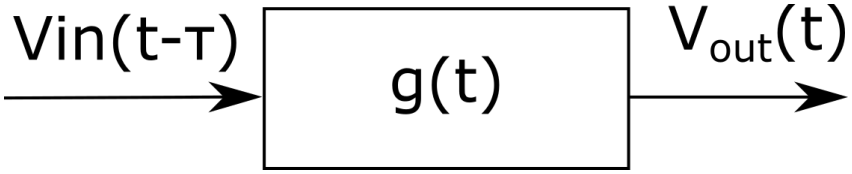

Figure 4.1: Convolutions principle

Therefore, each channel responds with a time delay related to photon flux propagation in the detector, the rise time of the detector, and the rise time from the converter module, leading to a time delay τ of the polychromator. This aspect can be expressed mathematically as a product between two time-dependent functions: a photon flux function $\phi(t)$ and an instrumental function $g(t)$, which describes the detector characteristic, see the illustration 4.1. Therefore, the k-th output voltage signal can be expressed from these two dependent functions by taking into account the time delay of the channel as:

$$V_{TS,k}(t) = \phi_{TS}(t) g_{poly,k}(t-\tau) \tag{4.1}$$

If one integrates over time the output signals coming from the polychromators channels (this might explain the necessity to reduce the noise impact on the voltage and relate the photon flux to the laser energy see section 3), then the relation 4.1 is known as convolution product between the functions mentioned before. From the Fourier transform property on the convolution, the relation 4.2 enables the expression of the polychromator channels signals from the wavelength (λ).

$$\int V_{TS}(t)dt = \int \phi_{TS}(t) g_{poly,k}(t-\tau)dt \tag{4.2}$$

$$TF\left[\int V_{TS}(t)dt\right] = TF\left[\int \phi_{TS}(t) g_{poly,k}(t-\tau)dt\right] \tag{4.3}$$

$$V_{TS}(\lambda) = \phi_{TS}(\lambda) g_{poly,k}(\lambda) \tag{4.4}$$

We propose to develop, with Python, a synthetic diagnostic that will simulate the TS signal based on the equation 4.4. This diagnostic aims to reproduce the diagnostic implemented in the WEST tokamak faithfully from a photonic diagnosis model.
Since we do not know which parameters will significantly impact the measurement of plasma parameters, I decided to create a synthetic diagnostic for the entire system, from the laser source to the signal measured in the machine. As illustrated in figure 4.2, this diagnostic comprises four modules that allow us to study the system's performance. Namely, this diagnostic comprises three main modules to simulate the diagnostic by assuming some parameters or by integrating the experimental parameters from TS diagnostic on WEST.
The first module allows the simulation of the laser beam propagation by considering the laser line system and the laser characteristics. Namely, it considers the laser beam size and the quality factor M^2, which impacts the waist size ω_0 and the scattering volume.
The second module simulates the radiation spectra in the case of the Raman or Thomson scattering model. The Raman spectra are needed for the absolute calibration, whereas the TS spectra are needed for estimating the electron temperature. In addition, this module simulates the Bremsstrahlung power for a given plasma equilibrium to determine the photon noise collected by the OCSs and, therefore, the SNR.
The third module simulates the signal by considering optical collecting system geometry, Monte Carlo rendering of photon statistics through the optics of the telescopes, the optical fiber, and finally, the instrumental functions of the detector. A fourth module retrieves the electron temperature and density for synthetic or experimental signals using fitting tools such as the ratio method or the least square regression.

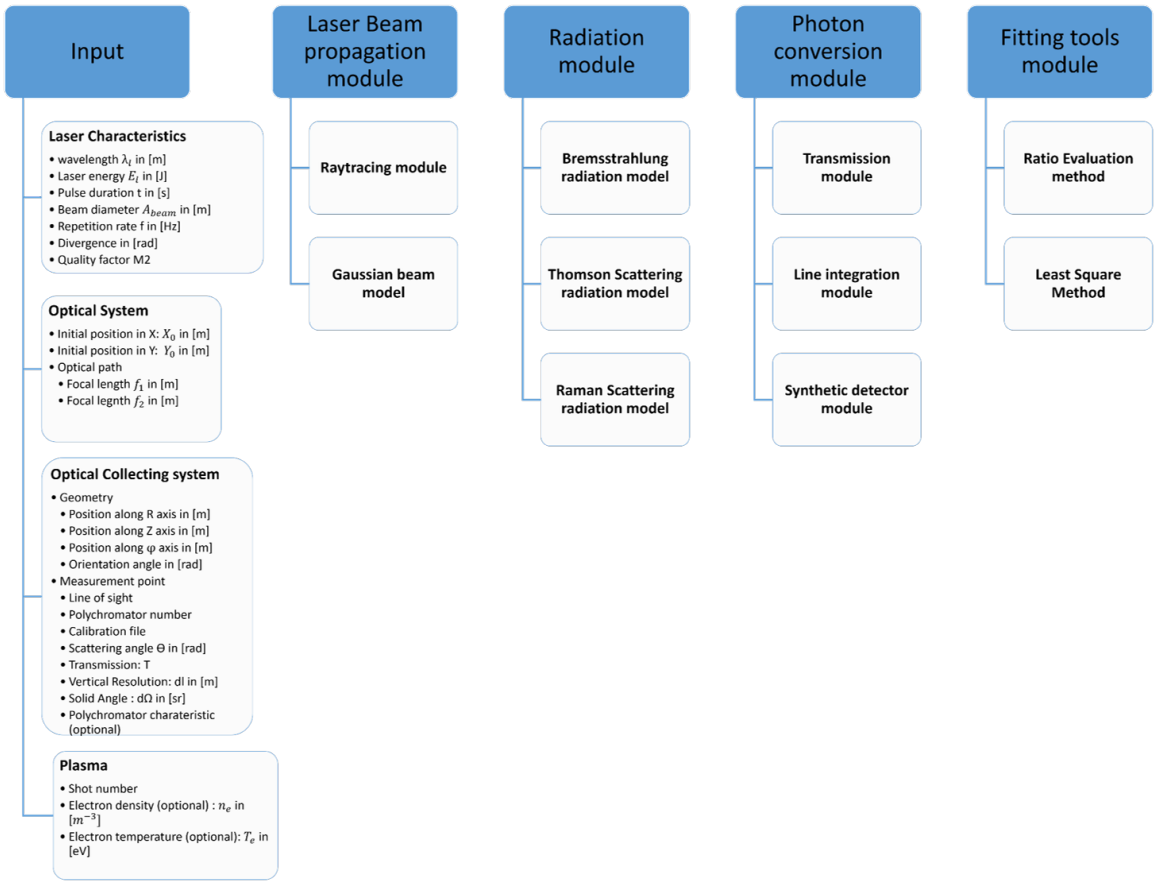

Figure 4.2: Synthetic diagnostic flowchart where 4 inputs parameters are needed

4.2 Thomson Scattering flux model

Until now, the scattered power has been expressed in terms of the Poynting vector. Although this equation is fundamentally correct, it does not consider experimental parameters that can be measured. For instance, the Poynting vector is not measured, but the energy in a laser pulse is. In the following sections, we explore the implications of this equation and demonstrate its usefulness through simulations.

$$\frac{d^3N_s}{d\lambda d\Omega dV} = r_e^2 n_e \phi_{inc} S(\epsilon, \theta, \alpha) \tag{4.5}$$

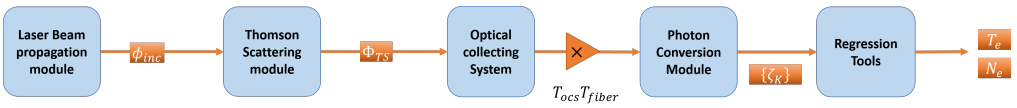

Figure 4.3: Schematic of the synthetic diagnostic workflow, illustrating the five modules implemented in the synthetic diagnostic.

4.2.1 Laser Beam propagation module

4.2.1.1 Laser model

In this section, we focus on the equation implemented to simulate the incident photon flux ϕ_{inc} regarding the laser characteristics, in particular the laser profile and its evolution along the optical path, see figure 4.3. This module will be beneficial in evaluating the diagnostic performances for steep gradients temperature and density gradient scenarios. For this purpose, we decided to model the laser beam shape to consider the scattering volume collected by the fiber bundle.
In addition, to generate the synthetic photon flux at position (R, Z), it is necessary to simulate the incident photon entering the Tokamak device. The incident photons can be modeled as an elementary photon flux $\delta\phi_{inc}$ in [ph.s^{-1}.m^{-2}]. Assuming that the laser intensity profile is Gaussian, the relations in the section 2.3.2 are implemented and used to model the laser propagating along the SLLS leading to :

$$\phi_{inc} = \frac{\lambda_l I(r,z)}{hc} \tag{4.6}$$

4.2.1.2 Optical matrix approach

Geometric optics is the first approach to modeling the trajectory of the wave vector $\vec{k}$ along an optical path called the optical axis. Using these rays, an object's final image can be drawn through various optical systems, such as mirrors, lenses, and so on ...

However, manually constructing the rays when these optical systems become complex and incorporate many components can become arduous or even impossible. The optical matrix is an effective method for addressing this problem. It is applied to geometric optics to simplify the calculations of light beam propagation. Although precise beam simulation can be complex, sometimes PIC simulation is needed. This method is particularly suitable for Gaussian beams, thus making the desired calculations more straightforward. Matrix optics allows easy access to the properties of Gaussian beams such as the waist ω_0 of the Rayleigh range z_r. It is simple to implement without requiring a long simulation time.

Let a beam spot propagate along a distance L with a divergence angle θ, illustrated in figure 4.4. The beam spot will grow by following the equation :

$$\begin{cases} AB' = AB + dx = AB + L.tan\theta & (4.7) \\ \theta = \theta & (4.8) \end{cases}$$

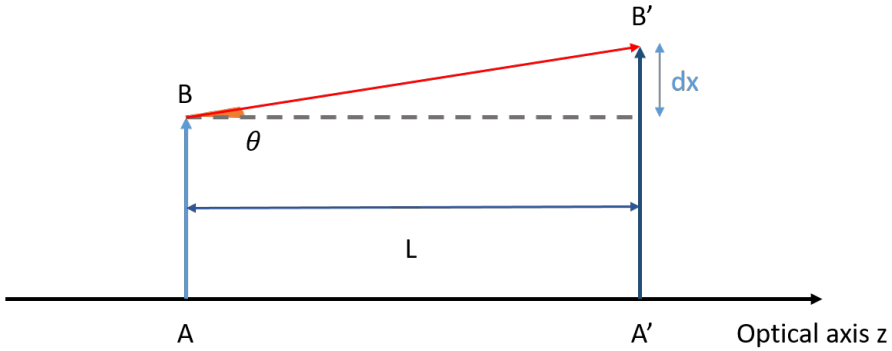

Figure 4.4: Optical matrix theory

From this relation and according to the paraxial approximation, one expresses the optical matrix and the output and input vector as :

$$x_{out} = \begin{pmatrix} 1 & L \\ 0 & 1 \end{pmatrix} \begin{pmatrix} x_{in} \\ \theta_{in} \end{pmatrix} \tag{4.9}$$

Matrix optics uses 2×2 matrices to represent a light ray's transformations as it passes through optical elements. Each optical element is associated with a transfer matrix, and the path of a ray through a complete optical system is described by multiplying these matrices together. A significant advantage of matrix optics is its ability to simplify the analysis of complex optical systems or equivalent systems in a first approximation. This method is applied within the framework of the paraxial approximation: The incident angle is considered very small ($\theta \ll 1$). Despite its advantages, matrix optics has certain limitations, particularly regarding aberrations and imperfections of real systems or even the light spot far from the optical axis. These limitations can be overcome by more sophisticated calculation techniques using ray-tracing software (Zemax, for instance) or Python libraries such as Cherab [83] or Tofu.

4.2.1.3 Simulation of the beam propagation from the laser to the tokamak entrance

As mentioned in chapter 3, the SLLS is designed to be fully controllable from the control room of the tokamak: precise alignment of the laser path is made possible thanks to piezo-actuated mirror holders, and monitoring cameras ensure visualization of laser positions on all optical components, as pictured in figure 4.5. In the following, we present the laser beam propagation simulation regarding the original setup planned for the diagnostic operation. Theoretically, the laser must be placed at 16 m of the Brewster window, with a pulse energy of 2 J. Therefore, we simulated the laser beam propagation following the equation above by assuming a quality factor equal to 1 and a natural divergence $\theta_l = 0.5$ mrad. We also integrate the loss parameter for each optics, approximately equal to 0.03% of the 1064 nm. In addition, we considered the focusing system that ensures the laser beam is wholly contained in the volumes of

sight of the OCS.
To do so, we calculate and associate these matrices with each fundamental optical element, such as the propagation of a ray in free space or the passage through a focal length lens f. Since the Gaussian approximation has been made in the scope of this thesis, determining the beam position and waist using matrix optics is possible from the transfer functions T computed from the optical design presented in chapter 3 (see figure 3.8). Using this method, the equivalent system of the laser line is represented by five matrices: The first matrix M_1 corresponds to the beam propagation from the laser source to the first lens. This matrix is a translation over a distance $d_1 (\sim 11$ m) in air (medium with optical index 1).
The second matrix M_2 corresponds to the first lens of the focusing system. It is a divergent lens $f1 (= -250$ mm), which will grow the beam size.
The third matrix M_3 is an other translation matrix with a distance $d_2 (\sim 0.55$ m).
The fourth matrix M_4 corresponds to the second lens of the focusing system. This has a convergent lens $f2 (= 200$ mm), which will shrink the beam size.
Finally, the last matrix M_5 is a translation matrix that gives the beam size at the position d_3.
The beam width at the output of the focus system is about 20 mm (minimizing possible damage to the Brewster window), and it is focused to approximately 1.4 mm around the equatorial midplane ($Z = 0$ m) of the tokamak chamber.

$$T = \underbrace{\begin{pmatrix} 1 & d_3 \\ 0 & 1 \end{pmatrix}}_{M5} \underbrace{\begin{pmatrix} 1 & 0 \\ 0 & \frac{1}{f_2} \end{pmatrix}}_{M4} \underbrace{\begin{pmatrix} 1 & d_2 \\ 0 & 1 \end{pmatrix}}_{M3} \underbrace{\begin{pmatrix} 1 & 0 \\ 0 & -\frac{1}{f_1} \end{pmatrix}}_{M2} \underbrace{\begin{pmatrix} 1 & d_1 \\ 0 & 1 \end{pmatrix}}_{M1} \tag{4.10}$$

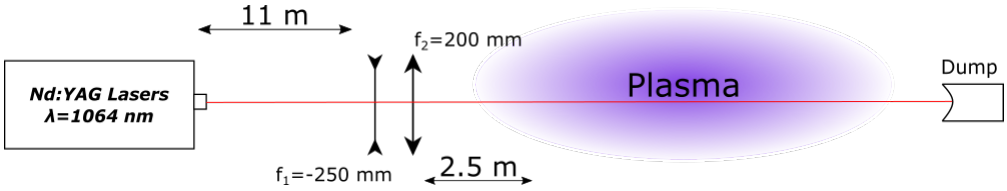

Figure 4.5: Schematic of the laser alignment system. The laser is first defocused by a focal lens ($f_1 = -250$ mm), then focused through a second translatable lens ($f_2 = 200$ mm). This allows tuning of the position of the laser waist inside the tokamak vessel concerning collecting lines of sight.

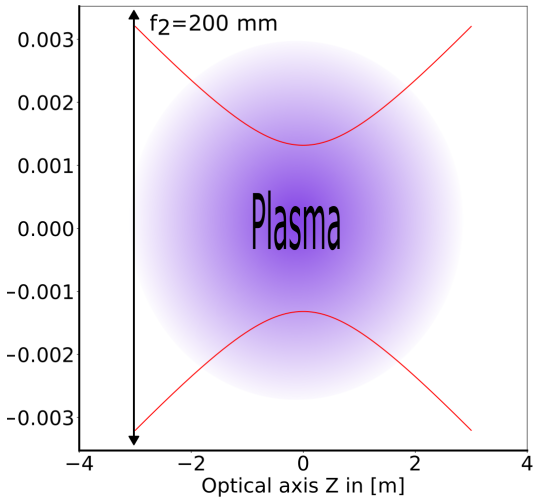

Figure 4.6: Simulation of the beam diameter along the optical path after the second lens. This simulation has been done for a beam diameter of 0.7 mm and a quality factor M^2 equals 1

Figure 4.5 shows the model used to simulate the beam propagation, and figure 4.6 shows the theoretical laser beam profile along the schematic laser line system at different z positions along the optical axis simulated by the SD.

4.2.2 Scattering photon flux

When the incident flux interacts with the electrons, these produce an elementary scattered photon flux with the same temporal characteristic as the incident flux (a pulse of the order of a nanosecond). This elementary scattered flux is called $\delta\phi_{TS}$ and is expressed in [ph.s^{-1}.sr^{-1}.m^{-3}] (in photon per second, per steradian, per cubic meter per unit of normalized wavelength) as :

$$\frac{d^3\phi_{TS,R,Z}}{d\epsilon d\Omega dV} = r_e^2 n_e(R,Z)\phi_{inc}S(\epsilon,\theta,\alpha)(\epsilon+1) \tag{4.11}$$

where $S(\epsilon,\theta,\alpha)$ is the scattering spectra mentioned before. To simulate a spectra S, the scattering angle θ must be fixed. The code computes the A, B, and C coordinates of the triangle formed by the laser interaction with the line of sight as illustrated in the figure 4.7: The cosines law is then applied to estimate it:

$$d_1^2 = d_2^2 + d_3^2 - 2d_2d_3cos\theta \tag{4.12}$$

$$\theta = arcos\left(\frac{d_2}{d_3}\right) \tag{4.13}$$

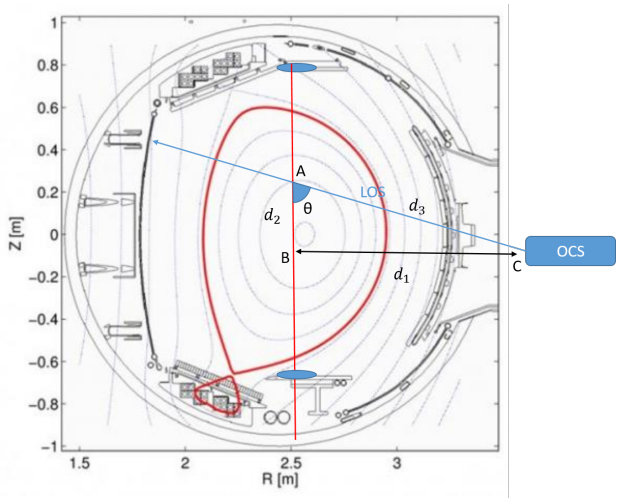

Figure 4.7: Scattering angle calculation from the HRTS design on WEST

4.2.3 Scattering photon flux collected

Once the incident photons are scattered, they are collected by an optical system that sets the solid angle $d\Omega$ and the scattering volume collected dV to carry the photons toward one detector. The method allows us to consider the misalignment regarding the experimental measurement or the absolute calibration. This will also enable us to consider different solid angles in the future. Indeed, in the scope of this thesis, the angle of the various measurement points is assumed to be constant. Solid angle and spatial resolution are not strictly identical within the measurement volume. However, in some cases, this can lead to an error in the measurement estimate.

In the following, the scattering photon flux collected is introduced. As mentioned in the chapter 3, in section 3.7, for a given line of sight, this flux must be integrated into space over the whole scattering volume and over the time duration of the pulse. This elementary flux $\delta\phi_{TS,R,Z}$ is further integrated over the whole solid angle toward the OCS.

Now $\Pi_l \equiv I(r,z)$

$$\frac{d\phi_{TS,coll}}{d\epsilon} = r_e^2 \frac{\lambda_l}{hc} \iint_{V,\Omega} \langle \Pi_l \rangle n_e(R,Z) S(\epsilon,\theta,\alpha)(\epsilon+1) dV d\Omega \tag{4.14}$$

By integrating over the pulse time duration and the normalized wavelength

$$\frac{dN_{TS,coll}}{d\epsilon} = r_e^2 \frac{\lambda_l}{hc} \iiint_{V,\Omega,t} I(r,z) n_e(R,Z) S(\epsilon,\theta,\alpha)(\epsilon+1) dV d\Omega dt \tag{4.15}$$

$$= r_e^2 \iint_{V,\Omega} \frac{\lambda_l E_l(r,z)}{hc} n_e(R,Z) dV d\Omega S(\epsilon,\theta,\alpha)(\epsilon+1) \tag{4.16}$$

$$= r_e^2 \iint_{V} \frac{\lambda_l E_l(r,z)}{hc} n_e(R,Z) dS dl \int d\Omega S(\epsilon,\theta,\alpha)(\epsilon+1) \tag{4.17}$$

From this equation, it is possible to assume that the electron density and temperature are constant. Hence, A_{beam} is the laser beam cross-section area in the scattering volume, and Δl is the vertical integration length over which the flux is collected for one measurement point. In the following, it will be named resolution or spatial resolution.

$$\phi_{TS,coll} = r_e^2 \frac{\lambda_l}{hc} I(r,z) n_e A_{beam} \Delta l \Delta\Omega S(\epsilon,\theta,\alpha)(\epsilon+1) \tag{4.18}$$

4.3 Bremsstrahlung photon flux model

The deflection of the particles induces photon radiation through energy conservation, generating a background of continuous radiation that the OCSs collect. The architecture of polychromators makes it possible to acquire the photon noise collected by imaging systems at kHz to MHz frequency. Part of this noise is Bremsstrahlung radiation. Since the Nectarine card's slow acquisition channels have a bit resolution of 24 bits, it seems possible to exploit these measurements to estimate the effective charge Z_{eff} along the various target lines. In this section, we present the Bremsstrahlung radiation model implemented in the synthetic diagnostics and illustrated in figure 4.9, which will be used in the future to estimate the effective charge.

4.3.1 Bremsstrahlung power

In magnetic confinement devices, the Bremsstrahlung is due to the electron deceleration when this last collides with an ion or another electron. The deflection of the particles induces photon radiation through energy conservation, generating a background of continuous radiation. In the literature, the spectral power of Bremsstrahlung $\left(\frac{dP_{brem}}{d\lambda}\ in\ [W.cm^{-3}.\text{Å}^{-1}.sr^{-1}\right)$ power [10, 12, 14–16, 42, 55, 56, 60, 63, 74, 84, 88, 91, 92]is expressed as follows:

$$\frac{d^3P_{brem}}{dV d\lambda d\Omega} = \frac{1.89.10^{-28}.n_e^2.Z_{eff}.g_{ff}.e^{-\frac{12400}{T_e\lambda}}}{\sqrt{T_e}\lambda^2} \tag{4.19}$$

Wherein n_e is the electron density in [cm^{-3}], T_e is the electron temperature in [eV], λ is the wavelength considered in [Å].

To take the impurity species and the ionization states into account in the Bremsstrahlung power, an effective charge Z_{eff} is introduced.

$$Z_{eff} = \frac{\sum_k n_{k,imp} Z}{n_e} \tag{4.20}$$

, where N is the number of impurities species at the density $n_{N,imp}$, with the charge Z in the plasma volume. The effective charge is used to interpret these interaction effects and simplify the particle behavior equations.

The Gaunt factor g_{ff} is used in plasma physics to correct radiative emission or absorption process calculations. It is mainly used in braking radiation, also known as Bremsstrahlung, resulting from the interaction process between the electrons and ions in the plasma. The Gaunt factor is a correction applied to the braking radiation calculation to account for other subtleties not covered by simplified formulas, such as quantum or relativistic effects. Therefore, the Gaunt factor $g(\nu, T_e)$ is used to adjust the results of theoretical formulas to correspond more closely to experimental observations. It depends on the frequency of the radiation (ν) and the plasma's local temperature (T_e). Figure 4.8 shows the Gauntt factor evolution over the wavelength for several electron temperatures. As observed, this factor is not constant and can vary according to specific plasma conditions, such as temperature.

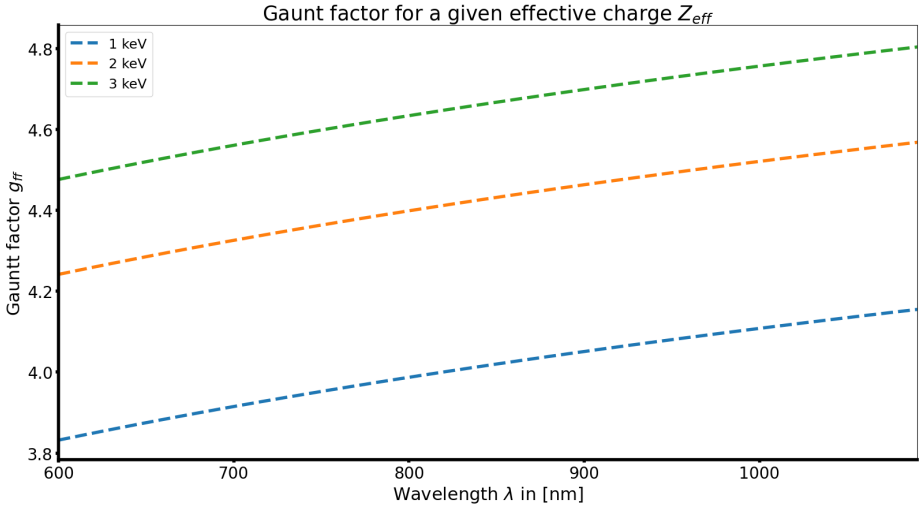

Figure 4.8: Free-free Gaunt factor model versus the wavelength for an effective charge Z_{eff} equal to 2 and several electronic temperatures T_e

4.3.2 Method

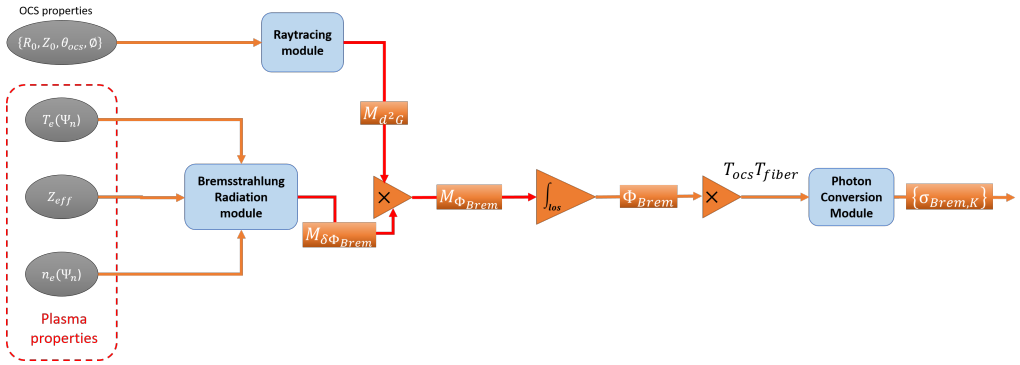

Figure 4.9: Bremsstrahlung photon flux model

The TS flux is a local measurement that depends on the interaction of the laser beam with the plasma. On the opposite, the Bremsstrahlung radiation is emitted by the entire plasma. Therefore, the Bremsstrahlung flux collected by an OCS corresponds to flux collected along several LOS.
To model this flux, the method consists of modeling the Bremsstrahlung photon flux ϕ_{brem} produced by the plasma for a specific plasma shot by considering the experimental magnetic equilibrium, the OCS geometry, n_e and T_e profiles. However, the synthetic diagnostic does not consider the tokamak wall, leading to neglect of reflections from internal walls (which may increase collected flux).

A radiative emission map must be produced to simulate Bremsstrahlung photon flux collected by one polychromator. The relation 4.19, is used to express the local emission coming from the plasma at (R,Z) position in [W.m^{-3}.nm^{-1}.sr−1]:

$$p_{\lambda,brem}(n_e,T_e) = 1,5.10^{-23} Z_{eff} n_e^2 \Gamma(Te,\lambda) \tag{4.21}$$

Wherein Z_{eff} is still the effective charge, T_e is the local electron temperature at the (R,Z) coordinates, n_e is the local electron density at the (R,Z) coordinates (now in [m^{-3}]), λ is the wavelength considered for range under consideration in [nm]. $\Gamma(Te,\lambda)$ is a local function depending on the free-free gaunt factor $g_{ff}(T_e,\lambda)$, the local electron temperature and wavelength given by :

$$\Gamma(Te,\lambda) = g_{ff}(\lambda,T_e)\frac{e^{-\frac{1240}{T_e\lambda}}}{\sqrt{T_e}\lambda^2} \tag{4.22}$$

4.3.2.1 Electron temperature and density profiles

Since the electron temperature and density profile are not uniform in magnetized plasma devices, the plasma parameters profiles must be considered to simulate the local radiative power emitted at different positions. This framework uses a hyperbolic tangent given in [80] to model the plasma profile in WEST.

$$F_{ped}(r,b) = \frac{b_{height} - b_{sol}}{2}\left(\frac{(1+b_{slope}x)e^{x} - e^{-x}}{e^{x} - e^{-x}}\right) \tag{4.23}$$

The particularity of this function is to model the plasma parameters profiles for L and H confinement mode by setting the pedestal height b_{height}, the SOL position b_{sol} or the pedestal slope b_{slope}. In addition, the x coordinate can correspond to several parameters such as ρ, ψ, R, Z, and so on ... In the scope of this model, the parameter used is the normalized poloidal magnetic flux Ψ_n. The main reason for this is that WEST's magnetic equilibrium is assessed during experimental campaigns. Measurements of density and temperature can therefore be mapped as a function of magnetic equilibrium ($n_e(\psi_n)$ and $T_e(\psi_n)$), which in turn depends on the (R,Z) coordinates.

4.3.2.2 Volumetric Bremsstrahlung power map

Let's consider the elementary Bremsstrahlung flux given by the relation:

$$\delta\phi_{brem} = \frac{\lambda}{hc} p_{brem} \tag{4.24}$$

$$= \frac{\lambda}{hc} 1,5.10^{-23} Z_{eff} n_e(\psi_n)^2 \Gamma(Te(\psi_n), \lambda) \tag{4.25}$$

The magnetic field equilibrium is considered to map the electron density and temperature at position $\psi(R,Z)$. The total flux is thus given by :

$$\phi_{Brem} = \iiiint \delta\phi_{brem} d^2G dl \tag{4.26}$$

$$\tag{4.27}$$

Wherein d^2G_j is the geometric extent.

4.3.3 Geometrical extent

Geometric extent is a quantity used in radiometry to characterize the fraction of light radiation emitted by an extended source that reaches a receiver. It is expressed in [m^2sr]. When a local emission source is located at a distance L from a receiving surface S, the geometric extent is given by :

$$d^2G_j = \frac{S_{em} S_{det} cos\gamma_1 cos\gamma_2}{L^2} \tag{4.28}$$

Where S_{det} is the receiver's surface element, S_{em} is the receiver's surface element, is the source's solid angle element, and theta is the angle between the normal to the receiving surface and the direction of the radiation, called obliquity. Geometric extent can be interpreted as a measure of a system's ability to collect light. In our context, it

is related to the photon flux perceived by the optical collection system. To simplify matters, for this thesis, we do not consider the variation in refractive index when calculating the geometric extent. In optics, the geometrical extent, also known as the optical extent or beam spread, is a crucial factor in designing and analyzing optical systems. It helps to understand the limits of light concentration and the effective transmission of light energy between a source and a detector.

4.4 Optical collecting systems model

Once the scattered flux is collected, losses from optical transmission must be considered. However, the imperfect imaging system leads to photon losses when the collected photons are carried to the spectrometer. The system must then be optimized to reduce the losses due to the transmission T from the optical requirement. The photon flux transmitted to polychromators ϕ_{trans} can be expressed as a fraction of the collected photon flux ϕ_{coll}:

$$\phi_{trans} = T\phi_{coll} \tag{4.29}$$

In addition to the Thomson scattering photons, the optical collecting system also collects other photons possibly emitted in the tokamak chamber, such as Bremsstrahlung plasma emission or direct wall emission in the case of hot surfaces. Considering the photon noise, they can add it to the Thomson scattering signal such as :

$$\phi_{coll} = \phi_{TS} + \phi_{Brem} + \phi_{stray-light} + ... \tag{4.30}$$

In the following, background emissions will be grouped into a generic Bremsstrahlung contribution considered steady-state compared to the nanosecond laser pulse duration. Two independent transmission factors are introduced, namely T_{ocs} across the OCS and T_{fiber} across the fiber bundles. The photon flux transmitted to polychromators ϕ_{trans} can be expressed as a fraction of the collected photon flux ϕ_{coll}:

$$\phi_{trans} = T_{ocs}T_{fiber}\phi_{coll} \tag{4.31}$$

Considering the optical design of both core and edge optical collecting systems shown in figure 3.10. Image quality simulations have been realized with Zemax software. These simulations have been done for several wavelengths between 800 nm to 1100 nm, where 98 % of the energy is transmitted from one mirror to the next mirror. These results have led to the assumption that, on average, the transmission factor for each mirror is fixed at $T_0 = 0.98$ independently of the wavelength. Regarding the OCS design, one can validate the transmission factor of the core and EOCS by estimating the photon scattering budget for the two optical collecting systems through Monte Carlo simulations.
Indeed, the first step has been to determine the OCS transmission factor, with the photons conversion module integrated into the code, by using a Monte-Carlo method

and assuming a loss of 2 % per optics and a loss of 60 % for the fiber bundles. However, since the EOCS comprises a second fiber bundle, which leads to additional losses, the transmission factor is further reduced by 20%. Moreover, for the OCSs, the polychromator losses have been taken into account by assuming a factor of 10 % of reduction. However, the attenuation inside the fiber is unknown and was not considered in this simulation; it will be added after the laboratory tests. In the first order, these transmission factors are assumed independent of the scattered wavelength, as initially imposed in the optical design of the optical elements. Transmission factors could be applied as proportionality factors for the total transmission, independent of the wavelength, as written in Eq.4.30. This method is used to infer ideal synthetic signals. On the other hand, due to the relatively low number of photons scattered during Thomson scattering in the low-density conditions of a tokamak plasma, Poisson statistics can be considered as a source of noise on the final transmitted photon flux to the detectors. In other words, a Monte Carlo selection is applied to randomly select if a collected photon will pass through the optical system or be absorbed. A random number p is generated between 0 and 1, and the photon is allowed to pass only if $p < T_{ocs}T_{fiber}$. As shown in figure 4.10, where expected values of the transmission factors are applied to a given collected scattered spectrum, a uniform drop of the spectrum amplitude is observed over the entire spectrum, corresponding to the attenuation in the ideal situation. In addition, the low number of photons translates into a Poisson noise along the spectral sampling, which is later considered for error propagation.

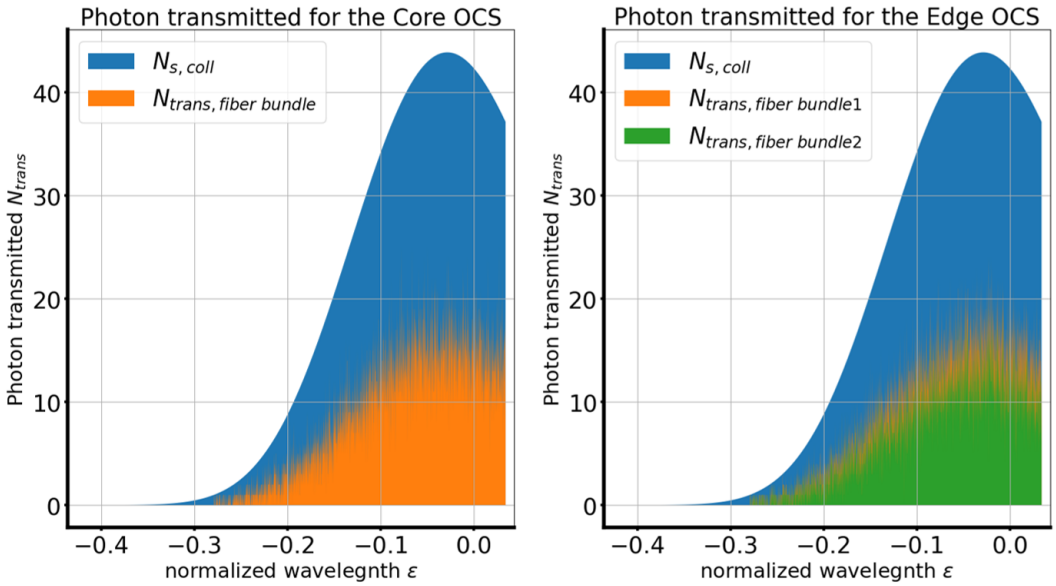

Figure 4.10: Transmission simulation of the COCS and the EOCS given by the Optical collecting system module for a scattering spectrum at 1 keV and n_e = 1.10^{19} m^{-3}. The equation 4.31 is applied by using a Monte-Carlo method to simulate the photon transmitted at each normalized wavelength for a laser at 1064 nm and a laser energy equals 2 J.

4.5 Synthetic Signal and processing method

Finally, the flux of photons transmitted by fiber bundles is injected into the polychromators. A first telescope transforms the diverging photon flux from the fiber into a quasi-collimated photon beam. For simplicity, the transmission factor of this telescope is assumed to be 1, as it can be injected into the previous factors. Photons are then directed toward a first interference filter. A Monte Carlo selection rule can also be applied for noise propagation, considering the transmission factor $T_{filter}(\epsilon)$ of the filter, the function of photon wavelength. If the photon is transmitted, it is absorbed by the APD. Otherwise, it is reflected in the optical path. The reflected photons are then directed toward a second interference filter, and so on, along the five filters composing a polychromator.
Photons absorbed by APD will finally generate a voltage increase at the polychromator output, given the quantum efficiency of the APD $\eta(\epsilon)$ (dependent on the photon wavelength) and an electric gain G.
Considering a given polychromator and a given channel (set of filter, APD, and gain) labeled by the index k, the time-varying voltage output during exposure to a photon flux is approximated as:

$$V_k(t) = \int T_{ocs} T_{fiber} T_{filter,k}(\epsilon) \eta_k(\epsilon) G_k(\phi_{TS,coll} + \phi_{Brem,coll}) d\epsilon \tag{4.32}$$

$$V_k(t) = T_{ocs} T_{fiber} \int g_k(\epsilon) \phi_{TS,coll} d\epsilon + \int g_k(\epsilon) \phi_{Brem,coll}(\epsilon) d\epsilon \tag{4.33}$$

$$V_k(t) = V_{TS}(t) + V_{Brem}(t) \tag{4.34}$$

, where the integral is performed over the normalized wavelength of the collected photon flux. Each channel k of a given polychromator is ideally characterized by a practical instrumental function depending on the wavelength: $g_k(\epsilon) \equiv T_{filter,k}(\epsilon) \eta_k(\epsilon) G_k$. This instrumental function is, in fact, the result of spectral calibration of the polychromator and will be considered in the following description of the polychromator function.

4.5.1 Signal modeled

This section presents the work realized to simulate the photon flux provided by the Thomson Scattering process while the electron density interacts with the laser pulse.

4.5.1.1 Thomson Scattering signal

The output voltage signals of polychromators are generally acquired at a GHz rate to resolve the pulsed dynamic of the Thomson scattering contribution above the background. The time dynamics shall follow the time dynamics of the Poynting vector in the scattered volume, but this is not a quantity that is precisely known in experiments. Instead, the energy of the Laser pulse can be measured (with a

pyrometer, for instance). So it is necessary to translate the time-varying voltage output of the polychromator channels, proportional to the Laser Poynting vector, into a time-integrated signal, defined as ζ_k, now proportional to the Laser energy. We approximate that all plasma quantities and other factors are constant during the nanosecond laser pulse.

$$\begin{cases} \zeta_{TS,k} \equiv \int_t (V_{TS})\,dt = A n_e \psi_{k,mod}(T_e,\epsilon,\theta) & (4.35) \\ A = r_e^2 T_{ocs} T_{fiber} \Delta l \Delta\Omega \frac{\lambda_l E_{laser}}{hc} & (4.36) \\ \psi_{k,mod} = \int g_k(\epsilon) S(\epsilon,\theta,T_e)(\epsilon+1)\,d\epsilon & (4.37) \end{cases}$$

, where n_e is the electron density and $\psi_k(T_e,\epsilon,\theta)$ is a function depending on the electron temperature T_e, the scattering angle θ and on the wavelength interval defined by the instrumental function g_k. A is a constant depending on the vertical resolution, the solid angle, laser energy, and the transmission factor from the OCS and the fiber bundle. The laser pulse energy could be measured during the diagnostic operation with the detectors installed on the laser alignment system. The factor $T_{ocs} T_{fiber} \Delta l \Delta\Omega$ is measured during the Raman calibration.

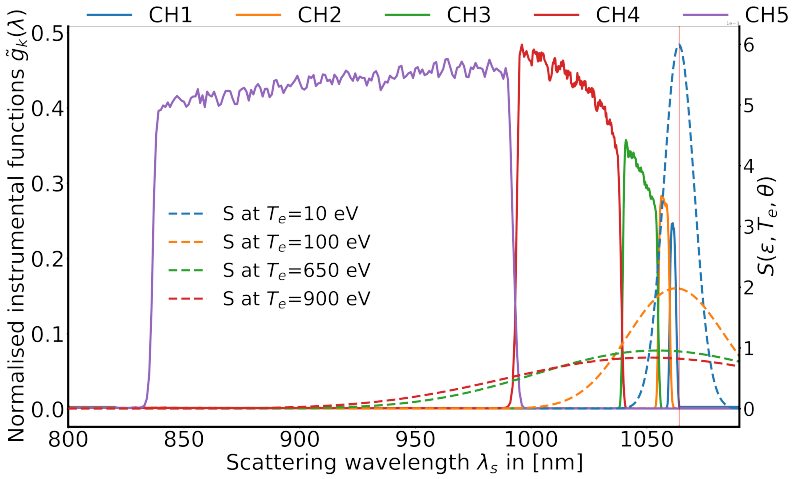

Figure 4.11: Edge polychromators: Instrumental functions of each channel function of the wavelength, shown as plain curves (left y-axis). The function integral of the first channel normalizes these functions. Several theoretical diffusion spectra S (from Eq.2.22) built for electron temperatures from 10 eV to 900 eV are shown in dashed curves (right y-axis). The thin red vertical line at $\lambda = 1064$ nm represents the laser wavelength.

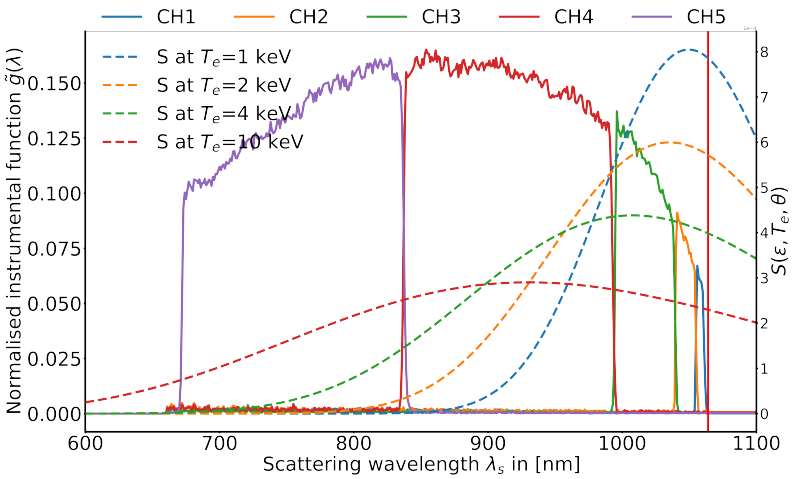

Figure 4.12: Core polychromators: Instrumental functions of each channel function of the wavelength, shown as plain curves (left y-axis). The function integral of the first channel normalizes these functions. Several theoretical diffusion spectra S (from Eq.2.22) built for electron temperatures from 1 keV to 10 keV are shown in dashed curves (right y-axis). The thin red vertical line at $\lambda = 1064$ nm represents the laser wavelength.

Figures 4.11 and 4.12 illustrate the normalized instrumental function $\tilde{g}_k(\epsilon)$ of each channel of edge and core polychromators. They are shown in plain curves; they are normalized by the first channel integral with simulated Thomson scattering spectra at low and high temperatures for a scattering angle $\theta = 90°$, shown in dashed curves. The thin red vertical line at $\lambda = 1064$ nm represents the Laser wavelength.
Figure 4.13 illustrates the $\Psi_{k,mod}(T_e)$ versus the electronic temperature modeled by the SD by using polychromator 19 instrumental functions for a scattering angle θ equal 102 °. This set is modeled by considering the data on the instrumental functions given by the manufacturer. We observe that only the two last channels are sensitive at high temperatures, which agrees with technical requirements.

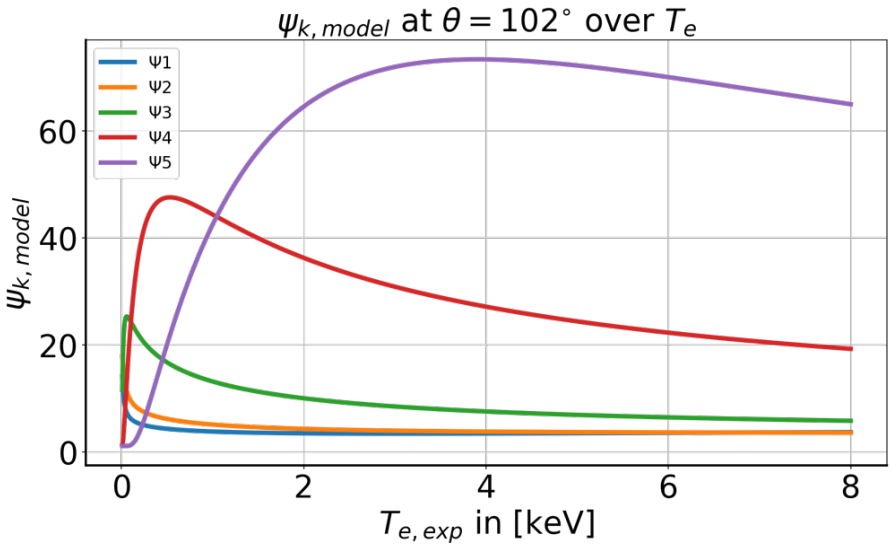

Figure 4.13: $\psi_{k,mod}$ over the T_e. The curves illustrate the pre-processed data which will be used to retrieve n_e and T_e. This data set corresponds to the polychromator 19, designed for the edge measurement.

4.5.1.2 Bremsstrahlung signal

The polychromator has a slow acquisition channel in the kHz frequency, and the slow acquisition channel from the Nectarine card has a high binary resolution; these might be useful to acquire the Bremsstrahlung radiation. From this radiation, it could be possible to estimate an effective charge Z_{eff}. We express the Bremsstrahlung signal modeled from the code to express the Bremsstrahlung signal into a time-integrated signal, defined as $\zeta_{Brem,k}$.

$$V_{Brem}(t) = \int g_k(\epsilon)\phi_{Brem,coll}(t)d\epsilon \tag{4.38}$$

$$\tag{4.39}$$

Now $\phi_{Brem,coll}(t) = Z_{eff}\tilde{\phi}_{Brem,coll}(t)$

$$V_{Brem}(t) = Z_{eff}\int g_k(\epsilon)\tilde{\phi}_{Brem,coll}(t)d\epsilon \tag{4.40}$$

$$\tag{4.41}$$

The equation above leads to expressing the Bremsstrahlung signal as :

$$\begin{cases} \zeta_{Brem,k} \equiv \int_t (V_{Brem})dt = AZ_{eff}\Xi_k(T_e,\epsilon,\theta) & (4.42) \\ A = T_{ocs}T_{fiber} & (4.43) \\ \Xi_k = \int g_k(\epsilon)\tilde{\phi}_{Brem,coll}(t)d\epsilon & (4.44) \end{cases}$$

, where $\Xi_k(T_e, \epsilon, \theta)$ is a function depending on the electron temperature and density profile and the wavelength interval defined by the instrumental function g_k. A is a constant depending on the transmission factor associated with one measurement point from the OCS and the fiber bundle.

4.6 Fitting tools module

The scattering spectra depend linearly on the electron density, which increases or decreases the intensity measured on the channels. The electron temperature affects the width of the spectrum, so the number of signals depends on the temperature. In this work's approximation of the incoherent Thomson scattering process, the electron temperature (at the given geometry) completely determines the spectral shape. The polychromator data will recover this parametric dependence.

4.6.1 Ratio evaluation method

The ratio method can be used to estimate these parameters. The ratio method involves comparing the relative voltages of the polychromator channels to extract the electron temperature :

$$R_k(n_e, T_e) = \frac{\int V_{k-1}(T_e)dt}{\int V_k(T_e)dt} \tag{4.45}$$

, where k is the index between 2 and N and $R_k(n_e, T_e)$ is the ratio computed between the signal from the channel k and $k+1$. A regression method is then used to estimate the parameters mentioned above using the logarithm of the ratios.

$$f_{linear}(T_e) = -\frac{1}{T_e} lnR_k + f_{offset} \tag{4.46}$$

where f_{offset} is a an offset depending on the gain ratio between two channels. The electron temperature T_e is obtained from the slope of the linear function.

4.6.2 Least Square regression method

The data will be inverted into temperature and density using a least square regression model. For a given polychromator, we introduce a set of $\{\zeta_k\}$ produced by the set of detectors. This set corresponds to either integrated portions of the incident Thomson scattering spectrum given by the synthetic code or the integrated temporal signals acquired. Hence, we define a square distance χ^2 between measured polychromator data $\{\zeta_{exp,k}\}$ and synthetic data produced by the above model $\{\zeta_{model,k}\}$:

$$\chi^2 = \sum_k \left(\zeta_{exp,k} - \zeta_{model,k}(T_e, n_e)\right)^2 \tag{4.47}$$

The minimization method consists of finding the minimum of χ^2 in the n_e and T_e space at given scattering angle θ and calibration coefficient A. A generic iterative algorithm can be deployed to find this minimum in 2D space.

For a given polychromator, the signals produced by the set of detectors $\{\zeta_k\}$ correspond to integrated portions of the incident Thomson scattering spectrum; see, for instance, figure 4.11.

Noticing that the dependence of the model data with density is purely linear, the least square problem can be simplified analytically to result in a new problem expression depending on electron temperature only. That is:

$$\frac{\partial \chi^2}{\partial n_e} = 0 \Leftrightarrow n_e \sum_j A^2 \psi_{mod,j}^2 = \sum_j A \psi_{mod,j} \zeta_{exp,j} \Leftrightarrow n_e = \frac{1}{A} \frac{\sum_j \psi_{mod,j} \zeta_{exp,j}}{\sum_j \psi_{mod,j}^2} \tag{4.48}$$

This relation directly expresses the electron density function of electron temperature (contained in ψ_k) along the local minima of $\chi^2(n_e)$. The electron density, in the χ^2 expression 4.47, can now be replaced using 4.48:

$$\begin{cases} n_e = \dfrac{1}{A} \dfrac{\sum_j \psi_{mod,j} \zeta_{j,exp}}{\sum_j \psi_{mod,j}^2} & (4.49) \\ \chi^2 = \displaystyle\sum_k \left(\zeta_{exp,k} - \frac{\sum_j \psi_{mod,j} \zeta_{exp,k}}{\sum_j \psi_{mod,j}^2} \psi_{mod,k} \right)^2 & (4.50) \end{cases}$$

where $j \in [1;5]$ is polychromator channel index.

Equation 4.50 represents the parametric dependence of the square distance function of electron temperature only (dependence contained in ψ_k), considering that we follow the local minima in density. In the following, the application of this model will rely on the use of pre-processed coefficients A and $\{\psi_{mod,k}(T_e,\theta)\}$ based on the synthetic model 4.36. These pre-processed coefficients are calculated on a pre-defined array of temperature values for each polychromator geometry (θ) and instrumental functions $\{g_k\}$. The practical application of the least square minimization will include finding the local minima along this defined array. Note that the temperature resolution of this array is chosen to be minor concerning uncertainties discussed in the following.

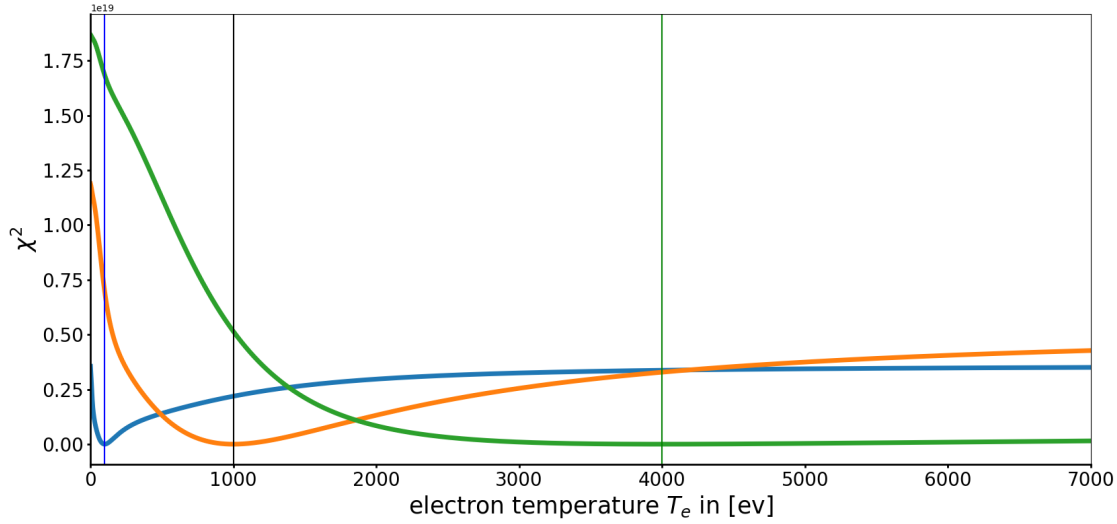

Figure 4.14: Least squares regression method test for 3 different electronic temperatures

4.7 Performances and sensitivity test

In this section, we focus on the HRTS's performance on WEST made with the least square regression method. The performance is assessed through a sensitivity test, defined by the capacity to estimate the plasma parameters using the least square regression method. For this purpose, we will assess the performance by computing the standard deviation.
In the following section, we assess the electron temperature and density error. At the same time, we consider the losses in the optical collecting system and the relative error on T_e. All the tests were conducted separately to estimate the impact of each parameter on the regression method.

4.7.1 Impact of the misalignment

Experimentally, the plasma parameters retrieving process will be done for each measurement point using synthetic data provided by the synthetic diagnostic. For instance, the scattering angle, controlling the shape of the scattered spectra, is defined either from the CAD model or in-situ alignment. We will consider the impact of a misalignment error on Te's estimate. This is done by defining the ideal angle and processing ideal coefficients for the least square regression (see section 4.5). Then, this perfect angle is perturbed with an error, and synthetic data are produced with this perturbed angle, mimicking an alignment error. These perturbed synthetic data are finally interpreted with the ideal coefficients, and the output temperature is compared to the imposed one. The results of the methodology are shown in figure 4.15 where the

relative error on T_e is plotted as a function of the error on the scattering angle. This is done for three different angles and three different temperatures. We can see that the error sensitivity (defined as $\frac{\delta T_e}{T_e} * \frac{\theta}{\delta\theta}$) is about 1.7 and is independent of angle and temperature. In practice, 1° error could lead to 2% systematic error on the temperature estimated.

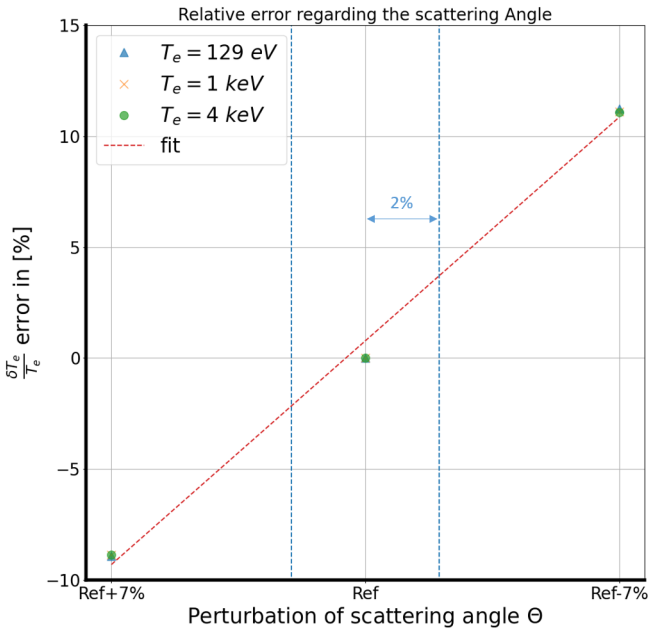

Figure 4.15: Relative error on T_e by considering a ±7% LOS misalignment around three reference angles 95°, 102°, 109°, for three different electron temperatures T_e 129 eV, 1 keV, 4 keV

4.7.2 Impact of the electronic noise on the least square regression method

Standard deviation is a statistical measurement that quantifies the dispersion of a data set. It indicates the extent to which the values in a data set deviate on average from the mean of that data set. A slight signal deviation suggests that the values are close to the mean and less dispersed. A significant standard deviation indicates that the values are widely distributed around the mean and, therefore, more widely dispersed. Since SD allows the TS simulation through the random process of the noise level, which could originate from transmission (see figure 4.10), the tokamak environment like the electronic noise or the plasma itself, like the Bremsstrahlung power fluctuations, which the OCS collects. In this section, we propose using the least square regression method to determine the T_e, n_e, p_e from perturbed synthetic signals. For this purpose, we will construct effective experimental signals $\{\zeta_{noisy,k}\}$ by adding a random Gaussian noise component $\delta\zeta_k$ to the ideal synthetic signals $\{\zeta_{mod,k}\}$ produced by polychromators. The standard deviation σ_k of this noise is defined as the product of the signal amplitude (for each channel k) times a NSR:

$$\begin{cases} \zeta_{noisy,k} = \zeta_{mod,k} + \delta\zeta_k & (4.51) \\ \sigma_k = NSR \times \zeta_{mod,k} & (4.52) \end{cases}$$

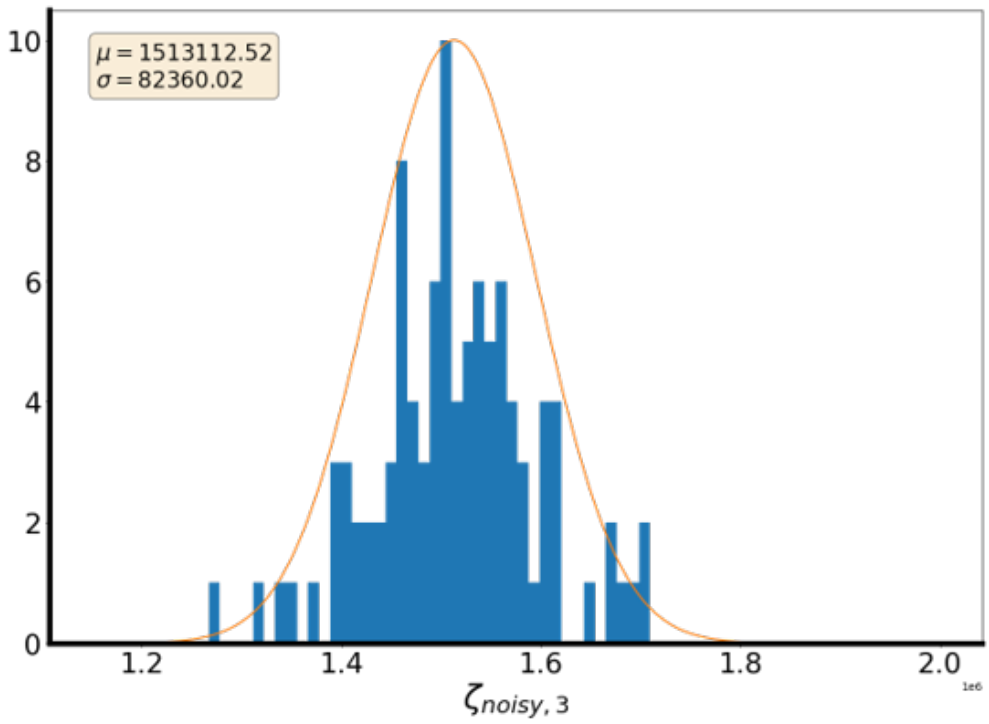

Figure 4.16: PDF of the signal model for channel 3 with an NSR of 5 % with 100 samples. This corresponds to the signal injected into the program to estimate the error on T_e

Then, these effective experimental signals are inverted in temperature and density using the ideal pre-processed coefficients. This is performed 100 times to represent the statistical distribution of noise, and statistical distributions of output temperature and density are computed on this data set.

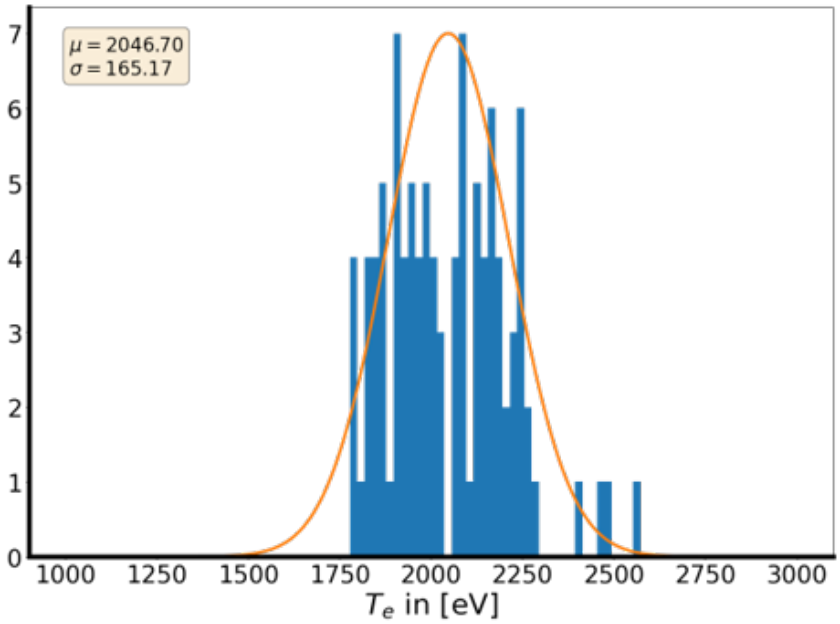

Figure 4.17: Output PDF of T_e model with an NSR of 5 % with 100 samples. T_e is estimated from the least square method by using the pre-processed data set $\psi_{k,mod}$

Remark:

The signals generated with the SD code allowed us to estimate the T_e, n_e and evaluate the diagnostics' performance. Initially, checking that the noise introduced in the simulations propagated correctly throughout the calculation process was essential. To do this, I used Figure 4.17, which shows the estimated temperature distribution. This figure highlights that the distribution of T_e follows a Gaussian distribution, confirming that the noise is correctly considered in the simulation. Nevertheless, we limited the number of simulations to 100 iterations due to computational time constraints. This restriction slightly degrades the probability distribution (PDF) shown in the Figure above compared with an ideal Gaussian, represented in orange.
Despite this approximation, the observed distribution remains sufficiently close to a Gaussian for the standard deviation to be a reliable estimator of the error in measuring T_e and n_e. This assumption agrees with the experimental results (see chapter 6) and simplifies the uncertainty analysis.

Let $\frac{\sigma_{Te}}{T_e}$ relative error on the electron temperature and on the electron density $\frac{\sigma_{ne}}{n_e}$ through a sensitivity test regarding the noise level on the signal.
Figure 4.18 represents the standard deviation T_e, normalized to the input one, versus the NSR. It is observed that the relative error increases linearly with the NSR, with a sensitivity $s \equiv \frac{\sigma_{Te}}{T_e \times SNR} \approx 1.2$: it does not exceed 10% for a NSR of 5 %.
The following simulations assume the same NSR for the five polychromator channels, given an input temperature of 1 keV (see figure 4.16 for instance). For sanity check,

two input densities $n_e = 10^{18}$ m^{-3} and $n_e = 10^{19}$ m^{-3} are considered.

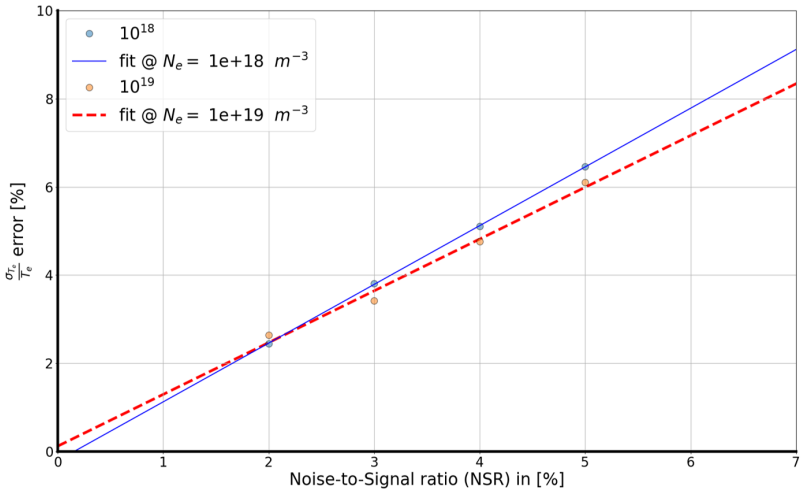

Figure 4.18: Relative error versus the NSR for TS signal simulated at 1 keV and a scattering angle θ at 102° and a constant noise for the 5 polychromator channels

Next, a fixed NSR of 5 % is assumed, and the inversion uncertainty is evaluated through a temperature scan from 10 eV to 8 keV (uncertainty evaluated using 100 simulations per temperature). Results are shown in figure 4.19 and 4.20 for the two OCS wherein the solid lines represent the relative error on T_e, and the dashed lines represent the relative error on n_e. The relative error for the COCS was calculated using the polychromator characteristic 19 allocated to the core region and the polychromator characteristic 23 allocated to the edge region. Assuming a constant NSR of 5% on each channel for the first LOS (orange) and the last LOS (blue). This sensitivity study found that both Thomson scattering systems (edge and core) and the implemented inversion algorithm provide a reasonable sensitivity (close to unity) to noise. For the core system (connected to specific core polychromators), it is found that the relative error on both temperature and density is in the range of 5 % over the entire temperature range. The system is, therefore, characterized by a unitary sensitivity to the 5 % noise level set as input.
On the other hand, The relative uncertainty on temperature estimate is below 6 % for the edge region. For the edge system (connected to specific edge polychromators), the relative error on temperature and density is also in the range of 5 % in the temperature range from 10 eV to 1 keV. Above 1 keV, the relative error on temperature estimate rises to 15 %, which is probably caused by the property of interference filters not adapted to high temperatures. These edge polychromators will, anyhow, not be used for estimating the plasma parameters in the hot core region.
This is, however, proven for a specific noise description, assuming that the noise level is proportional to the signal amplitude for each polychromator channel. In particular, we mentioned a first noise source due to statistical transfer through optics. A sensitivity

study was performed for both collecting systems and associated polychromators for a plasma density of 10^{19} m^{-3} and Laser energy of 2 J across a 10 eV to 8 keV temperature range. The resulting noise level on output signals ($\zeta_{noisy,k}$) is found to be extremely small, even though not compatible with a constant NSR model. Further experimental investigations in the real tokamak environment shall teach us about realistic noise description and guide future investigations on uncertainty quantification.

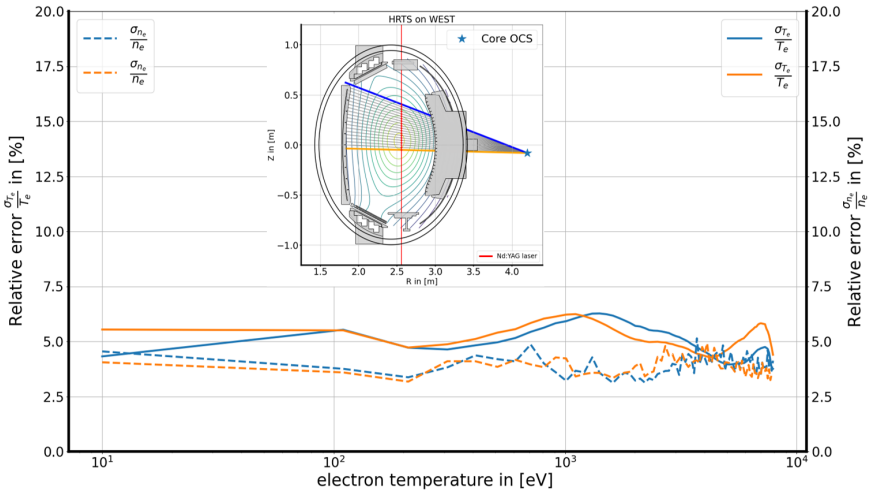

Figure 4.19: Relative error for the COCS by using the instrumental functions of the core polychromator.

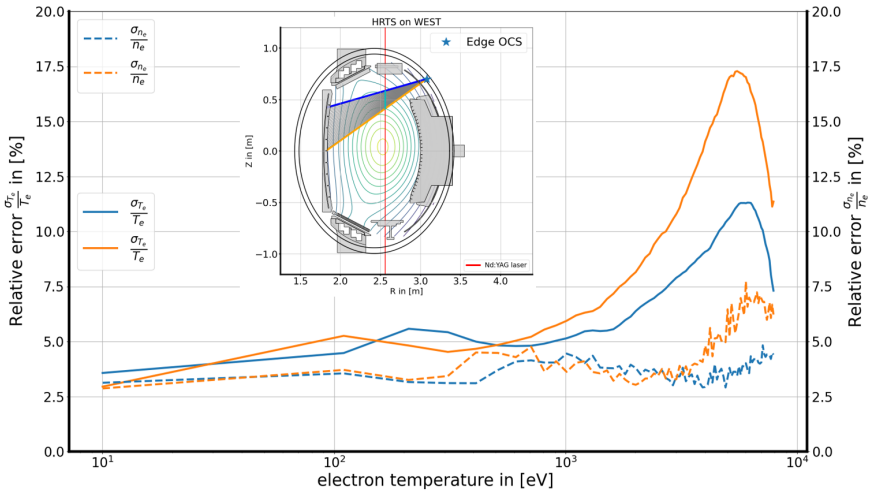

Figure 4.20: Relative error for EOCS by using the instrumental functions of the edge polychromator.

Impact on the electronic pressure estimated:

The final step was to study the relative error in the electronic pressure. To assess the electronic pressure p_e and its gradient in the edge with a good resolution, the

relative error in electronic pressure should be performed to understand better the diagnostic's performance to probe the SOL in the future. Theoretically, the electronic pressure is expressed as:

$$p_e = n_e k_b T_e \tag{4.53}$$

For each T_e simulated, we iterated the retrieving process 100 times to estimate the plasma parameter: n_e, T_e, and p_e. At each iteration, an error on n_e and T_e is made due to the noise propagation leading to a fluctuation called δn_e, δT_e as well as δp_e.
Hence, we can write for one iteration the expression of the electronic pressure $\hat{p_e}$ as:

$$\hat{p_e} = (p_e + \delta p_e) = (n_e + \delta n_e) k_b (T_e + \delta T_e) \tag{4.54}$$

$$\left(1 + \frac{\delta p_e}{p_e}\right) = \frac{1}{p_e} \left[(n_e k_b T_e + \delta n_e k_b T_e + n_e k_b \delta T_e + k_b \delta n_e \delta T_e)\right] \tag{4.55}$$

$$\frac{\delta_{p_e}}{p_e} = \frac{\delta_{n_e}}{n_e} + \frac{\delta_{T_e}}{T_e} + \frac{\delta_{n_e}}{n_e}\frac{\delta_{T_e}}{T_e} \tag{4.56}$$

Yet, the relative uncertainty product can also be written as:

$$\tag{4.57}$$

$$\frac{\sigma_{p_e}}{p_e} = \alpha_{error} \frac{\sigma_{n_e}}{n_e} + \beta_{error} \frac{\sigma_{T_e}}{T_e} \tag{4.58}$$

, where α_{error},β_{error} are the slope in density and temperature respectively. However, this relation is correct only if the correlation term between n_e and T_e equals 0. For this, we computed the correlation term r expressed as:

$$r = \frac{Cov(n_e, T_e)}{\sigma_{n_e} \sigma_{T_e}} \tag{4.59}$$

, where $Cov(n_e, T_e)$ is the covariance term between n_e and T_e.

First, the figure 4.22 shows that the correlation assessed for each temperature simulated is between -0.65 and 0.4 and changes with the temperature. Therefore, the relation 4.58 is wrong, and we can not suppose this law in the future.
Secondly, the figures 4.21a and 4.21b present the error on the electronic pressure versus the relative error on n_e and T_e respectively. The first observation is that the relative error on p_e is linearly proportional to the relative error on T_e. In addition, the figures show that the relative error on p_e increases when the relative error on n_e decreases. This could be problematic when we measure the density at the edge, where the signal could be degraded. Additional simulations must be performed to understand better the error propagation by simulating the signal regarding the NSR and its distribution over the polychromator channels.

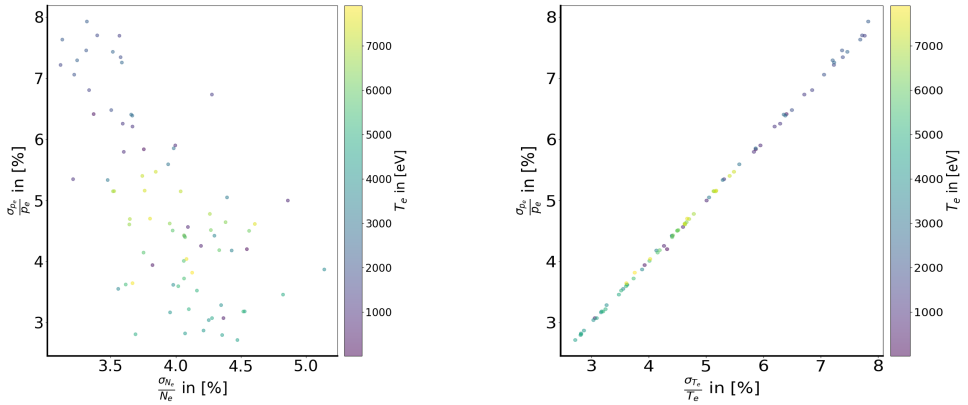

(a) $\frac{\sigma_{p_e}}{p_e}$ versus $\frac{\sigma_{n_e}}{n_e}$ (b) $\frac{\sigma_{p_e}}{p_e}$ versus $\frac{\sigma_{T_e}}{T_e}$

Figure 4.21: Relativistic error on the p_e regarding $\frac{\sigma_{n_e}}{n_e}$ and $\frac{\sigma_{T_e}}{T_e}$ for the polychromator 23, for NSR of 5 % and 100 iterations.

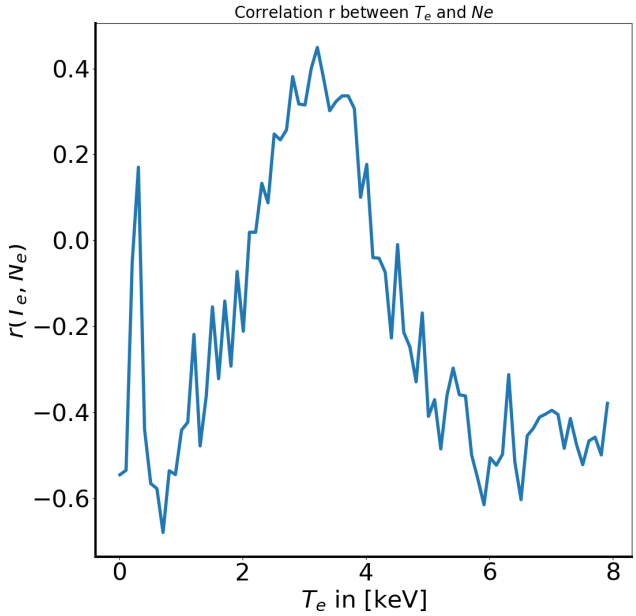

Figure 4.22: Correlation term computed from T_e retrieved for the polychromator 23, for NSR of 5 % and 100 iterations.

4.8 Summary

In this chapter, we present the new synthetic Thomson scattering diagnostic. The code implements all modules needed to simulate Thomson scattering diagnostics, from laser propagation to TS measurement, including the simulation of Bremsstrahlung radiation.
The modules associated with laser beam propagation have been implemented to simulate the propagation of the beam. This will enable the determination of the scattering volumes of each measurement point in the future. In particular, this tool will consider density profiles when gradient profiles are essential.
Based on the laser properties, scattered photon fluxes are simulated as a function of the diagnostic geometry, which sets the resolution, solid angle, and scattering angle. A second sub-module simulates the photon flux from Bremsstrahlung radiation. The method developed is different from Thomson scattering. This is explained by the measurement principle, which, in the case of Bremsstrahlung, corresponds to an integrated measurement along the line of sight. This forces us to consider electron density and temperature profiles.
The code then integrates a Monte Carlo method to simulate photon transmission in the optical collection system, which is defined by telescope and fiber transmission.

In addition, the methods implemented in the code have considered the experimental instrumental functions of the polychromators measured during the manufacturer's spectral calibration for simulation. The third module can simulate the signals from the fast channels in Thomson scattering or the signals from the slow channels in Bremsstrahlung photon flux. The section 4.6 presents the two regression methods implemented in the synthetic diagnostic. The section 4.7 presents the sensitivity tests made to assess the relative error on the electronic temperature, density, and pressure. We were interested in:

- The impact of misalignment of the target lines concerning the expected scattering spectrum.
- The impact of noise level on temperature estimation.
- Diagnostic performance at a noise level of around 5 %. Firstly, the relative error in temperature and electron density over a wide range of simulated core and edge telescope temperatures will be estimated. Secondly, the relative error in electron pressure for the onboard polychromator will be calculated. The results showed no linearity between the relative error of electron pressure and the relative errors of density and temperature.

5 Diagnostic Operation

Sommaire

5.1 Spectral calibration . . . 131
5.1.1 Monochromator: key instrument for the spectral calibration . . 131
5.1.2 Spectral calibration of the COMPASS polychromator . . . 132
5.1.2.1 Spectral calibration setup . . . 133
5.1.2.2 Spectral calibration procedure . . . 133
5.1.3 Spectral calibration bench for WEST polychromator . . . 135
5.1.3.1 Spectral calibration bench . . . 135
5.1.3.2 Beam splitter . . . 136
5.1.3.3 Avalanche Photo-diode Detector . . . 137
5.2 Absolute Calibration: Raman Scattering . . . 138
5.3 Summary . . . 141

The interaction of incident photons with charged particles in the medium produces scattering radiation, which, if collected, can be used to determine the electron density and temperature. The scattering power collected is converted into a voltage signal (see chapter 3 for more details). Regarding the HRTS design on WEST, the TS signal provided by each polychromator channel can be expressed as:

$$V_{TS,k}(t) = \int_{\lambda_{min}}^{\lambda_{max}} T_{ocs} T_{fiber} T_{filter,k}(\lambda) \eta_k(\lambda) G_k \phi_{coll}(t) d\lambda \tag{5.1}$$

From the relation 5.1, one observes that the TS system depends on parameters specific to the diagnostic: $T = T_{ocs} T_{fiber} T_{filter,k}(\lambda) \eta_k(\lambda) G_k$. This expression is justified because the OCS, the fiber, and the interference filter have a transmission factor leading to reduced photon flux, which the APD will detect and convert into electrons with a quantum efficiency $\eta_k(\lambda)$. In principle, these parameters do not react similarly for each polychromator. In addition, they could evolve in the future and impact the electron density and temperature measurement. Calibration involves characterizing the Thomson scattering system, particularly the polychromator, to guarantee quality measurements. For this purpose, evaluation of the parameter T is needed, and it is done with two calibration processes:

- A spectral calibration enables the characterization of the instrumental function of each polychromator channel ($T_{filter,k}(\epsilon)\eta_k(\epsilon)G_k$).
- An absolute calibration enables estimating the losses from the OCS and fiber that are assessed during the alignment procedure ($T_{ocs}T_{fiber}$).

5.1 Spectral calibration

The Thomson Scattering signal is a convolution product between an incident photon flux $\phi_{inc}(\lambda)$ and the instrumental function of the detector $g_k(\lambda)$. A monochromator is then used to create the Dirac function for each wavelength.

The spectral calibration characterizes each polychromator channel by determining its instrumental function. The instrumental function is defined by the product of the interference filter transmission $T_{filter,k}$, the APD quantum efficiency $\eta(\lambda)$, and the electric Gain G_k allocated to the channel k (see chapter 3 for more details). To estimate the instrumental, a spectral calibration bench scans the response of the polychromator channels over a wavelength range.

5.1.1 Monochromator: key instrument for the spectral calibration

A monochromator is an optical instrument that selects a wavelength from a light source. It consists of adjustable inlet and outlet slots, reflection mirrors (flat or concave), and a diffraction grating. The diffraction grating is mounted on a rotating stage that allows the modification of the incident angle of the photon flux onto the diffraction grating, which selects the wavelength by following the Bragg Law [22]:

$$m\lambda = d(sin\alpha + sin\beta) \tag{5.2}$$

, where m is an integer value called the diffraction order, λ is the wavelength, α and β are the incident and refractive angle respectively. This will create a Dirac function $\delta(\lambda)$ for each wavelength λ desired.

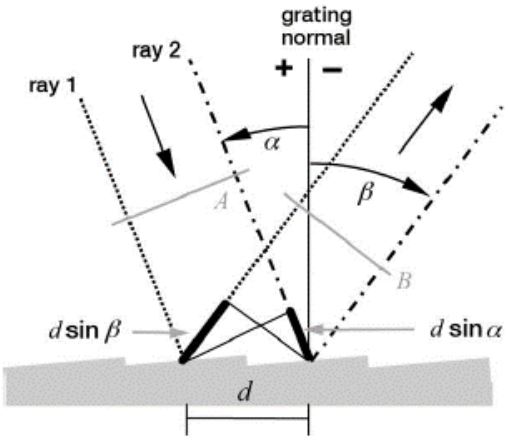

Figure 5.1: Diffraction grating principle, edited from [22]

However, it should be noted that creation is questionable and can be characterized by calculating the resolving power [19, 22] given by:

$$R = \frac{\lambda}{\Delta\lambda} \tag{5.3}$$

It depends on its specific characteristics, such as its imaging system, the properties of the mirrors, and the number of grooves.

5.1.2 Spectral calibration of the COMPASS polychromator

In 2022, the IPP in Prague and the IRFM collaborated to learn the spectral calibration method to understand better the subtleties associated with Thomson scattering diagnostics. Mastery of the spectral calibration is needed to determine whether the polychromator guarantees good data quality. We were interested in the spectral calibration of one polychromator from COMPASS (polychromator 504).

5.1.2.1 Spectral calibration setup

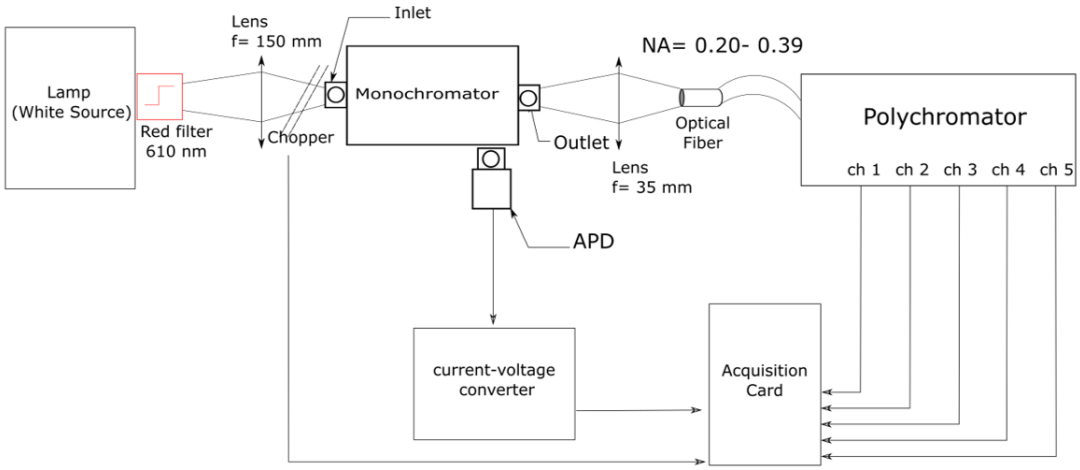

Figure 5.2: spectral calibration bench from COMPASS.

Figure 5.2 represents the spectral calibration set up from COMPASS. A 100 W halogen lamp provides a white light that emits photons in an extensive spectral range between $650-1075$ nm. A filter with a cut-off wavelength of $\lambda = 650$ nm (High-pass wavelength filter) is used to avoid higher diffraction orders while the monochromator will diffract the light. A chopper modulates the input signal to subtract the ambient background light. Two lenses are placed at the monochromator's input and output to maximize the photon flux injected into the polychromator's input fiber. Then, an acquisition card and a computer are used to acquire and process the signal. A monochromator of 1200 grooves selects the desired wavelength in the spectral range of interest. The output photon flux will either be guided toward the polychromator by a fiber bundle or sent to the APD to determine the photon flux injected into the polychromator.

5.1.2.2 Spectral calibration procedure

At a time t, an incident photon flux $\phi_\lambda(t)$ at wavelength λ is injected into the polychromator and detected by one of the channels returning a time-dependent output voltage $V_{out,k}(t)$. It is possible to write the following equation from the photon flux at the polychromator's input and the various channels' output voltage.

$$V_{out,k}(\lambda, t) = \int g_k(\lambda, t)\phi_\lambda(t-\tau)d\tau \tag{5.4}$$

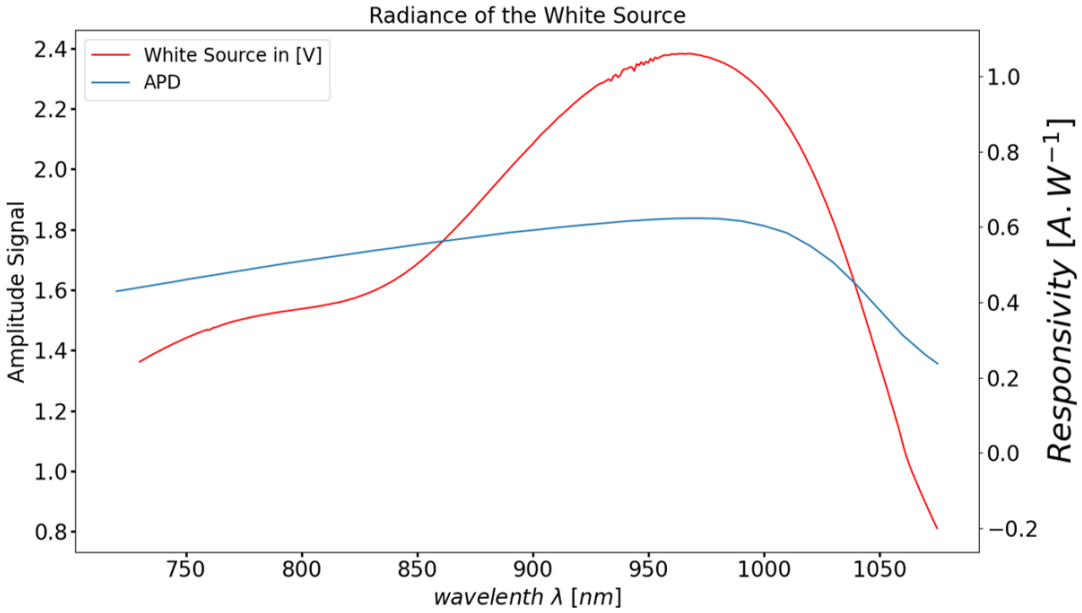

Figure 5.3: COMPASS APD detector responsivity and white source spectrum used for the spectral calibration as a reference

As mentioned, spectral calibration involves establishing a precise relationship between the incident light wavelengths and the polychromator output signals. The first step in the calibration procedure is to estimate the power emitted at each length of the white light source. This step is necessary to take account of any variations in the source during future calibrations.
This is achieved using a temperature-controlled APD to estimate the power emitted at the monochromator output at each scan length. The detector is calibrated absolutely to retrieve the light source emission spectrum. We retrieve the radiative power spectra from the detector response $R(\lambda)$ or estimate the number of incident photons, as shown in figure 5.3. The figure shows the APD's responsivity as a wavelength function, expressed in [A.W^{-1}]. Since the APD signal is low, the COMPASS team uses an APD's current-to-voltage converter to convert the APD current in V. This explains why the white source, in the figure 5.3, has an amplitude in [V]. Note that this conversion factor is considered a constant factor of 1V for 100 nA.

$$V_{mes,k} = G_{conv} V_{out} = G_{conv} R_{APD}(\lambda) \phi_\lambda \tag{5.5}$$

Where the measured voltage V_{mes} is equal to the product of a conversion factor from the current-voltage converter G_{conv}, the APD response $\sigma(\lambda)$ and the photon flux ϕ_λ at wavelength λ.

Once this has been done, we divide the signal acquired at a given wavelength by the radiated power given at the same wavelength for the white source for each:

$$g_k = \frac{V_{mes,k}}{\phi_{W,\lambda}} \tag{5.6}$$

, where $\phi_{W,\lambda}$ is the white source photon flux measured by the APD.

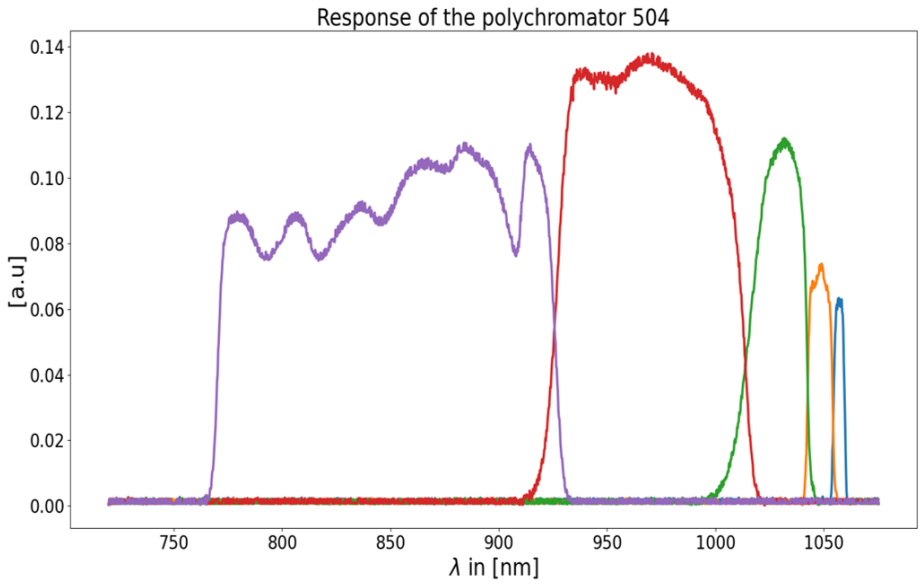

Figure 5.4: Normalized instrumental functions of the COMPASS polychromator 504 during the spectral calibration

5.1.3 Spectral calibration bench for WEST polychromator

5.1.3.1 Spectral calibration bench

Based on this collaboration, we have initiated the development of a spectral calibration bench for WEST. Our calibration bench will be similar to the COMPASS calibration bench. The main difference is the simultaneous measurement of the incident source and polychromator signals to consider temperature fluctuation on the light source or the detector. We purchased a semi-reflective plate, which will theoretically separate the radiative power at the monochromator output into two parts, as shown in the figure 5.5, with wavelength-dependent transmission and reflection factors.

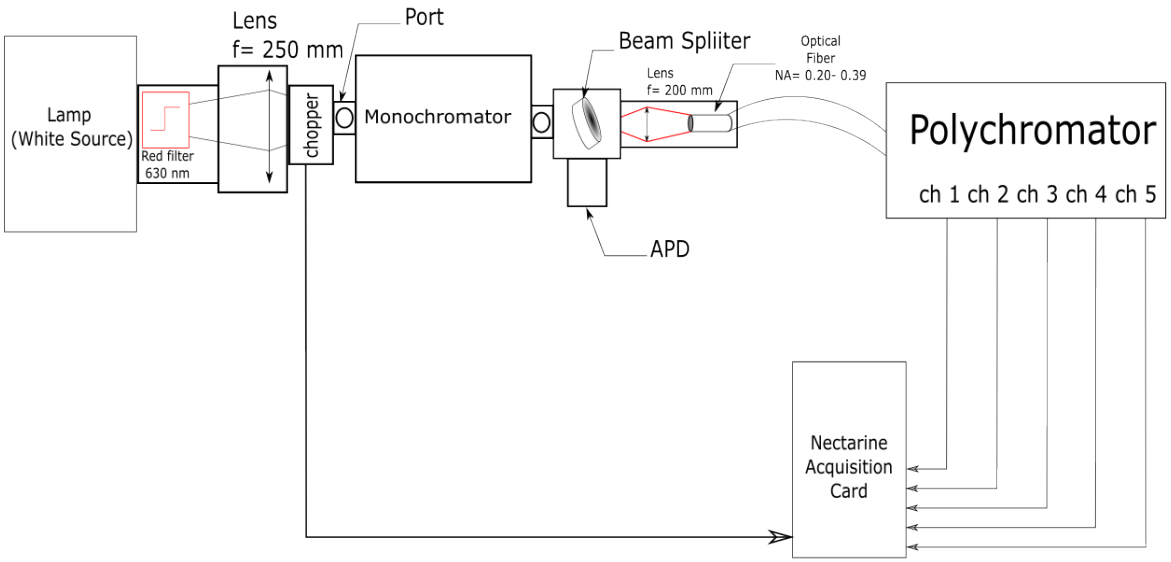

Figure 5.5: Schematic of the spectral calibration for WEST

The TM300c monochromator from Bentham was chosen for its price. According to the technical specifications, the monochromator is of the Czerny-Turner type. The monochromator has two diffraction grating to scan over a wide range from 200 nm to 500 μm. In our case, we will use one diffraction grating of 1200 g/mm diffraction grating with a dispersion of 2.7 nm.mm, a wavelength accuracy of 0.2 nm, and a rejection of 10^{-5} to match with a 300 mm focal length lens imaging integrated into the monochromator. This specification is essential for calibrating edge polychromators to measure low temperatures of 10 eV. It should be noted that in the case of low temperature and low density (of the order of 10 eV and 10^{18} m^{-3}), only the first three filters will provide a signal that can be used to estimate the plasma parameters. Consequently, fine calibration of the polychromators is necessary to ensure good measurement quality. For instance, for the edge polychromator, the width of the first filter is 2 nm, corresponding to a measurement range of 10 to 16 calibration points between 1059.1 nm and 1063.1 nm with a step of 0.25 nm.

5.1.3.2 Beam splitter

Figure 5.6 shows the transmission and reflectance of the beam splitter, which will be used to calibrate the WEST polychromator. We observe that the transmission and the reflectance factors are not constant over the wavelength and will modulate the signal during the spectral calibration operation. Due to a lack of time, testing the calibration setup and qualifying the beam splitter and its impact on the filter's calibration was impossible. This must be done in the future to validate the calibration bench according to a calibration procedure.

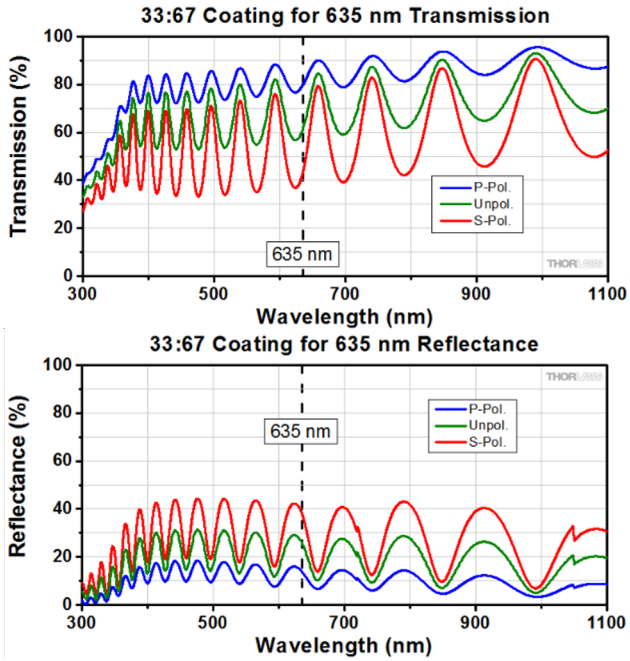

Figure 5.6: Beam splitter transmission and reflectivity, edited from [17]

5.1.3.3 Avalanche Photo-diode Detector

Let's examine its operating principle to justify the APD's choice. When a photon strikes the APD, it creates an electron-hole pair. Under the effect of the high electric field, the electrons (and/or holes) gain enough energy to ionize other colliding atoms, creating more electron-hole pairs. This cascading multiplication process is called an "avalanche." This avalanche amplifies the initial optical signal, making the APD highly sensitive to low light levels.

The breakdown voltage of an APD is the electrical voltage above which the APD goes into an avalanche, a phenomenon characterized by the rapid multiplication of charge carriers (electrons and holes) inside the photo-diode. APDs operate at a high reverse voltage, close to the breakdown voltage. This high voltage creates an intense electric field in the depletion region of the diode. The breakdown voltage is the minimum reverse voltage at which the avalanche process occurs, which is self-sustaining. In other words, it's the voltage at which charge carrier multiplication becomes uncontrolled, even without additional photons. At this voltage, the APD switches from a linear operating state, where the output current is proportional to the light intensity, to a breakdown (or discharge) state, where the current increases exponentially.

To maximize sensitivity, the APD generally operates at a voltage just below the breakdown voltage. At this level, the avalanche effect amplifies the optical signal while maintaining operating stability. This enables very low light levels to be detected. Breakdown voltage depends on several factors, including the semiconductor material used, junction design (geometry, size, doping), and operating temperature, as breakdown voltage can vary with temperature (an increase in temperature can often

increase breakdown voltage).
LaserComponent's APD [23], which consists of a module temperature-controlled current/voltage conversion module, was chosen as the APD of choice. The breakdown voltage can change as a function of temperature; according to the manufacturer, the breakdown voltage changes by $1V/°c$. In addition, the APD has a current-voltage conversion module whose gain is variable and can, therefore, be adapted according to signal amplitude. In addition, the responsivity is high, as shown in figure 5.7, where at 910 nm, the response is about 62 A.W^{-1}, and at 1050 nm, it is about 17 A.W^{-1}.

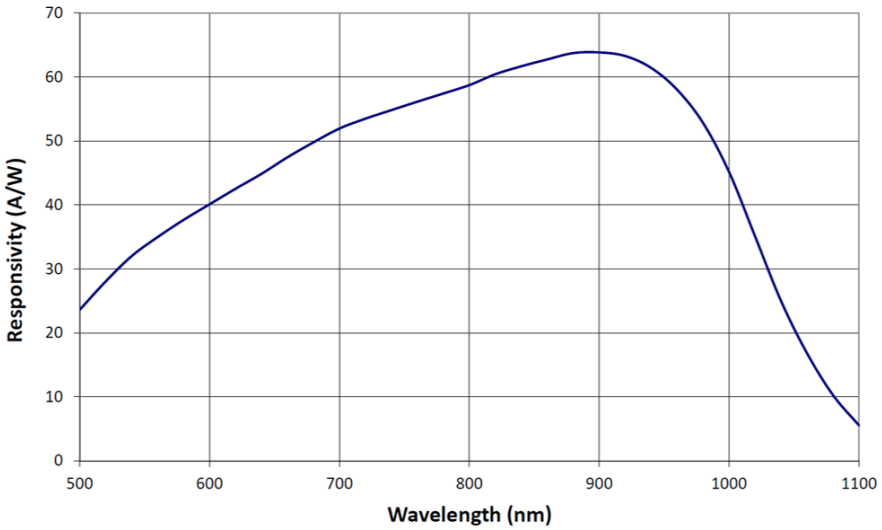

Figure 5.7: APD responsivity versus the wavelength, edited from [23]

5.2 Absolute Calibration: Raman Scattering

Absolute calibration corresponds to the calibration of the Thomson Scattering diagnostic system installed on the tokamak. Generally, the laser alignment in the machine is realized during the Raman Scattering process. This will help to characterize the alignment by processing the signal from the alignment fiber, and it will allow to measure the "instrumental function" of the diagnostic.
When subjected to an electromagnetic wave, molecules emit photons at different wavelengths due to dipole oscillation. This results in the scattering of light with a wavelength different from the incident light's.

A small fraction of the photons undergo an energy change by interacting with the vibrational modes of the molecule, resulting in inelastic scattering. These scattered photons have either a lower energy (Stokes shift) or a higher energy (anti-Stokes shift) than the incident photons. In the scope of this thesis, we do not go deeper into the Raman theory. However, we will use the anti-stokes Raman scattering to calibrate the Thomson diagnostics in absolute terms. To do this, we rely on Antistoke Raman's theory, which produces a line spectrum that can be calculated theoretically from the following equations:

$$\lambda_j = \frac{1}{\frac{1}{\lambda_l} + B_0(4J-2)} \tag{5.7}$$

, where λ_j is the wavelength of an emitting ray, λ_l is the laser wavelength, B_0 is a rotational constant, and J is the rotational state.

$$\rho_{Raman}(J) = F(J)S(J) \tag{5.8}$$

, where $\rho_{Raman}(J)$ is the Raman spectra depending on the fraction of molecule $F(J)$ and differential cross-section $S(J)$:

$$F(J) = Q^{-1} g(J)(2J+1) e^{-\frac{E(J)}{k_b T gas}} \tag{5.9}$$

$$S(J) = \frac{7(2\pi)^4 \gamma_{Raman}^2}{45\lambda_j^4} b_{J\rightarrow J-2} \tag{5.10}$$

, with γ_{Raman} represents the molecular anisotropy and $b_{J\rightarrow J-2}$ is the Placzek-Teller coefficient. Note that the $E(J)$ is the rotational energy given by:

$$E(J) = hc(B_0(J(J+1) - D_0(J(J+1))^2 + H_0(J(J+1))^3 \tag{5.11}$$

$$b_{j\rightarrow J-2} = \frac{3J(J-1)}{2(2J+1)(2J-1)} \tag{5.12}$$

The absolute calibration procedure measures the Raman scattering signal at different pressure values while measuring the gas density and temperature. The design of the collection chain determines the resolution, transmission, and solid angle of each measurement point. Although the signal amplitude is low, the first polychromator channel detects the Raman spectrum, enabling us to estimate the parameter T.

$$V_{Raman,k} = \underbrace{T_{ocs} T_{fiber} \Delta l \Delta\Omega}_{systems\ constants} n_{gas} \frac{\lambda_l E}{hc} \int \underbrace{T_{filter,k} \eta(\lambda) G_k}_{\phi_{cal,k}} \rho_{Raman} \tag{5.13}$$

Furthermore, since vertical resolution, OCS transmission, and fiber transmission depend on geometrical aspects, if we emit a signal for a given spectrum, we can estimate the solid-angle and the vertical resolution during the laser alignment procedure, losses associated with collection systems, and fiber bundles during diagnostic operation.

Note that in the WEST case, we will use nitrogen gas to calibrate the diagnostic in absolute, and the molecular parameters are given in the table 5.1.

Gas	Even J	Odd J	B_0 $[cm^{-1}]$	D_0 $[cm^{-1}]$	H_0 $[cm^{-1}]$	γ^2 $[cm^6]$
N_2	6	3	1.9895	$5,72.10^{-6}$	$3.7.10^{-10}$	$0.51.10^{-48}$
H_2	1	3	59.3392	$4,6.10^{-6}$	$5,2.10^{-10}$	$9,28.10^{-48}$
D_2	6	3	29,9105	$1,13.10^{-6}$	$3,6.10^{-10}$	9.10^{-48}
O_2	0	1	1.4378	$5,48.10^{-6}$		$1,29.10^{-48}$

Table 5.1: Molecular constant for the Raman scattering process, taken from [57]

5.3 Summary

This chapter presents the fundamental calibrations required for rigorous measurements of plasma parameters. It gives a non-exhaustive overview of the spectral calibration needed to characterize the instrumental functions of edge and core polychromators. This calibration is performed using a white light source and a monochromator. The monochromator selects a wavelength to determine the response of the various polychromator channels.

Collaboration with the IPP in Prague enabled us to understand the subtleties of calibration. Based on this collaboration, we have designed a calibration bench that will simultaneously measure the white light spectrum and detector response.

In the second section, we present absolute calibration and Raman theory. Absolute calibration refers to the calibration of Thomson scattering diagnostics once implemented on the machine. This calibration helps align the laser and determine the diagnostic transfer function for each measurement point. This corresponds to the transmission of the optical systems T_{OCS}, the transmission of the fibers T_{fiber}, the vertical resolution Δl, and the solid angle $\Delta\Omega$ associated with each measurement point.

Using these two calibrations, we can measure the temperature and electron density at the edge and core of the plasma. A reliable determination of electron density is impossible without absolute calibration, which estimates the system's parameters (see relation 5.13.

6 Experimental measurements

Sommaire

6.1 Steering laser line system . . . 143
6.2 HRTS commissioning during the 2024 experimental campaign . . . 145
6.2.1 First operation phase: HRTS setup . . . 145
6.2.2 Nectarine Acquisition card and raw data retrieving. . . . 147
6.2.2.1 Raw Data Signals . . . 147
6.2.2.2 Timestamp evaluation . . . 148
6.2.2.3 Data reconstruction . . . 148
6.3 Thomson signal Analysis . . . 150
6.3.1 Scattering pulse characterization . . . 151
6.3.1.1 Pulse duration . . . 151
6.3.1.2 Acquisition stability . . . 152
6.3.2 Noise characterization . . . 153
6.3.2.1 Nectarine card tests in laboratory . . . 153
6.3.2.2 Noise source identification . . . 154
6.3.2.3 Autocorrelation time on the fast channels . . . 156
6.3.2.4 Noise to Signal ratio . . . 157
6.3.3 Processing Signal method . . . 158
6.3.3.1 Post processing method . . . 158
6.3.3.2 Real-Time processing method . . . 160
6.4 Discussion . . . 161
6.5 Experimental Result from the C9 campaign. . . . 163
6.6 Discussion about the Noise-to-Signal Ratio observed experimentally . 167
6.7 Perspective . . . 168
6.7.1 Steering laser line system . . . 168
6.7.2 Plasma parameters retrieving . . . 170
6.7.3 Real-time measurement . . . 171

This commissioning was performed with a much-reduced system, different from the one presented in Chapter 3. The aim was to validate and debug the system before completing the diagnostic for the next campaign. This commissioning aimed to validate the system by:

1. By setting up the laser line control system. This included verifying the remote control capabilities of the laser system from the control room, which is crucial for enabling the laser to cross the plasma effectively.

2. By acquiring the Thomson signals with a fast acquisition system and validating the compatibility with the WEST CODAC infrastructure [71].

3. By validating the Thomson scattering data by analyzing the noise sources and testing the algorithm.

6.1 Steering laser line system

For the first commissioning, a simplified laser line system has been installed [1]. This last comprised one deflecting mirror set in a piezoelectric mount (mirror 5 in figure 4.5) and one camera installed in the Laser analysis chassis (LAC).
The difficulty of laser alignment lies mainly in the challenge of passing a 2 cm diameter laser beam through a 4 cm diameter hole while crossing the Brewster interfaces at the entrance and exit and minimizing reflections. During the operation, multiple reflections occur in the Brewster, leading to multiple stray lights with different intensities. This experience shows that the alignment could lead to alignment error if we are not rigorous. Figure 6.1 shows the alignment laser reflection observed on the first Brewster window (at the entrance) and some misalignment scenarios (picture a to picture e). Figure 6.1b shows the picture acquired by a camera (not the NIR camera) installed in the LAC while we aligned the laser. A piezoelectric mount containing the deflecting mirror was used to correct the misalignment and position the beam by moving the piezoelectric over a distance of about tens μm. Picture a, b, d, and e come from the deflecting mirror tilting too much. The picture c is not understood yet. The picture f represents the "best" scenario observed.
To solve this problem in the future, a near-infrared camera would be placed in front of the second Brewster window to identify the reflection. This is possible since the camera is sensitive to the alignment laser intensity. In addition, for the final SLLS, a NIR camera will observe a reference mirror, allowing control of the laser alignment.

[1] There has been a delay in wiring the diagnostics

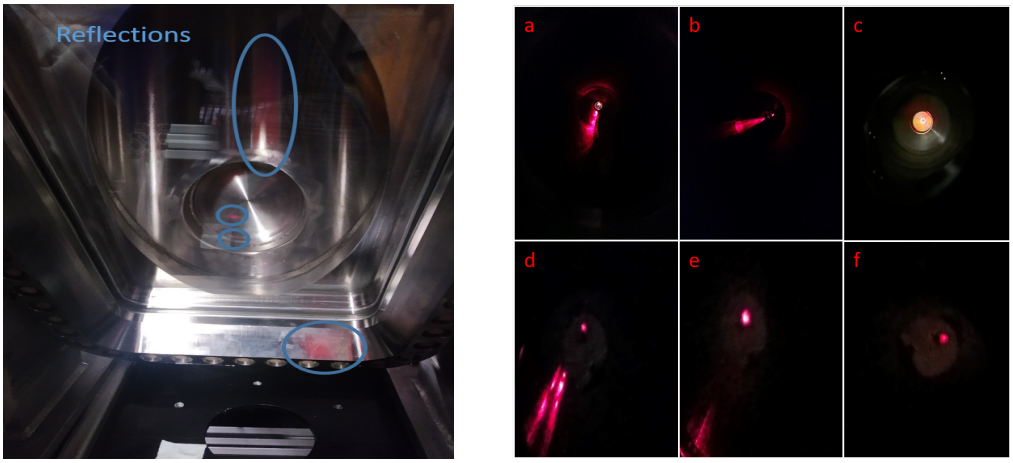

(a) Stray-light in the Brewster window

(b) Alignment scenarios

Figure 6.1: Alignment procedure during C9 campaign and stray light evidence from the laser alignment. The picture shows the Brewster windows and the multiple reflections observed. The picture b shows the alignment cases, whereas the picture f corresponds to the correct alignment.

Finally, thermal paper was used to observe the Nd:YAG laser spot going toward the beam dump. In the future, the laser beam size is measured using a camera, enabling the beam size measurement. However, in the first operation phase, a thermal paper was used to ensure the passage of the Nd:YAG beam. Figure 6.2b shows the pulse reflection provided by the Nd:YAG laser in LAC. A NIR camera using an optical density of 4 is installed in front of the camera to reduce the pulse energy.

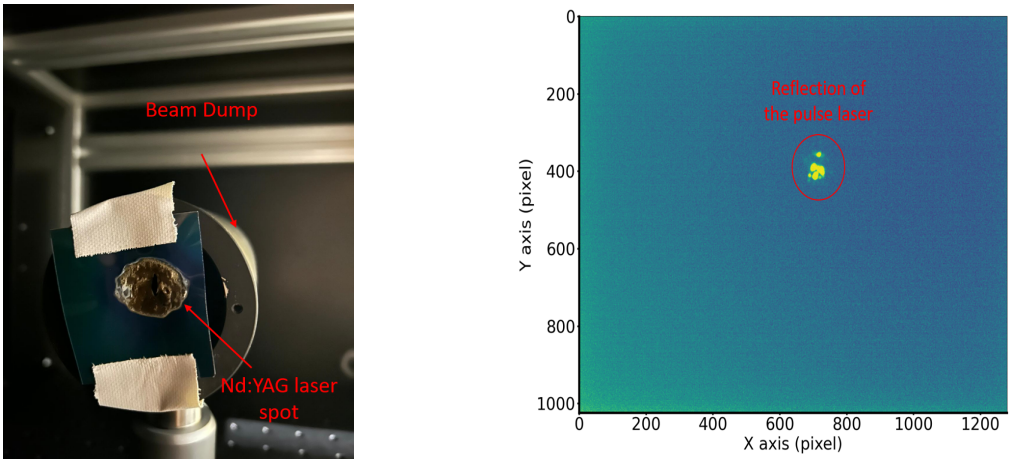

(a) Beam spot observation with a thermal paper.

(b) Reflection observed with the NIR camera in the LAC

Figure 6.2: Misalignment observed from the LAC. Misalignment is due to reflection in the two Brewster windows.

6.2 HRTS commissioning during the 2024 experimental campaign

6.2.1 First operation phase: HRTS setup

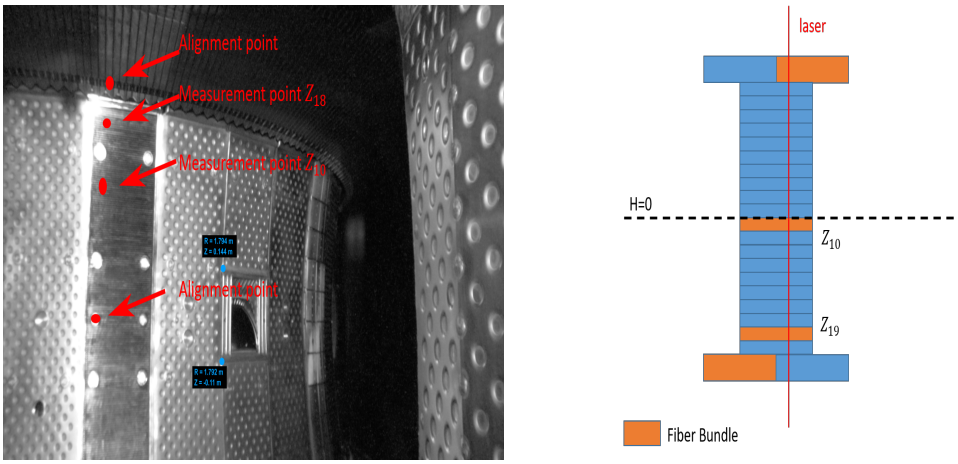

(a) COCS installation for the C9 campaign

(b) Fibers setup in the fiber arrays

Figure 6.3: COCS installation for C9 experimental campaign. The picture was taken with the AIA-embedded camera.

Firstly, the laser was aligned to pass vertically through the tokamak. Secondly, the core telescope was installed and aligned manually during a Raman scattering process inside the machine. The COCS was installed after the vacuum vessel closed, making it impossible to check the measurement points' positions inside the tokamak. Furthermore, the COCS was positioned manually as best as possible using external view and internal reference.
To achieve this, we connected the polychromators to an oscilloscope to visualize and optimize the signals from the two duplexed fibers. The HRTS diagnostic was composed of two multiplexed fibers. The first multiplexed fiber was used to align the laser to the optical collecting system, and the second multiplexed fiber was used for measuring the core region.
The fiber was positioned in a fiber array at the position $H_{10} = 1.5\ mm$ and d $H_{19} = 77.5\ mm$ from the telescope center (defined by the center of the lens). Figure 6.4 shows the signal detected by the fast polychromator channels. Since the optical fibers are duplexed, we expected four pulses of identical intensity during the Raman scattering process. However, we observed three pulses acquired by an oscilloscope: two pulses, represented in blue, with an amplitude between 10 and 20 mV, shifted by 100 ns, corresponding to the fiber allocated to measuring points, and a yellow pulse, corresponding to the signal collected by one alignment fiber. This observation suggests we are in the configuration shown in Figure 6.3b; consequently, the photons collected by the fiber bundles only cover three of the installed four bundles.

In addition, since the COCS was not set up at the rated position, the Articulated Inspection Arm (AIA) [9] camera was also used to estimate the measurement points position in the tokamak vessel. These positions were then used in the synthetic diagnostic to assess the scattering angle. Figure 6.3a illustrates the fibers back-lighting and the position in the machine reference seen by the AIA camera. According to the figure and the COCS location, the scattering angle of the first measurement point is 102°, and the second scattering angle is 109°. Through the SD, it is possible to trace the line of sight of the two measurement points, which correspond to $R = 2.56$ m, $Z_{10} = 0.14$ m, and $Z_{18} = 0.33$ m at the machine reference. The advantage of these points is that they are taken at high density (about $10^{19}\ m^{-3}$) and high temperature T_e, ensuring a measurement on the various polychromator channels. For this commissioning, we decided to use polychromator 19, customarily allocated to EOCS, to study the impact of noise on the polychromator signals.

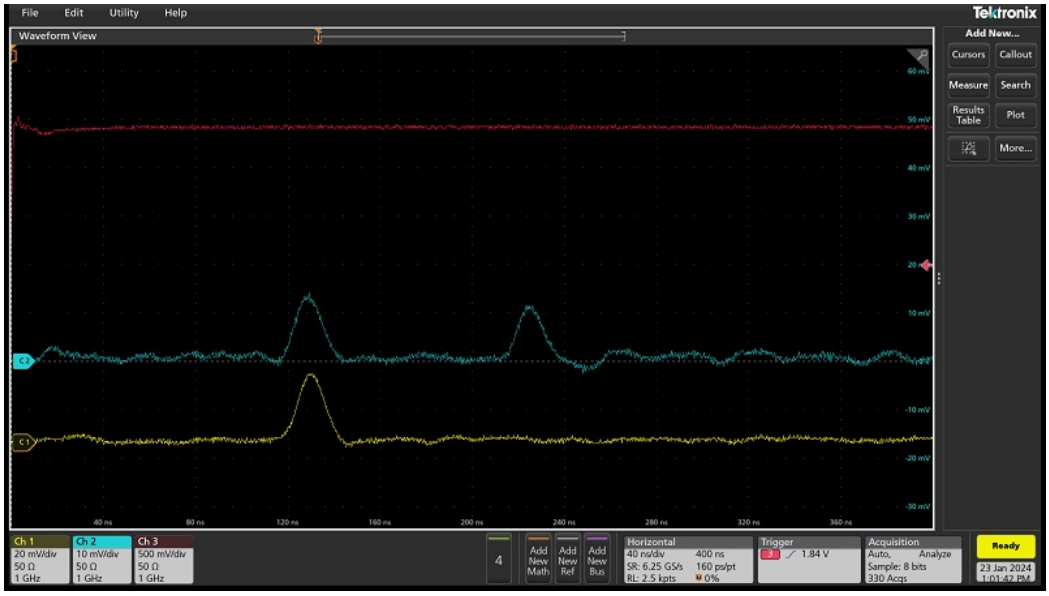

Figure 6.4: Laser alignment during the Raman Scattering

Note that the telescope was adjusted during a Raman scattering by injecting Nitrogen into the machine and maintaining the pressure constant. However, this procedure did not enable absolute calibration of the diagnostics, as measuring the laser energy was impossible. In addition, problems with the pressure transducers prevented us from estimating the density of Nitrogen injected into the machine. Nevertheless, we used the visualized signal to find a configuration that optimized the measurement channel signals.
In conclusion, electron density could not be estimated during this campaign. We will study the Thomson signal and calculate the electron temperature in different scenarios.

6.2.2 Nectarine Acquisition card and raw data retrieving.

A specific card is needed to acquire both the fast signal (laser pulse) and the slow signal (measurement of Bremsstrahlung radiation) to process Thomson scattering data. To this end, the Nectarine board incorporates two types of ADC chips, which convert the analog signal into a digital signal. The NECTAR chip is dedicated to acquiring fast signals with a sampling frequency of 1 GHz, while the chip dedicated to the slow channels operated with a sampling frequency of 1 kS.s^{-1}. As mentioned in chapter 3, the Nectar chip requires a trigger after recording the laser pulse. In practice, the trigger signal to the Nectarine boards should produced by the laser. For the commissioning, a solution was to use the Laser's Pockels Cell Sync output that has been delayed by 60 ns by an electronic function generator to acquire the diffusion pulses at the end of the data frame.

6.2.2.1 Raw Data Signals

During each laser pulse, the acquisition board's fast channels collect 1024 samples of the analog signal with 12-bit resolution. This data is transmitted to the acquisition PC via the UDP protocol. However, as the card is limited to transmitting 256 samples per transmission, each acquisition from the polychromators' high-speed channels is divided into four packets of 256 samples sent successively to the PC. We have decided to transfer all the raw data to understand the signal and noise sources for the commissioning. The different blocks are written in several text files that mix the fast and slow data. However, each block comprises a header of 9 "keys" of 32 bits designating:

- The Nectarine card is a number 1 to 36, designated the polychromator used to measure the plasma parameters.
- The channel is a number comprised between 1 and 7. The particularity of this key is that the numbers from 1 to 6 are allocated to fast acquisition. Contrary to the number 7 allocated to slow acquisition channels, which integrates all the signals from the slow acquisition channels at one timestamp.
- The shot number corresponds to the number of plasma shots sent by the CODAC supervision [71].
- The timestamp is a number, allowing the organization of the data chronologically.
- The block number is between 0 and 3, allowing the sorting of the data and retrieving the raw signals.
- and so on ...

All this information allows the reconstruction of the Raw signal, which will be presented in the following section.

6.2.2.2 Timestamp evaluation

Technically, the timestamps are between 0 to 2^{32} produced by a numerical counter that resets to zero 32 ms before each plasma shot. Figure 6.5 shows the difference between two consecutive timestamps (Δt) over the laser shot number. Theoretically, this value must be constant since the laser frequency does not change during the operation. The first point is high (10^7) and is explained by resetting the Nectarine card counter. However, the appearance of other peaks during laser operation is not normal. Data losses can explain low-amplitude peaks due to the UDP protocol. However, we also noticed a second peak at the 520th shot, which, for the moment, remains unexplained. Two possible solutions are that several consecutive laser shots were lost or the counter was reset to zero following a disturbance. Investigations must be carried out to answer these questions.

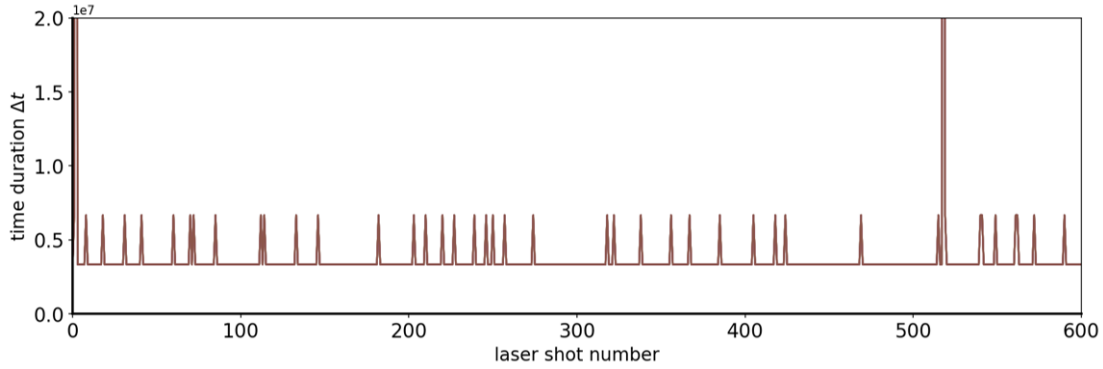

Figure 6.5: Timestamp difference for the plasma shot 59898

6.2.2.3 Data reconstruction

However, based on the useful data set, it was possible to reconstruct the Raw signal as shown in figure 6.6. It represents the Raw signals on 1024 samples for 1 μs acquisition time window. The signal is unusable, and two tasks must be done to retrieve the signals.
Due to the nectar chip architecture, a sample of 16 bits should be removed for every 17 samples. They correspond to different peaks shown in figure 6.6. Note that this process is possible if the 4 blocks are present; otherwise, the signal can not be reconstructed, preventing noise profile subtraction.
Since the register memory is a SCA with 16 rows, different load voltages are applied at each row, leading to an electronic noise impacting the acquired signal. Therefore, for each channel, a noise pattern repeating every 16 samples is evaluated on the first 640 points and subtracted from the 1024 acquired by the card.
Figure 6.7 presents the signal acquired by the Nectarine from the polychromator when the noise and the separators are removed. Since the fiber is multiplexed, the two measurement points are acquired on the same set of samples, and the second pulse

is delayed by 100 ns from the previous one (consistent with what we observe on the oscilloscope), allowing the acquisition of the two pulses on 200 samples.

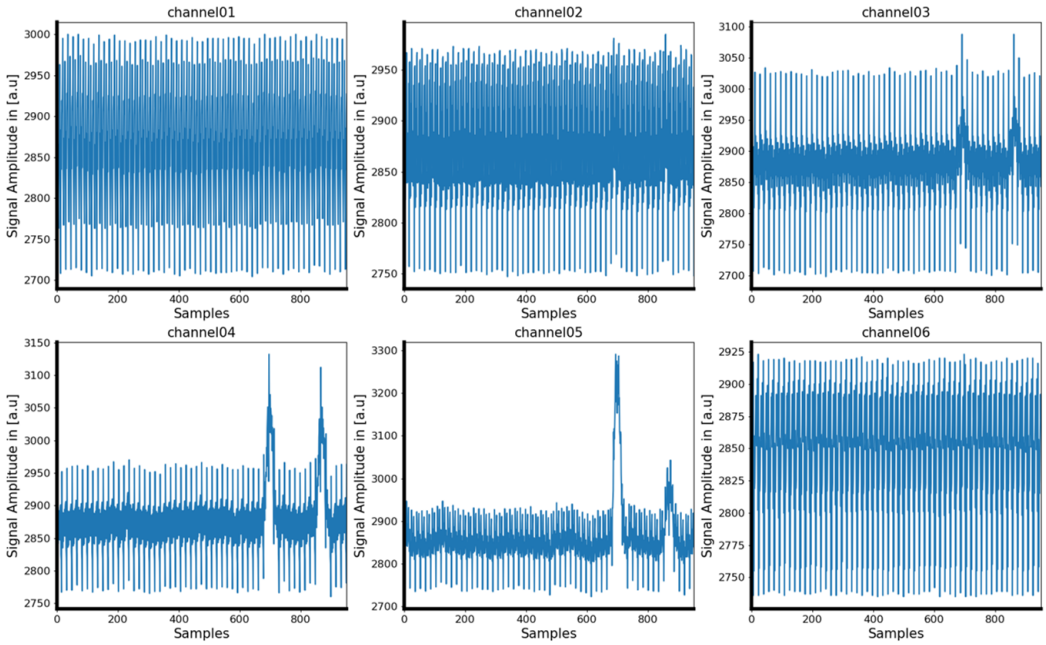

Figure 6.6: Raw Thomson scattering acquired during a plasma shot. The Raw Signal can be used until the 17th samples and the noise pattern are not removed.

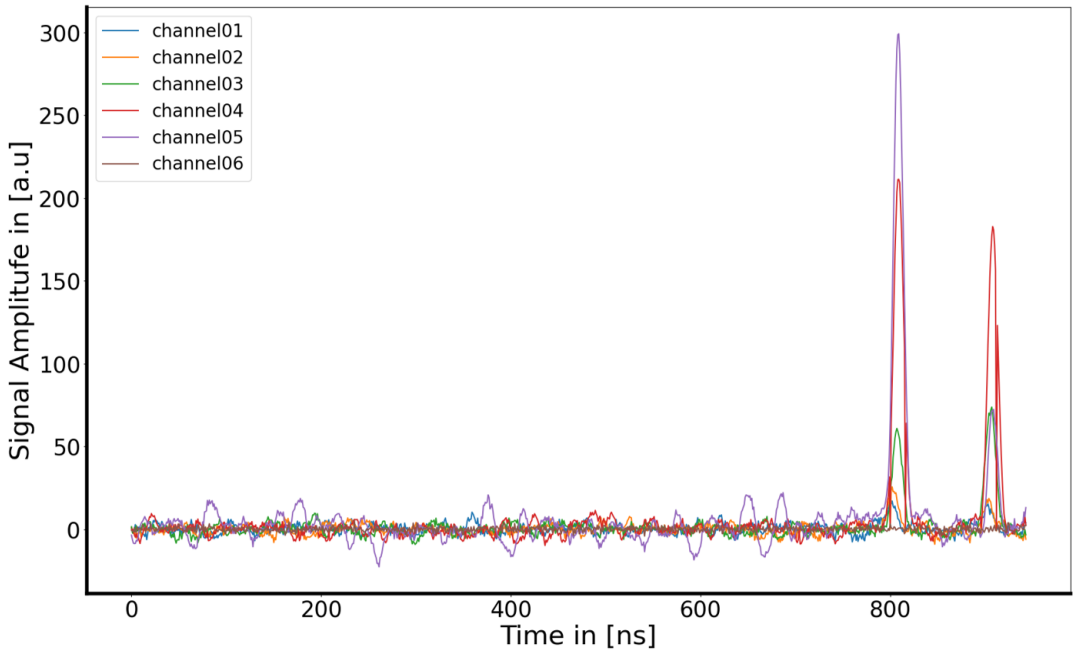

Figure 6.7: Thomson Scattering signals acquired during the experimental campaign after removing the periodic noise from the SCA.

It is consistent with the polychromator instrumental function used (see figure 4.11).

6.3 Thomson signal Analysis

The Thomson Signal analysis aims to understand the signal acquired during the plasma scenarios through its characterization. The noise sources must be identified for good data quality, and their influence on the raw TS signal must be determined. Figure 6.7 and 6.8 represent the signals acquired over time, for example, during the diagnostic operation. Two parameters characterize each raw TS scattering pulse:

The noise is defined as any undesirable perturbation affecting the Thomson scattering pulses. Noise can be random or systematic variations superimposed on the original signal (as shown in the figure 6.6), making it more difficult to process the scattering pulse. It is assessed by:

1. Its standard deviation σ_{noise}.
2. Its correlation time τ_{noise}. Generally speaking, noise correlation time is an essential characteristic that helps better understand, model, filter, and compensate for noise in signal processing systems. Noise correlation time measures how long noise is coherent with itself. A short correlation time means that the noise changes rapidly and unpredictably, while a long correlation time indicates that the noise has a more persistent and predictable structure.
3. Its maximum amplitude $A_{peak,noise}$.

The Thomson Scattering pulses $S_{TS,exp}$ are defined as the pulse provided by the electron density and the laser. It is described by:

1. Its pulse shape
2. The pulse duration τ
3. Its pulse Amplitude A_{TS}
4. Its peak position

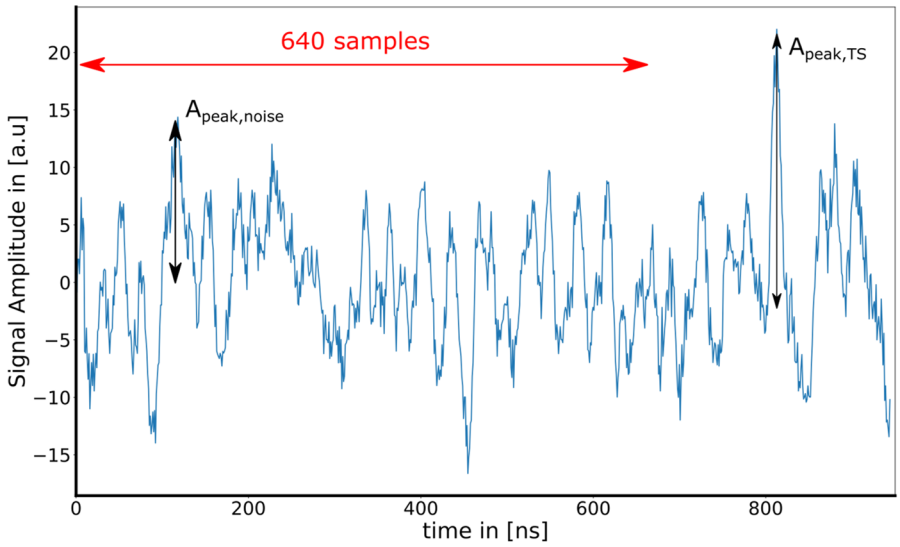

Figure 6.8: Signal characterization for the 50th laser shot of the 59901 plasma shot for the 4th channel of the polychromator 19 after chip noise correction.

6.3.1 Scattering pulse characterization

6.3.1.1 Pulse duration

Theoretically, the Thomson Scattering pulse has the same duration as the laser pulse. The time duration is defined as the time the laser emits a pulse. Measuring the pulse duration is the first step to guarantee that pulse duration is constant during the plasma operation. In practice, it is determined either by the FWHM or by $\frac{1}{e^2}$, observing that some signals are degraded at the beginning and the end of the plasma shot. To measure this duration, we used the acquisition chain to estimate the duration to ensure that the laser pulse duration does not degrade over the plasma shot time. Consequently, we decided to estimate the pulse duration with a theoretical Gaussian shape in the temporal domain given by :

$$G_{fit} = Ae^{-\left(\frac{t-t_{max}}{\tau}\right)^2} + b_0 \tag{6.1}$$

, where A is the TS signal amplitude, t_{max} is the instant where the signal is at the maximum amplitude, τ is the pulse duration, and b_0 is the offset.

Figure 6.9 shows the estimated pulse duration for each polychromator channel. An optimization algorithm obtains the time duration by fitting the theoretical Gaussian function to the TS pulses. τ measured are then multiplied by $\sqrt{2ln(2)}$ to get the pulse duration at the FWHM. The channels show the same trend for each polychromator channel except for channels 1 and 2. Figure 6.9 shows that the pulse duration is about 10 or 12 ns, consistent with 10 ns at the FWHM, given by Nd:YAG data sheet. Concerning the two first channels, the points are scattered, and an absence of scattering pulse

explains it; it is consistent with the polychromator instrumental function used. Note that the duration can be slightly different due to the "rise time" and the "fall time" of the acquisition system.

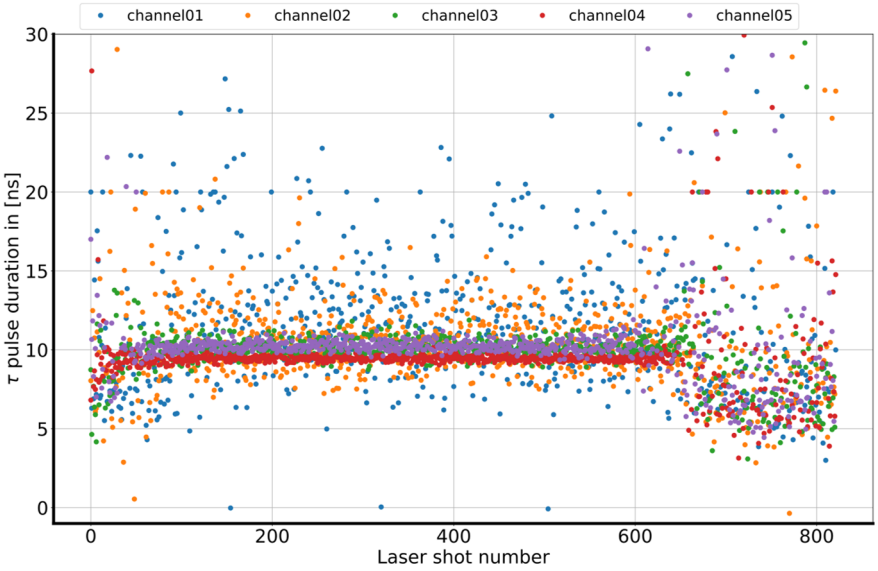

Figure 6.9: Pulse duration measured from the signal acquisition

6.3.1.2 Acquisition stability

The stability of a laser pulse concerns the consistency of its parameters to be stable for each acquisition. Indeed, the laser emits a pulse at a constant frequency, but the laser emission does not appear at a constant frequency; this is due to the laser electronic system and the flash lamp. In electronics, jitter refers to small temporal variations or signal fluctuations, particularly in digital or data transmission systems. These fluctuations translate into deviations in frequency, phase, or amplitude from an ideal signal and can disrupt the operation of electronic systems. Several types of jitter, such as phase jitter, periodic jitter, random jitter, and amplitude jitter, will not be discussed in detail in this thesis.
In our study, jitter was not analyzed in depth. However, Figure 6.10 shows the position of the amplitude maxima for the first pulses, and it can be seen that their position does not vary significantly during the diagnostic operation, except for channels 1 and 2. This is explained by the fact that the signals can not be distinguished from the noise, leading to the scattered points shown in the figure.
In addition, there is a slight offset of 1 ns between specific polychromator channels, but the positions of the amplitude maxima average around 800 and 900 ns. Pulse detection is sometimes significantly different from 800 and 900 ns, corresponding to the absence of scattering pulses.

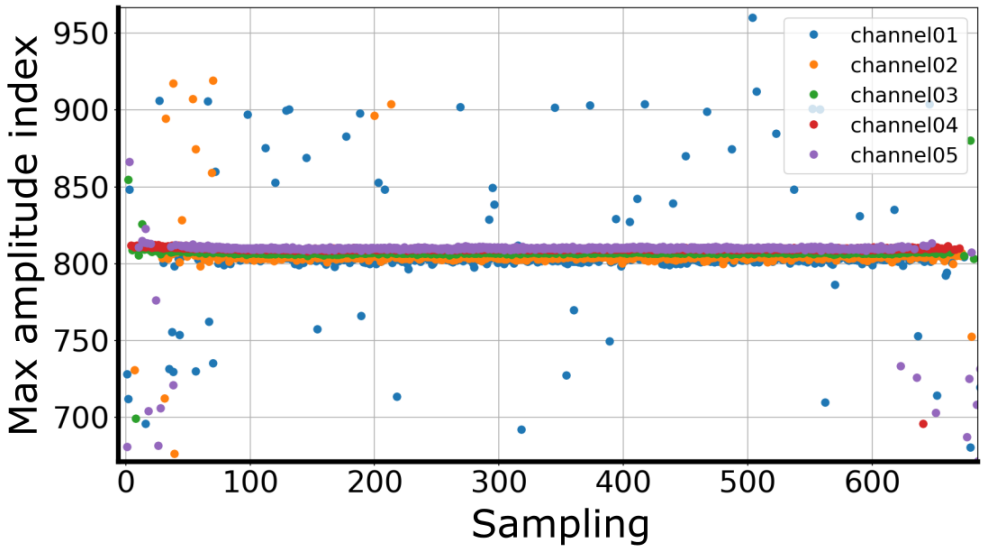

Figure 6.10: Index pulse maximum measured from the signal acquisition

In the future, measuring each NECTARINE card's jitter would be great for fixing the algorithm's maximum amplitude position for faster calculations.

6.3.2 Noise characterization

6.3.2.1 Nectarine card tests in laboratory

The cards were tested and evaluated in the laboratory to ensure they would provide low SNR measurements. In the laboratory, precise tests were carried out to compare the noise from the laboratory and the noise in the tokamak basement. The figure shows the noise histograms for the slow and fast channels, where it can be seen that the mean noise value is centered at 0. These laboratory tests provided a rigorous and reproducible noise assessment, essential for developing and improving the acquisition card. These tests served as a reference for noise characterization during the diagnostic operation.

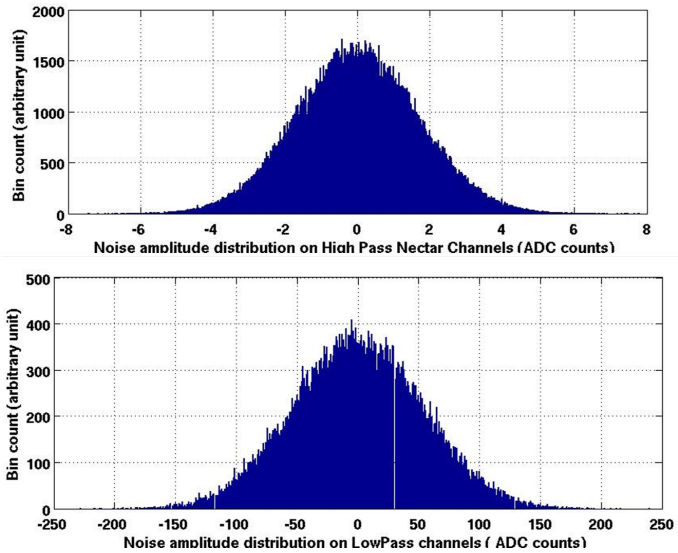

Figure 6.11: Electric noise at High and Low-frequency channel during laboratory test

6.3.2.2 Noise source identification

As mentioned in chapter 3, the NECTARINE card is used for one polychromator, to which five of the six fast channels are connected. However, all six channels are acquired during the diagnostic operation, enabling the noise level to be recorded when the card is located in the basement of the Tore hall. Figure 6.13 shows the noise histograms for the 640 samples where the diffusion pulse is known to be absent (see figure 6.12 at the plasma beginning). The histograms for channels 1, 2, and 3 are centered around 2.7, corresponding to the electronic noise level when the polychromator is connected to the card. In contrast, the noise of channel 6, which is not connected to the polychromator, is centered around 1.37. Furthermore, a comparison with the noise observed in the laboratory, centered at 0, leads to the conclusion that noise is higher in the Tore hall. This is logical, as auxiliary systems and other diagnostics interfere with the signals due to parasitic currents induced by the surrounding electromagnetic fields, amplified by the acquisition chain.
On the other hand, channels 4 and 5 show two distinct Gaussian distributions: one centered around 2.7, corresponding to electronic noise, and another centered around 7, indicating a second noise source. During tests and diagnostic operations on different scenarios, we conclude that these distributions seem correlated to Bremsstrahlung radiation—additional investigations are needed to confirm this. However, the figure 6.14 shows the evolution of σ_{noise} and Bremsstrahlung radiation measured by visible spectroscopy, which supports this hypothesis.

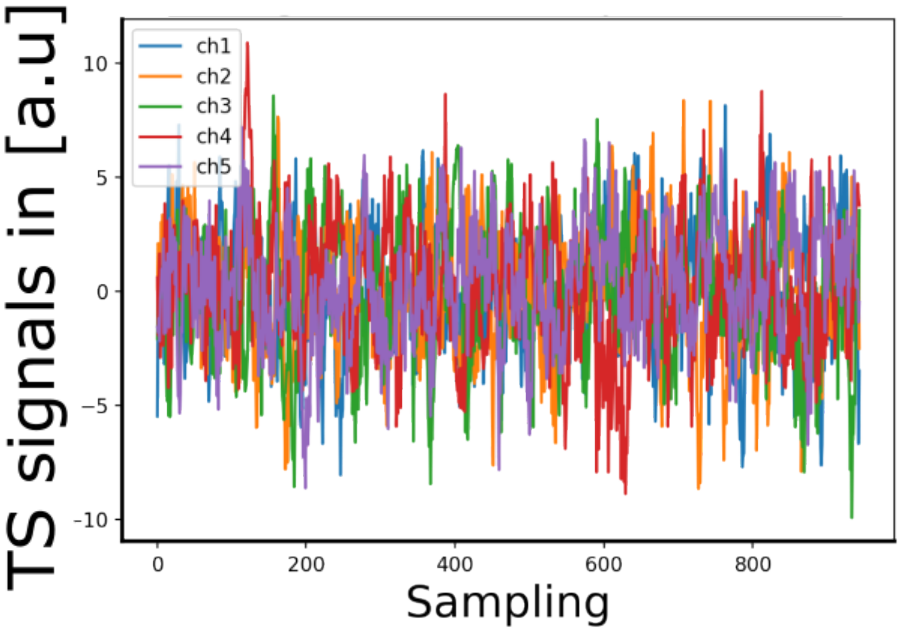

Figure 6.12: Noise visualization for the 5 channels for the plasma shot 60030

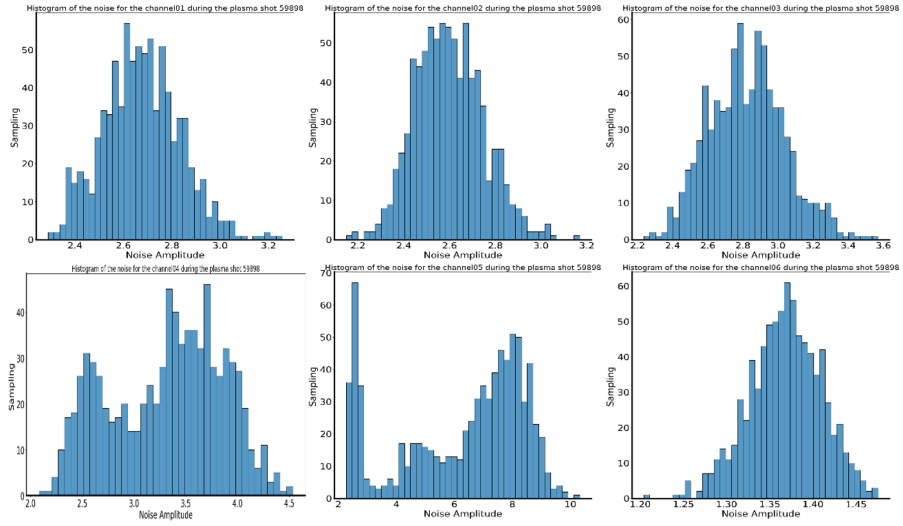

Figure 6.13: PDF of noise from all channels of a nectarine card.

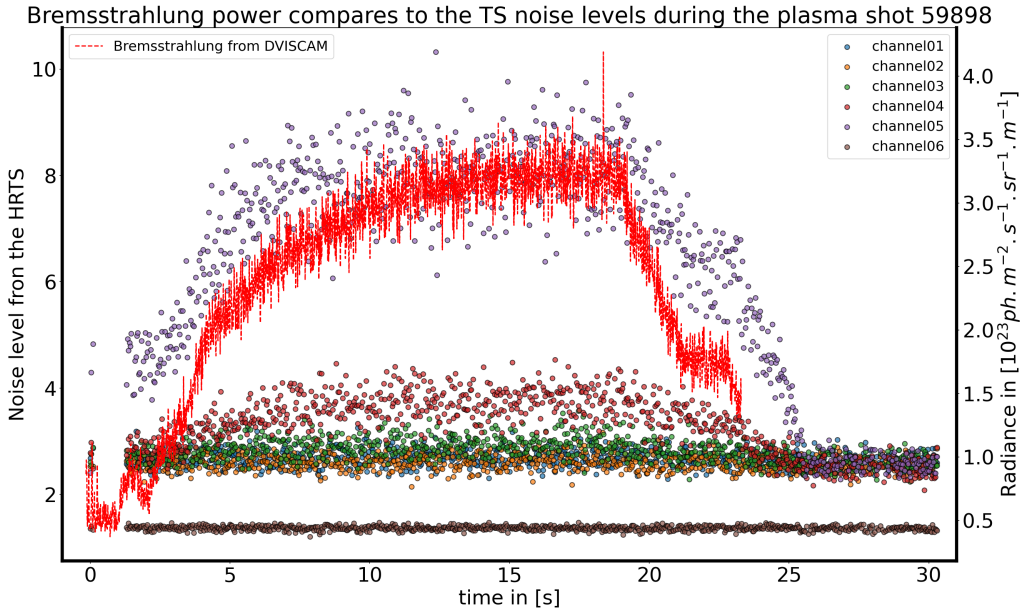

Figure 6.14: Noise estimated on 640 first samples for each acquisition during the plasma shots

6.3.2.3 Autocorrelation time on the fast channels

Consequently, as shown in the figures 6.8 and 6.17, these two noise sources impact Thomson scattering pulses, particularly at low densities where pulse amplitude is low. Although the nanosecond Laser impulse makes a significant frequency selection for usual global plasma dynamics in Tokamaks, background photons still impact the treatment of pulse scattering signal. Indeed, for some situations, as the second pulse represented in figure 6.17, the pulse signal is degraded.

To understand this, we measure the noise correlation time of each fast channel by computing the correlation using the Wiener-Kintchi Theorem:

$$\begin{cases} S_{SDP}(f) = \left| \int_{\infty}^{\infty} S_{noise}(t) e^{-i\omega t} dt \right|^2 & (6.2) \\ C(\tau) = TF^{-1}\left[\int |S_{SDP}(f)|^2 \right] & (6.3) \end{cases}$$

, where S_{SDP} is the spectral density function, $C(\tau)$ the correlation function, and by fitting the following equation (see figure 6.15):

$$C_{fit}(t) = Ae^{-\frac{\Delta t}{\tau_{corr}}} + c_0 \quad (6.4)$$

The table 6.1 gives the correlation time for each channel, which is the order of the pulse duration (ns). Consequently, noise can induce an error in pulse identification and bias the temperature estimate.

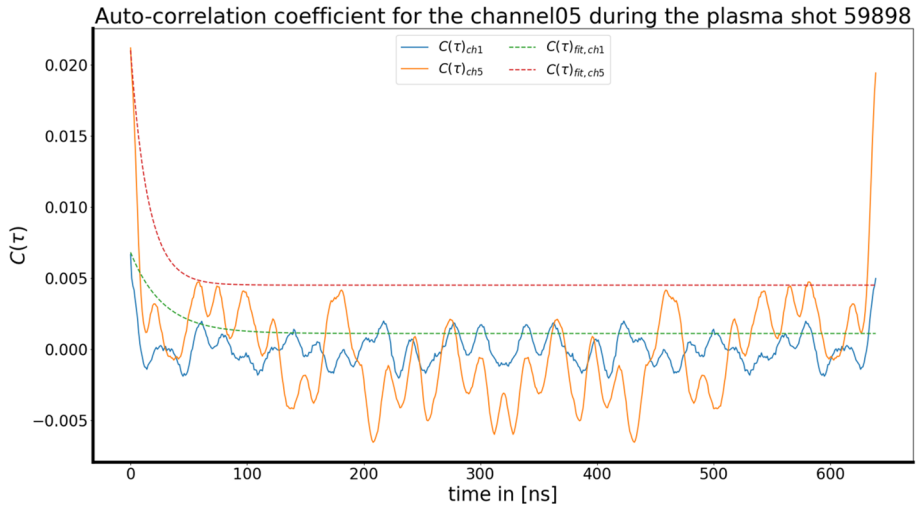

Figure 6.15: Correlation time estimation

Correlation time	channel 1	channel 2	channel 3	channel 4	channel 5
τ_{corr} in [ns]	11	10	13	7	8

Table 6.1: Optical collecting systems parameters for the HRTS on WEST.

6.3.2.4 Noise to Signal ratio

The last step is to estimate the NSR, which is defined as:

$$NSR = \frac{\sigma_{noise}}{A_{TS}} \tag{6.5}$$

Since noise is intrinsic to the signal, improving it is impossible. Therefore, the NSR informs us about the data validity and uncertainty regarding the electron temperature. Figure 6.16 shows the NSR for the polychromator channel 03 at each Nd:YAG pulse versus the time. At the plasma shot's beginning and end, the NSR is above 20 % for a σ_{noise} between 2 and 4, where the signal amplitude is under 100. These results can be explained by the low electron density inducing a Thomson signal amplitude of the same magnitude as the noise. NSR reinforces the idea that signals are degraded and cannot be quickly evaluated
A second region comprise between 0 and 5 % for a σ_{noise} in the range 4 to 10 is represented. This corresponds to a plateau where the electron density and the temperature are high and stable (see section 6.2). The NSR is low in this region, and the TS amplitude is above 100. Then, the signal is high, and the signal is not degraded anymore.

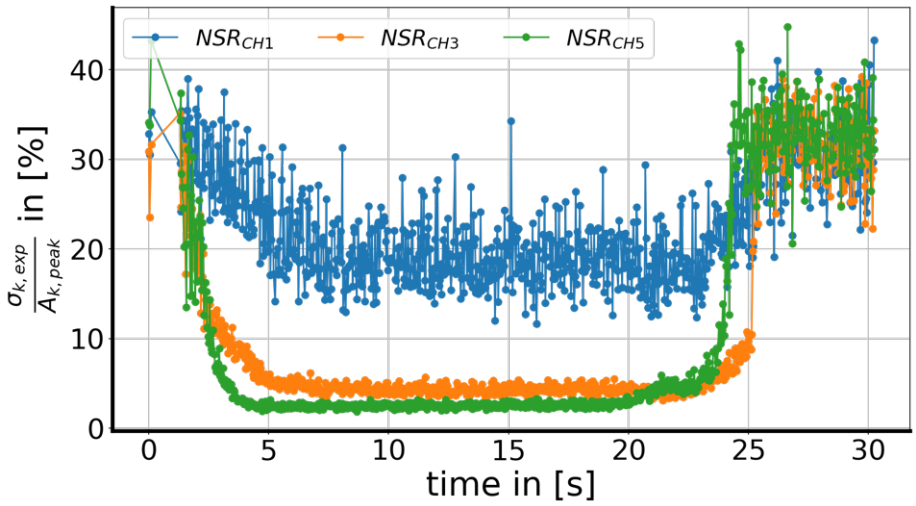

Figure 6.16: NSR estimate for three channels for the fast measurement during shot 59898 for the polychromator 19

6.3.3 Processing Signal method

6.3.3.1 Post processing method

Post-processing of Thomson signals is based on data pre-processed by synthetic diagnostics at a given scattering angle. This program is automated to estimate temperature and density for each acquisition using a least-squares regression method. Processing is based on a Gaussian fit (see relation 6.1) of the pulse, and an optimization algorithm is used to set the parameters (A, t, τ,b_0) and subtract the noise associated with the signal, to estimate the pulse integral best.

$$\zeta_{exp} = \int G_{fit} dt \tag{6.6}$$

Figure 6.8 shows that when the signal amplitude is close to the noise peak maximum A_{peak}, the integral can be distorted and become negative, making no physical sense and introducing a temperature estimation bias.
To solve this problem, it was decided to evaluate the maximum amplitude of the scattering pulse A_{TS} and the maximum noise peak A_{peak} for each channel when commissioning the diagnostics. If the maximum diffusion peak is less than 2.5 times the maximum noise peak, the latter is imposed to 0, as shown in the figure 6.18 for channel 1.

In the future, this processing will be improved by considering the detectors' calibration error and monitoring the laser pulse. This will enable the calculation of the correlation of the TS pulse with the laser pulse. This will be particularly useful during plasma start-up or transition phases when the noise level increases, accentuating the error in temperature estimation.

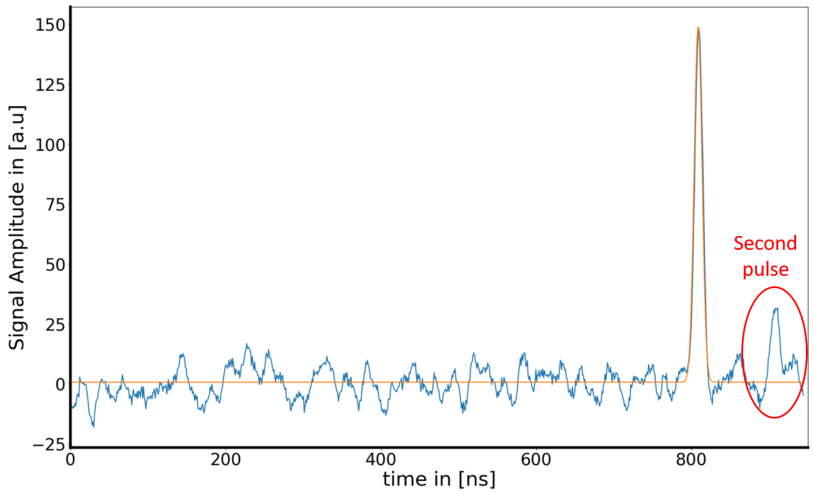

Figure 6.17: Post-processing method: Gaussian fitting with the Thomson Scattering pulse

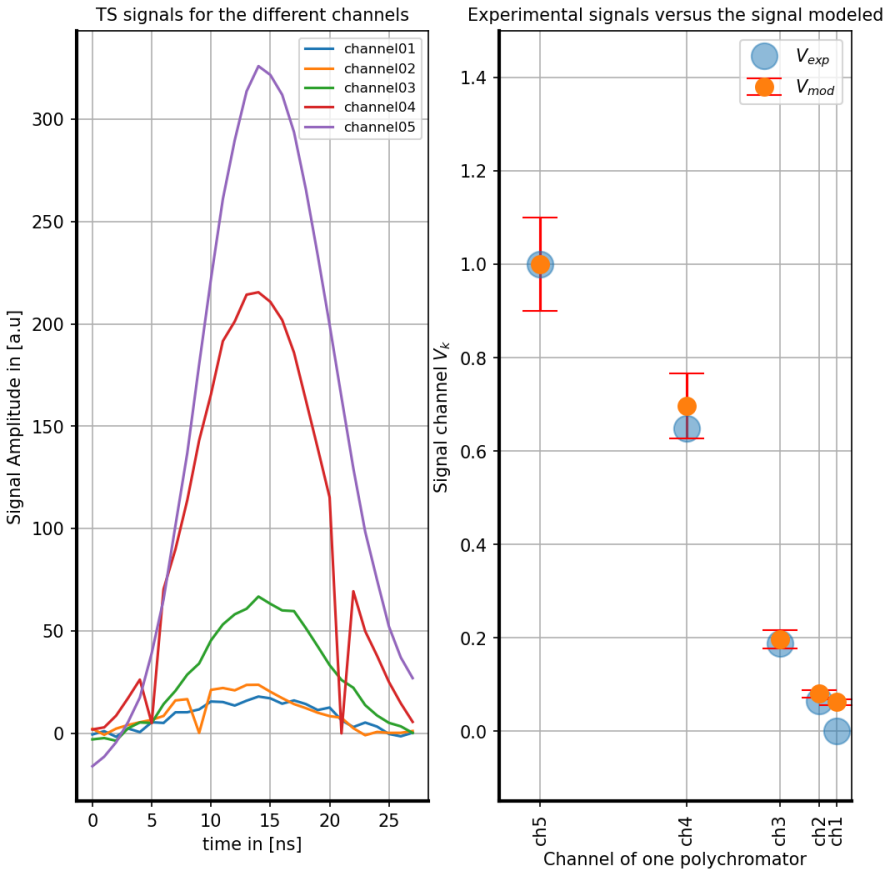

Figure 6.18: Comparison of synthetic signals with experimental signals

6.3.3.2 Real-Time processing method

We tested the data processing algorithm that will be used for real-time measurements, confirming its robustness and efficiency under actual experimental conditions. The characterization of the signal presented above has highlighted the impact of noise and the characteristics of the pulse. Based on this information, developing a real-time algorithm for estimating plasma density and temperature during future diagnostic operations has been proposed. This algorithm aims to minimize the number of instructions required to obtain a faster program better suited to real-time processing requirements.
This program will also use the preprocessed synthetic diagnostic data and the least-squares regression method to estimate the plasma parameters. However, the algorithm will not fit a Gaussian function in real-time processing but will exploit the raw signal directly.
It will look for amplitude maxima and their positions over the 1024 samples. From this information, a window of 50 ns (i.e., 50 samples at 1 Ghz) will be defined, within which an estimate of the average noise will be calculated to the left Bg_1 and right Bg_2 of the signal. The median noise value will then be subtracted from the signal before integration. Once integration is complete, the results will be used to estimate temperature using the least-squares method.

$$\begin{cases} \bar{B}_0 = \frac{Bg_1+Bg_2}{2} & (6.7) \\ \zeta_{exp,RT} = \int V_{TS,exp} - \bar{B}_0 dt & (6.8) \end{cases}$$

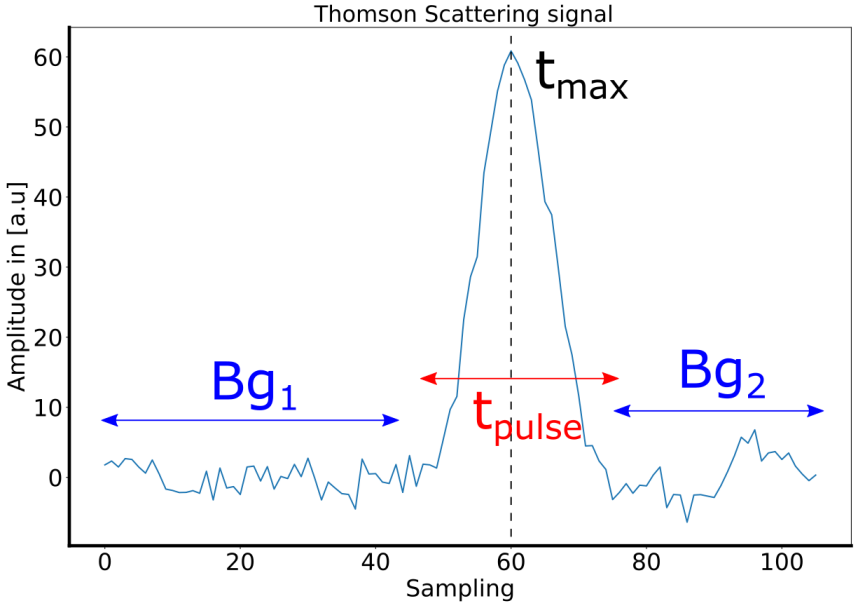

Figure 6.19: Pulse characterization for the real-time processing

In addition, the density estimate will be determined from one channel of the polychromator according to the line of sight.

$$n_{e,RT,k} = \frac{\zeta_{exp,RT}}{A\psi_{mod,k}} \tag{6.9}$$

As mentioned before, the tests carried out during commissioning showed that not all polychromator channels are affected by noise similarly. Therefore, we decided to estimate the electron density from channel 3 of the polychromator 19. This channel is only impacted by electronic noise and has a significant amplitude during the plasma shot.

6.4 Discussion

Figure 6.20 and 6.21 compare the electron temperature T_e and density n_e estimated by the real-time and the post-processing method. From this representation, a linear regression is made to understand the the performance of the real-time program.

$$f_{linear} = \alpha \Xi_{e,postprocessing} + \beta_0 \tag{6.10}$$

, where α is the slope, $\Xi_{e,postprocessing}$ represents either T_e or n_e retrieved with the post processing algorithm, and β the initial value.

The figure shows that the real-time algorithm agrees with the post-processing method. Indeed, the temperature evaluated is in the same order as the post-processing one.

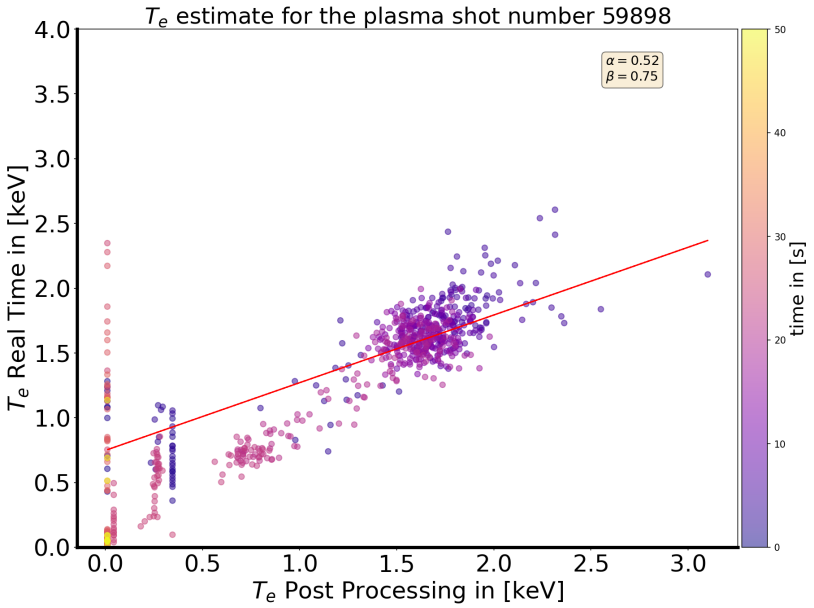

Figure 6.20: Fit comparisons of real-time and post-processing TS evaluation for the electron temperature

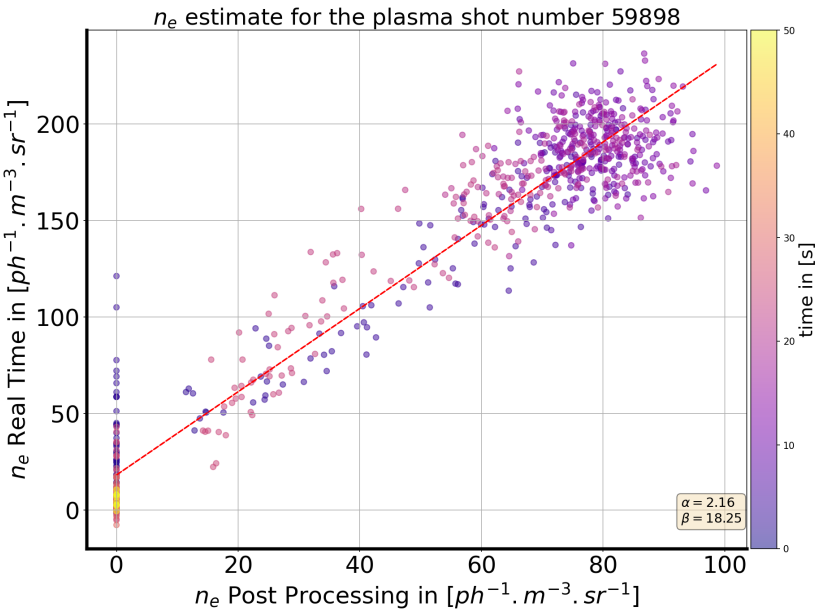

Figure 6.21: Fit comparisons of real-time and post-processing TS evaluation for the electron density

It is not equal to 0 at the origin, suggesting a systematic error will be present from this algorithm onwards. Consequently, a new, more robust algorithm will be necessary to reduce the error in temperature estimation.

The main interest of this algorithm is its speed, which is around 3 ms (2.6 strictly) to process the two pulses, as opposed to the post-processing algorithm, which is run at 16 ms for the two pulses. Both algorithms are fast enough to process the TS pulse between two laser shots (33 ms between two shots). However, this algorithm must be repeated 50 times to obtain a real-time density and temperature profile, leading to a running time of 150 ms. This running time is too long for Real time (RT), but it will improve.
Firstly, from the signal analysis, we observe that only 200 samples are needed to process the two pulses. Since the pulse duration and position are constant, we can reduce the data frame transmitted and modify the algorithm to process the data by assuming that the pulse will be in the same position.
Secondly, the algorithm has been tested on the cluster, not the Nectarine card or the acquisition computer. This will change the running time and might change the algorithm. Consequently, a C program has been developed, and it will be tested on Nectarine to reproduce the RT algorithm tested with the actual code. Once these tests have been carried out and the signal deepened, a new version of the algorithm will be developed to enable better real-time temperature and electron density estimation.

6.5 Experimental Result from the C9 campaign.

From the raw data, estimating an electron temperature T_e during the experimental campaign for several plasma shots has been possible. This first operation phase has been helpful to study the HRTS diagnostic in a noisy environment. During the experimental campaign, the electron temperature T_e has been estimated and compared to the electron temperature measured with the ECE and XICS diagnostics, [18, 75].

Shot with heating power: Figure 6.22 shows one of the first temporal traces of the electronic temperature obtained during the experimental campaign. It is observed that the HRTS temporal trace agrees with the two other diagnostics; however, the temperature estimate seems slightly different. The cause of such discrepancy could come from the Bremsstrahlung noise, which impacts the temperature evaluation. Another possibility could be that the laser energy decreases during the plasma shot, and the temperature assessment is inaccurate. In the future, monitoring the laser pulses and improving the acquisition setup will be essential to reduce discrepancies with the other diagnostic measurements.

X point Radiator Scenario:

An X point radiator (XPR) refers to a region near the X-point of magnetic equilibrium in a tokamak, where an intense emission of radiation is generated. The X-point is a feature of magnetic equilibrium in a tokamak in divertor configuration, formed by the action of toroidal coils that confine the plasma to the center by closing the magnetic field lines and opening them at the edge. In XPR experiments, impurities (such as nitrogen) are injected at the X point to induce plasma radiation, thereby reducing the heat flux reached by the divertor. This scenario exploits plasma collisionality to dissipate the energy of particles extracted from the plasma core. The aim is to control the radiation so that a large proportion of the thermal power is dissipated before the plasma reaches the divertor, thus avoiding damage to the divertor and reducing the tungsten impurity in the plasma core.

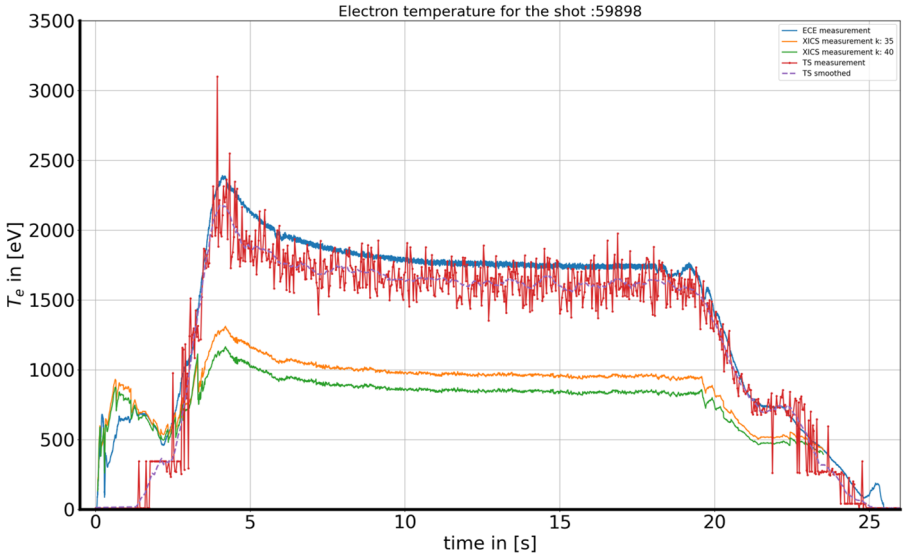

Figure 6.22: Electron temperature evolution in the plasma core over the time for different diagnostics

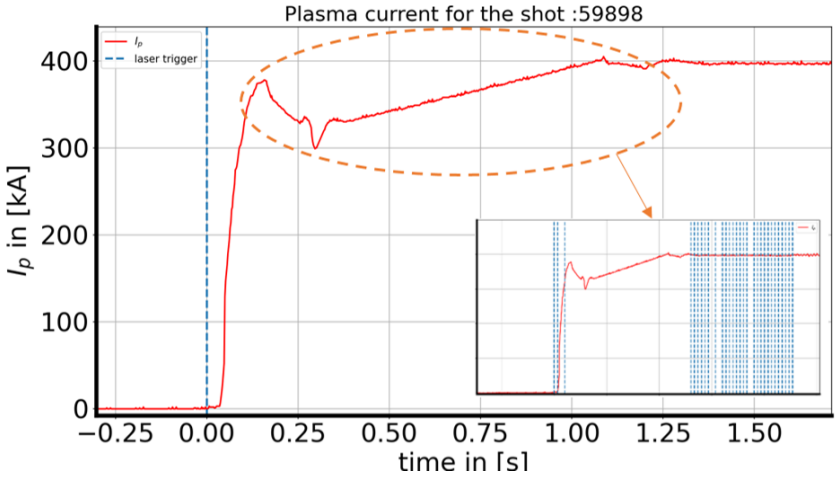

Figure 6.23: Plasma current for the shot number 59898

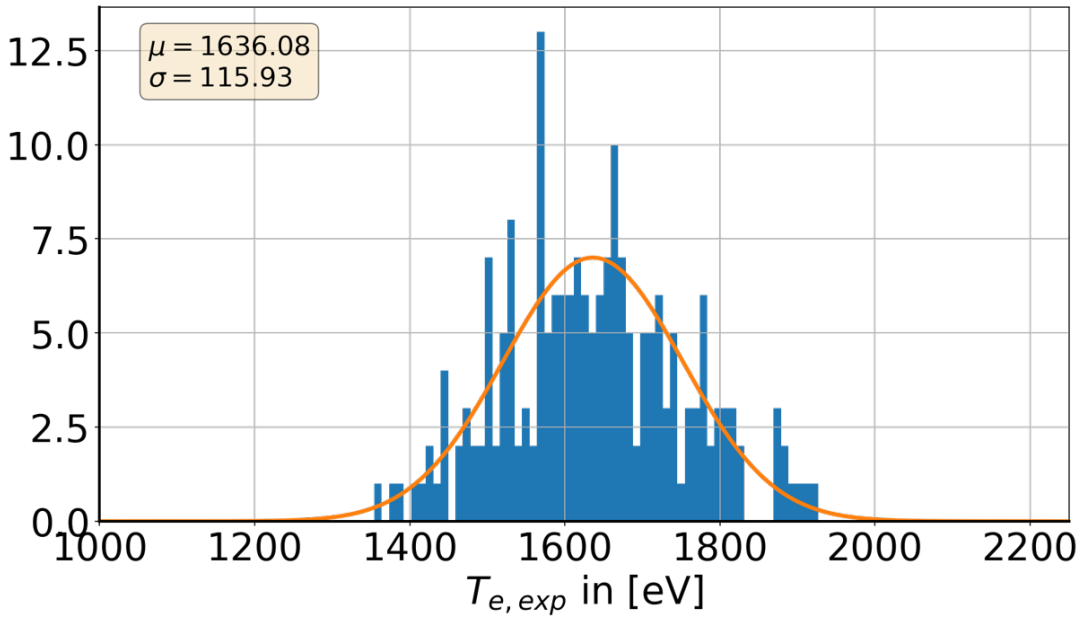

Figure 6.24: PDF of T_e for the first measurement point during a plateau for the shot 59898.

A lack of measurements at the start of the plasma shot due to a high NSR makes it impossible to estimate the temperature (see figures 6.22 and 6.16). In addition, some measurements are also missing due to data loss. This is easily understood by examining Figure 6.23, which superimposes the plasma current on the laser shots and highlights a lack of shots between t=0.003 s and t=1.5 s.
It should be noted, however, that despite fluctuations in the temperature measurements, an average trend in T_e emerges following the evolution of the plasma current: T_e remains constant when the plasma current is constant. This observation applies to the ECE and XICS measurements.
We were interested in this plateau to analyze the distribution of T_e, which follows a Gaussian distribution, as assumed when evaluating the performance of the diagnosis with the standard deviation. Therefore, the standard deviation seems to be a good estimator of the uncertainty in measuring T_e.

Based on the previous analysis and our understanding of the signal, we are now interested in estimating an experimental relative error of the temperature measurement. To compare this relative error with the simulation results of the chapter 4, we estimate an average temperature value and the deviation over a 3 s time window between t=7 and t=11 s where the plasma current is constant. The assumption is that on these plateaus, the electron temperature is constant. Figures 6.26 and 6.27 show the time trace of the electron temperature at the two measurement points, presented in section 6.2.1. Over this time window, the estimated temperature measurements fluctuate around an average value ($\bar{T}_e$). By plotting this relative experimental error $\left(\frac{\sigma_{exp,T_e}}{\bar{T}_e}\right)$ as a

function of plasma current, we can see that, at constant plasma current, the error does not vary (see figure 6.25). Consequently, although the number of shocks is limited to 5, the graph shows no dependence of the relative error on plasma current. The reader should be aware that this work needs to be extended. Since some plasma scenarios are performed with nitrogen injection for XPR or LH power injection, visualization of these parameters may be interesting. In addition, a comparison with the temperatures and emissivities of the walls in front of the telescope should be investigated to ensure that the error is only due to electronic noise and Bremsstrahlung radiation.

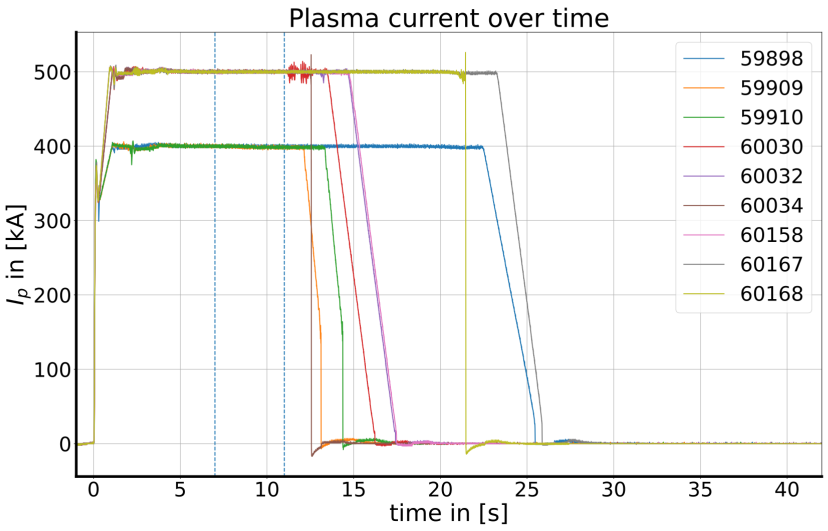

Figure 6.25: Plasma current for several plasma shots

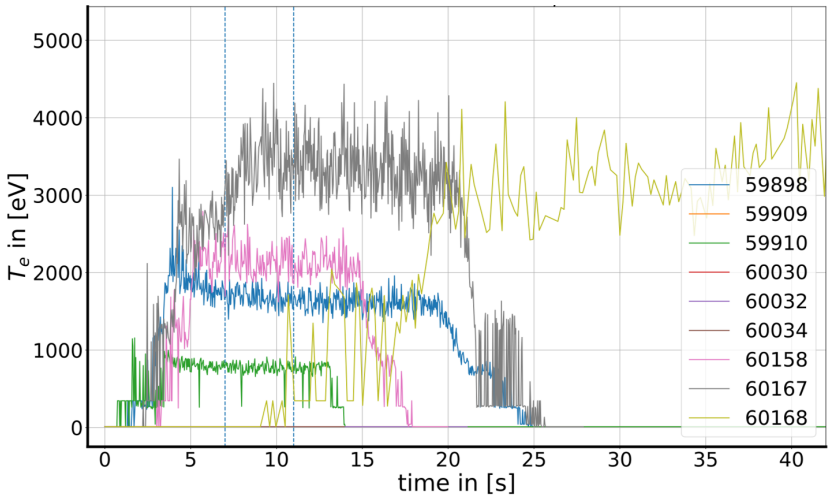

Figure 6.26: Temporal trace for the line of sight 10

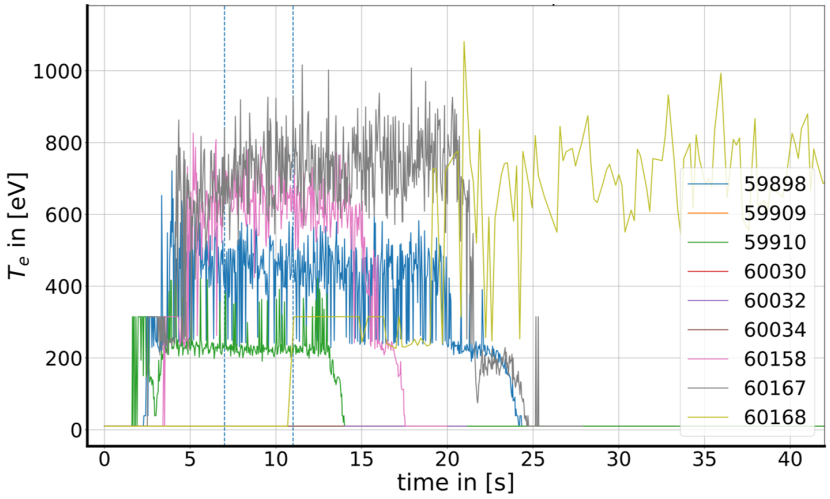

Figure 6.27: Temporal trace for the line of sight 18

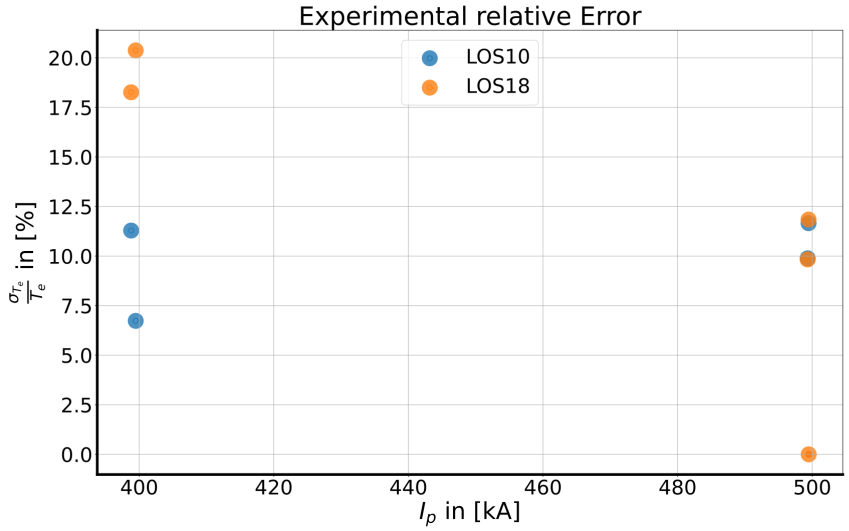

Figure 6.28: Experimental Relative error estimation during a plateau for the shot 59910,59898,60158,60167

6.6 Discussion about the Noise-to-Signal Ratio observed experimentally

Finally, it's important to note that the relative error in temperature is of the order of the values simulated by synthetic diagnostics. We observe differences, which can be explained by the fact that the numerically simulated noise was considered identical in all five acquisition channels. For an NSR of 5 %, the relative error on the T_e is about 5 %, according to the synthetic diagnostic. This is not the case in the experiment, so a

more detailed model would be attractive to get closer to the experimental values and thus be able to interpret the data obtained experimentally, see table 6.2.

Shot	Channel 1	channel 2	channel 3	channel 4	channel 5
59898	> 5%	10 – 15%	~ 5%	< 5%	< 5%
59909	> 5%	10 – 15%	~ 5%	< 5%	< 5%
59910	> 5%	10 – 15%	~ 5%	< 5%	< 5%
60158	> 5%	10 – 15%	~ 5%	< 5%	< 5%
60167	> 5%	10 – 15%	~ 5%	< 5%	< 5%
60168	> 5%	10 – 15%	~ 5%	< 5%	< 5%

Table 6.2: NSR of polychromator channel for several plasma shots

6.7 Perspective

The Thomson diagnostic is fundamental in fusion, and it is expected to be used in the following experimental campaign to see profiles for studying confinement modes and power extraction. Preliminary results have shown that, despite the limitations of the simplified laser line, reliable estimates of the electronic temperature can be obtained. This paves the way for future improvements and optimization of the laser alignment system for future experimental campaigns.

6.7.1 Steering laser line system

For instance, the pyroelectric detector will be installed in the SLLS to measure the laser pulse energy. Figures 6.29 and 6.30 show the test made after the experimental campaign with the pyroelectric. We varied the laser pulse energy to study the pyroelectric detector response by acquiring the signal amplitude and observing the dynamic. These tests have shown that the signal in the ms time scale and the amplitude can be measured from 0.05 V to 0.48 V. Therefore, they can be used and plugged into the Slow acquisition channel of the Nectarine card to estimate each laser pulse energy that could be useful to assess the electron density in RT.

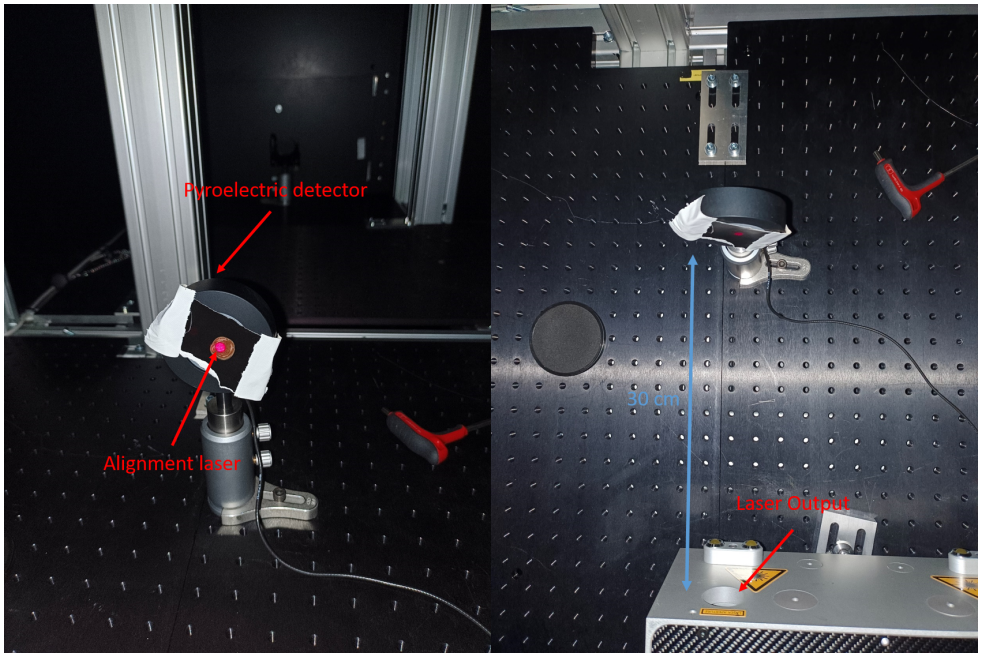

Figure 6.29: Pyroelectric test

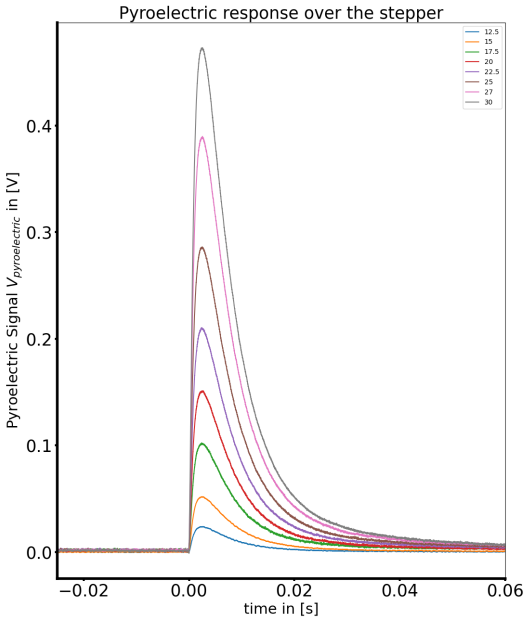

Figure 6.30: Signals acquired during the pyroelectric test

6.7.2 Plasma parameters retrieving

For this thesis, we focused, in particular, on estimating the electron temperature. This parameter does not require measuring the electron density, which can be compared with that of ECE and XICS. Once the laser energy has been measured and the spectral calibration performed, the electron density can be estimated in the future. However, the figure shows the time trace of the electron density relative to laser energy, scattering volume, and solid angle. This time trace is compared with interferometry, which broadly shows the same trend. This result gives us confidence in estimating electron density using post-processing or a real-time method.
In addition, it would be possible to get T_e profile as illustrated in the figure 6.32. This one represents a T_e profile obtained with the TS diagnostic, which is compared with the ECE profile for position measure in the tokamak.

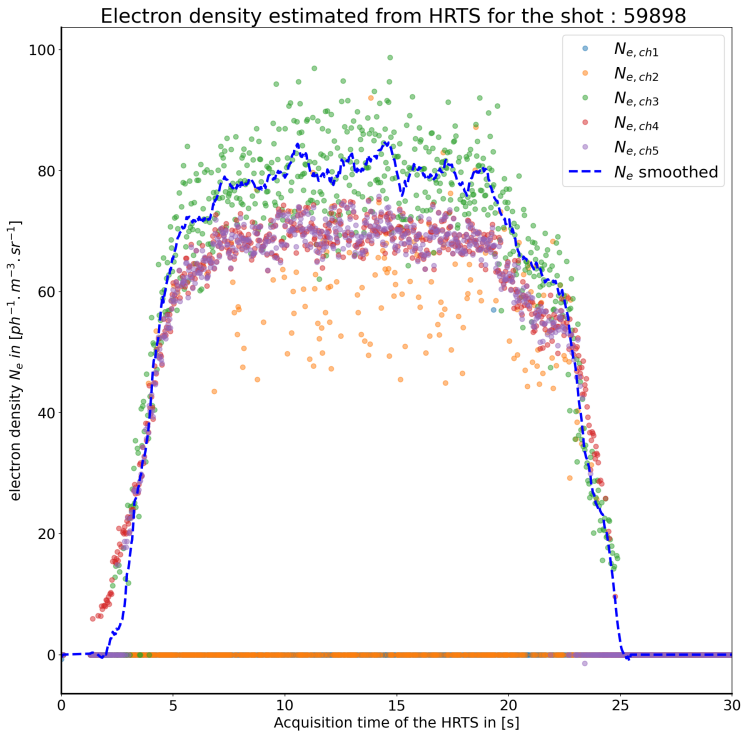

Figure 6.31: Electron density trace

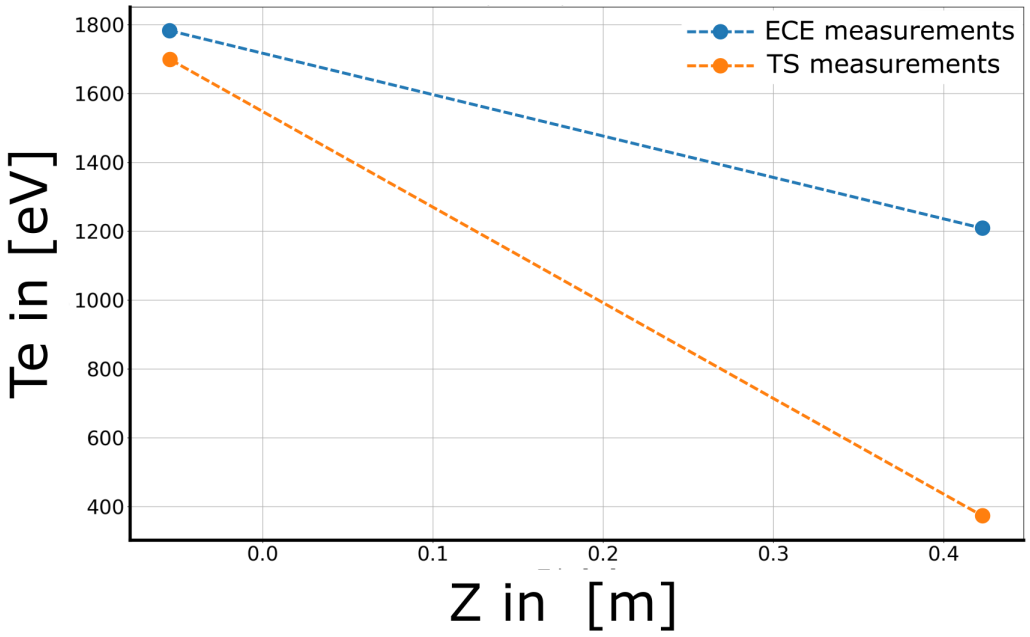

Figure 6.32: T_e profile for the plasma shot 59898. This is compared with the ECE measurement at the same position.

6.7.3 Real-time measurement

Finally, integrating the C code and testing it on the acquisition PC will enable us to evaluate its real-time performance. We haven't pointed out that the tests and programs used were developed in Python. Unlike the C language, a low-level compiled language, Python is a level language with lower execution time than C. Therefore, we can expect that the C code's performance will be better than Python's, allowing us to improve the algorithm to achieve a RT HRTS. Figure 6.33 represents the real-time processing method and how Synthetic Diagnostic will be used with this last.

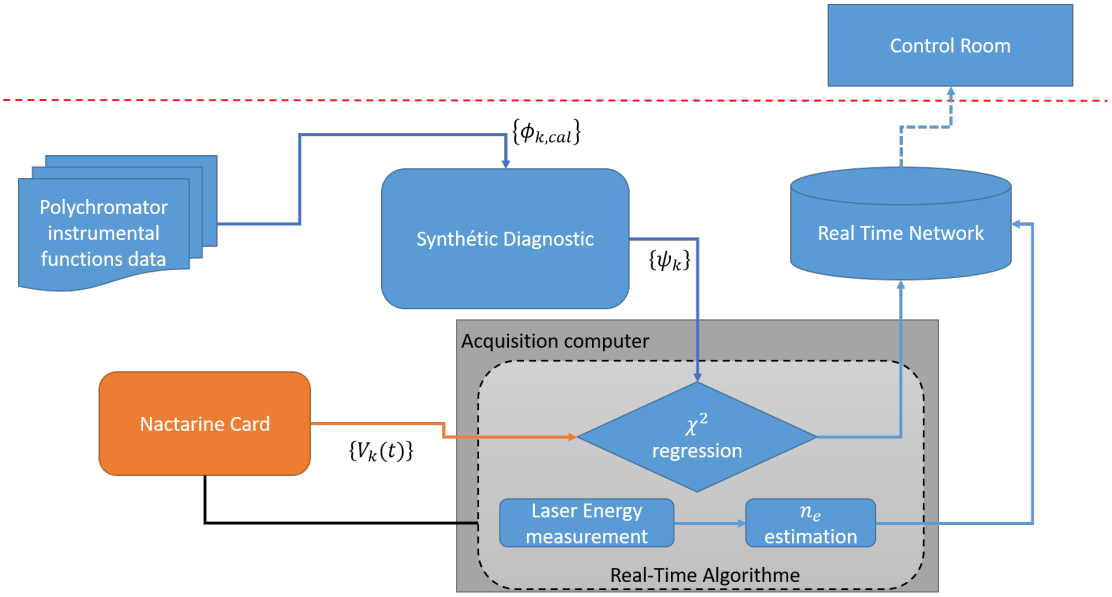

Figure 6.33: Real time diagram

7 Conclusion

Magnetic confinement fusion represents a new way of meeting the world's energy needs. However, the fusion process has yet to be mastered, so several scenarios must be studied for controlled fusion power generation. The WEST tokamak, a medium-sized tokamak with Tungsten inner walls, stands out for its unique ability to generate long-duration plasmas (around 1000 s) in single or double null configurations. This distinct feature allows for studying various scenarios for controlled fusion power generation. To maintain a plasma over relatively long periods, two actively cooled divertors receive the heat flux extracted from the fusion reaction (a low divertor made of solid tungsten and a high divertor with tungsten cladding).
Diagnostics, such as reflectometry, Langmuir probes, spectrometers, etc., are used to measure plasma temperature and electron density and characterize the plasmas produced in the different scenarios. Existing diagnostics on WEST, such as reflectometry and Langmuir probes, have limitations. They do not allow local measurements of these parameters in the machine references and are sensitive to magnetic equilibrium or plasma perturbations. A high-resolution Thomson scattering diagnostic has been developed to overcome these limitations and better understand fusion plasmas to complete the measurement at the plasma edge. This new diagnostic will enable the estimate of local density and electron temperature, with 20 measurement points at centimetric resolution and 30 at millimetric resolution at the core and the edge, respectively. The project focused on developing Thomson scattering diagnostics to obtain electron density, temperature, and pressure profiles.

Part of the work-study subject consisted of defining the laser control system that would enable the beams' misalignment to be corrected. During the first PHD year, a selection of optical components was made to set up a test bench to control the piezoelectric mounts, and we started the installation on the Tokamak plant. The cameras will be controlled by a LabVIEW program to control the Steering Laser Line System from the control room. The second part of the project was to work on the laser line implementation to ensure that the diagnostics would function properly during operation. In particular, the design will enable the system to be upgraded for real-time measurements of the three parameters mentioned above. High-quality measurements will be ensured using several detectors to estimate laser energy and a calibration bench to characterize the instrumental functions of each polychromator.

Secondly, a synthetic diagnostic was developed to study the diagnostic sensitivity, predict the diffused power, and interpret the signal to get the electronic temperature.

The first simulations demonstrated that the least squares regression method can determine the electron temperature. Based on this synthetic diagnostic, the relative temperature, density, and electron pressure errors were estimated to validate the system design and enable future prediction or interpretation of experimental results. During these simulations, we supposed that the Noise-to-Signal Ratios were identical for each polychromator channel, leading to a relative error of around 5% for density and temperature. In comparison, an error of 15% was evaluated for electronic pressure.

The work on the laser design and the development of the numerical twin led to the first diagnostic commissioning in 2024. The Steering Laser Line system allowed to steer vertically in the tokamak chamber with millimetric accuracy, while the synthetic diagnostic allowed the interpretation of the raw signals and estimate of the electronic temperature in two different positions.
A program has been developed to estimate the plasma parameters automatically and used during the experimental campaign for different plasma shots. This has demonstrated the feasibility of estimating a temperature from the acquired signals. Furthermore, a comparison with ECE and XICS diagnostics shows that the evolution over time agrees; however, the temperature estimate is not identical, and investigations must be carried out.
This commissioning will also enable signal characterization of the diagnosis's sensitivity and the measurement's uncertainty. The diagnostic's performance during the operation was evaluated to identify the various noise sources, validate the signal processing for post-processing and real-time, and compare the temperature and relative density measurements with the diagnostics already present on WEST. This work concluded that the primary noise source comes from Bremsstrahlung radiation, which significantly impacts temperature estimation.
On the other hand, although the NSR assumption in the simulation could be discussed, the estimated errors are similar to those in scientific papers. We also compared these results with the experimental relative errors assessed during the plasma steady state for several plasma shots. The relative error on T_e is higher. However, the relative error seems to be of the same order of magnitude.

In conclusion, the work done in this thesis represents an essential step in installing and operating a complex diagnosis such as Thomson scattering diagnostic. The work carried out over the last three years has led to the development of a laser system enabling the diagnostics to be operated, as well as the development of a synthetic diagnostic allowing the experimental signals to be interpreted to trace the electronic temperature and the relative errors in the measurement. During the diagnostic operation, we highlighted the significant sources of noise affecting temperature estimation. However, the relative errors estimated are between 5% to 20 % (according to the plasma scenarios) and do not correspond to the error evaluated by the synthetic diagnostic. Nevertheless, note that the experimental relative errors are in the same range as the

relative error simulated with the synthetic diagnostic. Therefore, the work validates the model implemented in the synthetic diagnostic and the temperature estimate for the various plasma scenarios. In the future, the diagnostic will be able to operate with two Nd:YAG lasers to improve temporal resolution and estimate temperature and electron density vertically. This will allow studying heat flux transport and L and H confinement modes.

Bibliography

[1] Jiri Adamek, J Seidl, M Komm, V Weinzettl, R Panek, J Stöckel, M Hron, P Hacek, M Imrisek, P Vondracek, et al. "Fast measurements of the electron temperature and parallel heat flux in ELMy H-mode on the COMPASS tokamak". In: *Nuclear Fusion* 57.2 (2016), p. 022010 (cit. on p. 41).

[2] Milan Aftanas. "Thomson Scattering Diagnostic on COMPASS Tokamak". PhD thesis. Charles University in Prague, 2015 (cit. on p. 68).

[3] T. Ashton, M. Backes, A. Balzer, D. Berge, J. Bolmont, S. Bonnefoy, F. Brun, T. Chaminade, E. Delagnes, G. Fontaine, M. Füßling, G. Giavitto, B. Giebels, J.-F. Glicenstein, T. Gräber, J.A. Hinton, A. Jahnke, S. Klepser, M. Kossatz, A. Kretzschmann, V. Lefranc, H. Leich, J.-P. Lenain, H. Lüdecke, I. Lypova, P. Manigot, V. Marandon, E. Moulin, T. Murach, M. de Naurois, P. Nayman, S. Ohm, M. Penno, D. Ross, D. Salek, M. Schade, T. Schwab, K. Shiningayamwe, C. Stegmann, C. Steppa, J.-P. Tavernet, J. Thornhill, F. Toussenel, and P. Vincent. "A NECTAr-based upgrade for the Cherenkov cameras of the H.E.S.S. 12-meter telescopes". In: *Astroparticle Physics* 118 (2020), p. 102425. ISSN: 0927-6505. DOI: https://doi.org/10.1016/j.astropartphys.2019.102425. URL: https://www.sciencedirect.com/science/article/pii/S0927650519302282 (cit. on p. 96).

[4] Petra Bílková, Milan Aftanas, Petr Böhm, Vladimír Weinzettl, David Šesták, Radek Melich, Jan Stöckel, Rory Scannell, and Mike Walsh. "Design of new Thomson scattering diagnostic system on COMPASS tokamak". In: *Nuclear Instruments and Methods in Physics Research Section A: Accelerators, Spectrometers, Detectors and Associated Equipment* 623.2 (2010). 1rs International Conference on Frontiers in Diagnostics Technologies, pp. 656–659. ISSN: 0168-9002. DOI: https://doi.org/10.1016/j.nima.2010.03.121. URL: https://www.sciencedirect.com/science/article/pii/S0168900210007047 (cit. on p. 98).

[5] P. Bohm, D. Sestak, P. Bilkova, M. Aftanas, V. Weinzettl, M. Hron, R. Panek, L. Baillon, M. R. Dunstan, G. Naylor, and M. J. Walsh. "Laser system for high resolution Thomson scattering diagnostics on the COMPASS tokamak". en. In: *Review of Scientific Instruments* 81.10 (Oct. 2010), p. 10D511. ISSN: 0034-6748, 1089-7623. DOI: 10.1063/1.3460450. URL: http://aip.scitation.org/doi/10.1063/1.3460450 (visited on 06/21/2021) (cit. on p. 75).

[6] Christophe Bouchand, Yassir Moudden, Eric Delagnes, Thomas Chaminade, Alain Barbuti, Mathieu Carole, Gilles Colledani, Nicolas Fedorczak, Alexandre Magnino, Gilles Moureau, et al. "The Data Acquisition System of WEST's New Thomson Scattering Diagnostics". In: *IEEE Real time* (2024) (cit. on pp. 83, 96).

[7] C. Bourdelle, J.F. Artaud, V. Basiuk, M. Bécoulet, S. Brémond, J. Bucalossi, H. Bufferand, G. Ciraolo, L. Colas, Y. Corre, X. Courtois, J. Decker, L. Delpech, P. Devynck, G. Dif-Pradalier, R.P. Doerner, D. Douai, R. Dumont, A. Ekedahl, N. Fedorczak, C. Fenzi, M. Firdaouss, J. Garcia, P. Ghendrih, C. Gil, G. Giruzzi, M. Goniche, C. Grisolia, A. Grosman, D. Guilhem, R. Guirlet, J. Gunn, P. Hennequin, J. Hillairet, T. Hoang, F. Imbeaux, I. Ivanova-Stanik, E. Joffrin, A. Kallenbach, J. Linke, T. Loarer, P. Lotte, P. Maget, Y. Marandet, M.L. Mayoral, O. Meyer, M. Missirlian, P. Mollard, P. Monier-Garbet, P. Moreau, E. Nardon, B. Pégourié, Y. Peysson, R. Sabot, F. Saint-Laurent, M. Schneider, J.M. Travère, E. Tsitrone, S. Vartanian, L. Vermare, M. Yoshida, R. Zagorski, and JET Contributors. "WEST Physics Basis". en. In: *Nucl. Fusion* 55.6 (June 2015), p. 063017. ISSN: 0029-5515, 1741-4326. DOI: 10.1088/0029-5515/55/6/063017. URL: https://iopscience.iop.org/article/10.1088/0029-5515/55/6/063017 (visited on 06/21/2021) (cit. on pp. 41, 44).

[8] S.A. Bozhenkov, M. Beurskens, A. Dal Molin, G. Fuchert, E. Pasch, M.R. Stoneking, M. Hirsch, U. Höfel, J. Knauer, J. Svensson, H. Trimino Mora, and R.C. Wolf. "The Thomson scattering diagnostic at Wendelstein 7-X and its performance in the first operation phase". en. In: *J. Inst.* 12.10 (Oct. 2017), P10004–P10004. ISSN: 1748-0221. DOI: 10.1088/1748-0221/12/10/P10004. URL: https://iopscience.iop.org/article/10.1088/1748-0221/12/10/P10004 (visited on 06/21/2021) (cit. on p. 70).

[9] V. Bruno, L. Allegretti, A. Barbuti, S. Bremond, Y. Cheng, C. Dechelle, N. Dufour, H. Feng, L. Gargiulo, D. Mouyon, B. Santraine, S. Shi, Y. Song, Y. Sun, E. Villedieu, B. Vincent, and L. Zheng. "WEST regular in-vessel Inspections with the Articulated Inspection Arm robot". In: *Fusion Engineering and Design* 146 (2019). SI:SOFT-30, pp. 115–119. ISSN: 0920-3796. DOI: https://doi.org/10.1016/j.fusengdes.2018.11.050. URL: https://www.sciencedirect.com/science/article/pii/S0920379618307579 (cit. on p. 146).

[10] KJ Callahan, Colin Chrystal, BA Grierson, SR Haskey, WW Heidbrink, and Jeffrey L Herfindal. "Integrated Zeff analysis on the DIII-D Tokamak". In: *Journal of Instrumentation* 14.10 (2019), p. C10002 (cit. on p. 109).

[11] T. N. Carlstrom, G. L. Campbell, J. C. DeBoo, R. Evanko, J. Evans, C. M. Greenfield, J. Haskovec, C. L. Hsieh, E. McKee, R. T. Snider, R. Stockdale, P. K. Trost, and M. P. Thomas. "Design and operation of the multipulse Thomson scattering diagnostic on DIII-D (invited)". en. In: *Review of Scientific Instruments* 63.10 (Oct. 1992), pp. 4901–4906. ISSN: 0034-6748, 1089-7623. DOI: 10.1063/1.1143545. URL: http://aip.scitation.org/doi/10.1063/1.1143545 (visited on 06/21/2021) (cit. on p. 75).

[12] Choong-Seock Chang and FL Hinton. "Effect of impurity particles on the finite-aspect ratio neoclassical ion thermal conductivity in a tokamak". In: *Physics of Fluids* 29.10 (1986), pp. 3314–3316 (cit. on p. 109).

[13] Brahim Chelihi, Gilles Colledani, Louis Doceul, Nicolas Lefèvre, Tristan Batal, Silvia Garitta, Frédéric Faïsse, Jean-Marc Verger, and Antony Bec. "Analysis of the New Thomson Scattering Diagnostic System on WEST Tokamak". In: *Applied Sciences* 12.3 (2022). ISSN: 2076-3417. DOI: 10.3390/app12031318. URL: https://www.mdpi.com/2076-3417/12/3/1318 (cit. on p. 88).

[14] Yingjie Chen, Zhenwei Wu, Wei Gao, Ang Ti, Ling Zhang, Yinxian Jie, Jizong Zhang, Juan Huang, Zong Xu, and Junyu Zhao. "Application of visible bremsstrahlung to Zeff measurement on the Experimental Advanced Superconducting Tokamak". In: *Review of Scientific Instruments* 86.2 (2015) (cit. on p. 109).

[15] Yingjie Chen, Zhenwei Wu, Wei Gao, Ling Zhang, Yinxian Jie, Jizong Zhang, Qing Zang, Juan Huang, Guizhong Zuo, and Junyu Zhao. "Measurement and analysis of Zeff in EAST tokamak". In: *Plasma Physics and Controlled Fusion* 56.10 (2014), p. 105006 (cit. on p. 109).

[16] MB Chowdhuri, R Manchanda, J Ghosh, KA Jadeja, Kaushal M Patel, Vinay Kumar, Ketan M Patel, PK Atrey, Y Shankara Joisa, SB Bhatt, et al. "Investigation of the behavior of effective charge of ADITYA tokamak plasmas". In: *Plasma Physics and Controlled Fusion* 62.3 (2020), p. 035015 (cit. on p. 109).

[17] *CM1-BP150*. 2024. URL: https://www.thorlabs.com/newgrouppage9.cfm?objectgroup_id=4138&pn=CM1-BP150 (cit. on p. 137).

[18] A. Da Ros, D. Vezinet, G. Colledani, Christel Fenzi-Bonizec, G. Moureau, G. Bertschinger, and the WEST Team. "Electron and ion temperature measurement with a new x-ray imaging crystal spectrometer on WEST". In: *Review of Scientific Instruments* 95.4 (Apr. 2024), p. 043505. ISSN: 0034-6748. DOI: 10.1063/5.0179905. eprint: https://pubs.aip.org/aip/rsi/article-pdf/doi/10.1063/5.0179905/19870452/043505_1_5.0179905.pdf. URL: https://doi.org/10.1063/5.0179905 (cit. on pp. 53, 163).

[19] Adrien Da Ros. "Modelling of a X-ray imaging crystal spectrometer on WEST tokamak and Tungsten spectrum analysis". PhD thesis. Aix-Marseille, 2024 (cit. on p. 132).

[20] *GV-5240CP-NIR-GL (AB02557)*. Datasheet camera (cit. on p. 80).

[21] *Information on UKAEA Polychromator design*. Datasheet (cit. on pp. 92, 93).

[22] *Diffraction Grating Handbook*. MKS datasheet (cit. on pp. 131, 132).

[23] *Avalanche photodiode*. a cube manual (cit. on p. 138).

[24] *Edmund Optics*. Nov. 2024. URL: https://www.edmundoptics.fr/knowledge-center/tech-tools/gaussian-beams/ (cit. on p. 72).

[25] Blaise Faugeras. "An overview of the numerical methods for tokamak plasma equilibrium computation implemented in the NICE code". In: *Fusion engineering and design* 160 (2020), p. 112020 (cit. on p. 53).

[26] J. Figueiredo, G. Naylor, M. Walsh, M. Dunstan, R. Scannell, and F. Serra. "MAST YAG Thomson scattering upgrade alignment system". en. In: *Review of Scientific Instruments* 81.10 (Oct. 2010), p. 10D521. ISSN: 0034-6748, 1089-7623. DOI: 10.1063/1.3475377. URL: http://aip.scitation.org/doi/10.1063/1.3475377 (visited on 06/21/2021) (cit. on p. 75).

[27] G Fiocco and E Thompson. "Thomson scattering of optical radiation from an electron beam". In: *Physical Review Letters* 10.3 (1963), p. 89 (cit. on p. 56).

[28] W Fundamenski. "Parallel heat flux limits in the tokamak scrape-off layer". In: *Plasma physics and controlled fusion* 47.11 (2005), R163 (cit. on p. 41).

[29] C Gil, G Colledani, M Domenes, D Volpe, A Berne, F Faisse, C Guillon, J Morales, P Moreau, B Santraine, et al. "Renewal of the interfero-polarimeter diagnostic for WEST". In: *Fusion engineering and design* 140 (2019), pp. 81–91 (cit. on p. 49).

[30] C Gil, C De Michelis, D Elbeze, C Fenzi, JP Gunn, F Imbeaux, PH Lotte, D Mazon, O Meyer, M Missirlian, et al. "Diagnostic systems on tore supra". In: *Fusion science and technology* 56.3 (2009), pp. 1219–1252 (cit. on p. 49).

[31] Christophe Gil, D Elbeze, A Beraud, B Echard, JC Patterlini, J Philip, L Toulouse, M Lipa, and A Litnovsky. "Retro-reflected channels of the Tore Supra FIR interfero-polarimeter for long pulse plasma operation". In: *Fusion Engineering and Design* 82.5-14 (2007), pp. 1238–1244 (cit. on p. 49).

[32] Alex Grosjean. "Impact of geometry and shaping of the plasma facing components on hot spot generation in tokamak devices". PhD thesis. Aix-Marseille, 2020 (cit. on p. 43).

[33] Feng Guo, Rongzhen Zhu, Ang Wang, and Xiang'ai Cheng. "Damage effect on CMOS detector irradiated by single-pulse laser". en. In: ed. by Farzin Amzajerdian, Astrid Aksnes, Weibiao Chen, Chunqing Gao, Yongchao Zheng, and Cheng Wang. Beijing, China, Sept. 2013, p. 890521. DOI: 10.1117/12.2034724. URL: http://proceedings.spiedigitallibrary.org/proceeding.aspx?doi=10.1117/12.2034724 (visited on 07/13/2022) (cit. on p. 80).

[34] A Hadni. "Applications of the pyroelectric effect". In: *Journal of Physics E: Scientific Instruments* 14.11 (Nov. 1981), p. 1233. DOI: 10.1088/0022-3735/14/11/002. URL: https://dx.doi.org/10.1088/0022-3735/14/11/002 (cit. on p. 81).

[35] NZ Hakim, BEA Saleh, and MC Teich. "Generalized excess noise factor for avalanche photodiodes of arbitrary structure". In: *IEEE transactions on electron devices* 37.3 (1990), pp. 599–610 (cit. on p. 93).

[36] C Honoré, P Hennequin, A Truc, and A Quéméneur. "Quasi-optical Gaussian beam tracing to evaluate Doppler backscattering conditions". In: *Nuclear fusion* 46.9 (2006), S809 (cit. on p. 50).

[37] A. Hossain and M.H. Rashid. "Pyroelectric detectors and their applications". In: *IEEE Transactions on Industry Applications* 27.5 (1991), pp. 824–829. DOI: 10.1109/28.90335 (cit. on p. 81).

[38] Ian H Hutchinson. *Principles of plasma diagnostics*. Vol. 44. 12. 2002, pp. 2603–2603 (cit. on pp. 48, 49, 51, 64, 67).

[39] Arne Kallenbach, M Bernert, M Beurskens, L Casali, M Dunne, T Eich, L Giannone, A Herrmann, M Maraschek, S Potzel, et al. "Partial detachment of high power discharges in ASDEX Upgrade". In: *Nuclear Fusion* 55.5 (2015), p. 053026 (cit. on p. 57).

[40] Mitsuru Kikuchi. *Fusion physics*. International Atomic Energy, 2002 (cit. on pp. 34, 41, 49).

[41] H Kimura, H Maeda, N Ueda, M Seki, H Kawamura, S Yamamoto, M Nagami, K Odajima, S Sengoku, and Y Shimomura. "Heat flux to the material surfaces in a tokamak". In: *Nuclear Fusion* 18.9 (1978), p. 1195 (cit. on p. 41).

[42] Sehyun Kwak, U Hergenhahn, U Höfel, M Krychowiak, A Pavone, J Svensson, O Ford, R König, S Bozhenkov, G Fuchert, et al. "Bayesian inference of spatially resolved Zeff profiles from line integrated bremsstrahlung spectra". In: *Review of Scientific Instruments* 92.4 (2021) (cit. on p. 109).

[43] *Lasers*. Non-serial Publications. EDP Sciences, 2002. ISBN: 9782868835284. URL: https://laboutique.edpsciences.fr/produit/242/9782759802777/lasers (cit. on p. 70).

[44] F. Leroux, L. Manenc, and M. Moreau. "Thomson scattering upgrade on Tore Supra". In: *Fusion Engineering and Design* 85.3 (2010). Proceedings of the 7th IAEA Technical Meeting on Control, Data Acquisition, and Remote Participation for Fusion Research, pp. 335–339. ISSN: 0920-3796. DOI: https://doi.org/10.1016/j.fusengdes.2010.02.019. URL: https://www.sciencedirect.com/science/article/pii/S0920379610000451 (cit. on p. 74).

[45] *Les lasers*. Non-serial Publications. Dunod, 2013. ISBN: 9782100590506. URL: https://www.dunod.com/sciences-techniques/lasers (cit. on p. 70).

[46] J Li, JL Chen, HY Guo, and GM McCracken. *Plasma-Wall Interactions*. 2012 (cit. on p. 52).

[47] SC Liew, CH Tan, YL Goh, AR Marshall, and JPR David. "Modeling of avalanche multiplication and excess noise factor in InAlAs avalanche photodiodes using a simple Monte Carlo model". In: *J. Appl. Phys* 104.1 (2008), p. 013114 (cit. on p. 93).

[48] Jochen Linke, Juan Du, Thorsten Loewenhoff, Gerald Pintsuk, Benjamin Spilker, Isabel Steudel, and Marius Wirtz. "Challenges for plasma-facing components in nuclear fusion". In: *Matter and Radiation at Extremes* 4.5 (2019) (cit. on p. 41).

[49] B Lipschultz, X Bonnin, G Counsell, A Kallenbach, A Kukushkin, K Krieger, A Leonard, A Loarte, R Neu, RA Pitts, et al. "Plasma–surface interaction, scrape-off layer and divertor physics: implications for ITER". In: *Nuclear Fusion* 47.9 (2007), p. 1189 (cit. on p. 41).

[50] Alberto Loarte, B Lipschultz, AS Kukushkin, GF Matthews, PC Stangeby, N Asakura, GF Counsell, G Federici, A Kallenbach, K Krieger, et al. "Power and particle control". In: *Nuclear Fusion* 47.6 (2007), S203 (cit. on p. 41).

[51] Kuniaki Matsuo, Malvin Teich, and B Saleh. "Noise properties and time response of the staircase avalanche photodiode". In: *Journal of Lightwave Technology* 3.6 (1985), pp. 1223–1231 (cit. on p. 93).

[52] JP Matte and J Virmont. "Electron heat transport down steep temperature gradients". In: *Physical Review Letters* 49.26 (1982), p. 1936 (cit. on p. 41).

[53] RJ McIntyre. "Factors affecting the ultimate capabilities of high speed avalanche photodiodes and a review of the state-of-the-art". In: *1973 International Electron Devices Meeting*. IEEE. 1973, pp. 213–216 (cit. on p. 93).

[54] H. J. van der Meiden, J. W. M. Vernimmen, J. van den Berg, and I. G. J. Classen. "Incoherent and Collective Thomson Scattering for the Determination of Electron and Ion Properties in Low-Temperature Plasma". en. In: *J Fusion Energ* 39.5 (Oct. 2020), pp. 251–260. ISSN: 0164-0313, 1572-9591. DOI: 10.1007/s10894-020-00262-5. URL: http://link.springer.com/10.1007/s10894-020-00262-5 (visited on 07/01/2021) (cit. on p. 67).

[55] H Meister, R Dux, LD Horton, B Kurzan, H Zohm, ASDEX Upgrade Team, and PJ McCarthy. "An integrated system to measure the effective charge of fusion plasmas in the ASDEX Upgrade tokamak". In: *Review of scientific instruments* 74.11 (2003), pp. 4625–4633 (cit. on p. 109).

[56] H Meister, R Fischer, LD Horton, CF Maggi, D Nishijima, ASDEX Upgrade Team, C Giroud, K-D Zastrow, JET-EFDA Contributors, and B Zaniol. "Z eff from Spectroscopic Bremsstrahlung Measurements at ASDEX Upgrade and JET". In: *Review of Scientific Instruments* 75.10 (2004), pp. 4097–4099 (cit. on p. 109).

[57] Miroslav Sos. "Optimisation of processing raw data from Thomson scattering diagnostic on the COMPASS tokamak". PhD thesis. Czech Technical University in Prague, 2018 (cit. on p. 140).

[58] O. Naito, H. Yoshida, T. Hatae, A. Nagashima, and T. Matoba. "Relativistic incoherent Thomson scattering spectrum for generalized Lorentzian distributions". en. In: *Physics of Plasmas* 3.4 (Apr. 1996), pp. 1474–1476. ISSN: 1070-664X, 1089-7674. DOI: 10.1063/1.871740. URL: http://aip.scitation.org/doi/10.1063/1.871740 (visited on 06/28/2021) (cit. on p. 68).

[59] Nicolas Rivals. "Understanding density regimes and divertor detachment in ITER relevant conditions Régimes en densité et détachement dans le plasma de bord d'ITER". PhD thesis. Aix-Marseille Université, 2023 (cit. on pp. 33, 35, 36, 40).

[60] A Patel, PG Carolan, NJ Conway, and RJ Akers. "Z eff profile measurements from bremsstrahlung imaging in the MAST spherical tokamak". In: *Review of scientific instruments* 75.11 (2004), pp. 4944–4950 (cit. on p. 109).

[61] Kiran Patel, Vishal Pillai, Neha Singh, Vishnu Chaudhary, Jinto Thomas, and Ajai Kumar. "GPIB based instrumentation and control system for ADITYA Thomson Scattering Diagnostic". en. In: *Fusion Engineering and Design* 112 (Nov. 2016), pp. 860–864. ISSN: 09203796. DOI: 10.1016/j.fusengdes.2016.06.021. URL: https://linkinghub.elsevier.com/retrieve/pii/S0920379616304215 (visited on 06/21/2021) (cit. on p. 96).

[62] paul toto paul. *MKS Newport : Pyroelectric description*. Nov. 2024. URL: https://www.newport.com/n/pyroelectric-physics (cit. on p. 81).

[63] A Pavone, U Hergenhahn, Maciej Krychowiak, U Hoefel, S Kwak, J Svensson, P Kornejew, V Winters, R Koenig, M Hirsch, et al. "Measurements of visible bremsstrahlung and automatic Bayesian inference of the effective plasma charge Zeff at W7-X". In: *Journal of Instrumentation* 14.10 (2019), p. C10003 (cit. on p. 109).

[64] Petr Böhm. "Temporally and spatially resolved evolution of plasma in the COMPASS tokamak". PhD thesis. Czech Technical University in Prague, 2011 (cit. on p. 68).

[65] S L Prunty. "A primer on the theory of Thomson scattering for high-temperature fusion plasmas". In: *Physica Scripta* 89.12 (Nov. 2014), p. 128001. DOI: 10.1088/0031-8949/89/12/128001. URL: https://dx.doi.org/10.1088/0031-8949/89/12/128001 (cit. on pp. 63–65).

[66] SK Rathgeber, L Barrera, T Eich, R Fischer, B Nold, W Suttrop, Matthias Willensdorfer, Elisabeth Wolfrum, ASDEX Upgrade Team, et al. "Estimation of edge electron temperature profiles via forward modelling of the electron cyclotron radiation transport at ASDEX Upgrade". In: *Plasma Physics and Controlled Fusion* 55.2 (2012), p. 025004 (cit. on p. 51).

[67] Rory. "Investigation of H-mode edge profile behaviour on MAST using Thomson scattering". PhD thesis. Oxford University, 2007 (cit. on p. 68).

[68] Luigui Salazar, Stéphane Heuraux, Roland Sabot, Andreas Krämer-Flecken, Tore Supra Team, TEXTOR Team, et al. "Extraction of quasi-coherent modes based on reflectometry data". In: *Plasma physics and controlled fusion* 64.10 (2022), p. 104007 (cit. on p. 50).

[69] Bahaa EA Saleh, Majeed M Hayat, and Malvin C Teich. "Effect of dead space on the excess noise factor and time response of avalanche photodiodes". In: *IEEE transactions on electron devices* 37.9 (1990), pp. 1976–1984 (cit. on p. 93).

[70] Mohammad A Saleh, Majeed M Hayat, Paul P Sotirelis, Archie L Holmes, Joe C Campbell, Bahaa EA Saleh, and Malvin Carl Teich. "Impact-ionization and noise characteristics of thin III-V avalanche photodiodes". In: *IEEE Transactions on Electron Devices* 48.12 (2001), pp. 2722–2731 (cit. on p. 93).

[71] B. Santraine, A. Berne, G. Caulier, J. Colnel, N. Ravenel, and F. Leroux. "From tore Supra to WEST: Evolution of the CODAC infrastructure". In: *Fusion Engineering and Design* 160 (2020), p. 111822. ISSN: 0920-3796. DOI: https://doi.org/10.1016/j.fusengdes.2020.111822. URL: https://www.sciencedirect.com/science/article/pii/S0920379620303707 (cit. on pp. 143, 147).

[72] R. Scannell, M. J. Walsh, P. G. Carolan, A. C. Darke, M. R. Dunstan, R. B. Huxford, G. McArdle, D. Morgan, G. Naylor, T. O'Gorman, S. Shibaev, N. Barratt, K. J. Gibson, G. J. Tallents, and H. R. Wilson. "Design of a new Nd:YAG Thomson scattering system for MASTa)". In: *Review of Scientific Instruments* 79.10 (Oct. 2008), 10E730. ISSN: 0034-6748. DOI: 10.1063/1.2971971. eprint: https://pubs.aip.org/aip/rsi/article-pdf/doi/10.1063/1.2971971/15727481/10e730_1_online.pdf. URL: https://doi.org/10.1063/1.2971971 (cit. on pp. 75, 94, 98).

[73] *Schematic of Compton scattering*. 2024. URL: https://www.radiation-dosimetry.org/fr/quelle-est-la-definition-de-la-diffusion-compton-definition/?utm_content=cmp-true (cit. on p. 62).

[74] B Schunke, GTA Huysmans, and PR Thomas. "Evidence of the influence of reflections on the Zeff profile measurements in the Tore Supra tokamak and their mitigation". In: *Review of scientific instruments* 76.8 (2005) (cit. on p. 109).

[75] J. L. Ségui, D. Molina, G. Giruzzi, M. Goniche, G. Huysmans, P. Maget, M. Ottaviani, and The Tore Supra Team. "An upgraded 32-channel heterodyne electron cyclotron emission radiometer on Tore Supra". In: *Review of Scientific Instruments* 76.12 (Dec. 2005), p. 123501. ISSN: 0034-6748. DOI: 10.1063/1.2140225. eprint: https://pubs.aip.org/aip/rsi/article-pdf/doi/10.1063/1.2140225/15902628/123501_1_online.pdf. URL: https://doi.org/10.1063/1.2140225 (cit. on p. 163).

[76] J. L. Ségui, D. Molina, G. Giruzzi, M. Goniche, G. Huysmans, P. Maget, M. Ottaviani, and The Tore Supra Team. "An upgraded 32-channel heterodyne electron cyclotron emission radiometer on Tore Supra". en. In: *Review of Scientific Instruments* 76.12 (Dec. 2005), p. 123501. ISSN: 0034-6748, 1089-7623. DOI: 10.1063/1.2140225. URL: http://aip.scitation.org/doi/10.1063/1.2140225 (visited on 07/13/2022) (cit. on p. 51).

[77] S. Shibaev, G. Naylor, R. Scannell, G. McArdle, T. O'Gorman, and M.J. Walsh. "Control and acquisition for MAST Thomson scattering diagnostics". en. In: *Fusion Engineering and Design* 85.5 (Aug. 2010), pp. 683–686. ISSN: 09203796. DOI: 10.1016/j.fusengdes.2010.03.035. URL: https://linkinghub.elsevier.com/retrieve/pii/S0920379610001067 (visited on 06/21/2021) (cit. on p. 96).

[78] Weston M Stacey. *Fusion plasma physics*. John Wiley & Sons, 2012 (cit. on p. 38).

[79] PC Stangeby. "Plasma sheath transmission factors for tokamak edge plasmas". In: *The Physics of fluids* 27.3 (1984), pp. 682–690 (cit. on p. 41).

[80] E. Stefanikova, M. Peterka, P. Bohm, P. Bilkova, M. Aftanas, M. Sos, J. Urban, M. Hron, and R. Panek. "Fitting of the Thomson scattering density and temperature profiles on the COMPASS tokamak". In: *Review of Scientific Instruments* 87.11 (Aug. 2016), 11E536. ISSN: 0034-6748. DOI: 10.1063/1.4961554. eprint: https://pubs.aip.org/aip/rsi/article-pdf/doi/10.1063/1.4961554/15616260/11e536_1_online.pdf. URL: https://doi.org/10.1063/1.4961554 (cit. on pp. 42, 111).

[81] HJ Sun, E Wolfrum, T Eich, B Kurzan, S Potzel, U Stroth, ASDEX Upgrade Team, et al. "Study of near scrape-off layer (SOL) temperature and density gradient lengths with Thomson scattering". In: *Plasma Physics and Controlled Fusion* 57.12 (2015), p. 125011 (cit. on p. 57).

[82] M Teich, Kuniaki Matsuo, and B Saleh. "Excess noise factors for conventional and superlattice avalanche photodiodes and photomultiplier tubes". In: *IEEE journal of quantum electronics* 22.8 (1986), pp. 1184–1193 (cit. on p. 93).

[83] M Tomes, M Carr, A Meakins, M Sos, P Bohm, P Bilkova, M Imrisek, F Jaulmes, I Borodkina, J Hecko, et al. "Thomson scattering synthetic diagnostic module for the Cherab framework". In: *Review of Scientific Instruments* 92.5 (2021) (cit. on p. 105).

[84] EA Tukhmeneva, S Yu Tolstyakov, GS Kurskiev, VK Gusev, VB Minaev, Yu V Petrov, NV Sakharov, A Yu Telnova, NN Bakharev, PB Shchegolev, et al. "Development of Zeff diagnostic system on the Globus-M (M2) tokamak and the first experimental results". In: *Plasma Science and Technology* 21.10 (2019), p. 105104 (cit. on p. 109).

[85] Laure Vermare, P Hennequin, C Honoré, M Peret, Guilhem Dif-Pradalier, X Garbet, J Gunn, Clarisse Bourdelle, Frédéric Clairet, J Morales, et al. "Formation of the radial electric field profile in the WEST tokamak". In: *Nuclear Fusion* 62.2 (2021), p. 026002 (cit. on p. 50).

[86] F Wagner. "A quarter-century of H-mode studies". en. In: *Plasma Phys. Control. Fusion* 49.12B (Dec. 2007), B1–B33. ISSN: 0741-3335, 1361-6587. DOI: 10.1088/0741-3335/49/12B/S01. URL: https://iopscience.iop.org/article/10.1088/0741-3335/49/12B/S01 (visited on 06/28/2021) (cit. on p. 42).

[87] R W Whatmore. "Pyroelectric devices and materials". In: *Reports on Progress in Physics* 49.12 (Dec. 1986), p. 1335. DOI: 10.1088/0034-4885/49/12/002. URL: https://dx.doi.org/10.1088/0034-4885/49/12/002 (cit. on p. 81).

[88] DG Whyte, DA Humphreys, and PL Taylor. "Measurement of plasma electron temperature and effective charge during tokamak disruptions". In: *Physics of Plasmas* 7.10 (2000), pp. 4052–4056 (cit. on p. 109).

[89] H. Yoshida, O. Naito, O. Yamashita, S. Kitamura, A. Nagashima, and T. Matoba. "Beam combiner for transient phenomena measurement in the JT-60 Thomson scattering diagnostic". en. In: *Review of Scientific Instruments* 66.1 (Jan. 1995), pp. 143–147. ISSN: 0034-6748, 1089-7623. DOI: 10.1063/1.1145247. URL: http://aip.scitation.org/doi/10.1063/1.1145247 (visited on 06/21/2021) (cit. on p. 75).

[90] H. Yoshida, O. Naito, O. Yamashita, S. Kitamura, T. Sakuma, Y. Onose, H. Nemoto, T. Hamano, T. Hatae, A. Nagashima, and T. Matoba. "Multilaser and high spatially resolved multipoint Thomson scattering system for the JT-60U tokamak". en. In: *Review of Scientific Instruments* 70.1 (Jan. 1999), pp. 751–754. ISSN: 0034-6748, 1089-7623. DOI: 10.1063/1.1149397. URL: http://aip.scitation.org/doi/10.1063/1.1149397 (visited on 06/21/2021) (cit. on p. 79).

[91] Hangyu Zhou, Zhengying Cui, Shigeru Morita, Bingzhong Fu, Motoshi Goto, Ping Sun, Chunfeng Dong, Yadong Gao, Yuan Xu, Ping Lu, et al. "Absolute sensitivity calibration of vacuum and extreme ultraviolet spectrometer systems and Zeff measurement based on bremsstrahlung continuum in HL-2A tokamak". In: *Review of Scientific Instruments* 83.10 (2012) (cit. on p. 109).

[92] HY Zhou, S Morita, M Goto, and CF Dong. "Zeff profile diagnostics using visible bremsstrahlung continuum for nonaxisymmetric plasmas with finite β in large helical device". In: *Journal of Applied Physics* 107.5 (2010) (cit. on p. 109).

[93] J. D. Zook and S. T. Liu. "Pyroelectric effects in thin film". In: *Journal of Applied Physics* 49.8 (Aug. 1978), pp. 4604–4606. ISSN: 0021-8979. DOI: 10.1063/1.325442. eprint: https://pubs.aip.org/aip/jap/article-pdf/49/8/4604/18381009/4604_1_online.pdf. URL: https://doi.org/10.1063/1.325442 (cit. on p. 81).